UNIVERSITY OF NAPLES FEDERICO II

School of Polytechnic and Basic Sciences

Department of Chemical, Materials and Industrial Production Engineering

XXXII° Ph.D. Programme in
Industrial Products and Processes Engineering

Ph.D. Thesis

Post-process Surface Finishing Treatments for AlSi10Mg Parts made by Selective Laser Melting Technology

Ph.D. Course Coordinator

Prof. Eng. Giuseppe Mensitieri
Department of Chemical, Materials and
Industrial Production Engineering
University of Naples Federico II

Ph.D. Supervisor

Prof. Eng. Antonino Squillace
Department of Chemical, Materials and
Industrial Production Engineering
University of Naples Federico II

Ph.D. Student

Eng. Andrea El Hassanin

ID: DR 992827

Academic Year 2016-2017

Contents

Abstract

It is well established nowadays that Additive Manufacturing (AM) represents one of the most intriguing manufacturing processes family on the actual market. Given the high design flexibility, the more effective usage of materials and the possibility to tailor the physical and mechanical properties, AM could represent the starting point for a remarkable change in the traditional manufacturing contexts based mainly on material subtraction processes. Although AM processes belong to the near-net-shape processes family, a consistent series of pre and post-process operations are required to meet the desired product specifications. In this context, the post-process surface finishing step represents a fundamental operation that is needed to achieve a satisfactory surface quality, representing very often also a high cost operation when carried out manually and leading to a not reliable and repeatable output. All these considerations are particularly true when considering metal AM processes, among which the ones based on powder feedstock as the raw material are the most sensitive to the mentioned surface quality issues.

Assumed that different surface treatments are currently object of study, aimed to reduce the surface roughness of metal AM parts, this Ph.D. thesis proposes an experimental and critical analysis of three different surface treatments, chosen according to their different interaction nature with the surface, i.e. mechanical, chemical and thermal. In order to investigate and understand the dynamics of the chosen treatments, the experimental activity reported in this work refers to flat geometry samples produced by means of the Selective Laser Melting (SLM) technology and employing one of the most widespread and studied alloys: the AlSi10Mg Aluminum alloy.

In Chapter 1, a comprehensive overview of AM technologies and their related challenges and constraints is provided, according to the state of the art. In Chapter 2, the metal AM processes generalities are described as well as their main issues, with a specific focus on Powder Bed Fusion -based (PBF) technologies and the mechanisms that imply the poor surface quality of the final parts. With this premise, in Chapter 3 a general overview of the actual surface treatments for metal Additive Manufactured parts is reported, followed by a detailed description of the theoretical background of the investigated surface finishing treatments.

On the basis of all the information reported and discussed, Chapter 4 describes in detail the aim and the scope of this Ph.D. thesis, considering all the provided theoretical elements.

The description of the experimental work starts from Chapter 5, where the case study used for all the experiments is presented as well as the general characterisation methodology, used to analyse and quantify the effects of the investigated finishing treatments.

Chapter 6 reports the results of the preliminary experiments carried out by means of the Fluidised Bed Machining treatment, that represents the mechanical interaction-based surface treatment considered in this work. To carry out the tests, a purposely made Plexiglas reactor was used to carry the experiments under different configurations. The process parameters considered in the reported preliminary experimental campaign are described, chosen according to the process background reported in Chapter 3.

In Chapter 7, the preliminary experiments related to the Chemical Polishing treatment are described. According to the process theoretical basics reported in literature for the Aluminum alloys, a two-stage process is proposed that enables a consistent surface quality improvement in terms of smoothing effect as well as the enhancement of the surface symmetry and brilliance. As a matter of concern, the superficial chemical composition changes were investigated.

Chapter 8 presents the results of the thermal interaction-based treatment considered: the Laser Surface Re-melting treatment (LSR). The premise of the experiments was to investigate the possibility to use a CO_2 laser radiation to perform the desired smoothing process. Considering the Aluminum alloy examined, it is known that CO_2 laser is not an effective solution due to the very low radiation absorption for its wavelength from traditionally machined Aluminum alloy surfaces, with lower roughness values compared to SLM. On the other hand, the high surface roughness of the considered SLM processed alloy allows to increase the absorption of the CO_2 radiation, in accordance with the laser surface processing theory. Therefore, for the latter case, CO_2 lasers could still represent a viable option for surface re-melting. Given the higher maturity level of LSR compared to the previous treatments about the identification and choice of the critical process parameters, as well as the more ease in changing the experimental process conditions, an experimental campaign based on the Design of Experiments (DoE) approach was used. Moreover, the influence of the treatment on the microstructure features of the considered alloy was investigated.

According to the preliminary conclusions provided for each of the studied finishing treatments, more general conclusions are reported in Chapter 9, referring both to the main experimental outcomes observed as well as to the main limitations highlighted with respect to the experimental campaign and characterisation methodology. Furthermore, the aim of this Chapter is also to provide some insights for future work as well as a more detailed comparison of the investigated surface treatments, considering different aspects that deserves a critical analysis.

1. Introduction of Additive Manufacturing

In this chapter, the general principle of Additive Manufacturing technologies is first presented and discussed. Consequently, according to the specific operating conditions in terms of material class, material feedstock and specific manufacturing principle, the different available technologies are briefly presented and discussed referring to the more recent implementations. Finally, a brief overview of the current applications and usable materials for Additive Manufacturing is provided.

1.1. Introduction

In the actual manufacturing market, distinguished by more challenging needs from the customers in terms of design, performances and higher products customization capability, there is more need from the industry side to employ manufacturing processes that are able to respond efficiently to rapid production changes, expressed in terms of batch volumes, lead time, and products characteristics. All these aspects are expected to be accomplished without compromising the quality of the final products. In this general context, a particular family of manufacturing technologies known as *Additive Manufacturing (AM)* could be located. As suggested by the term itself, these processes are defined in contrast with the traditional manufacturing processes based on the subtraction of material, starting from its raw form. According to the most widespread definition, the term Additive Manufacturing refers to all the technologies that, starting from a 3D CAD model, are able to produce near-net-shape parts through the deposition and/or stratification of material in a layer-wise manner [1, 2].

Emerged for the first time around the second half of the 80's, AM technologies were initially employed to realize prototypes, in order to have a visual idea of what would be manufactured subsequently with the most traditional technologies, according to the 2016 Wohlers report [3]. Nowadays, considering the great efforts carried out about the research of materials, new processes forms and the development of more sophisticated softwares assisting the designers (CAD, CAM, but more generally CAE), additive-based processes possess a maturity degree that doesn't allow them to be considered just for simple prototyping applications, therefore they actually represent effective manufacturing processes. With this premise, the term to identify this technologies family switched from *Rapid Prototyping* to *Additive Manufacturing* or *Solid Freeform Fabrication (SFF)* [1].

Despite the consistent number of actually available AM technologies that, as it will discussed later, are differentiated mainly with criteria based on the different material classes and feedstocks, there is a common principle that links them, i.e. the layer-wise consolidation of material mentioned above. The most generic subsequent steps involved in an AM process, as illustrated in Fig. 1.1, could be synthesized as follows [4]:

- Design of the 3D virtual part, using a CAD software;
- Information acquisition by the AM machine about the contours of the object, through the transformation of the CAD model into a *standard triangulation language file (.stl file)*;
- Proper placement and orientation of the solid model in the working space;
- Slicing of the virtual model generated by the AM machine software and process parameters setup;
- When needed, supports generation to hold the part under consolidation;
- Manufacturing of the part through layer-wise consolidation;

- Removal of the final part from the building volume;
- Supports removal though post-process finishing.
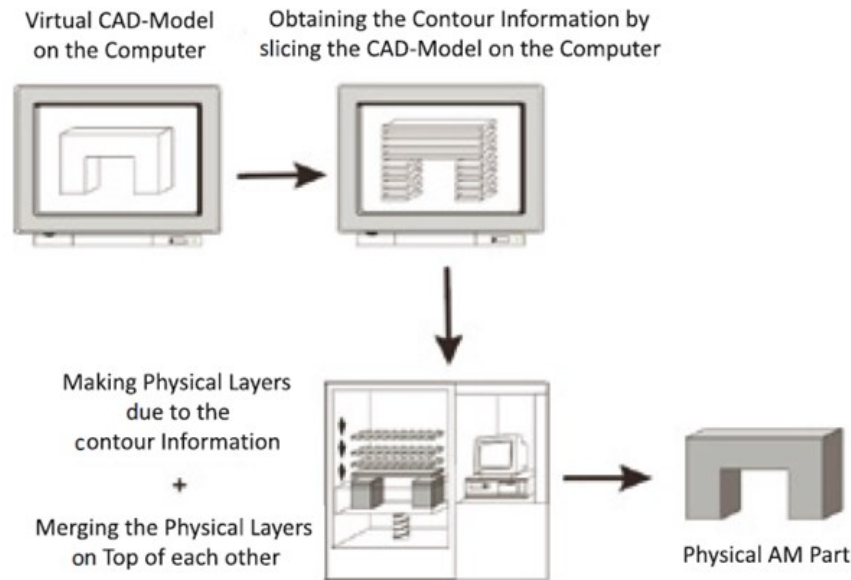
Figure 1.1. Fundamental steps involved in a generic AM process [4].

Considering this basic principle it seems clear that, in general, AM is able to provide major freedom of design of parts if compared to the traditional technologies based on material subtraction. More specifically, the bottom-up approach of AM does not involve the presence of any physical tool, with undeniable benefits related to the absence of a huge number of operations needed (if applicable) to produce parts with high geometry complexity, typically found on traditional manufacturing processes like CNC machining [5]. This latter aspect, as it will be discussed later, implies a second huge advantage over traditional manufacturing processes, i.e. the more effective use of raw material. In fact, the capabilities offered from AM technologies to build parts through the consolidation of material only where needed, allow to overcome several issues generally found, for instance, in CNC machining such as high waste production, the need for cutting fluids, high machine idle times and so on [6]. Therefore, AM could also promote a higher degree of sustainability in the manufacturing industry [7].

From a more general point of view, the feasibility of AM processes could represent a radical change of the traditional production paradigms, according to their high potential. Furthermore, AM represents one of the *Key Enabling Technlogies* that allows the manufacturing industry to move forward to its highest evolved form, the *Industry 4.0*. The latter is characterized by the adoption of highly integrated manufacturing solutions, a strong interconnection between the elements of a production system, and a deeper involvement of the final customers in manufacturing decisions through some other fundamental elements such Cloud computing, Internet of Things and Big Data Analysis [8].

1.2. Classification of AM technologies

As mentioned above, many different AM technologies are available nowadays, mainly categorized by the material class and feedstock considered. These variables actually dictates the specific AM technology to employ, considering the final applications. Moreover, considering the very first applications of AM for prototyping, the processes consequently developed were meant for processing low cost materials with limited structural properties. As an example, the mentioned first applications of AM around the second half of the '80s were related to the development of the *StereoLithography (SL)* technology from 3D Systems, a process that follows the principle of consolidation of parts through photopolymerization of a liquid polymer bath [3]. A few years later, different AM processes were developed such as *Fused Deposition Modeling (FDM)*, whose material input is mainly a polymer filament that is subsequently extruded through a deposition nozzle [9], or *Selective Laser Sintering (SLS)* that involves a laser beam and powder feedstock materials, the latter spread on a building plate and selectively fused [10]. Nowadays, the number of AM technologies for polymers increased significantly: in order to provide a comprehensive view, Fig. 1.2 illustrates the actually available AM technologies for polymers, according the categorization criteria discussed before.
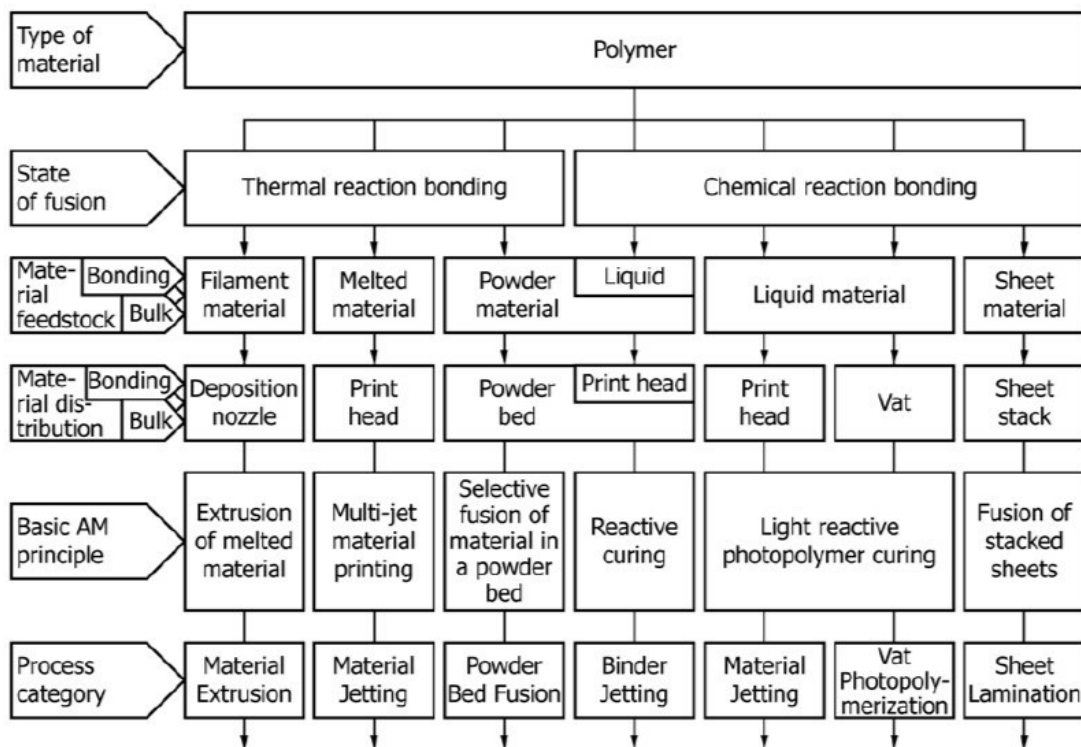
Figure 1.2. General classification of AM technologies for polymer materials [2].

Given the main benefits of AM technologies in comparison with the traditional manufacturing processes such CNC machining, it is clear that, over the years, the interest in these processes increased a lot especially in terms their applicability to materials that represent a larger cost fraction in the manufacturing chain.

The first material class that naturally matches this issue are metals, whose raw material and machining costs are generally larger compared to polymers and depending on the specific metal (or more frequently, alloy) considered. With this aim, a parallel research field and subsequent

technologies development was born to optimize the employment of AM for metallic materials.

The main AM technologies for metals (but not all of them), discussed in detail in Chapter 2, belong to three main categories according to a review paper published by Frazier in 2014 [11], i.e. Powder Bed Fusion (PBF), Directed Energy Deposition (DED) and Wire-feed technologies. Among these, the powder-based AM technologies would represent a crucial step forward in near-net-shape manufacturing, given the great benefit deriving from usage of metal powders that imply a significant amount of savings due to a more effective use of material. In this context, PBF technologies such as *Selective Laser Melting (SLM)* and *Electron Beam Melting (EBM)* represent the leading metal AM technologies in which both research and industry is paying the major attention [12]. On the other hand, Wire-feed AM technologies such as Wire Arc Additive Manufacturing (WAAM) ensures a major freedom in terms of building volume, given the major ease to handle a ductile wire instead of reactive powders, but with a higher lack in dimensional accuracy.

As for some metals, different process considerations needs to be done for ceramic materials. Generally speaking, these materials are processed through AM in more than a single step using typically ceramic powders, employed in pure form or mixed with binding agents as illustrated in Fig.1.3 [2]. Therefore, starting from the raw feedstock, ceramic powders are manipulated through AM in order to produce dense compacts with the desired geometry, subsequently sintered by means of furnace treatments according to the established ceramics powder manufacturing technologies or, in some specific technologies, through direct selective powder fusion [13-15]. The main AM technologies used to process ceramic materials include SLS, LENS and SLM as single-step options, while technologies based on the Material Jetting principle (i.e. Direct Inkjet Printing, Binder Jetting, Aerosol Jetting and so on) are typically used to produce dense parts (*green parts*) that undergoes to a subsequent selective fusion or a post-process sintering step.
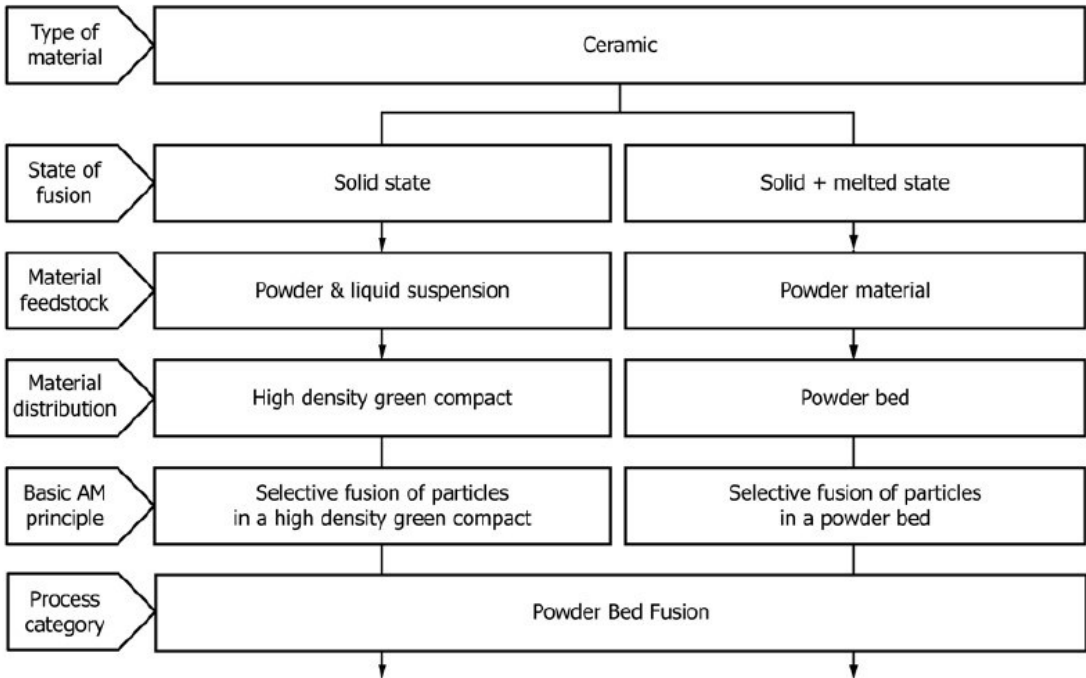

Figure 1.3. General classification of AM technologies for ceramic materials [2].

Based on all these considerations for the individual materials, a further AM research field is dedicated to the manufacturing of composite materials parts. In fact, another appreciable benefit given by AM technologies, resulting from the combination of the layer-wise consolidation approach and the optimized use of materials with respect to the design, is represented by the ability to mix different materials. In this way it is possible to produce, through single or multi-step processes, composite structures with tailored properties and even functionally graded properties inside a single part [16-19]. This benefit could be appreciated by processing materials that were previously blended as a powder mixture, applicable for instance in the SLM process, or the mixing process could even carried out directly, taking advantage of the concurrent deposition and consolidation through DED based processes. Following these application principles, a lot of material and feedstock are possible, like direct AM for Carbon Fiber Reinforced Plastics (CFRP), Metal Matrix Composites (MMCs), Ceramic Matrix Composites (CMCs) and so on. Moreover, reinforcement phase in a composite material could be used with different feedstock, such as fibers, powders, nanoparticles and more.

It is worth to note that the presented overview of AM technologies does not take into account a lot of specific emerging technologies, due to quite rapid changes and developments of these processes occurring in this era, in order to find the best manufacturing configurations for different materials and applications. However, standing on the actual knowledge and standards, the different material classes investigated over the last twenty years shares, under proper process conditions, the characteristics of the main AM processes mentioned. For sake of clarity, Fig. 1.4 highlights the general multi-step AM processes principles shared between metals, ceramics and composites [2].
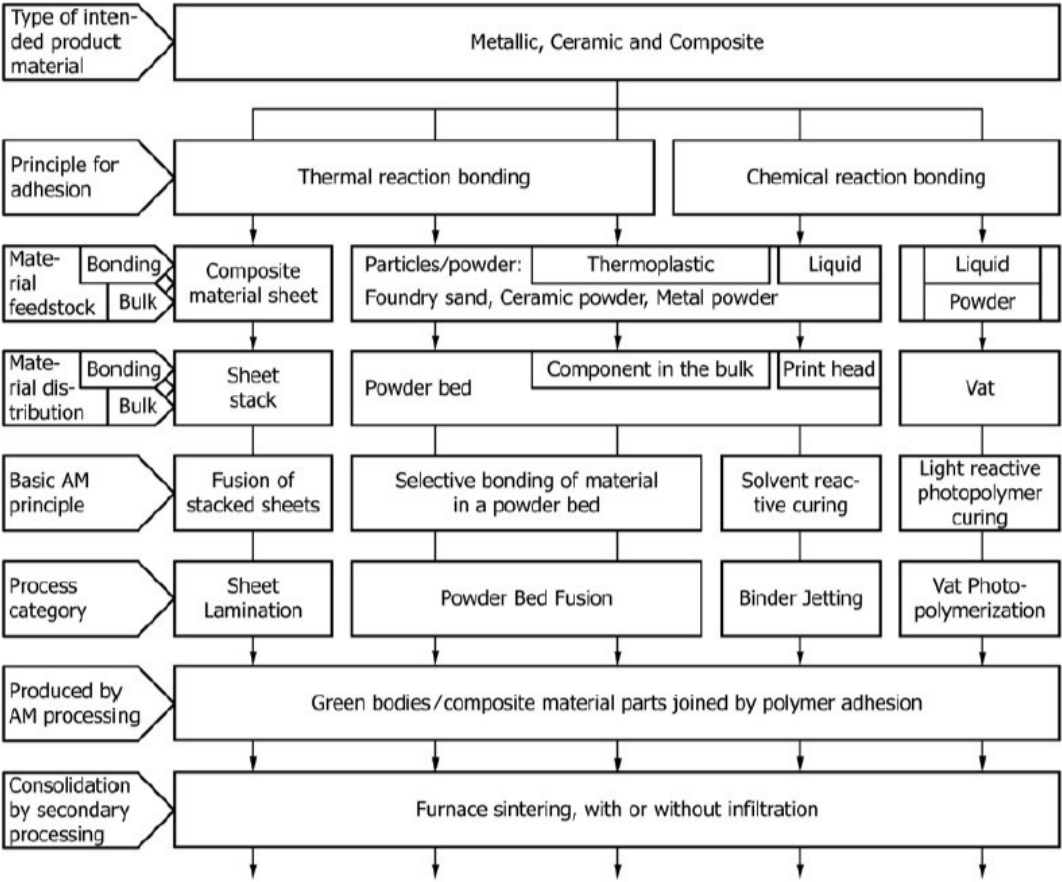

Figure 1.4. General principles of multi-step AM processes for metals, ceramics and composite materials [2].

1.3. Materials and applications of AM

According to the previous section, it is quite clear that — considered the wide spectrum of available AM technologies, the very high design flexibility and their capabilities to process the four main material classes such as polymers, metals, ceramics and composites — the corresponding applications would be practically infinite. Naturally, the application of an AM technology is, as mentioned before, dictated by the choice of the proper material. For instance, it is well established that polymer parts produced by FDM technology are not suitable for structural applications, given the low mechanical properties that does not allow a part to bear significant mechanical loads.

The most promising AM technologies for structural applications, i.e. aeronautic, aerospace, automotive, but also biomedical and so on, are metal AM processes whose development to a satisfactory degree would represent an important development for the manufacturing industry. Moreover, the cited benefits of high material savings, final properties tailoring and general process sustainability, makes AM technologies feasible for applications at different levels, as witnessed by the high interest spent from all the research institutions and industries around the world. One of the examples of the leading sectors that are pushing forward the development of efficient AM processes is the aerospace sector, where AM feasibility would represent a great advantage for the production of high value critical parts like, for instance, jet engines parts as reported in Fig. 1.5. Another example of great application of AM technologies, due to the fulfillment of the design and properties requirements, is the biomedical sector: the most appreciable applications in this case would be the manufacturing of highly customized implants for surgery, as the example reported in Fig. 1.6 of Ti6Al4V hip prosthesis realized with EBM technology developed by Arcam. Moreover, AM actually satisfies also the requirements for sectors were parts complexity and high material costs are privileged instead of mechanical properties: for instance, an example would be jewelry as reported in Fig. 1.7 that shows the feasibility of metal AM processes to manipulate precious metals like gold. However, as a general consideration, the feasibility of metal AM is particularly high when high added value parts are considered.

Figure 1.5. Fuel nozzle tip for the LEAP jet engine produced by GE. The part is produced by means of SLM process, with high benefits in terms of ease of design, productivity and performances (Source: www.ge.com/additive/stories/).
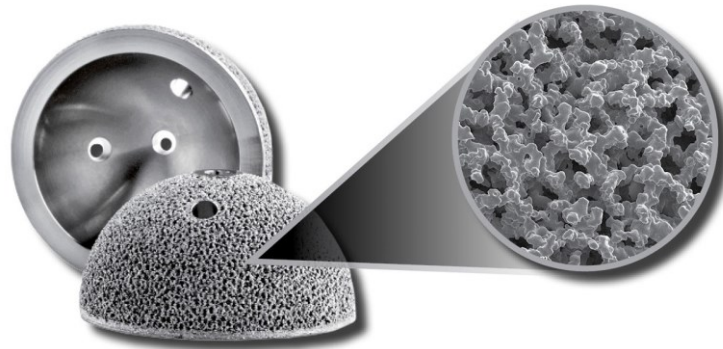
Figure 1.6. Arcam Delta-TT Cup, first produced in 2007. The prosthesis is produced through EBM technology and is made with trabecular structure (highlighted in the SEM image on the right) that facilitates bone growth (Source: www. http://www.arcam.com/solutions/orthopedic-implants/).

Figure 1.7. Gold ring with complex features produced through metal AM (Source: www.spilasers/ whitepapers/innovative-uses-of-metal-additive-manufacturing-in-industry/).

However, all these capabilities comes from several years of research and, as a fundamental step, is based on the proper material feedstock preparation. As discussed previously, materials represent the first step in the choice of the right AM technology. As well stated by Bourell et al. [20], for each of the mentioned technologies, the fundamental material related issue for AM is to find the most suiTable process for which the feedstock is feasible, i.e. the possibility to transform the raw material into the proper feedstock and to be properly consolidated trough AM.

In order to classify, in a non-exhaustive manner, the actual spectrum of available materials for AM, for each of the four main materials classes some of the issues referring to materials and feedstock will be highlighted, as well as some practical cases reported in literature.

Polymers

According to [20], the main concern regarding the use of polymers in AM is related to their viscosity and crystallinity. Polymers, in a general view, could be classified into amorphous, semi-crystalline and thermosets. Amorphous polymers possess a wide softening range, therefore they are more prone to be easily processed by extrusion at low temperatures without significant issues related to viscosity changes. On the other hand, semi-crystalline polymers are more applicable to powder bed fusion AM technologies, since their viscosity reaches accepTable values only in narrow temperature ranges.

Based on these considerations, thermoplastics (amorphous, semi-crystalline) are more easily processed through FDM and, in some cases, also with PBF technologies. For these two process families, AcriloButadieneStirene (ABS), PolyLacticAcid (PLA) and Polyamide 12 (Nylon) represents the most widespread materials.

For thermosets, the most investigated process is SL where, initially, UV photo-initiators with acrylate monomers were employed. However, acrylates caused shrinkage problems and residual stresses, a problem that has been addressed in the '90s with the introduction of epoxy resins. Standing on the actual knowledge, the actual material feedstock for AM processes like SL is made with mixtures of acrilates, ensuring a sufficiently rapid reaction kinetics, and epoxies to provide strength and toughness [21].

Metals

The feasibility of metals for AM relies mainly on their ductility, weldability and castability properties. This aspect is valid for all the AM technologies applicable to metals, among which powder and wire-based processes are the most widespread.

The actual materials palette includes different types of stainless steel, Aluminum and Titanium alloys, cobalt-chromium alloys and a few Nickel superalloys. Moreover, also precious metals like gold, silver and platinum are nowadays directly feasible for AM. However, the spectrum of available materials is growing quite fast given the huge efforts from all the research activities spreaded around the world, in order to increase the maturity degree of metal AM. Regardless of the specific material investigated, other fundamental concerns for metal AM refer to the following points:

- For PBF processes, size distribution and shape of the powders has a significant influence on the resulting properties of manufactured parts, mainly density. As a general consideration, it is preferable to use spherical powders with precise size distribution, that is often different for processes like SLM and LENS;

- Some materials like Aluminum, Titanium and Nickel alloys, presents a high affinity to the atmosphere elements (mainly Oxygen and Nitrogen). This aspect, under non proper process conditions, might cause the entrapment of gas inclusions in the part under consolidation and, due to formation of thin oxide films on the molten material, might induce delamination and cracks in the final part;

- Still referring to PBF processes, the high reflectivity and thermal conductivity of some materials like Aluminum and Copper alloys, if not processed by the correct heat source and process parameters that maximizes the radiation absorption, gives as a result parts with unaccepTable densities and a consistent number of defects caused by lack of fusion;

- Special attention has to be paid for alloys with a high content of alloying elements that promotes precipitation and solution strengthening, such as some Nickel superalloys or stainless steel. In fact, if the material possess different phases with different melting points, phenomena like liquation or lack of fusion could occur during the AM process. This may result, as a function of the high cooling rates involved, in a poor density of parts, whose defects acts also as crack initiators.

A more detailed description of the related phenomena involved in metal AM, as well as a major exploration of different metals and alloys available, is presented in Chapter 2.

Ceramics

AM challenges for ceramics are related to their fundamental characteristics: high melting point and low toughness. For this reason, this material class is difficult to use as a feedstock for single-step AM and, generally speaking, these materials are typically mixed with a binding agent in order to be processed through multi-step AM technologies. In fact, the initial attemps to use ceramics directly, for instance in PBF processes, led to parts affected by cracking. To mitigate cracks formation, different paths were pursued, i.e. process parameters optimization, addition of toughening agents and use of external assisting devices (thermal, magnetic and so on) [20]. In the last years, more recent developments led to the conclusion that direct AM processes, under proper conditions, are feasible for ceramics. To cite some examples reported in literature, [22, 23] investigated with success the DED process of alumina (Al_2O_3) while, for the same material, [24, 25] obtained crack-free parts (but with no full density) using PBF processes. Other appreciable efforts in this field are represented by the experimental works about the application of the sheet lamination process to Silicon Carbide (SiC), Silicon Nitride (Si_3N_4), and blends of alumina and zirconia (Al_2O_3/ZrO_2) [26-28]. Moreover, the feasibility of resin dispersed mixtures of Al_2O_3 and Si_3N_4 for SL was investigated by [29-30], while similar mixtures were processed by means of PBF process [31].

Polymer Composites

As for any manufacturing process involving composite materials, the fundamental concern is the correct choice of materials and feedstocks in order to optimize the interface between matrix and reinforcement and, therefore, guarantee the correct load transfers as well as the protection from voids and fibers corrosion. Extrusion based AM processes, such as FDM, were subject of investigations for different combinations of materials, but mainly for CFRP and GFRP [32]. A noTable result is achieved in this context with the introduction of the *Markforged Mark® series* machines, that are able of embedding carbon fibers (continuous, chopped), Kevlar and glass fibers into a nylon matrix. Onyx is another typical material of use for AM composite parts [33]. Hybrid material embedding represents another example of use of FDM technology for polymer matrix composites, for instance to deposit silver inks on electronic circuit plates, the former formulated to be a quite higher electrical conductive compared to thermoplastic filaments [34].

MMCs production through AM includes particulate composites, fibrous composites, nano-reinforced composites, functionally graded materials and so on [20, 35]. The most typical AM processes used in this case are SLM and LENS, although other processes were extensively investigated for MMCs like, for instance, the Liquid Phase Sintering for the production of a WC-Co/Cu composite [36]. NoTable investigations were also carried out for the evaluation of applicability of the LENS process for MMCs with ceramics reinforcements. Some examples are MMCs made by Ti6-4/TiAl [37], Ti6-4/WC [38, 39], Inconel/WC [40, 41].

Ceramic Composites

The leading application field in this case is the biomaterial field, assumed that ceramic scaffolds in polymer are readily usable products, without the need for any post-process treatments [42, 43]. In this context, the leading technologies are SLS, Binder Jetting and SL, while the most investigated materials are Si-SiC composites, alumina-ZnO composites. Other investigations reported in literature refers to processes like Freeze-form Extrusion Fabrication (FEF) applied to functionally graded materials made with alumina/zirconia [44] or zirconia carbide/tungsten [45].

1.4. Actual challenges and constraints

In the previous paragraphs, the main advantages of AM processes have been highlighted. However, in order to have a comprehensive view of all the aspects related to AM, it is also necessary to discuss about the drawbacks and weaknesses of these technologies, with respect to the actual state of the art. Different criteria could be used to classify the issues that hamper the expected steep diffusion and sTable integration of AM in the manufacturing industry however, from a general view, all of them refer to three main categories, i.e.:

- limitations and challenges strictly related to the different AM processes;
- limitations and challenges related to the whole value chain in which AM processes are located;
- limitations and challenges strictly related to the integration in industry.

In this paragraph, some insights are provided for each one of the presented points. As also mentioned before, assumed that in the present era AM technologies are in a full development phase, which is characterized therefore by quite rapid changes and evolutions, the discussion covered here does not pretend to be completely exhaustive, but it is meant to provide information of the main elements that identify the maturity achieved in the AM field.

Limitations and challenges strictly related to the AM *processes*

Mechanical properties: One of the main concerns about this limitations category is surely the compromised mechanical properties of the produced parts. Standing on the actual knowledge, final parts produced by AM present internal defects that hampers their performance. For instance, AM technologies used for polymers and composites such as FDM does not allow, at the actual state, a proper manufacturing with long fibers, considering some fundamental issues such as the high

curvature of fibers during the deposition as well as porosity and shrinkage problems. For this reason, the application of AM in this field can be considered as mature only for short fibers of micro-nanoparticles reinforcements. On the other hand, metals processed by AM technologies are even more prone to present internal defects, as it will be discussed in Chapter 2. The subsequent undesired poor mechanical properties are the result of a limited know-how related to process parameters.

Limited number of available materials: The limited processes knowledge leads also to the narrow palette of materials that are actually usable, as also discussed above. It is worth to note that, compared to traditional manufacturing processes, AM technologies present a quite higher number of process parameters that are actually tunable, determining longer times needed from researchers to find the best process conditions for each material considered. Fortunately, the development and diffusion of more rigorous experimental methods based on statistical models helps to reduce significantly the time required to investigate the effects of combinations of two or more process parameters simultaneously.

Surface Quality: Another issue that greatly affects the sTable implementation of AM is the poor surface quality. This is due to its high cost fraction when considering the value chain in AM. The very high roughness of AM processed materials — among which metals are the most subjected — actually compromise mechanical, tribological, and corrosion resistance properties of the final products. Moreover, the surface roughness values are also unsTable and very different as a function of the specific AM technology considered.

Limited builing volumes: Referring again to the specific case of metal AM processes (powder based), the limited building volumes also represents a significant limitation for the widespread use of AM [46]. Generally speaking, the actual building volumes for PBF AM processes rarely exceeds 500 x 500 x 500 mm^3, an issue that does not involve other powder based AM technologies such as DED. This limitation is dictated by the need to closely control the environment conditions for processes such as SLM and EBM, given the high reactivity of metal powder subjected to melting, as well as bigger volumes implies a reduced productivity. These aspects, in combination with the considerably higher costs for AM machines with bigger volumes, determines as a preferable solution the simultaneous production of sub-parts to be joined of assembled in a subsequent step.

Low dimensional accuracy: This limitation is strictly related to shrinkage problems and residual stresses formation when processing materials through AM, as well as the limited resolution of some specific AM machines and parts orientation on the building platforms [47, 48].

Low productivity: AM processes productivity cannot be intended in absolute sense, but it needs to be related to the complexity of the parts that needs to be produced. Considering parts that are feasible for both AM and traditional CNC machining, the former presents a general low productivity with respect to the dimensions of the parts. More specifically, AM processes starts to become less competitive when the height of parts becomes considerable [49]. However, the productivity of a given AM process has to take into account also the specific choice of the process parameters, the design decisions and the pre-post process operations needed in order to make the final part compliant to the application.

<u>Limitations and challenges related to the whole value chain in which AM processes are located</u>

Although AM processes belong to near-net-shape technologies family, it is well known that they are not a fully stand-alone technologies. A series of pre-post processing steps are required to complete the manufacturing process through AM. The best example related to this aspect is the need for post-process surface finishing steps, in order to proper remove the supports used to build the parts and to reach the desired surface quality. Another example is represented by the powder handling-related operations like, for instance, procedures for powders re-use for subsequent new AM builds [50]. In addition, AM processes and their related steps requires new standards for metrology and characterisation in order to ensure the requested quality of the final products. This further issue slows the expected sTable implementation in industry.

<u>Limitations and challenges strictly related to the integration in industry</u>

Considering the combination of all the challenges presented above, it is clear that the integration of AM technologies in effective manner is still far from the expectations. All the issues discussed, indeed, determines also difficulties for the actual cost estimation and modeling resulting from the adoption of AM technologies. Standing on the actual knowledge, costs strictly related to AM processes are in general higher compared to traditional manufacturing processes (when feasible). Some authors in literature reported and described the structure of the first attempts to create cost models for AM [51]. These models consider as the main inputs two cost categories: *primary structured costs*, that refers to machines, materials, labor and extra costs, and *accidental structured costs* that refers to idle times, errors prevention, failure costs and so on. However, considering again the whole AM value chain, the way to a sTable implementation of AM is still long.

2. AM processes for metals

In this chapter, a brief description of the most widespread metal AM technologies is presented. More specifically, attention will be focused on PBF AM processes, highlighting the opportunities, applications and related issues, standing on the actual maturity level. About the issues, at the end of the chapter particular emphasis is given for the surface quality, in order to point out the main reasons why post-process surface finishing treatments are needed to achieve a satisfactory surface texture for parts produced by PBF AM processes.

2.1 Classification of metal AM processes

As stated in the previous chapter, metal AM processes would represent a significant revolution of the traditional paradigms for the manufacturing, mainly for parts intended for structural applications. Moreover, the benefits associated with the use of this particular AM processes family were highlighted, with particular emphasis given to the wiser use of material, higher design freedom and high properties tailoring possibilities. These advantages are particularly true when powders are used as feedstock, considering their flexibility related to the localized manipulation and the absence of materials waste, if compared to the different feedstocks used in traditional manufacturing processes.

In order to categorize the actually available AM processes for metals, several authors presented review papers to provide clear descriptions [11, 52]. However, the actual processes spectrum could be classified according to:

- The feedstock used as the raw material;
- The external heat source used to melt the material, a necessary step to provide the desired final shape upon layer-wise solidification;
- The material displacement and consolidation systems;

On the basis of these criteria, metal AM technologies can be generally classified into *Powder Bed Fusion (PBF), Powder feed-based* and *Wire feed-based* processes.

2.1.1. Powder Bed Fusion (PBF) based processes

These processes are distinguished for the melting of metal powders that are previously spreaded over a building platform, as illustrated in Fig. 2.1. The raw material is initially kept in a feeding tank and subsequently displaced over the platform by means of roller or recoater blade. Once the powder bed fills the entire area of the platform, having a predefined layer thickness depending upon the design decisions and the particles size distribution, the selective melting of the powders by means of a focused heat source occurs to allow the consolidation upon cooling of the single section of the final part. After the lowering of the building platform along the vertical direction, the building of the whole part takes place by the repetition of this elemental step, following the common layer upon layer approach of all AM processes.
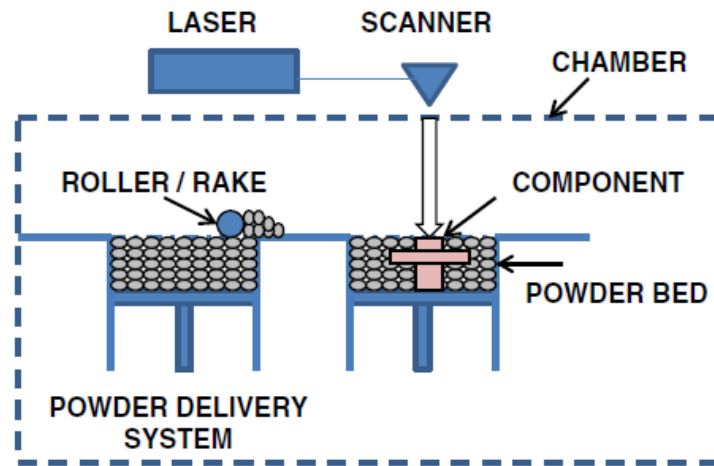
Figure 2.1. Schematic principle of PBF AM processes [11].

According to the specific heat source selected for the process, whose choice depends upon the materials processed and applications, PBF processes are practically represented by two technologies:

- *Selective Laser Melting (SLM)*: PBF process that uses one or more lasers to selectively melt the powders feedstock. It is also refered with other terms, such as Laser Beam Melting (LBM), Direct Metal Laser Sintering (DMLS), Laser Metal Fusion and Laser CUSING [53-56];

- *Electron Beam Melting (EBM):* same as SLM, but melting energy is provided by a focused electron beam.

These two processes present several differences related to constructive features, the typically processed materials and the final parts applications. Consequently, also the process parameters adopted, schematized later in a detailed way, are quite different [52]. With this premise, it is still worthy, for sake of clarity, to give emphasis of some of the main practical difference between SLM and EBM, i.e.:

- *Layer thickness:* Generally speaking, EBM process is able to manage effectively higher layer thicknesses compared to SLM, given the higher penetration power of the electron beam compared to laser. For this reason, the feedstock powder size is usually greater than SLM [57];

- *Scanning speed:* As a consequence of the previous point, EBM possess a higher productivity compared to SLM, due to the possibility to use higher scanning speed. Moreover, this parameter is more difficult to manage using an electron beam as the heat source instead of laser, therefore it is typically controlled through the so called *speed functions* already implemented in the EBM machines [58]. The speed function are algorithms purposely made by the EBM machines manufacturers, with the aim to optimize the energy input distribution in the different areas of a given layer and/or at the different build heights of a part. These functions are the result of process optimization work carried out by the same manufacturers, in order to provide a default process parameters set for the specific case of EBM, although predefined process parameter sets are also offered for the other PBF processes;

- *Process chamber conditions:* Given the higher heat input provided by EBM, the building platform is practically always preheated in order to minimize the high temperature gradients involved. The latter represents one of the main causes for high residual stresses and distortion of the parts [59]. Preheating is typically achieved at the early stage of the process by employing defocused process parameters of the electron beam, directly on the platform causing the temperature increase. This practice is not always found and/or applied in SLM. Another aspect related to the comparison of the process chamber operating conditions is that, considering the high stability needed for the electron beam compared to lasers, EBM process requires necessarily the vacuum [60], while in SLM inert gases such as Argon or Nitrogen are typically used to prevent the oxidation of the processed metal powders;

- *Surface quality and parts density:* Given the higher build rates involved for EBM, surface quality is unavoidably affected and it is general poorer compared to SLM [62]. This result is, again, also related to the high thermal input given by EBM [62];

2.1.2. Powder-feed based AM processes

These AM technologies are considered as a part of the *Directed Energy Deposition (DED)* processes family, that includes also the wire feed-based AM technologies described later such as Wire Arc AM (WAAM) [63]. Other terms found in scientific literature are *Direct Metal Deposition (DMD)* or *Laser Metal Deposition (LMD)* [11, 59]. As illustrated in Fig. 2.2, this powder based process presents a different configuration compared to PBF processes: more specifically, the powder spreading, melting and the subsequent consolidation occurs almost simultaneously, thanks to a conveying nozzle that is coaxial with the heat source (i.e. laser). Moreover, in order to protect the powders from the atmosphere and oxidation, their transportation is provided by means of a carrier gas flux that takes them from the powder supply to the nozzle, acting also as a shield for the molten material.
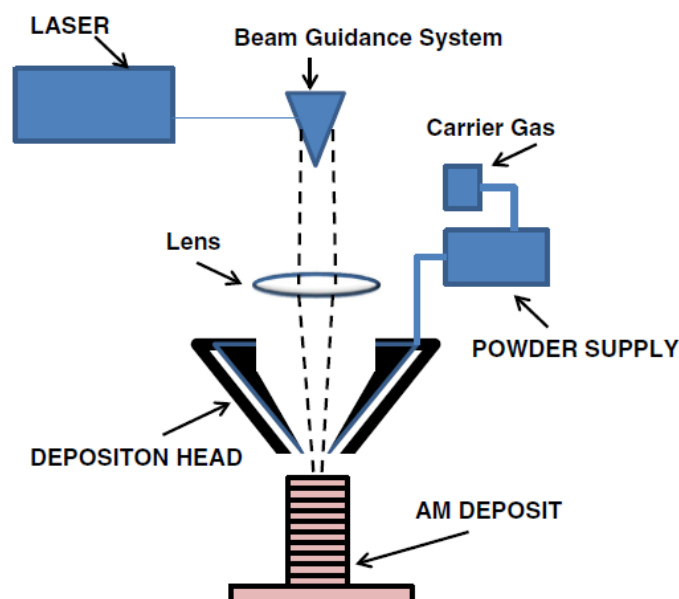

Figure 2.2. Schematic principle of Powder feed based AM processes [11].

The most common machine configurations for the powder feed DED process comprise a deposition head that contains the heat source and the powder delivery system, mounted in closed machines or robotic arms in open environments. Moreover, the major degrees of freedom could belong either to the deposition head or to the building platform. This leads to the following considerations about the comparison of powder feed DED with SLM and EBM:

- powder feed DED process provides a considerable higher building rates compared to SLM and EBM [64]. For this reason, it is gaining an increasing interest from industry given the major productivity;

- The design freedom offered by powder feed DED in higher than SLM/EBM considering the highly localized feedstock manipulation. For instance, special attention should be paid when employing PBF processes for the manufacturing of particular geometries with closed cavities, in which the loose powder might be trapped upon the material consolidation;

- Still considering the higher build rates provided by powder feed DED, it is clear that this process becomes more cost-effective compared to PBF processes as the raw material costs increases [59];

- As a consequence of the major freedom of design, powder feed DED represents a feasible process not only for manufacturing of new parts, but also for materials build ups and parts refurbishing [11];

- As a drawback, powder-feed DED requires time consuming CAM procedures. Therefore, the overall build time is significantly increased in comparison to SLM/EBM, if this setup time is taken into account.

- The feedstock and the molten material protection from the environment is more difficult or not applicable to powder feed DED machines, given their architecture and/or application.

2.1.3. Wire-feed based AM processes

As stated before, this DED process variant uses metal wires as the feedstock. However, a noTable difference with LENS process is represented by the different heat sources applicable for melting and consolidation, such as laser, electron beam or plasma arc. The most widespread process configuration refers to the previously mentioned WAAM process, schematically illustrated in Fig. 2.3, appearing quite similar to welding processes such as Tungsten Inert Gas welding [59].

Compared to LENS, WAAM provides a further increase of build rates and volumes, given also the minor sensitivity of the material in the wire state. Moreover, another great advantage compared to powder-based processes is higher percentage of material usage that actively participates to the final product, making the process even more appreciable with respect to powder-feed DED for applications in which high cost materials are involved [64]. On the other hand, this process does not possess the same freedom in terms of achievable parts complexity, therefore careful considerations should be taken into account when considering parts with specific features such as large thickness variations, complex structures such as trabeculars and so on. Nevertheless, dimensional accuracy and surface quality are greatly affected, given the macroscopic texture

generated by the layering of wires, similarly (but on a different scale) to the texture observed in the FDM process.
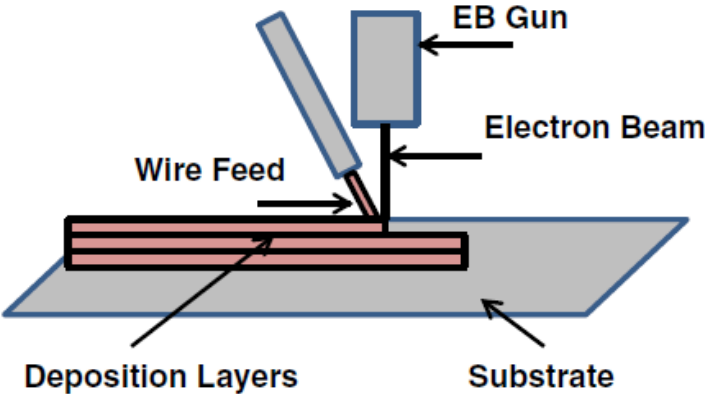

Figure 2.3. Schematic principle of WAAM process [11].

2.2. Materials for metal AM processes

In the previous chapter, the main metals and alloys employed for AM have been cited. According to the ISO/ASTM 52911 [65], a detailed (but not exhaustive) list of materials is proposed for each of the available metallic materials classes. These available materials are listed in Table 2.1.

Table 2.1. List of the main metals and alloys feasible for AM, according to the ISO/ASTM 52911 standard [65].

Stainless steels	Tool steels	Titanium alloys	Aluminium alloys	Hard metals	Nickel-based alloys	Cobalt alloys	Precious
1.4404 X2CrNiMo17-12-2 (316L)	1.2083	TiAl6V4	AlSi25		IN625	CoCr	Gold
	1.3344	TiAl6Nb7	AlSi12		IN718		Silver
1.4410 X2CrNiMoN 25-7-4	1.2343 (H13)	Pure Titanium	AlSi10Mg		Hastelloy X		CuSn
1.4540 X4CrNiCuN b16-4 (15-5 PH)	1.2344 (H13)		AlMg3		Inconel HX		
1.4542 X5CrNiCuNb16-4 (17-4 PH)	1.3342				Hastelloy C-276		
	1.2709 1.2709				C-1023		

As stated in the previous chapter, the range of available materials is in continuous expansion given the increasing know-how about the processes for different materials, as well as the enrichment of the AM machines capabilities. A good example related to this aspect is represented by the proved feasibility of AM for processing Copper and its alloys, that implies a large number of new application possibilities for metal AM, ranging from electronics to high temperature components

with cooling properties [66, 67]. Generally speaking, considering the great effort required to enrich the actual materials palette, since the first developments of metal AM technologies the number of possible applications experienced an impressive boost despite of the limited number of actually feasible materials. In order to provide an overview of the possible applications, in the following points some examples are reported for each of the main metal alloys classes, i.e. stainless steel, Aluminum and Titanium alloys, and Nickel superalloys:

- *Stainless Steel:* Given the high mechanical properties, ductility and biocompatibility, one of the most promising applications of AM processed stainless steel refers to medical sectors [68], overcoming some of the main limitations related to products customization. Typical examples in this case are dental prostheses [69, 70]. Another promising sector involved refers to the production of stainless steel parts with specific features such as cooling channels for heat exchanging applications [71], as well as highly ordered and repeated structures for tailored compressive behavior for impact dumping applications [72]. Moreover, one of the typical applications of steel, i.e. tooling, can be pursued by means of AM [73];

- *Titanium alloys:* These alloys could be considered as the second main candidates after steel for high demanding structural applications. However, given the higher strength to weight properties (mainly Young modulus and tensile strength) and better biocompatibility than stainless steel, the major applications of Titanium alloys are found in medicine and lightweight structures. More specifically, in the former case dental and bone customized prostheses are the most promising applications [74], while in the latter aerospace and automotive applications are the most intriguing [59, 75]. In these contexts, commercially pure Titanium (cpTi) and Ti-6Al-4V represents the most used materials;

- *Aluminum alloys:* This metallic material class is surely one of the most appreciated for their low density and excellent mechanical properties achievable after heat treatments such as precipitation hardening [76]. However, several issues are related to AM processing of these materials, such as high thermal conductivity, relatively low radiation absorption and, similarly to Titanium alloys, the superficial oxide formation due to passivation in uncontrolled atmospheres [20, 77]. On the other hand, different authors investigated the process parameters optimization, mainly considering the SLM process and a specific alloy originally designated for casting applications: the AlSi10Mg alloy [78-80]. However, more recent investigations involves also the know-how increase for other Aluminum alloys using other AM processes and such as AA2024 processed by means of LENS [81];

- *Nickel superalloys:* It is well known that Nickel superalloys, given the combination of high ductility coming from a Face Centered Cubic lattice structure of Nickel and a considerable number of alloying elements that promotes solution-strengthening and precipitation, possesses great mechanical properties, high corrosion and wear resistance, and high creep resistance under challenging operating conditions [82]. Therefore, the combination of these properties with the design freedom given by AM represents a very intriguing research topic. In this context, the possible number of applications is large, but practically limited to the manufacturing of gas turbine engine hot parts such as turbine blades and combustion chambers components [83, 85]. The most investigated alloys in this case are surely the Inconel family alloys, such as Inconel 625 and 718 [86, 87], given their excellent physical and mechanical properties. Moreover, the main challenges and opportunities related to this

topic refers to the study of the proper post-AM treatments that are necessary to improve the final characteristics of the produced parts.

Regardless of the specific material considered, the limited know-how that does not allow to use any already known metal or alloy for AM is also related to the respective feedstock production methods. In this context, the major attention is paid again to powder feedstock compared to wires, given their practical advantages in the AM process context mentioned before. Metal powders for AM are typically produced and commercialized from the providers starting from well established methods such as water, gas or plasma atomization, hydride-dehydride process, mechanical grinding and electrolytic reduction of metal oxides [88 - 90]. The choice of a specific production method relies mainly on the desired powders characteristics (shape, dimensions, microstructure, chemical composition) as well as their reactivity with atmosphere, with consequent oxides formation that brings detrimental effects on powder particles weldability and, therefore, on the final parts density and mechanical properties [91]. Moreover, considering the most oxidation sensitive alloys such as Titanium and Aluminum ones, even the choice of the specific atomization gas used affects powders properties, primarily their microstructure [92, 93]. On the other hand, analyzing the influence on a macro-scale, powders characteristics such as size distribution and shape has a direct influence on the powder bed compaction [94].

2.3. Process parameters for PBF based metal AM processes

In PBF-AM technologies, the process parameters can be categorized in four groups, such as:

- **Heat source related parameters:** i.e. laser power (electron beam power), spot size, focus offset, pulse duration (if applicable to lasers), pulse frequency and so on;
- **Heat source scanning parameters:** i.e. scanning speed, distance between consecutive beam tracks (hatch spacing), scanning strategy, building direction;
- **Powders related parameters:** size distribution, material, shape, powder bed density;
- **Heat related parameters:** i.e. building platform preheating, temperature of the building chamber, temperature gradients in the spreaded powder layer and so on.

Considering that all these parameters present interactions, the effective understanding of the process dynamics represents a labor process. For instance, the specific laser power chosen for processing a material depends on the melting point of the powders, which is a parameter that depends again from their reflectivity. In brief, the thermal-physical history at which the material is subjected is a very complex mechanism. Therefore, it may be difficult in this sense to give attempts in understanding the influence of the process parameters by the evaluation of one of them at time. With this premise, according to the scheme reported in Fig. 2.4 that illustrates the general powder bed-heat source interactions [95], the process parameters group that should be investigated as a whole should comprise the heat source power, the scanning speed, the hatch spacing and the layer thickness. In this way, the *energy density* applied to the material is defined, according to Eq. 2.1 that represents the most simple analytical model that described the influence of the mentioned parameters on the resulting heat input [96, 97]:

$$E_d = \frac{P}{vht} \tag{2.1}$$

where:

E_d = Energy density (J/mm^3);

P = Laser power (W);

v = Scanning speed (mm/min);

h = Hatch spacing (mm);

t = Layer thickness (mm).

However, it is worth to note that, although the presented energy density model represents the most used group of parameters in order to optimize the process for a given material, it is quite trivial. In fact, the above model does not take into account the actual power absorbed from the material, that is a function of the processed metal or alloy, the powder bed compaction and so on. Even so, the aforementioned energy density model could represent a first indicator to judge the choice of the process parameters to correlate with different process output, such as parts density, microstructure features, surface roughness and so on.

Regardless of the specific process parameters used, the local interaction of the heat source with the feedstock causes — after rapid melting and solidification — an elemental structure, which is repeated and overlapped in the microstructure of the produced part, called *melt pool* [95]. In the following points, a brief discussion about the concurring parameters in Eq. 2.1 and some of their interactions are reported.
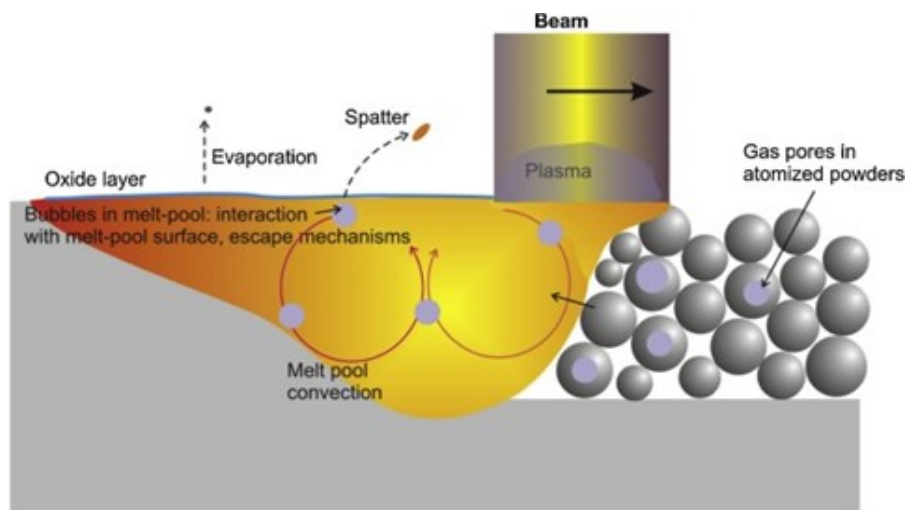
Figure 2.4. Schematization of a PBF process, with illustration of the main process parameters that defines the energy density provided to a material [95].

Laser power and scanning speed:

The energy density increases when laser power is increased, as well as it diminishes for higher scanning speeds. These two parameters are the first to determine the single melt pool dimensions, if the reheating of the adjacent tracks and previous consolidated layers are not taken into account. However, power and scanning speed are strongly related, therefore they are typically changed as a P/v ratio, being the other parameters fixed. From a general point of view, the general approach

used to study the influence of the process parameters, such as P and v, is to generate a process map that describes the different materials response as a function of the specific regions of this map. An example in this sense is reported in Fig. 2.5, that illustrates a process map obtained by [96] for the SLM process of the 316L stainless steel.

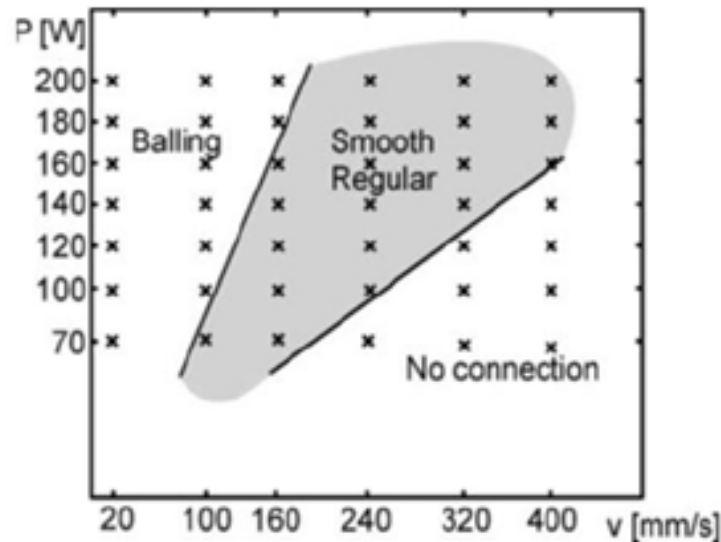**Figure 2.5.** P/v process map for the SLM process of 316L stainless steel [96].

As it can be observed, three regions were defined for the P/v parameters investigated span:

- the *balling region*, observed for high laser power and low scanning speed. In this region, different phenomena could be observed, such as the formation of keyhole and balling defects, whose mechanisms are described later;

- the *smooth regular region*, observed for P/v ratios proximate to optimal ones. This results in well consolidated material after cooling, maximizing the density and, in first instance, optimizing the surface roughness;

- the *lack of fusion region*, observed for low laser power and high scanning speed. In this case, a considerable portion of material could not be melted, resulting in high porosities that also act as crack nucleation sites.

Scanning strategy and hatch spacing:

Scanning strategy represents the heat source pattern necessary in order to consolidate the material layers. The choice of the scanning strategy for a given material and part geometry has a direct influence on the part density, residual stresses and surface roughness [98-100]. The most simple scanning strategy refers to uni- or bi-directional linear patterns, as illustrated in Fig. 2.6a-b. In practical cases, when a linear scanning strategy is adopted for a single layer, it is usually rotated with a predefined angle such as 90°, as illustrated in Fig. 2.6c. The effect of the layer pattern rotation is to provide a more uniform heat input as possible, minimizing therefore the residual stresses in the final part.
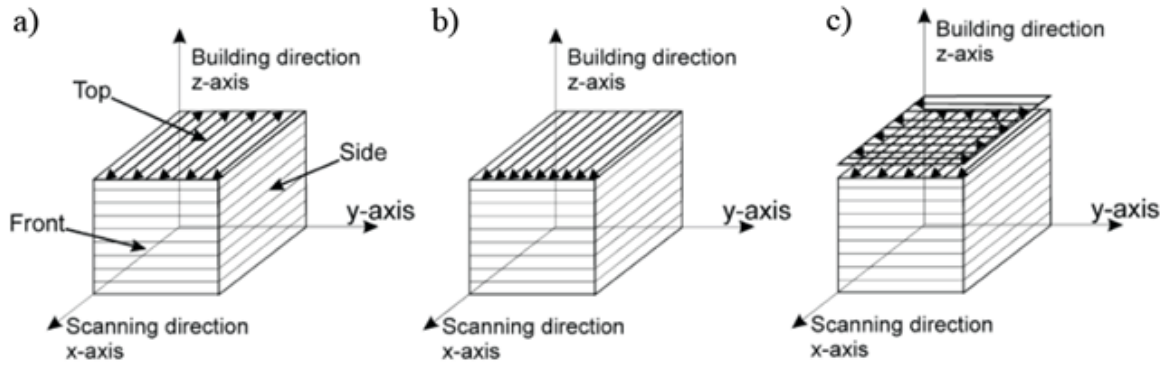
Figure 2.6. Different scanning strategies of the heat source for powder melting and consolidation: (a) bi-directional, (b) uni-directional and (c) rotated for each layer.

However, scanning strategy includes another characteristic parameter, i.e. the *hatch spacing*, that defines the distance between the centers of two melting tracks and, therefore, the overlap percentage between them as illustrated in Fig. 2.7a. Conventionally, low values of the hatch spacing determines a high overlap rate between the melting pools, whereas high hatching spacing means that the melting pools are basically separated. As for the previous process parameters, hatch spacing requires an experience-based considerations in order to find the correct trade-off between overmelting and lack of fusion conditions, according to Eq. 2.1. As a general observation, literature suggests not to employ an overlap between tracks more than 50% [101]. Furthermore, even considering the single layer pattern, it is usually rotated by a predefined angle called *hatch angle*, as illustrated in Fig. 2.7b. The reasons for the adoption of the hatch angle are the same as for the rotated scanning strategy, i.e. a more homogeneous heat distribution and residual stress minimization.
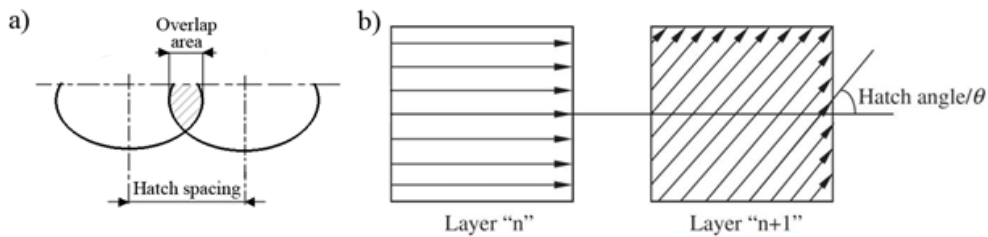
Figure 2.7. (a) hatch spacing and (b) hatch angles [101].

A more recent approach for the further minimization of residual stresses involves the so called *islands scanning strategy* or *chessboard scanning strategy*, illustrated in Fig. 2.8 [1]. In this case, the whole layer is divided in a discrete number of islands and each island is typically scanned by uni-directional pattern. Moreover, in order to minimize the effects of microstructure anisotropy caused by a high preferential solidification direction, the scanning strategy of adjacent islands is typically rotated.
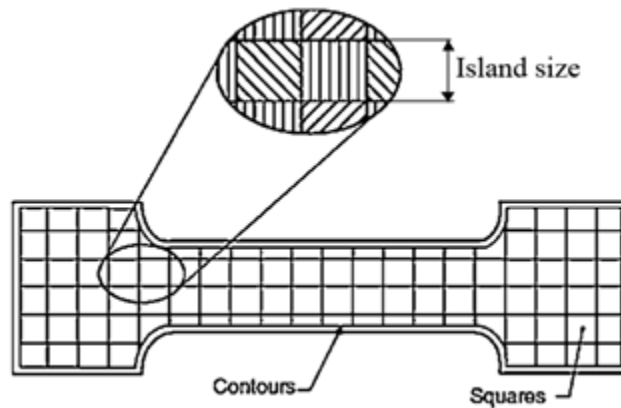
Figure 2.8. Illustration of the islands scanning strategy.

As for any scanning strategy, different process parameters for the geometry edges are needed in order to avoid overmelting caused by the reduced heat dissipation area. Moreover, the choice of these latter parameters is also dictated by the need to optimize the surface roughness, as it will be discussed later. therefore, the process parameters set for this condition is called *contour strategy*.

Layer thickness:

According to Eq. 2.1, the layer thickness has a direct influence on the heat input experienced by the material. More specifically, it dictates the melting depth of the actual layer over the previously consolidated one. As stated before, a practical example of this influence refers to the different layer thickness processed by SLM and EBM. Besides the influence on the heat input, layer thickness also influences the surface roughness of parts, according to the well known *staircase effect* that will discussed later about the surface quality issues. Referring to the influence of the heat source-powder interaction, layer thickness is not considered strictly as a process parameter, so that the energy density, following the general approach for laser processing, is meant as a areal energy density and expressed in J/mm^2.

2.4. Issues in PBF metal AM processes

As previously mentioned, metal AM technologies are characterized by undoubted advantages over traditional manufacturing processes, but also by several drawbacks that hamper their expected rapid diffusion and stable implementation in industry, mainly deriving from incomplete understanding of the process dynamics and know-how. Focusing the attention on PBF-AM technologies, in the following points some of the main defects and issues typically found in the final parts are discussed.

Loss of alloying elements:

When considering the application of PBF processes to metal alloys, there is a concern regarding the search for the proper energy densities that promotes the correct material consolidation. However, due to the presence of different alloying elements with different melting temperatures, defects such as lack of fusion and/or loss of alloying elements occurs. Regarding the latter, when

the melt pool reaches high temperatures, some more volatile elements might leave the melt pool determining a change in the chemical composition of the consolidated alloy. As a consequence, several physical and mechanical properties are affected. As an example, Fig. 2.9 illustrates the vapor pressure of some alloying elements for different metal alloys [97]. Considering the temperature range reported, these diagrams suggests that, without a deeper knowledge and control of the actual temperature profile inside the melting pool, loss of alloying elements could occur easily due to ablation of material instead of melting if excessive energy input is provided.
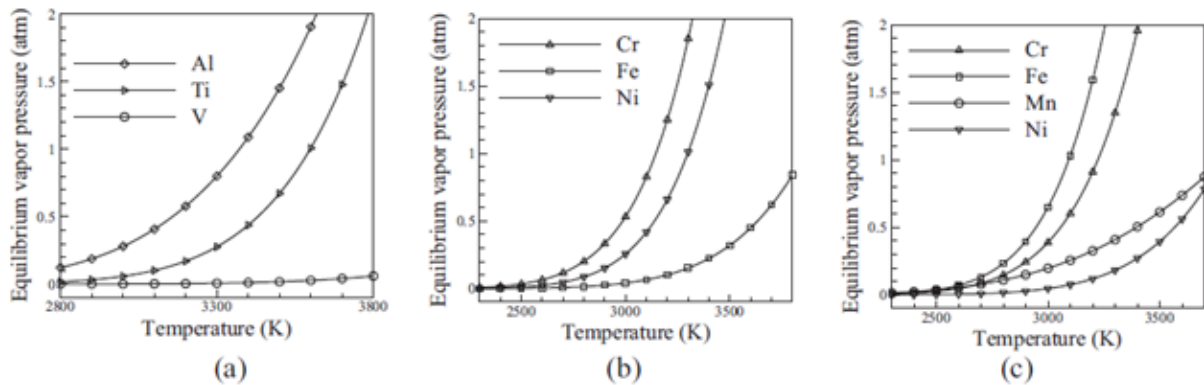
Figure 2.9. Vapor pressure of the main alloying elements for different alloys: (a) Ti-6Al-4V, (b) Inconel 625, (c) SS316L [97].

Lack of fusion and porosities:

As it may be expected, lack of fusion defects and porosities can significantly reduce the mechanical properties of AM processed parts. Referring to porosities, the main formation mechanisms are two [102]:

- The entrapment of gas inside the molten material, typically the gas used for the process chamber conditioning;

- The impossibility of alloy elements in the vaporized state to evacuate from the molten material. This particular mechanism refers also the formation of *keyholes* inside the material when, in a specific area, the energy density reaches excessive values;

Moreover, regardless of the PBF processes related porosities, the latter can also be found already in the powder feedstock. The illustration of the mentioned defects is reported in Fig. 2.10a-b and Fig. 2.11. It is worth to note that porosities caused by the above mentioned mechanisms possess, in general, spherical shapes, although keyhole defects might be slightly different.
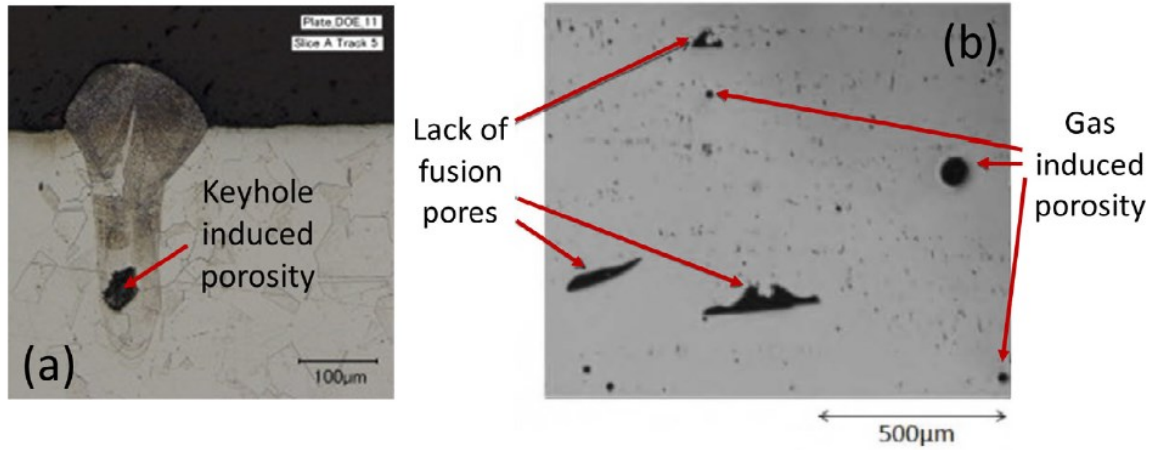
Figure 2.10. Porosities found in SLM processed SS316L: (a) keyhole, (b) lack of fusions and gas porosities [97].
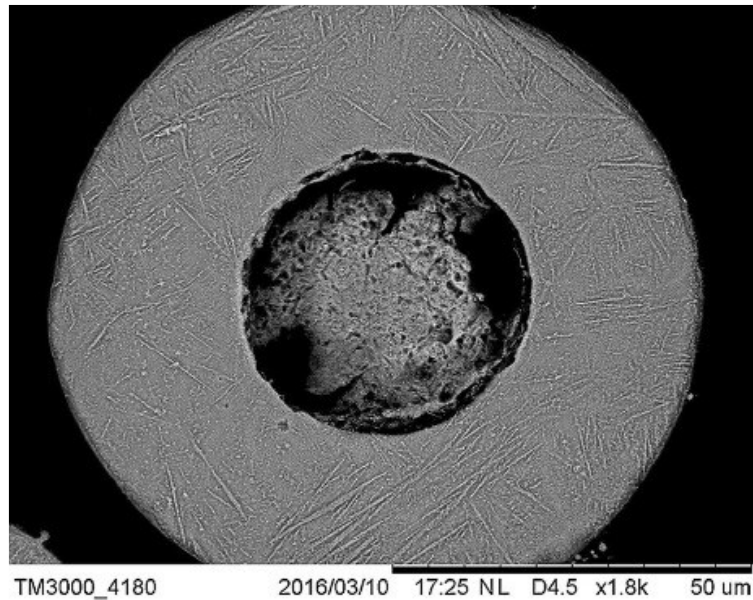
Figure 2.11. Porosities caused by gas-atomization process inside a single Ti-6Al-4V powder particle [102].

Different considerations needs to be done for irregularly shaped defects caused by lack of fusion, illustrated in Fig. 2.10b. More specifically, the main dimension of these defects could represent an indicator of the direction that is more lacking in heat input. To take into account these defects, a specific index is reported in literature, called the *Lack of fusion index (LF)* [97], defined as the ratio between the melt pool depth and the layer thickness. However, this aspect represents surely a non completely explored field. As an example, Fig. 2.12 illustrates the calculated LF for different PBF processed material under different values of linear heat input provided, whose results are also supported by the macrographs reported in Fig. 2.13 as a function of different process parameters for the Ti-6Al-4V [97].
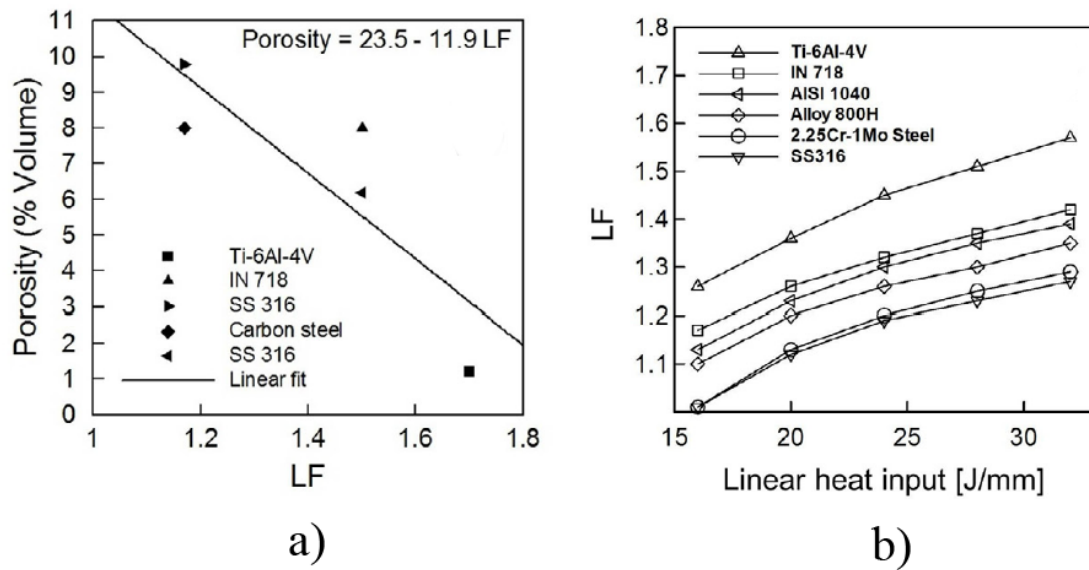
Figure 2.12. Lack of fusion index, correlated with percentage of porosities (a) and linear energy input (b), considering different processed alloys by means of AM [97].
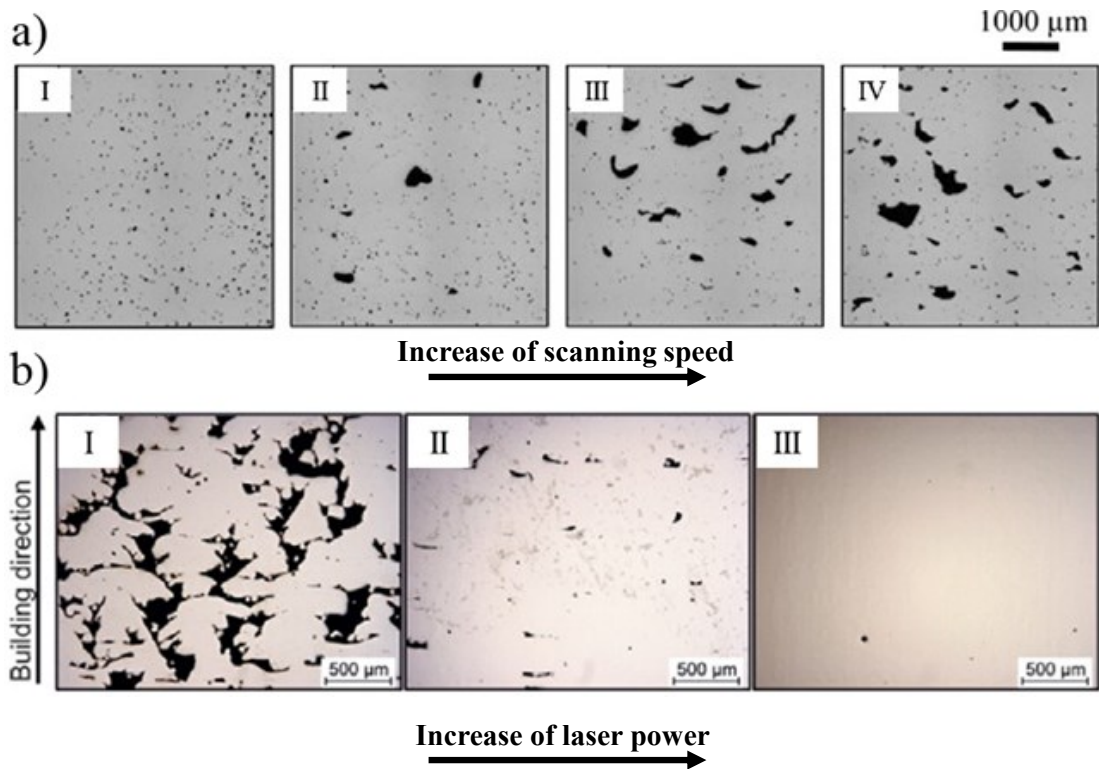
Figure 2.13. Lack of fusion in Ti-6Al-4V alloy processed by AM, as a function of different process parameters: (a) influence of increasing scanning speed values, (b) influence of increasing laser power [97].

Distortions, cracks and delamination:

Based on the fundamental principle of PBF AM process and material related issues discussed above, it is easily understandable that, very often, the formation of defects such as distortions, cracks and parts break-up due to delamination take place. Indeed, all of these can be correlated to the high thermal gradients at which the metal powders are subjected, for both melting and subsequent cooling and consolidation steps. According to the issues related to the scanning strategy, an unbalanced heat input to the consolidating layers can result in parts with high residual stresses and distortions. Therefore, sometimes the AM process itself has to be stopped due to failure. If not, when incorrect process parameters are adopted, different materials characteristics largely contributes to the formation of cracks [103] . The latter are typically the sensitivity to shrinkage (especially for Titanium-Aluminum alloys), the presence of alloying elements and secondary phases with different melting points (i.e. Nickel superalloys) and highly reflective materials with respect to the heat source (i.e. Aluminum and Copper alloys).

Moreover, the combination of these factors, that therefore promotes the nucleation of several crack growth sites, may result in a complete detachment of material in the in-layer and between-layers conditions. An example of this is illustrated in Fig. 2.14 [97]. To overcome these limitations, besides the different attempts about the optimization of the process parameters for different materials, several authors investigated and provided useful information about the need to retrieve, with proper methodology, on-line process information such as melt pool temperature, heat input distribution and so on [104, 105].
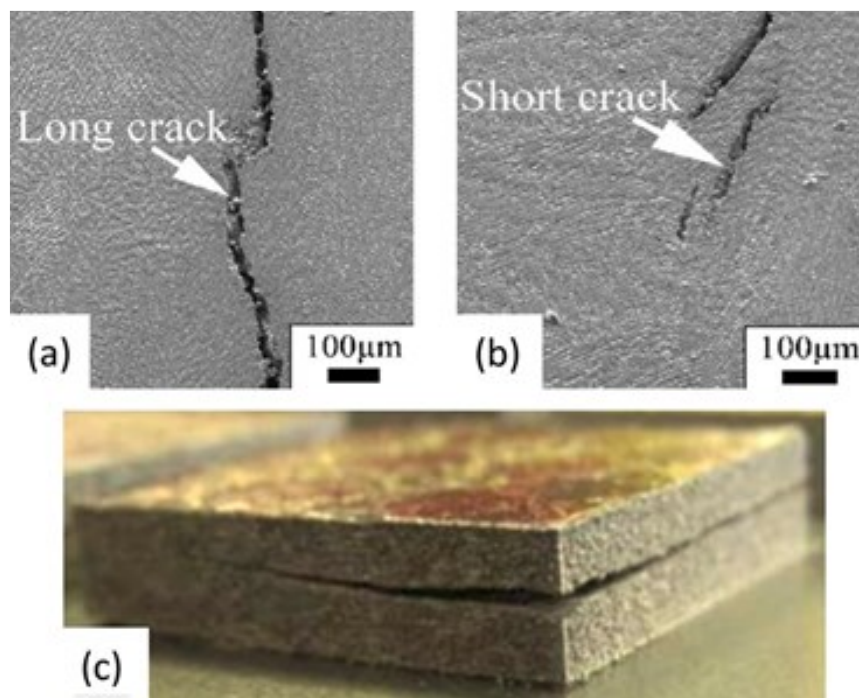

Figure 2.14. SEM images of cracks generated inside a single layer (a-b) and illustration of a delamination between layers (c). [97].

2.5. Surface finish of parts made by PBF metal AM processes

Any kind of interaction between an object and the environment passes through surfaces. With this premise, it is clear that surface properties significantly affects these interactions, especially in engineered materials and parts, thus determining their functionality. Considering the specific field of engineering, the knowledge of the surface characteristics is essential in order to explain their behavior with respect to many properties. Some examples of this relationship are wettability behavior, corrosion resistance, wear properties, reflectivity to radiations, adhesion, and so on [106]. With no exception, these considerations are surely applicable also to AM products. Referring in first instance to the whole family of AM technologies, the surface quality of the produced parts are greatly affected by the choice of the specific process parameters adopted. More specifically, the parameters that greatly influence the surface characteristics are the layer thickness and the part orientation with respect to the building platform. Considering the layer thickness influence, assuming that the minimum value is dictated by the size of the feedstock [97] as well as the maximum is dictated by the melt pool depth, it can be anyway tuned in order to accelerate the building rate and take more advantage of the design flexibility given by AM.

However, as a drawback, this choice implies a poorer surface quality when considering curved surface: this result is due to the so called *stair-step effect*. This effect is ascribable to the approximation of a free-shape surface with one made by stacking a series of material layers of a given height. As expectable, the higher is the layer thickness, the more pronounced is the stair-step effect. Moreover, the contribution of this phenomenon is also strictly related also to the build angle. In this context, [107] explained very clearly the effect of this process variables on the resulting surface texture of parts made by FDM technology. In Fig. 2.15, the correlation between these factors is clearly observable. In addition, the same authors provided a predictive model of the surface roughness, reported in Eq. 2.2 and expressed in terms of arithmetic mean roughness on profiles (R_a), that takes into account the effect of both the layer thickness (t) and the build angle (θ). Referring to the influence of the latter, [108] provided, with a similar approach, its influence on the resulting surface roughness of SS316L parts made by SLM. In the experimentation, truncheon geometries were used as case study, reported in Fig. 2.16 with the related roughness values measured by means of a contact profilometer and expressed as R_a.
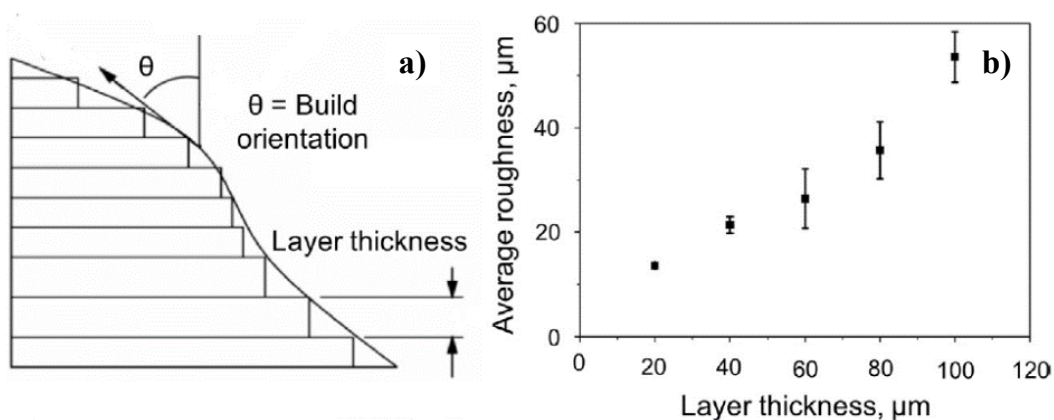

Figure 2.15. Schematic representation of parameters that promotes the stair-step effect (a) and correlation of layer thickness with surface roughness (R_a) in FDM produced parts. [107].

$$R_a = 1000 \, t \, \sin\left(\frac{90-\theta}{4}\right) \tan\left(90-\theta\right) \qquad (2.2)$$
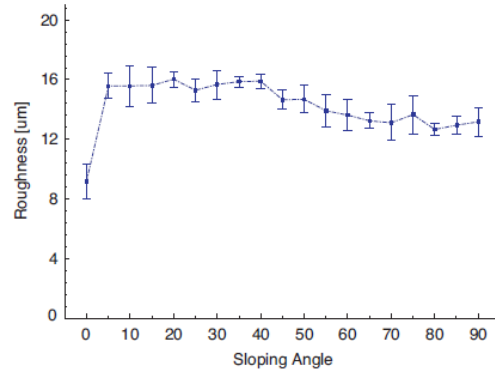
Figure 2.16. Illustration of a truncheon sample (the rotation angle between each step is 5°) and R_a values for each step, calculated as the average of the four sides of each step. [108].

Assumed that the stair-step effect significantly affects the surface roughness of all AM parts, it is not the only reason of poor surface finish when it comes to PBF metal AM parts. In fact, the addition of two other phenomena contributes to the high surface roughness, i.e.:

- the lack of fusion of the processed powders;
- the *balling effect* [97];

The lack of fusion, according to the considerations discussed before, is caused typically by an incorrect choice of the process parameters related to the heat source, as mentioned above, i.e. too low power and too high scanning speed.

On the other hand, the balling effect is the result of very complex phenomena related to the melt pool dynamics. In first instance, the approach that better describes the balling effect is the *Plateau Rayleigh capillary instability* phenomenon [109]. Considering a single melting track under the effects of a heat source providing a fixed power level, an excessive increase of the scanning speed determines an instability of the melt pool under different forces, i.e. gravitational, surface tension and wetting with the substrate. If the speed is too high, the melt pool becomes very elongated and unstable, causing eventually its break-up into multiple shorter tracks. The latter tend to assume a spherical shape, resulting in a molten and solidified track constituted by backfilled and dry areas, as illustrated in Fig. 2.17 [110]. More specifically, this phenomenon occurs when the given energy input induces a melt pool dynamic in which surface tension overcomes the aforementioned forces involved during the process of melting and subsequent solidification and cooling of the material. In geometrical terms, the Plateau Rayleigh capillary instability criterion is expressed with following Eq. 2.3, where L represents the single track length and D its width [97]:

$$\frac{L}{D} \geq \pi \qquad (2.3)$$

In relation with the surface roughness issue, this phenomenon, therefore, contributes to the formation of a surface characterized by isolated metal balls and craters that induce the already mentioned poor surface quality of PBF-AM surfaces.
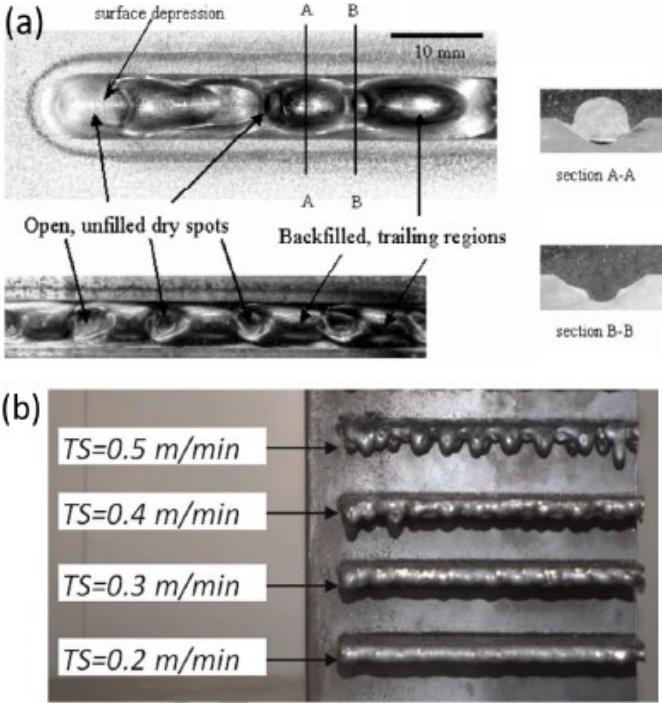
Figure 2.17. Experimental observation of the balling effect during: (a) a traditional welding and (b) the deposition through DED process, as a function of the scanning speed (TS) [97].

However, the described phenomenon is not the only one that determines the presence of partially melted powders inside the consolidated layer and on the outer surface of PBF AM parts. Another phenomenon, also related to the surface tension, is the *Marangoni effect* [111]. Considering the single melting pool, a temperature gradient is established from the free molten surface, directly exposed to the heat source, towards the cooler region represented by the building platform (or a previously consolidated layer). This temperature gradient also promotes a surface tension gradient, considering the lower viscosity of the molten material at higher temperature near to heat source, compared to the higher one in the cooler region. The latter gradient establish a convective flow of a portion of material closer to solidification from the one directly exposed to the heat input. This convection speed can be seen as a dragging force of this almost solidified material, attracted for this reason towards the melt pool region where the surface tension is higher, i.e. the cooler. The final result, as illustrated in Fig. 2.18, is the presence of trapped powder grains at the edges of the consolidated melt pool that, as for the balling phenomenon, determines the formation of porosity inside a layer and the poor surface finish on the outer surfaces of PBF-AM processed parts [97]. Moreover, considering the surrounding powder bed, a small portion of powders can be "wetted" and trapped due to this material flow, thus worsening the resulting surface finish.
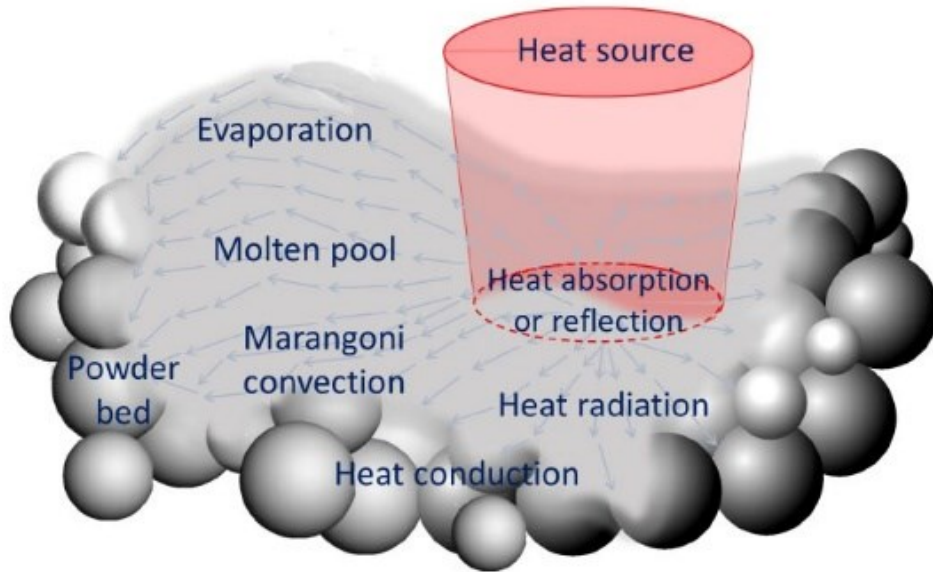
Figure 2.18. Comprehensive illustration of the melt pool dynamics in PBF processes, including all the heat and mass transfer phenomena [97].

It is worth to note that all the presented mechanisms are also emphasized when high reflective, poly-dispersed powders are employed in the process. As also mentioned before, a great contribution to the formation of defects, including poor surface finish based on the discussed mechanisms, is given by powder alloy composition [112].

As a further consideration, the combination of a partially molten powder layer on the surface and stair-step effect gives different results as a function of the building angle. First of all, if an inclined built part is considered, it is expected that the surface roughness would be different between the inner surface (the one "looking" at the building platform) and the opposite one. These two surfaces, in addition to the first and the last few building layers, are called *downskin* and *upskin* respectively [65]. According to the experimental results obtained by [108], the surface roughness measured on the upskin and downskin surfaces for the different steps of the truncheon samples is different, i.e. higher for the downskin, due to the effect of gravity forces on the non-completely solidified material during the SLM process. Another notable observation reported and analytically modeled by the authors, is that when the layer thickness adopted was near to the particles size distribution, the latter tends to "lay" on the subsequent stair-step created for inclined surfaces, as illustrated by their schematization reported in Fig. 2.19. On the other hand, as illustrated in Fig. 2.20 [108], the presence of a sintered powder layer on the surface of PBF parts still represents an issue considering the gravity effects, although vertical surfaces should not represent generally the worst condition in terms of surface quality.

Figure 2.19. Deposition of sintered powders on a stair-step, created for an inclined built surface during PBF processes [108].

Figure 2.20. Sintered powders layer on the 90° inclined surface of the SS316L investigated by [108].

3. Surface finishing techniques for metal AM parts

Given the PBF-AM surface quality issues, in this Chapter a first general overview of the post-process surface finishing treatments is reported. S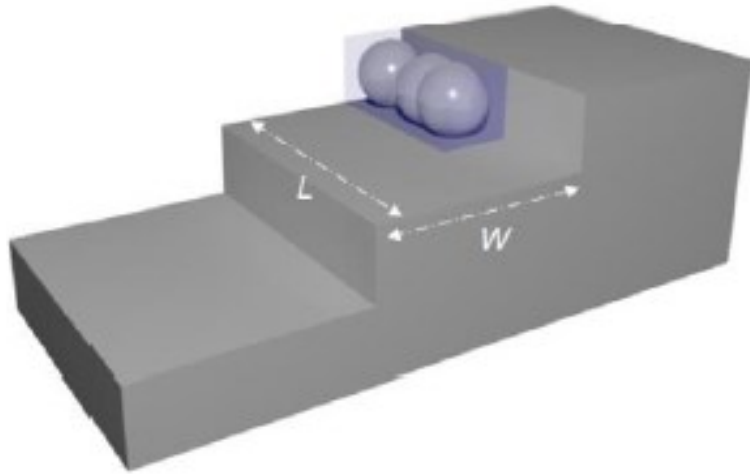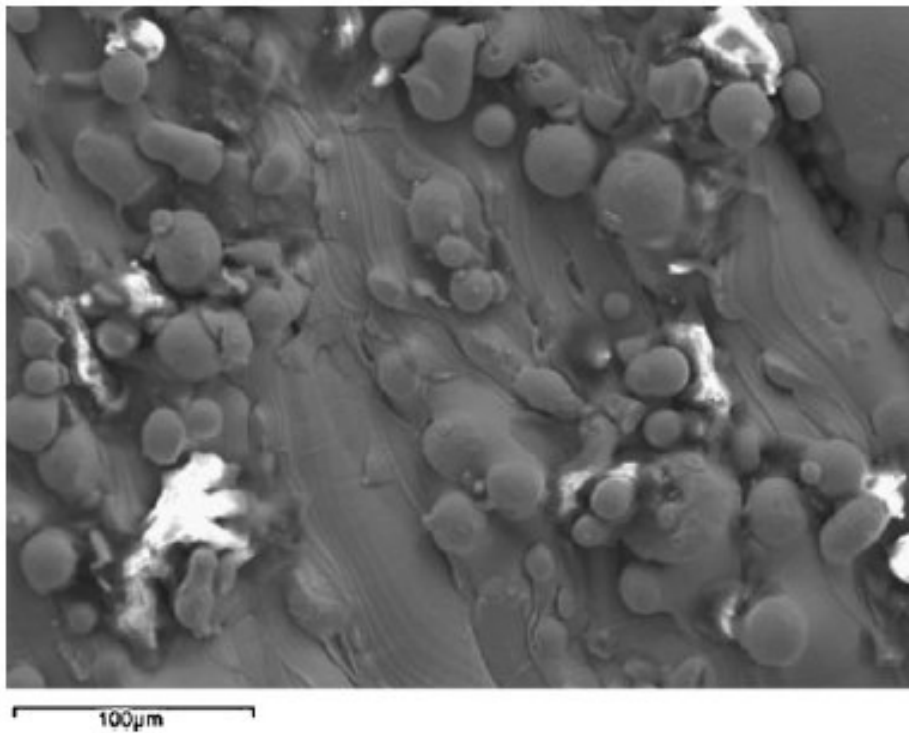ubsequently, the theoretical background of the three different surface treatments investigated experimentally in this Ph.D. thesis is discussed, i.e. Fluidised Bed Machining (FBM), Chemical Polishing (CP), and Laser surface Re-melting (LSR). More specifically, a comprehensive overview of the fundamental mechanisms occurring during these processes are reported, according to the existing literature.

3.1. Overview of surface finishing processes

In the previous chapters, a comprehensive view of the main advantages and drawbacks of AM have been discussed. More specifically, the attention has been focused on metal AM technologies, considering the huge interest involved in this specific process family. Referring to the drawbacks, in the previous chapter a detailed description of the concurring phenomena that determine the poor surface finish of PBF metal AM parts has been reported. All these considerations lead to the need to employ post-process surface finishing methods for AM parts in order to achieve the desired surface characteristics. On the other hand, most of the end users of metal AM processes take into consideration manual finishing operations for this step, typically carried out by means of manual supports removal sand-blasting of the surfaces. As expectable, this approach leads to uncontrolled and non-repeatable results, as well as high costs and labor. Therefore, for the research point of view, this represents a relevant issue, as well as a great opportunity to develop a more efficient and cost-effective set surface treatments.

About the latter point, in order to provide a general (but not exhaustive) indication of the increasing interest in research about surface finishing of metal AM parts, Fig. 3.1 reports the number of published papers considering a time span from 2010 to 2019. It is worth to note that the reported number refers to all the surface finishing techniques discussed in the following section of this chapter, but the aforementioned increasing interest in this context leads to an exponential growth of the possible solutions. Consequently, the analysis does not pretend to be exhaustive and it does not take into account some new emerging and unconventional techniques. The analysis was carried out by an online research on Scopus (for more details, see Appendix), considering journal papers, conference papers, book chapters, and articles under press. As it can be observed, in the latest ten years, the research interest in this topic has grown up considering the increase of one order of magnitude of the published papers. Moreover, considering the high industrial relevance of the development of effective post-process surface finishing technologies, this number is expected to see a further steep increase in the next years.
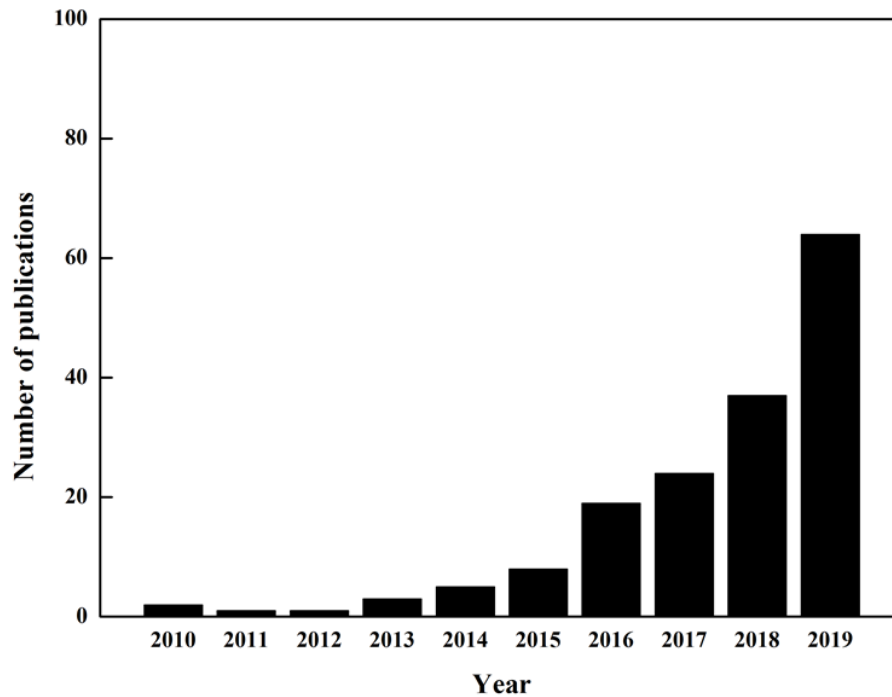
Figure 3.1. Total number of publications about surface finishing of metal AM parts, evaluated globally per year.

Since the AM technologies started to come out, surface finish has always been an issue. Moreover, depending on the specific AM technologies considered, the resulting surface qualities can be quite different. For instance, *Campbell et al.* reported a range of possible values of R_a for different AM technologies with polymers as the main material processed [113], while *Frazier* reported similar considerations but for PBF metal AM processes [11]. Referring to the latter case, is not surprising that SLM is able to produce smoother surfaces compared to EBM, based on the practical comparison between these two technologies reported in the previous chapter. Considering the random nature of the surface texture generated by PBF-AM processes, as illustrated in Fig 2.20 and given by the widely discussed mechanisms, the very interesting issue is the wide span of possible roughness values, although they are generally higher compared to traditional casting and CNC machining technologies. More specifically, this aspect leads to more difficulties in terms of proper quantitative evaluation of surface texture, as well as in determining the effectiveness and stability of a surface finishing process. These concepts will be widely discussed in Chapter 4 in relation with surface metrology issues for AM, as well as in the following Chapters dedicated to the investigated finishing treatments.

Referring to the surface treatments for metal AM parts and standing on the actual knowledge, a certain number of finishing processes have been investigated and developed, some of them of new concept. Regardless of the specific process, surface finishing processes could be categorized according to their prevalent interaction nature with the surfaces to be processed, i.e. mechanical, chemical and electrochemical, and thermal. Different combinations of these interactions are possible. According to this classification, in the following points a brief description of the main surface finishing processes investigated for metal AM parts is reported. Furthermore, some results found in literature for different case studies are reported, highlighting some of the issues related to the different processes.

Mechanical interaction-based treatments

In this category, the surface treatments could be further distinguished in two categories: the treatments based on the material removal by CNC machining and the treatments based on the material removal and/or deformation through the action of abrasive particles, i.e. grinding.

Referring to the former case, several authors investigated the machinability of PBF metal AM parts. One of the most intriguing solutions refers to the integration of CNC machining directly into the AM machines, a configuration typically called *Hybrid Manufacturing* [114]. In fact, this solution allows to take advantage of both the high manufacturing flexibility given by AM and the very high precision of traditional CNC machining for controlling the dimensional accuracy and surface quality of critical features of the manufactured parts, as stated by *Flynn et al.* [115] in their review paper. As an example, [116] applied with success the hybrid process configuration for the manufacture of maraging steel molds, obtaining high accuracy and surface finish as well as surface hardness, starting from near-net-shape molds with excellent starting density and very fine microstructure. However, one of the main drawback of this solution is the impossibility of machining tools to directly access into some of very complex structures achievable by means of AM, i.e. narrow internal channels, lattice structures and so on.

On the other hand, the second category of mechanical interaction-based surface treatments based on abrasive particles allows to partially overcome this limitation. In this context, the most widespread surface treatments are *vibratory polishing*, *shot peening*, *sand blasting*, *Abrasive Flow Machining (AFM)* and so on.

Considering the main issues involved in metal AM surfaces, shot peening surely represents a valid solution. Shot peening consists in a hammering operation on the considered surface through the impacts of hard metal beads, giving rise to a considerable residual compressive stress that compensates the naturally present residual ones (tensile). This process is typically carried out on parts for which high superficial mechanical properties are required. Although it could not be formally classified as a finishing process, the severe plastic deformation imposed surely guarantees a surface roughness improvement in the case of metal AM parts. Nevertheless, the fatigue properties of the shot peened surfaces are higher compared to the AM as-ease ones. These benefits, as an example, were investigated with satisfactory results by different authors on the AlSi10Mg and 17- 4 PH1 alloys respectively [117, 118]. With respect to the complex features accessibility, shot peening is more flexible than CNC machining, although it is limited to external surfaces whose features and sizes are often not suitable even for the small impinging spheres employed for the treatment. Moreover, features such as internal channels are not treatable with this process.

Similar considerations are also valid for the vibratory polishing and sand blasting treatments. These treatments differs from shot peening mainly for the process effect on the surface. In this case, the particles possess high abrasive capabilities, thus performing a smoothing action by material removal rather than plastic deformation (although it is still present). In vibratory polishing, the smoothing of the surfaces is achieved through the dipping of the parts in vibratory bowls containing solid abrasive media. The dimension of the media is generally higher compared to the most intriguing features that can be realized through metal AM. With a different approach but similar conclusions, sandblasting presents similar limitations. More specifically, the smoothing effect exerted by the abrasive particles can be achieved only through strong directional fluxes, due to the presence of high air flow rates. Therefore, although good results can be achieved,

the main limitations related to this process are the inhomogeneity of treatment, typically carried out by manual operations, as well as the accessibility of the abrasive mixture into specific part features. Referring to the achievable results, some application examples of these processes are reported in literature by several authors [119, 120].

Most of these limitations were superseded with the introduction of *Abrasive Flow Machining* processes. In principle, this process family involves the alternative motion of the part under treatment and an abrasive media, generally considered as a slurry, that is able to access into complex internal features due to its liquid-like behavior. Since its first development in 1960, several improvements and know-how about this process were achieved over the years, allowing to employ AFM for a large number of applications, including super-polishing of critical application parts. A comprehensive review of AFM processes and their applications is provided in literature by *Petare et al.* [121]. However, one of the most limitations of this processes family refers to the orientation of the internal features to be polished: considering that the relative motion between the part and the holding cylinder is carried out by vertical movements, the polishing of some features whose orientation is not parallel to this direction is hampered. More recent research developments considered the potential use of *Fluidised Bed* technology, in which abrasive particles could be used to effectively polish AM parts. According to the detailed description reported later, this process could be optimized in order to find application as a very cost and time-effective polishing technology, overcoming almost all the limitations mentioned for the mechanical surface treatments discussed in this paragraph. Moreover, the further advantages of the Fluidised Bed-based polishing technology are the easy process scale-up and the environmental-friendly process conditions.

Chemical and electrochemical interaction-based treatments

Referring to the geometrical complexity achievable through metal AM processes, chemical and electrochemical based surface treatments represent a very intriguing solution. The main advantage of these treatments is due to the physical accessibility of chemically aggressive solutions in the internal features of complex parts, such as the previously mentioned internal channels and lattice structures. Therefore, compared to the most widespread mechanical and thermal treatments, this category has surely the major potential of application. Moreover, the capabilities of chemical interaction-based treatment can be further improved, orienting the smoothing process on the main surface asperities by means of an external voltage applied between the parts to be treated and a reference electrode: in this configuration, the process is called *electrochemical polishing*. A detailed description of the fundamental principles of these two processes is reported later in this chapter.

Several authors carried out experimental investigations by means of chemical polishing: for instance, *Tyagi et al.* [122] employed the chemical treatment for the polishing of SS316L components, obtaining very satisfactory results, i.e. R_a reductions for inner and outer surfaces of about the 92%. *Arredondo et al.* [123] applied the same principle for the chemical milling of Titanium alloys, with the specific aim of removing the α-case. However, it is worth to note that chemical smoothing processes present several drawbacks, such as the use of toxic and not environmental-friendly chemical baths, a poorly controllable dimensional accuracy, high process costs, and so on.

Since it is based on the same fundamental principle, electrochemical polishing process presents the same limitations. As mentioned before, the main benefit achievable in comparison with chemical treatments is the major localized action of the treatment on the surface asperities. However, the selective smoothing of these features is mainly related to the distance of the surface from the reference electrode. Therefore, the treatment might be less effective compared to the simple chemical process for internal features. In terms of applications, some authors investigated the performances of electrochemical polishing on Titanium alloys [124, 125], given the excellent mechanical and physical properties mentioned in the previous chapter.

Thermal interaction-based treatments

The surface finishing processes included in this category mainly refers to laser polishing processes. Regardless of the specific process configuration, laser sources and materials treated, laser polishing consists in providing a certain heat input on a surface, in order to promote its smoothing through different morphology modification principles that will be discussed later in detail. From a comparison between laser-based surface treatments and the previously mentioned mechanical and chemical/electrochemical processes, it can be observed that the former are characterized by a greater process control, given the precise laser source characteristics and high controllability of the process parameters such as laser power, scanning speed, overlap between the single tracks and so on. This aspect is quite desirable for a surface smoothing process applied to a random-texture surface like the ones obtained through metal AM processes. On the other hand, similarly to some of the mechanical interaction-based surface treatments, the adoption of laser polishing techniques is hampered considering the need for the physical access of the laser beam into complex internal features. Therefore, the resulting number of possible applications is reduced compared, for instance, to chemical/electrochemical methods or mechanical abrasion processes designed specifically for treatment of complex parts. However, when applicable, laser-based surface finishing represents a more robust solution that guarantees a high final surface quality. Based on these considerations, the improvement of laser characteristics as well as the evaluation of the process feasibility for different materials still represent one of the key issues in this context. Besides the surface finishing applications, a lot of research topics covered in the last decades refers to the improvement of laser-surface interaction. One of the most relevant examples in this sense is represented by the evolution of the laser sources over the years. Initially, gas lasers, such as *carbon dioxide (CO_2), nitrogen (N_2), helium (H_2),* were the first used in laser processing in general, i.e. cutting, welding, engraving, polishing and so on. These laser sources (especially CO_2), has the advantage of readily available high power (hundreds and/or thousands of Watts), very high laser efficiency (more than 20% of the pumped energy is transformed into an applicable laser radiation) and a power density distribution close to the pure gaussian [126]. However, given the high wavelength (for CO_2: 9.6 – 10.6 μm), the processing efficiency related to some materials such as Aluminum alloys decreases dramatically due to the low material absorption, making necessary the adoption of very high powers in order to overcome this issue. For this reason, the development of shorter wavelength laser sources begun around the '70s. The latter are typically made starting from solid state mediums like, for instance, *neodymium-doped yttrium Aluminum garnet (NdYAG)*, having a wave length which is approximately one tenth of CO_2 source [127]. In this case, more flexible laser radiation delivery systems such optical fibers — also meant to amplify the laser gain in the doped form — are employed in comparison with the more traditional optical chains employed for gas lasers. For this reason, most of the metal AM machines based on laser processing

involves such a source, given also the quite higher laser absorption for different metals in the shorter wavelength regions [20]. This developments were naturally applied also to laser polishing applications. In this context, a wide number of contributions from independent work is reported in literature. For instance, *Yasa et al.* studied the influence of the SLM process parameters applied in-situ during the building process of SS316L parts, in order to reduce the porosities and improve the surface quality [128]. The main experimental outcome was that, under properly modified process parameters used to re-melt the surface of the already consolidated layers, a significant reduction of surface roughness can be obtained (approx. 70%) as well as an appreciable increase in parts density. With a similar premise and for the same material, *Rosa et al.* evaluated the effects of the process on parts with different thickness features produced through DED process, obtaining notable results in terms of roughness reduction (> 90%) [129]. On the other hand, several authors investigated the post-process laser polishing configuration, considering also different materials from the most widespread SS316L, such as AlSi10Mg Aluminum alloy and Ti-6Al-4V Titanium alloy, obtaining similar satisfactory results in terms of roughness reduction [130, 131]. It is worth to note that, as stated in the latter works, laser polishing significantly affects, the microstructure of the processed material as well as its chemical composition, as expectable. In conclusion, given some of the main insights about laser polishing applications, a description of the process principles will be presented later in this chapter.

3.2. Theoretical background of the investigated surface finishing treatments

3.2.1. Fluidised Bed Machining (FBM)

Principles of Fluidisation

Fluidisation is process in which a body of fine solid particles acquires properties comparable to the ones of fluids [132]. This is due to the employment of a carrying fluid, usually a liquid and/or a gas, that promotes an ascending motion and dragging effects on the particles. Fluidisation of solid particles is usually carried out in reactors having circular or rectangular sections, and the particles are typically held in stationary conditions by porous distributor plates, that also allows the ascending flow to be established through the inlet of the carrying fluid. This configuration allows to describe the inception of the fludisation process and, as it will discussed later, also the establishment of different fluidisation regimes.

If there is no presence of a carrying flux impacting the solid particles, they tend to occupy the minimum volume in the reactor, configuration related as the *fixed bed condition*. When the external carrying fluid is imposed (whose inlet is typically from the bottom of the reactor) but with an insufficient superficial speed applied to the particles (from now referred as *U*), the former just goes through the vacancies of the fixed bed, that preserves consequently its state, generating only energy dissipation translated into friction forces. When the superficial speed increases, the friction forces applied to the particles increase as well, until they become equal to gravity, decreased by Archimede's thrust force. The latter condition is defined as *minimum fluidisation* and the multiphase system composed by the solid particles and the carrying fluid becomes a *fludised bed*. As mentioned above, in this configuration the solid particles assume a fluid-like behavior and the multiphase system possesses a density, ρ_ε, that can be calculated according to the following Eq. 3.1 [133]:

$$\rho_\varepsilon = (\rho_s - \rho_f)(1 - \varepsilon) \qquad (3.1)$$

Where ρ_f, ρ_s and ε represents the carrying fluid density, the solid particles density and the vacancy degree respectively. The described system shows some characteristic properties, whose some are illustrated in Fig. 3.1, such as:

- If an object immersed in the reactor possess a lower density compared to the fluidised bed, it will be ejected from the latter. Viceversa, if the object density is higher, it will fall down into the reactor according to Archimede's law;

- If the reactor is subjected to inclination, the free surface of the fluidised bed remains flat and horizontal;

- If a hole is performed on a reactor containing the fluidised bed, the latter will flow out like a liquid;
- If two or more reactors are connected, the free level of the respective fluidised beds will be balanced between each other according to the communicating vessels law;
- The differential pressure ΔP between two axial points of a fluidised bed identified by h, can be calculated as for the case of a liquid according to Stevino's law, reported in the following Eq. 3.2:

$$\Delta P = g\, \rho_\varepsilon h \qquad (3.2)$$

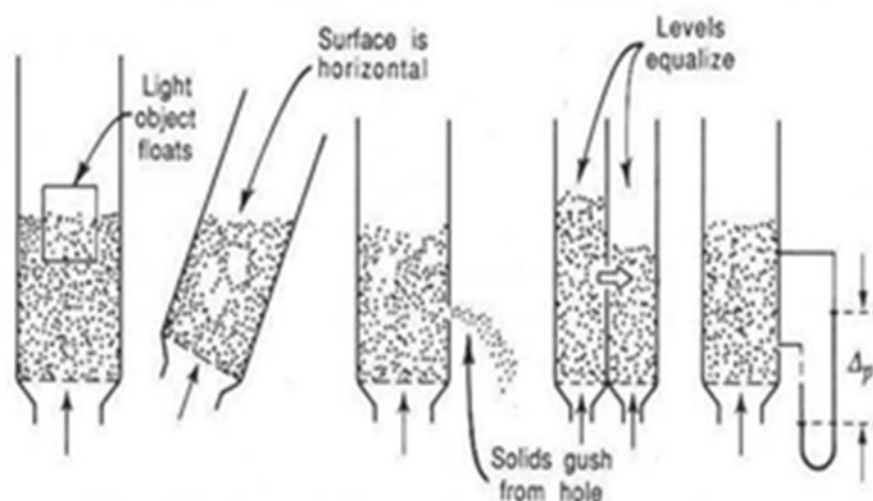Where g represents the gravity acceleration.

Figure 3.1. Similitudes between the behavior of a fluidised bed and a liquid [133].

From the considerations presented above, the pressure drop of the carrying fluid passing through the solid particles bed depends, through the reactor's section, on the drag force that the former applies to the latter. These forces present a direct linear correlation with the superficial carrying fluid speed for laminar regimes and it becomes quadratic for turbulent flow conditions. With this premise, the minimum fluidisation regime depends on the reactor's section S according to the Eq. 4.3, expressed as the combination of Eqs. 3.1 and 3.2 [133]:

$$\Delta PS = (\rho_S - \rho_f)(1 - \varepsilon)\, gSh \tag{3.3}$$

When this condition is satisfied, the superficial gas speed related to the established regime is called *minimum fluidisation speed (U_{mf})*, whose value is dependent on the physical properties of the carrying fluid and the solid particles, the latter expressed in terms of density, shape, size and mechanical properties. Accordingly, a vacancy degree can be defined for the minimum fluidisation regime as ε_{mf}. From this particular regime, even slight changes implies a consistent increase in the vacancy degree. Moreover, if the system is ideal, the pressure drop after the minimum fluidisation establishment remains constant. From a general point of view, two possible fluidisation regimes can be established if the superficial speed of the impinged particles is increased, as illustrated in Fig. 3.2:

- *Aggregative fluidisation:* the excess of carrying fluid compared to the minimum fluidisation tends to form bubbles while ascending the fluidised bed, the pressure drop remains constant and the whole bed tends to expand;

- *Particle fluidisation*: the fluidised bed expands homogeneously, increasing the average distance between the particles until the *minimum bubbling speed (U_{mb})* is reached. Afterwards, the previous regime takes place after the collapse of the bubbles.

It is clear, at this point, that for the latter case U_{mf} is equal to U_{mb}, determining the so called *normal fluidisation*, whereas the aggregative fluidisation condition is also called *abnormal fluidisation.* For a normal fluidisation, U_{mf} is therefore determined by the intersection of the two pressure drop curves related to the fixed and fluidised bed conditions, as also illustrated in Fig. 3.2. It is worth to note that the horizontal trend reported in the diagram represents the mass of the fluidised particles, highlighting also the *minimum fluidisation height H_{mf}*, which represents the difference in the fluidised bed height at minimum fluidisation for the aforementioned normal and abnormal operating conditions.
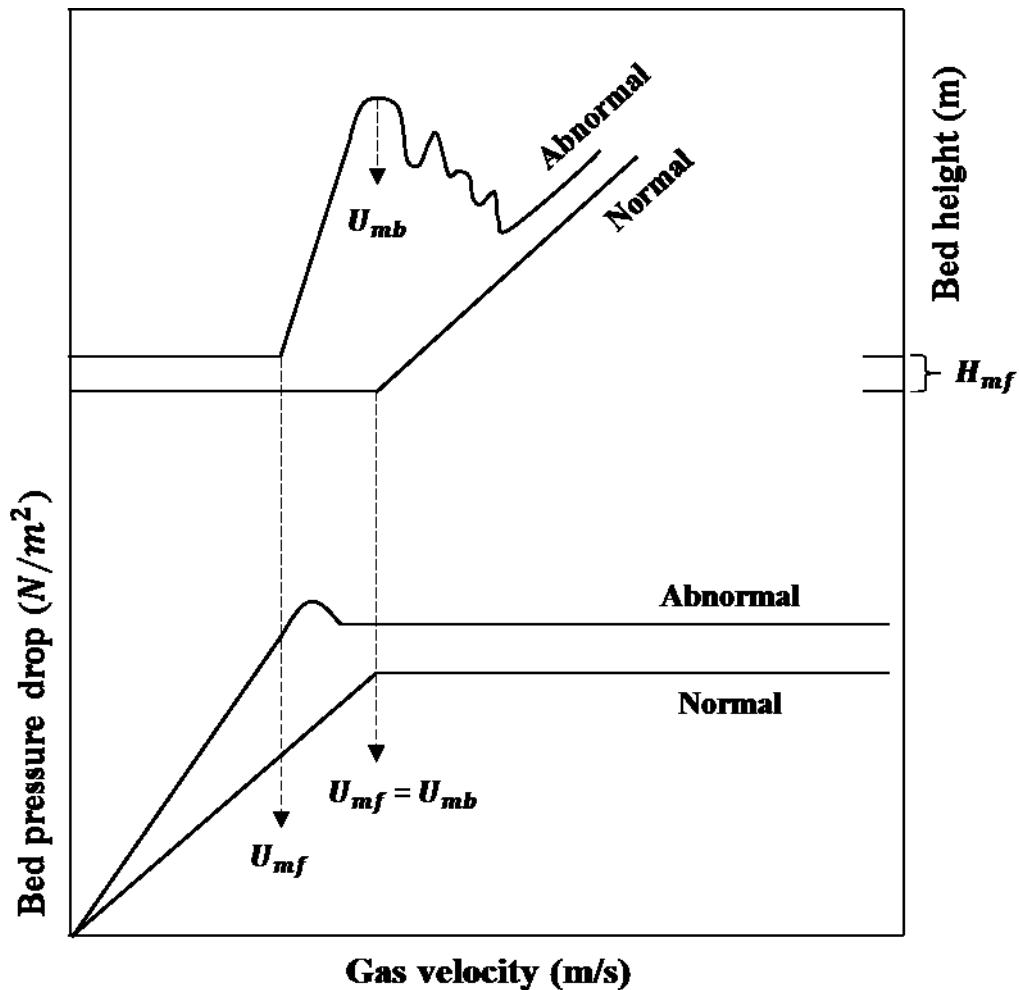
Figure 3.2. Solid particles bed pressure drop and fluidised bed height as a function of the superficial carrying fluid speed (adapted from [133]).

For superficial speeds equal or greater than U_{mb}, the fluidised bed is composed in two phases: the *dense phase (or emulsion)* and the *bubble phase.* The former is represented by all the solid fraction of the bed and carrying fluid fraction that passes through the vacancies without formation of bubbles, whereas the latter represents the remaining fraction of carrying fluid, whose volume is determined by coalescence and splitting phenomena between the bubbles.

For further increases of the carrying fluid speed, the bubbles dimensions tend to increase, without an appreciable expansion of the fluidised bed, until their diameter is equal to the reactor section: this fluidisation regime is called *minimum slugging*, identified by the corresponding U_s, and is typical of reactors with small dimensions. Finally, for values of the carrying fluid speed greater than U_s, the fluidisation regime becomes *turbulent*, characterized by a missing free height inside the reactor, and then *pneumatic* with an ejection of the solid particles outside the reactor (this specific regime is typically used in recirculating fluidised beds). All these considerations are schematically reported in Fig 3.3 that illustrates the mentioned fluidisation regimes.

Figure 3.3. Schematization of the different fluidisation regimes: (a) fixed bed, (b) minimum fluidisation, (c) bubbling, (d) slugging, (e) turbulent and (f) pneumatic [133].

The behavior of the fluidised bed and the establishment of the fluidisation regimes is also dependent on the characteristics of the solid particles to be fluidised. With the aim to clarify this relationship, a semi-empirical classification of the parti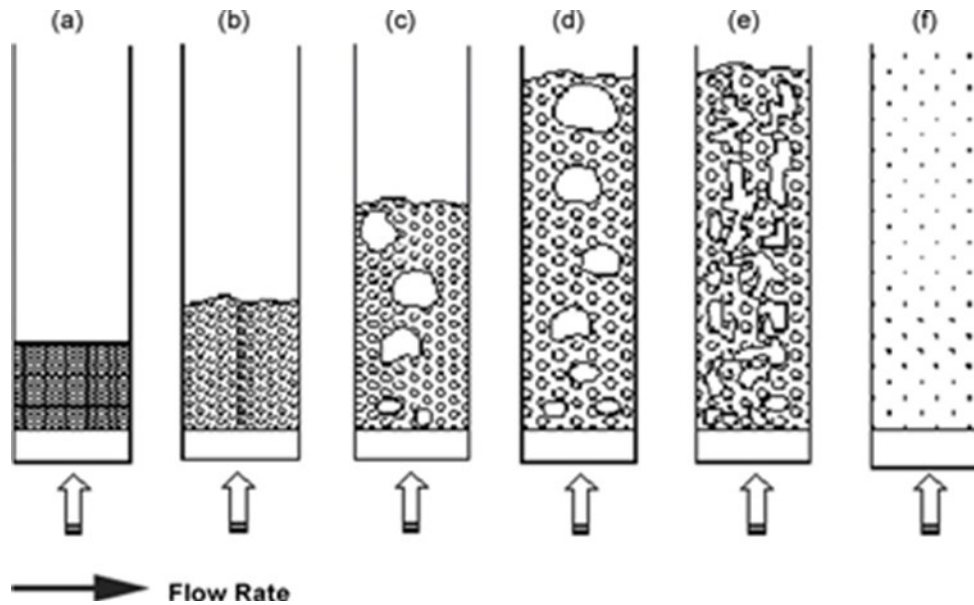cles proposed by Geldart is used as a reference [134]. This classification provides four main groups of particles, according to their behavior with respect to the fluidisation, as a function of the average particles diameter and the density difference between the solid particles and the carrying fluid (in this case, air at room temperature). According to the diagram reported in Fig. 3.4, these main groups are:

- *Group A*: *Aeratable particles:* particles with relatively small diameters (30-50 μm) and/or density (< 1500 kg m^{-3}). The particles of this group tend to fluidise quite easily, with appreciable and homogeneous bed expansions from low values of superficial gas velocity. Moreover, the bubbling regime is stable and controlled, with formation of small bubbles at high gas speed values. In terms of regimes, the bubbling regime is well separated from the minimum fluidisation ($U_{mb} > U_{mf}$) and the bubbles possess a higher ascending speed compared to the remaining portion that passes through the vacancies between the particles;

- *Group B: Sand-like particles: p*articles characterized by the establishment of an aggregative fluidisation, promoting the formation of bubbles even from values slightly higher than U$_{mf}$. These particles are often identified as "sand-like", with typical dimensions of 150–500 μm and densities of 1500–4000 kg m^{-3}. As for the group A particles, in this case the bubble ascending speed over the solid bed is higher compared to the superficial speed of the remaining portion between the particles vacancies, and the vacation degree is comparable to ε_{mf};

- *Group C: Cohesive particles:* Very small particles (<30 μm) with strong cohesive behavior and irregular shape. These particles are very hard to fluidise and tend easily to promote the *channeling* phenomenon, consisting in the formation of a carrying gas channel inside an undisturbed fixed bed. This condition is established even for U values greater than U_{mf} and the vacancies degree is never higher than ε_{mf}; In order to break the gas channel and promote the fluidisation, high values of the gas speed are required;

- *Group D: Spoutable particles:* particles with large diameters and density, with a mainly aggregative fluidisation behavior. The bubbling regime is established for carrying gas speed values next to the minimum fluidisation ($U_{mb} \cong U_{mf}$) and the bubbles ascending speed is quite lower than the speed between particles vacancies.
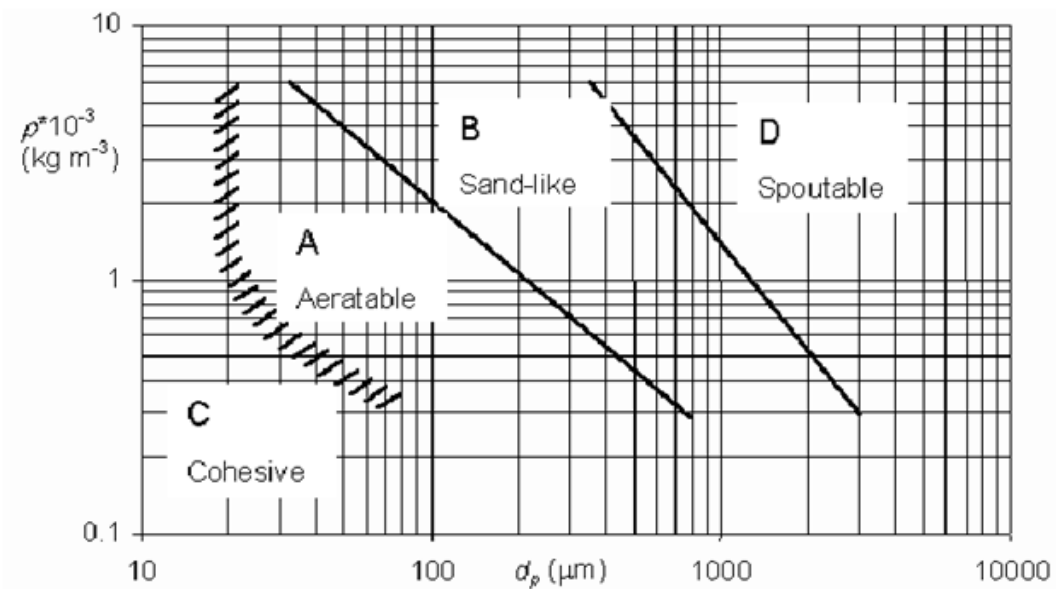
Figure 3.4. Geldart semi-empirical classification of particles, as a function of their average diameter (d_p) and difference between densities of the particles and carrying air (ρ) [134].

Fluidised Bed Machining (FBM)

Based on the discussed principle, a fluidised bed could be effectively used for machining AM processed parts. In fact, given the high particles mobility due to fluidisation, the machining processes based on this principle could guarantee an homogeneous treatment even for complex objects with internal features, the most feasible application for AM. FBM consists in the dipping of parts under controlled conditions into a reactor, as schematically described in Fig. 3.5. [135]. The surface treatment consists, therefore, in a huge number of impacts of the fluidised abrasive particles on the part surfaces, establishing different interaction mechanisms.
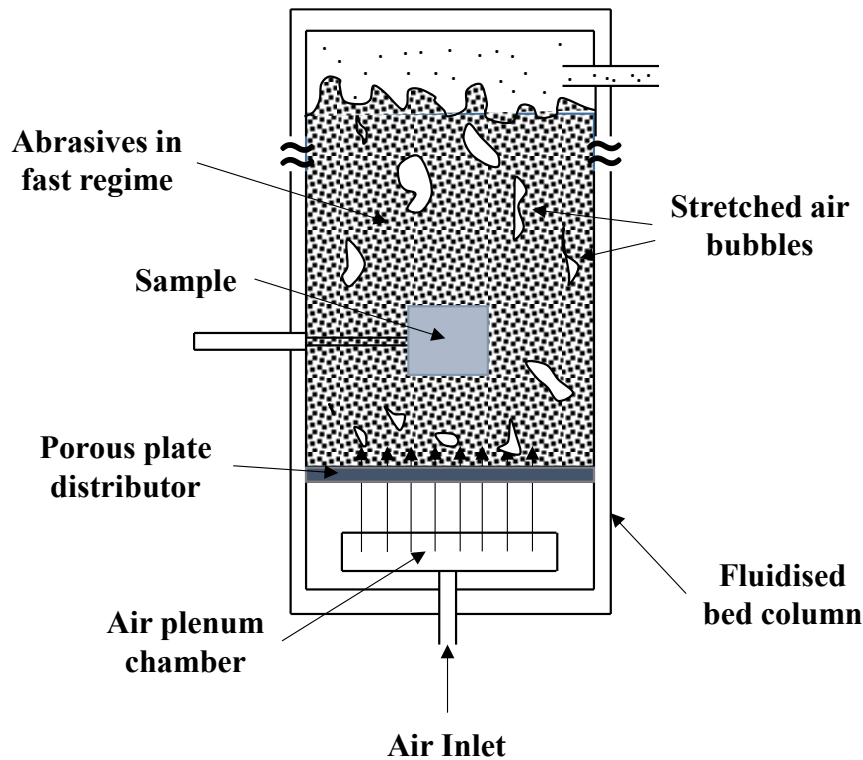
Figure 3.5. Fundamental principle of FBM treatment and process schematization (adapted from [135]).

According to the review proposed by [136], the substrate-abrasive interaction mechanisms can be summarized into two fundamental categories:

- Abrasives *rolling* of the on the surface (Fig. 3.6a): these impacts are characterized, ideally, by the absence of shear stresses transferred from the particles on the sample surface;

- Abrasives *sliding* of the on the surface (Fig. 3.6b): in this case, both shear and normal stresses transfer from the particles to the sample surface occurs.

From these two conditions, a total of four micro-scale interaction mechanisms were identified, considering that, in general, rarely the two fundamental interactions occur separately. These mechanisms, as reported in Fig. 3.7, are:

- *Micro-peening*: The impact of the surface causes a pure plastic deformation, not causing therefore any material removal;

- *Micro-cutting*: Strictly related to sliding impact conditions, in this case the material removal is the predominant effect;

- *Micro-fatigue:* As a result from the huge number of impacts, under specific process conditions this mechanism could be activated. The resulting effect could be both plastic deformation and material removal, determined by the progressive yielding of the substrate material;

- *Micro-cracking:* Like for the previous mechanism, micro-cracking occurs after a considerable amount of time, depending on the specific process conditions. In this case, the detachment of material occurs, caused by the progressive formation and propagation of cracks.
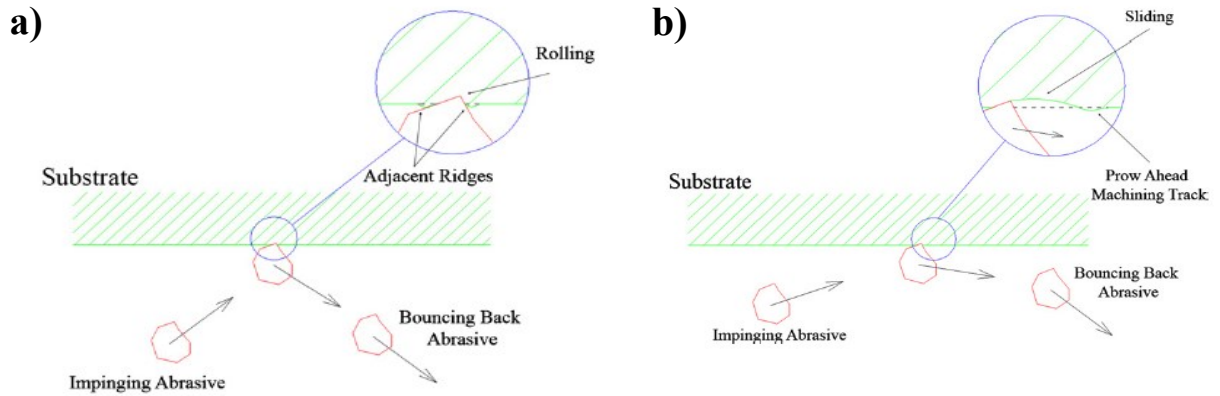
Figure 3.6. Main substrate - fluidised particles interactions in FBM [136].

Figure 3.7. Schematization of the specific substrate-abrasives interactions in FBM: (a) micro-peening, (b) micr-cutting, (c) micro-fatigue and (d) micro-cracking. [136].

Still according to [136], given that the simultaneous presence of two or more mechanisms occurs practically always, the predominance of a mechanism over another is dictated by the following process parameters:
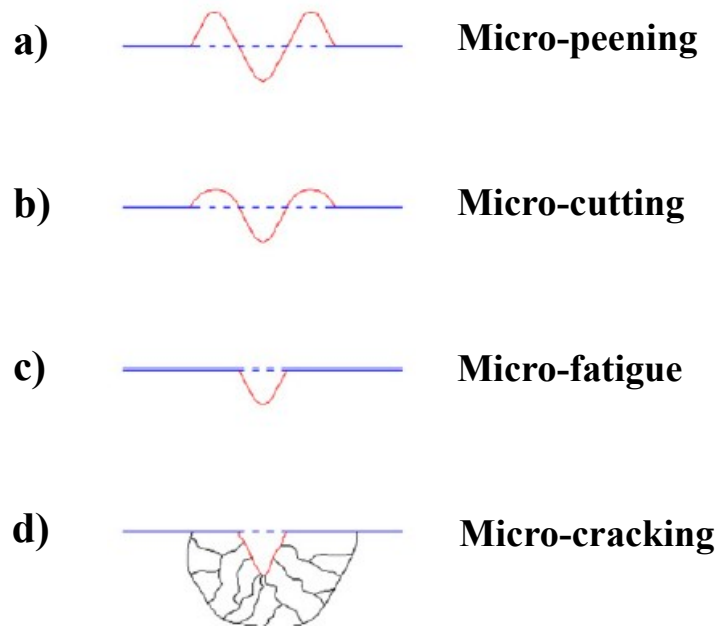
- *Process time*: exposure time of a part immersed into an abrasive fluidised bed should be the first parameter to take into consideration in order to decide the proper process setup. In other terms, it represents the necessary primary input to decide the other process parameters;

- *Carrying gas speed*: As discussed before, the carrying fluid (in this case, typically air) dictates the fluidisation regime. Generally speaking, in order to cover all the fluidisation regimes described before, abrasives speed should be comprised from 0.5-10 m/s. It is necessary to point out that different superficial gas speeds are needed in order to establish a given fluidisation regime, since it is a function of the abrasives properties (primarly, density). In relation to the machining process, the gas speed determines the impact energy transferred from the abrasives to the substrate and, consequently, has a primary influence on the occurring interaction mechanisms described before. With this aim, as a consequence of process modeling and experimental validation for AJM processes, but with same valid considerations for the FBM treatment, *Yabuki et al.* demonstrated the existence of a specific threshold value of impact speed called *critical impact velocity* [137, 138]. The latter essentially determines a change in the process mechanisms, i.e. switching from rolling to sliding when the abrasives speed supersedes this particular value that depends on the operating conditions;

- *Impact angle on the surface*: As the fluidisation regime is fixed, it is well established that a process optimization could be carried out by changing the impact angle of the substrate with respect to the main axial direction of the fluidised abrasive. Typical benefits related to the consideration of this parameter refers to the increase of the relative speed between the substrate and the abrasives, i.e. the possibility to employ less turbulent fluidisation regimes, given a fixed impact speed value. Moreover, it improves the process homogeneity due to the reduced shaded areas on the substrate caused by the formation of bubbles. In terms of direct influence on the mentioned interaction mechanisms, it was proved that that angles of 10-15° maximizes the contribution of material removal mechanisms, while values of 20-25° maximizes the contributions of all the mentioned mechanisms;

- *Abrasives properties:* The choice of the abrasive determines, not always in an expectable way, the contribution of each of the specific interaction mechanisms with the substrate. It is worth to mention that, in fluidisation processes, the mutual impacts between the abrasive particles determines both a partial energy dissipation and a *self-sharpening effect* [132], the latter implying shape changes and a reduction of size distribution after use. According to literature, the most common materials used for the FBM treatment are sand, alumina, glass and stainless steels [139, 140], whereas for wear resistant materials such as tungsten carbide, diamond represents an effective material [141].
The influence on the specific interaction mechanisms occurring during the FBM process also greatly depends on the shape and dimensions of a given abrasive material. Abrasives with nearly spherical shape and relatively small sizes (< 500 μm) are generally employed for time spending machining conditions (2 ÷ 6 h) that do not induce particular stresses to the substrate but returning at the same time an excellent surface quality (micro-cutting presents the less contribution). Viceversa, irregular shape abrasives with greater

dimensions optimise the process time (generally not more than 1 h) but, due to the presence of several cutting edges, tends to leave a notable fingerprint on the final surface;

- *Hardness and initial surface roughness of the substrates*: In general, a direct linear correlation has been observed between the hardness of the substrate and the overall process time. It has been also noted that harder substrate materials provide a better final surface finish compared to softer ones. Moreover, the initial surface roughness of the substrates seems not to be a significant parameter considering that, for a given process set condition, an asymptotic final value surface roughness is reached [139].

Modeling of the FBM process

Since the first applications of the FBM were explored, different authors made attempts in order to provide an analytical description of the process. The investigations carried out in this field refer to the possibility to predict the wear expressed as material removal rate as a function of the process parameters [136]. The first attempts in this context were carried out by Finnie et al. [142], by correlating the wear to the superficial gas speed, the impact angle, the mass of the abrasive particles and the yield strength of the substrate. The results indicated a clear relationship between wear and gas flow rate imposed to fluidise the abrasives. Another attempt reported in literature was carried out by *Zahr* [143], that proposed a modified wear model that takes into account the abrasives hardness, considering a normal impact on the substrate. Based on the same model proposed by *Finnie et al.*, *Jain et al.* introduced some corrective factors that also considered the micro-cracking and micro-fatigue interactions, as well as the mechanical behavior of the substrate under treatment, such as strain hardening and morphological evolution [144]. However, the reported models refer to the abrasive process related to particles impacting at high speeds, typical of turbulent and/or pneumatic regimes, and characterized by sliding as the main interaction mechanism involved. Therefore, the presented models does not take into account some conditions that, for less turbulent regimes such as bubbling or minimum fluidisation regimes, guarantees comparable values of the material removal for instance, provided by an external speed component introduced for the part. In order to fill this gap, *Jain et al.* [144], proposed a semi-empirical model that correlates the material removal in conditions of low or moderate impacts of particles with the number of impacts per unit time, the average size distribution, depth of cut of the impinging particles, and the roughness evolution of the substrate. This model, based on the fluidisation through liquids, was reformulated by *Barletta et al* [136] considering the FBM treatment of Aluminum and Brass with normal impact of abrasives, conditions that promotes the greatest contribution of plastic deformation of the substrate over the others mentioned. The described model is reported in Eq. 3.4.

$$W_m = 2\sqrt{t(d_g - t)}\alpha N_0 \left[\frac{d_g^2}{4} \sin^{-1}\left(\frac{2\sqrt{t(d_g - t)}}{d_g} \right) - \sqrt{t(d_g - t)}\left(\frac{d_g}{2} - t \right) \right] \sum_{i=1}^{n}\left[1 - \frac{R_a^i}{R_a^0} \right]^{\beta} \rho_w \qquad (3.4)$$

52

Where:

W_m = amount of material removed per unit time;

 t = depth of cut for each abrasive particle considered;

d_g = average particle diameter;

N_0 = Number of estimated impact for a defined process time span;

ρ_w = substrate density;

R_a^0 = initial roughness of the substrate;

R_a^i = actual roughness after FBM treatment after *i* iterations;

α = empirical coefficient that takes into account the plastic deformation and material removal contributions (mainly micro-fatigue and micro-cracking), as a function of the mechanical properties of both the substrate and the abrasive particles. For Aluminum and brass, Barletta et al. found that this value is 0,0003 and 0,00009 respectively;

β = empirical coefficient that takes into account the morphological evolution of the surface, regardless of the specific material processed. *Barletta et al.* This value was found to be 2 both for Aluminum and brass.

It is worth to note that if the surface roughness does not significantly change between the i and i+1 iteration, the model can be simplified considering that the contribution related to the roughness variation becomes equal to 1. Therefore, the model becomes as reported in the following Eq. 3.5:

$$W_m = 2\sqrt{t(d_g - t)}\alpha N_0 \left[\frac{d_g^2}{4} \sin^{-1} \left(\frac{2\sqrt{t(d_g - t)}}{d_g} \right) - \sqrt{t(d_g - t)} \left(\frac{d_g}{2} - t \right) \right] \rho_w \qquad (3.5)$$

3.2.2. Chemical Polishing

This section reports the basic principles of chemical and electrochemical polishing treatments. Although electrochemical polishing was not experimentally investigated in this work, the surface interaction phenomena behind this process allows also to understand the mechanisms involved in chemical polishing. Therefore, the theoretical background of both the mentioned processes is discussed. Generally speaking, both chemical and electrochemical polishing consider the immersion of an object into a purposely made aggressive solution. The latter is made with specific components — such as acids, surfactants, viscous solvent and passivating chemical species — so that the metal part to be treated represents the anode of an electrolytic cell [145]. If the process is carried out without the presence of a physical electrode representing the cathode and the process is not driven by an imposed external electric potential, it is called *Chemical Polishing (CP)*. Vice versa, if these two elements are present in the process apparatus, the process is called *Electrochemical Polishing (ECP)*. From a general point of view, the basic mechanisms occurring

in CP and ECP processes are based on concurring electrical and chemical phenomena [145]. The former — that is mainly related to ECP, based on the premise reported above — is basically represented by a specific voltage/current relationship that needs to be set for the specific metal to be polished. The latter — that represents the fundamental principle of CP — can be summarized into three main phenomena that are very complex and dependent on the specific case analysed: As reported in literature [145], these phenomena are mainly:

- the formation of a transient anodic (i.e. passivation) layer on the surface of the metal part, as a result of the first interactions with the chemical bath;
- the metal dissolution into the bath, generally consisting of precipitation of metal salts that normally tends to saturate the solution, making it unusable after a certain time period;
- The presence of a viscosity gradient of the chemical bath in proximity of the surface of the anode. This leads to significant variations of conductivity of the solution, thus indicating a change in the mechanisms involved in the polishing process.

With this premise, in order to clarify the main issues related to CP and ECP processes, a critical overview and comparison is needed.

ECP: fundamental mechanisms

A lot of factors play a key role in ECP, whose importance is mainly dependent on the metal to be treated and the corresponding electrolytic solution. With this premise, *Yang et al.* proposed a comprehensive overview of the ECP fundamental mechanisms — most of them also valid for CP given its similar operating principle — as well as of the developed process theories and analytical models from different authors [146]. In the following points, these models are briefly recalled and presented:

- *Jacquet Theory:* One of the first investigated key factors in ECP was the ohmic resistance of the metal/solution interface during the process, affecting the current density involved in the cell and, therefore, the dissolved mass. The first fundamental analytical models that describes the relationship between the mass dissolved and the process variables are represented by *Faraday's laws of electrolysis*, whose physical meaning is synthetically reported in the following Eq. 3.6:

$$m = \frac{QM}{Fz} = \frac{ItM}{Fz} \tag{3.6}$$

Where:

m = mass dissolved and removed from the surface of the workpiece (g);

Q = total charge passed through the surface of the workpiece (C);

I = applied current (A);

t = process time (s);

M = molar mass of the workpiece material (gmol^{-1});

F = Faraday's constant (Cmol^{-1});

z = valence number for the workpiece material (number of charges per ion);

Based on this premise and the aforementioned viscosity gradient of the electrolytic solution towards the surface of the anode (workpiece), the Jacquet theory of ECP was based on the hypothesis that this gradient leads to a not uniform current density acting on the different areas of the surface to be polished, leading to different mass transfers. More specifically, the resulting current density would be higher on the peaks of the anode surface rather than its valleys, leading to a smoothing effect mainly based on the levelling of the surface due to the prevalent dissolution of the metal of the peaks;

- *Elmore Theory:* In the ECP model proposed by Elmore, the anode dissolution (i.e. the workpiece surface smoothing in this specific case) is driven by diffusion phenomena at the interface between the anode surface and the bulk electrolytic solution — instead of electrolytic migration through mass transfer — through the so called *Nernst diffusion layer*. By carrying out experiments on ECP of Copper in orthophosphoric acid, Elmore proved that the amount of metal dissolved in the electrolytic solution increases with current density up to a certain value of the latter, called *limiting current (i_L)*. The dissolution of the metal can continue beyond this value only if metal ions can diffuse into the bulk electrolyte passing through the Nernst diffusion boundary layer. Since the latter presents a higher thickness (δ) in the valleys rather than on the peaks of the anode surface, the resulting process kinetics is accelerated on the surface asperities according to the following Eq. 3.7:

$$i_L = \frac{nFD(C_s - C_d)}{\delta} \tag{3.7}$$

Where:

i_L = limiting current density (A/m^2);

n = total number of ions involved;

F = Faraday's constant (Cmol^{-1});

D = diffusion coefficient of the rate limiting species (m^2/s);

C_s = metal ions concentration on the interface between the anode surface and the bulk electrolytic solution (mol/m^3);

C_b = metal ions concentration in the bulk electrolytic solution (mol/m^3);

δ = Nernst diffusion layer (m);

Moreover, it was proved that the higher is the viscosity of the solution, the higher is its polishing capability [147];

- *Acceptor Theory:* In this theory, initially proposed by *Halfway* [148] and lately re-formulated and experimentally validated by *Edwards* [149], the metal dissolution through the anode surface is driven by the surface distribution of the anions provided from the electrolytic solution rather than migration and diffusion phenomena, as stated by the previously discussed theories. More specifically, the theory proposed by Edwards is based on the *acceptor* capabilities of these anions with respect to the metal ions of the workpiece surface. In other words, the polishing effect is dictated by the concentration on the workpiece surface of the anions that are able to reduce the metal ions into metal salts, subsequently brought into the bulk electrolytic solution. This model of ECP was further investigated and analytically solved from *Wagner* for an ideal ECP process [150], considering the surface profile as a sinus wave and using the *Fick's second diffusion law* to determine the acceptor concentration distribution at the workpiece surface. It is worth to note that the results obtained from Wagner were fully consistent with the theory proposed by Edwards, but they rejected Elmore's theory about the inconsistency of metal concentration at the constant current density at wide variation of anodic potential;

- *Passivation Theory:* The sensitivity to passivation of some materials, such as Aluminum alloys, steel, Titanium and so on, is greatly affecting the polishing capability. It is well established in literature that for materials with passivating behavior, the polishing process is carried out by means of an alternating phenomena of passivation and oxidation of the workpiece surface, depending on the transient formation of passivation films and on the composition of the chemical bath. The equilibrium and rate of these two processes is strictly dependent on the specific polishing conditions (more specifically temperature, stirring and viscosity of the solution) [151]. From these considerations, it was also noted that the transitory formation of oxide layers on these materials can improve the capability for polishing on a higher roughness scale and that this result can be valid also for CP, in which local galvanic cells takes place in regions with high peaks and valleys. This result was demonstrated to be dependent from the greater oxide film stability in the valleys rather than the peaks on the workpiece surface. Moreover, this differential dissolution effect could represent a great advantage for the polishing of surfaces with high roughness components such as the additive manufactured ones.

Nevertheless, the chemical composition of the material to be polished determines the achievable result. In fact, all the mechanisms and theories cited above were initially related to pure metals, but it is obvious that almost any engineering material is represented by metal alloys. Therefore, all the observations made before should take into account the different response of the different alloying elements immersed in the given electrolytic solution, presenting different behavior in terms of dissolution rate and specific polishing mechanism prevalence. In conclusion, the ECP process (and also the CP process discussed later) will rarely give an exact final surface status once the process conditions are set, but it will generate a certain range of surface finishes, ranging from the mirror-like finish to the etched-like finish [145].

CP: fundamental mechanisms

Since its first developments in the early 40's, CP — and more specifically *Chemical Brightening* — was widely used for different metals, such as copper, zinc, cadmium and so on [145]. However, over the years the process has been optimized for the treatment of more metals such as Aluminum and Titanium alloys, Nickel, Stainless Steel and so on [152, 153]. It was also stated at that time that, in order to achieve the desired surface quality, the process had to be carried out in two steps, i.e. a first step that employs alkaline or acid baths to remove the major contribution of roughness at the macro-scale, followed by a second step that improves brilliance and symmetry, known as Chemical Brightening. As an example, one of the first process optimized for Aluminum alloys was the *Alupol* process, in which an alkaline bath was responsible for the greatest smoothing effect and a second acid bath was employed for the brightening step. A revised version of the process was proposed after by *Hérenguel* [154] in which, at different concentrations, two acid baths were used to carry out the two mentioned steps. In general, it is established nowadays that the acid baths employed for the chemical polishing of Aluminum and its alloys are typically made by mixtures of Sulphuric, Nitric, Hydrofluoridric, Phosphoric and Acetic acid [155].

It is worth to mention that, despite the several attempts made over the years, these processes still have limitations on the following aspects:

- the need to use high temperatures, i.e. 55 – 90 °C, and high acid concentrations in order to achieve a satisfactory etch rate and surface finish;
- the corrosion and damaging of the bath tanks (glass and/or polymer tanks are more widely used);
- the quite rapid saturation of the polishing solutions.

Some of these limitations were addressed for some metals like copper, in which more dilute acid solutions with additives were employed at 25-35 °C. This setup still gives good results after a considerable quantity of metal dissolved, but it represents a not fully explored research field [145].

Comparison between chemical, electrochemical and mechanical polishing

Any kind of surface treatment operates somehow on the basic surface characteristics, i.e. micro-geometrical, physical and chemical. Depending on the specific treatment used, the contributions on these individual aspects might be different. With this premise, it can be observed that, in first analysis, even if the appearance of surfaces obtained with different methods is similar, the mentioned characteristics are generally quite different.

As a general example, alloys surfaces generated by mechanical polishing operations such as grinding, polishing and machining are quite different from those generated by CP and ECP. Even the latter could be considerably different between each other, given the different (but still high) sensitivity of the two processes on the operating conditions. In terms of micro-geometrical characteristics, a comparison between the three mentioned treatments gives as a result three completely different surfaces. On one hand, the presence of different phases in the material to be treated, that generally possess also great differences in mechanical properties such as hardness or stiffness, naturally respond in a different way to the mechanical stress imposed from a mechanical abrasion, resulting in final surfaces with scratches and reliefs. Similar considerations, but with different results, could be formulated for CP and ECP: the same material heterogeneity induces a

different response in terms of etch rate, thickness of anodic layers, microstructure relief effect and revelation of defects such as pores and cracks. In a more general view, it could be said that different treatments operate differently on the macro, micro and sub-micro geometric scales.

Moreover, surface treatments affects the physical and chemical properties of a material. In a similar way observed for the micro-geometrical issues, mechanical and chemical/electrochemical polishing leads to different final surfaces status.

When referring to surfaces, the term physical properties generally indicates their stress-strain status. Therefore, it can be quite easy to understand that mechanical polishing induces major residual stresses compared to chemical/electrochemical methods. This aspect was experimentally proved by *Beilby* [156], recognizing the existence of an amorphous layer on metals surface after mechanical polishing, resulting from the severe plastic deformation that causes he loss of the metal crystal structure. This layer was named after his discoverer as the *Beilby layer*. This layer, whose thickness is in general of 1-2 μm, is connected with the undisturbed material through recrystallization and polygonalization phenomena.

Considering the chemical properties of treated surfaces, it can be observed that surface contamination is generally due to the formation of oxide layers and the formation of chemical compounds, such as corrosion products. The former is practically always present for mechanical polishing of metals, in which the removal of passive layers is accompanied by the exposure of the metal to the atmosphere, air and water, while chemical contamination might be due just for the presence of abrasive particles typically dispersed in the solutions for polishing. Chemical contamination from generation of chemical compounds is, instead, very typical of CP and ECP processes but, remembering the mechanisms described above, also the formation of oxide film occurs quite often.

The discussion can be further specified for CP and ECP separately: in the first case, there is a lack of literature about the purity of a chemical polished surface, and some insights for the AlSi10Mg alloy processed by SLM and subsequently chemical polished will be given in Chapter 7. Regarding ECP, it is well known that, depending on the applied current densities and voltages, chemical composition of the electrolyte solution, temperature and so on, the final chemical composition of metals surface could vary in a remarkable way.

3.2.3. Laser surface re-melting

Laser Surface Re-melting (LSR) represents a specific process variant of laser polishing, in which the heat input provided from a laser promotes the material melting and subsequent relocation from the prominent peaks and asperities into the valleys of the original surface morphology [127]. It represents a specific variant since the surface modifications achievable though laser processing, as stated before, can be different. In fact, another possible way to perform the desired surface smoothing of a surface is the *ablation* (i.e. vaporization) of the main surface roughening material contribution of a given part. Moreover, according to the methodology applied to provide the specific heat input to the surface, laser polishing by means of ablation could be either localized or related to a larger area [128, 157]. The difference between these process configurations is more clearly explained in the scheme reported in Fig. 3.8, illustrating the effects of the different processes on a milled surface [127].
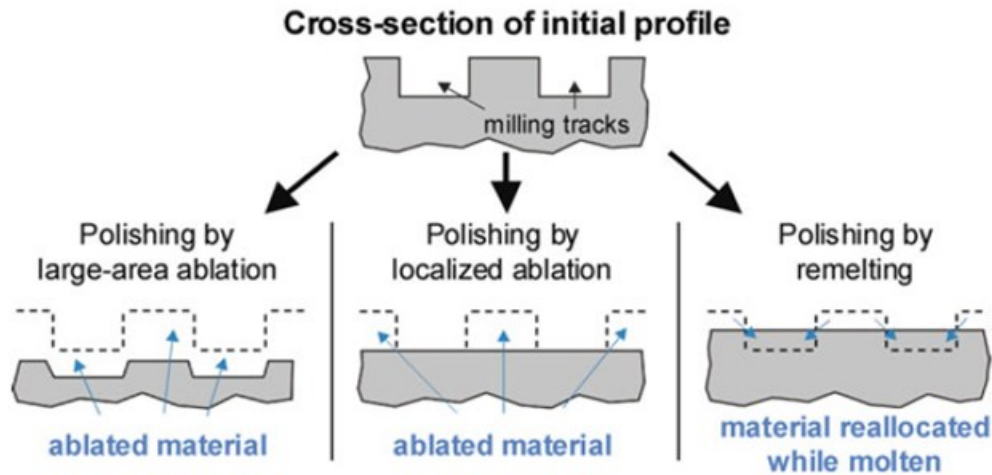
Figure 3.8. Schematic illustration of the different surface modification induced by laser polishing through large area ablation, localized ablation and re-melting [127].

As a general consideration, laser processing by large area ablation and re-melting are mainly used for the surface finishing of different materials, also with different thicknesses [158, 159], whereas polishing by means of localized ablation are more suitable for surface texturing and functionalization [160]. Regardless of the specific process adopted, there are some advantages related to the adoption of this surface finishing category, such as:

- Higher control of process conditions: From a comparison with the previously discussed processes, laser processing is surely more robust and tunable with respect to the process parameters;

- Compared to CP and ECP processes, is surely more environmental-friendly given the absence of pollutants and use of toxic substances;

- High degrees of automation are possible;

- Very high surface quality achievable;

- For some materials (more likely, alloys used for casting), the microstructure alterations induces some beneficial effects due to high cooling rates involved such as grain refinement, leading to an increased surface hardness and, consequently, an improved corrosion and wear resistance.

On the other hand, as mentioned before, the main drawback of laser processing is the limited accessibility of lasers into specific parts features such as internal channels or highly ordered structures of a micron-scale. This leads to a hampered applicability of laser processing to AM metals parts, whose main advantage is exactly the possibility to manufacture parts with those features. However, for parts with a reasonable complexity, LSR represents a very intriguing process, especially considering the high degree of automation achievable and the different laser sources available nowadays. In this context, LSR could become more feasible if combined to the parts manufacturing process, performing therefore the material consolidation and the surface improvement simultaneously.

Moreover, according to [127], the laser surface polishing could be applied to remove either some texture components with sizes of tens to hundreds of μm (macro-polishing) as well as to promote further surface quality improvements on surfaces with roughness components confined in the few to some tens of μm (micro-polishing). It is worth to mention this aspect because, given the dispersed size distribution of the powder feedstock used for powder-based metal AM processes, depending on the process parameters applied it is possible, to a certain extent, to merge the benefits of both the polishing principles.

With respect to the experimental activity reported in the Chapter 8 of this Ph.D. thesis, a specific issue related to the LSR was investigated. More specifically, the aim of the experiments was to investigate the effects of the high surface roughness of AlSi10Mg samples made through SLM on the CO_2 laser radiation when performing LSR. In this context, it is well known that Aluminum alloys are generally not suitable materials for CO_2 laser processing, given the very low radiation absorption with respect to the CO_2 laser wavelength. In Fig. 3.9 is reported, as a comparison, the percentage laser absorption for different materials and for different wavelengths [161]. However, when the surface features (i.e. height of the peaks and valleys) are comparable to the characteristic wavelength of the laser source, the interaction behavior shifts from the ideal reflection and refraction theories to absorption phenomena related to multiple optical reflections [162]. In other terms, taking into consideration, for instance, R_a as the parameter identifying the characteristics of the considered surface and λ as the laser wavelength, the mentioned shift of behavior takes place when R_a/λ is greater than 1 [127].
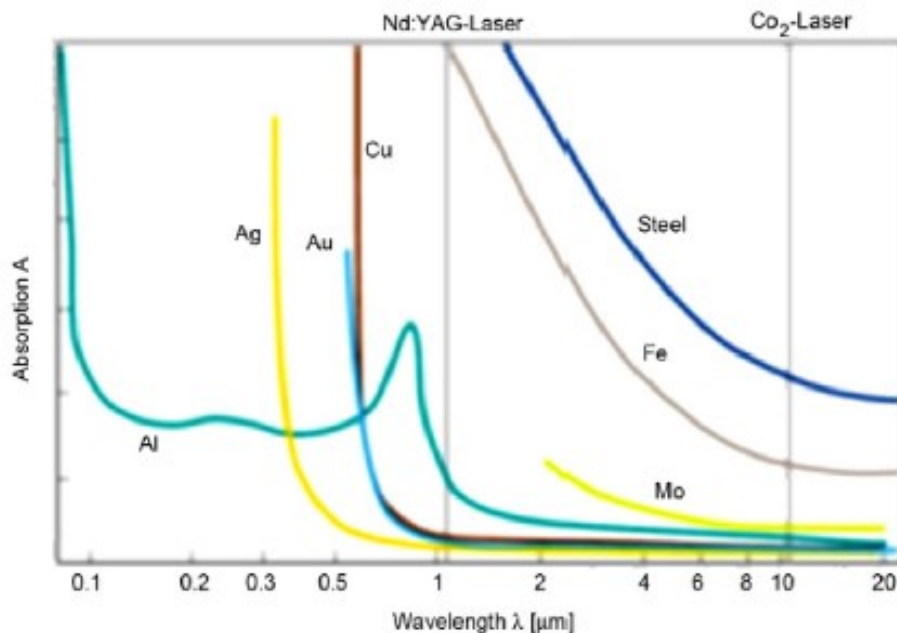
Figure 3.9. Laser absorption of different metals, as a function of different laser wavelengths [161].

With this premise and based on some experimental results obtained in literature that confirms the improved absorption of Aluminum alloys by means of surface roughening [163], the assessment of the surface roughness improvements achievable by means of CO_2 LSR of SLM processed AlSi10Mg alloy is later proposed and discussed in detail.

4. Aim and contents of the thesis

The aim of this Ph.D. thesis is to enrich the actual landscape of the post-process surface treatments for metal AM parts field, based on all the literature and theoretical elements provided in the previous Chapters. More specifically, this work explores the feasibility and illustrates the experimental outcomes for three surface treatments, differing for the nature of the interaction with the surface i.e. mechanical, chemical and thermal. The analysed surface treatments based on these three interactions are represented in this work by Fluidised Bed Machining (FBM), Chemical Polishing (CP) and Laser Surface Re-melting (LSR), respectively. Moreover, considering their very different operating principle, each one of the investigated treatments is treated in a separate Chapter, but following a common scheme based on the detailed illustration of the equipment used, the motivation and the description of the experimental conditions explored, and a critical discussion of the obtained results. Finally, still considering the surface treatments seen individually, the main conclusions and the experimental gaps covered with respect to the scientific literature are provided.

Before the illustration of the experimental conditions and the results of the three surface treatments, the case study used for all the experiments is described in the first section of Chapter 5. In order to better understand the dynamics of the processes, the attention was focused on samples with a simple flat geometry made by means of SLM technology — manufactured in collaboration with MBDA Italy S.p.A. — starting from AlSi10Mg powder feedstock.

The effects of the considered treatments in terms of surface roughness improvement — which represents the main focus of this work — were analysed quantitatively and qualitatively by means of a coherent characterisation methodology, reported in the second section of Chapter 5. The surface modifications and improvements were evaluated quantitatively by means of Confocal Microscopy, considering different surface texture parameters that provides also a more comprehensive view of the mechanisms involved for the different surface treatments. For a qualitative comparison of the actual surfaces before and after the treatments, Scanning Electron Microscopy (SEM) analyses were carried out. Further investigations were carried out by means of Optical Microscopy, Energy Dispersive X-ray Spectroscopy (EDS) and weight loss analysis, depending on the expected surface treatment-induced modifications.

The first surface treatment proposed is FBM, discussed in detail in Chapter 6. The experimental setup and campaign were chosen on the basis of different process configurations, i.e. *stationary* and with *rotating* sample. For the stationary sample configuration, the experiments reported in this work were carried out on the basis of similar experiments conducted by *Barletta et al.* [139], using Aluminum substrates obtained through traditional manufacturing technologies, dipped into a Fluidised Bed operating in bubbling regime and evaluating the process effects on surface quality at different time steps. On the other hand, the rotating sample configuration was considered according to similar experiments carried out by *Atzeni et al.* [135], in which AlSi10Mg flat samples made by SLM were used and dipped into a Fluidised Bed operating at the minimum fluidisation regime, but introducing an external speed component through the rotation of the immersed sample and fixing the total process time.

Besides the process configuration, the effect of different abrasive materials was considered for the experiments, chosen in order to emphasise some of their properties such as hardness and density and investigating also, at the same time, the effect of the abrasive particles shape for some specific cases. Still taking into consideration the stationary and rotating sample configurations, the effect of the impact angle was always considered, according to the premise reported in Chapter 3 about

its influence on the FBM process. On the other hand, the effect of the rotational speed was considered only for the rotating sample configuration, inducing different values of average relative tangential speed between the fluidised abrasive and the surface under treatment. Concerning the characterisation tests, weight loss was also investigated for the FBM treatment, since it can be considered as a grinding process, making expectable a weight change of the sample due to material removal.

The second surface treatment proposed in this work is CP, presented in Chapter 7. In this case, the samples were dipped into custom aggressive solutions, contained in a thermostatic bath that enabled to control the temperature and the stirring of the chemical solution. Moreover, the smoothing effect of the process was investigated at different time-steps, in order to observe the evolution of the treated surfaces.

Standing on the actual knowledge of the author, in this case there is lack in literature about the study of CP for Aluminum alloy parts made by means of SLM. Therefore, the identification of the process parameters as well as the experimental campaign were established only according to the theoretical background of CP provided in Chapter 3, since there are no available data in literature for a comparison.

According to the process background discussed in Chapter 3, the experiments were carried out considering a two-stage process. The first stage is represented by *Chemical Machining*, which is responsible for the greatest smoothing effect within the whole process: in this case, an aqueous solution of Hydrofluoridric and Nitric acids was used. The choice of these two acids was dictated by the preliminary microstructure analysis carried out on a sample, suggesting the need to use substances that are able to perform an etching of the surface as more uniform as possible, according to the high silicon content of the AlSi10Mg alloy that responds differently with respect to the Aluminum matrix. The second stage of the process was the *Chemical Brightening*, performed to further reduce the surface roughness of the Chemically Machined samples, but promoting at the same time an improvement of symmetry and brilliance. The chemical bath used in this case was chosen on the basis of the commercially available *Phosbrite®* solution, already used for the brightening of Aluminum alloys. However, according to the same consideration done for the Chemical Machining solution, Hydrofluoridric acid was added to the Phosbrite in order to promote a more uniform effect of the treatment. According to literature, the mechanism of Chemical Brightening is based on different premises with respect to Chemical Machining, leading to the choice of a chemical bath with different characteristics. More specifically, the effects of the brightening step are due to a more selective smoothing effect on the asperities than the valleys, based on the differential migration speed of the dissolved metal into the bulk chemical bath, i.e. higher for the asperities compared to the valleys. This effect is promoted by adopting a high viscosity chemical bath, in this case represented by the modified Phosbrite, whose main component is Phosphoric acid.

Concerning the varied process parameters, three values of temperature were investigated for each process step, that is generally higher for the Chemical Brightening compared to Chemical Machining, according to considerations reported in literature. About the process time, Chemical Machining was set to longer times compared to the Brightening step. For the former, the whole process time was split into five time-steps, whereas for the Chemical Machining the total process time and the steps number was lower, still according the indications reported in literature. Furthermore, for the Chemical Machining step the process effects were also analysed in terms of percentage weight reduction and *etch rate*, not considered for the Chemical Brightening since the latter is not supposed to promote significant material loss. Finally, before and after each stage of the process, EDS analyses were carried out in order to compare the resulting material chemistry, investigating therefore the possible surface composition alterations induced by the treatment.

The third surface treatment proposed is LSR, carried out by means of CO_2 laser equipment and widely discussed in Chapter 8. As stated in Chapter 3, the aim of the experiments in this case was to explore the possibility to take advantage of the undesired high surface roughness of the as-built samples to promote a higher laser absorption of the CO_2 laser radiation. In fact, it is well established that the latter is poorly absorbed from Aluminum surfaces resulting from traditional machining processes, the latter presenting a lower roughness. This is the reason why, over the years, the research has moved in the direction of usage of laser sources that promote a higher absorption due to shorter wavelengths. On the other hand, as stated by *Poprawe et al.* [127], it is also well known that the surface roughness possesses a great influence on the laser radiation absorption from a given material, if the roughness component is greater than the wavelength of the radiation itself. Moreover, given the wide and intensive use CO_2 lasers for different applications such as cutting, welding, engraving and so on, the objective of the experiments reported in this work could represent the starting point for an extent of the use of CO_2 lasers for polishing Aluminum parts produced by PBF-AM technologies.

Based on this premise and the higher maturity level of LSR compared to the previous treatments, the experiments reported in this Ph.D. thesis were based on a more systematical approach based on the Design of Experiments (DoE). More specifically, considering that the most critical process parameters in LSR are the laser power, the scanning speed and the overlap between the single re-melting tracks, a full factorial DoE was carried out in order to identify a first useful process window that maximizes the surface smoothing effect. The levels used for the DoE factors were established after a series of necessary preliminary tests, given the absence of available data in literature to perform a comparison in this specific LSR process case, similarly to the aforementioned CP surface treatment. The resulting surfaces treated with the different process parameters were analysed by means of the Response Surface Method (RSM) and statistical analysis, in order to establish the significance of the chosen parameters and to identify the values that gives the best surface roughness improvements within the considered process window.

After the identification of the best process conditions, repeatability tests were carried out, performing also a comparison with the process parameters that provided the minimum and the maximum areal energy density on the surface.

Furthermore, considering that for the DoE tests the laser focus position was fixed on the peaks of the as-built surface, the effect of this process parameter was considered in a further sub-set of experiments, carried out using the process parameters that provided the best results from the DoE. More specifically, the focus position was shifted above the peaks of the surface up to 3 mm, with a 1 mm step, with the aim to promote a more uniform areal energy distribution — with respect to the random surface texture of the as-built samples — and to minimize the microstructure alterations induced by the heat input. The results and the evaluation of the process stability was investigated also in this case by means of three repeatability tests for each focus shift considered. Given the heat input provided on the surface, a detailed microstructure analysis was carried out on each treated sample. The analyses were carried out by means of optical microscopy and SEM, after a proper specimen preparation for metallographic analyses. The latter were carried out in order to investigate the re-melting depth under different process conditions, as well as to investigate the microstructure alterations induced by the treatment.

Finally, on the basis of the obtained results, in the last Chapter of this work are reported more general conclusions about the investigated surface finishing processes. More specifically, a quantitative comparison of the surface roughness improvements induced by the different treatments is reported. The latter is followed by a brief critical comparative analysis of the benefits and drawbacks of the considered processes, whose detail is still limited due to the low maturity level of the investigated treatments.

Moreover, considering some of the issues observed in relation with the experimental results and characterisation methodology, some insights and recommendations for future works are discussed.

5. Case study and characterisation tests

In this chapter, a description of the samples used as the case study is reported. Furthermore, the information related to the samples building process through the SLM process are provided. Finally, given the application to all the surface treatments investigated in this thesis, a detailed description of the characterisation techniques and procedures is provided, as well as their motivation of choice and use.

5.1. AlSi10Mg samples manufacturing with SLM technology

As stated in the previous Chapter, the surface treatments were performed considering flat samples with simple geometry. More specifically, the case study consisted in square flat samples (dimensions: 20 x 20 x 2 mm^3), built in vertical direction with respect to the building platform. Therefore, the build angle — an SLM process variable that has a remarkable influence on the resulting surface quality, according to the considerations reported in Chapter 2 — was not considered in this work. In Fig. 5.1 is illustrated a typical sample used for the experimental investigations. The samples manufacturing was carried out in collaboration with MBDA Italy S.p.A., starting from AlSi10Mg powder feedstock provided by EOS GmbH [164] and associated with the use of an EOSINT M280 SLM machine (property MBDA Italy S.p.A). In Fig. 5.2 is reported an SEM image of the employed alloy powders. The particle size distribution, reported elsewhere [165], and chemical composition were confirmed by means of a Malvern MS2000 laser diffraction analyser according to ASTM B822-17 [166] and an Hitachi TM3000 SEM, according to ASTM F1877-16 [167]. Moreover, the process parameters used to build the samples refers to the locked exposure profile *EOS Part Property Profile AlSi10Mg Speed 30 μm*, provided by the EOS GmbH, and stress relieved at 300 °C for 2 h similarly to other works reported elsewhere [165].

Figure 5.1. Illustration of an AlSi10Mg squared flat sample produced in collaboration with MBDA Italy S.p.A through SLM technology (a 10 cents coin is reported as a scale marker).
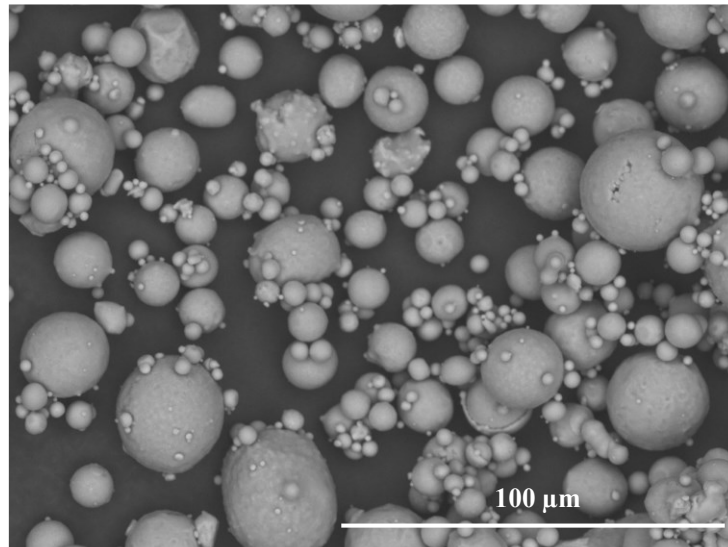
Figure 5.2. SEM image of the AlSi10Mg powders feedstock used to build the samples (magnification 1000x).

5.2. Characterisation tests

With the aim to provide a more comprehensive view of the effects of the investigated treatments, several characterisation techniques were employed. The aim was to emphasize the different aspects related to the specific interactions with the surface, according to their different nature with respect to the surface treatments discussed later. It is worth to highlight that, right after the build, loose powders on the samples and some impurities were present, that would affect the characterisation tests. Therefore, before and after any treatment step the samples were accurately cleaned in an ethanol ultrasonic bath for 15 min, followed by drying at 80 °C for 1h.

5.2.1. Confocal Microscopy

As well stated before, surfaces produced by PBF-AM technologies are basically characterized by a random texture, due to the presence of a layer of sintered powders attached to the underlying surface. This result, as also well clarified before, is more due to the balling effect rather than the stair-step effect, although the latter can significantly influence the entity of the former [108]. As a result, it is expectable that surface characterisation would not be necessarily compatible with the well consolidated surface metrology techniques in industry as well as in academia, i.e. contact probe profilometry. With this aim, *Townsend et al.* [168] provided an excellent overview of the issues in surface characterisation related to metal AM surfaces. In their work, it was mainly stated that the traditional surface characterisation procedures adopted in the past would be no longer suitable for metal AM surface or, at least, not sufficiently exhaustive in terms of gaining the proper surface status information. In this sense, a more efficient characterisation of surfaces is related to techniques that provides texture information on a larger scales, i.e. areas and/or volumes. In this context, Confocal Microscopy is getting more and more attention due to its capabilities to provide areal surface texture information [169]. Based on a non-contact acquisition, it addresses some of the issues of stylus profilometry, as well as the possibility to perform acquisition stacks and surface texture indicators availability. With this premise, Confocal Microscopy was used to gain the necessary texture information, presented later for the three different surface treatments. Moreover, it represents the main characterisation technique used to provide quantitative

information related to analyses carried out on the samples before and after the treatments. In the following points, a detailed description of the operations performed to quantify the improvements of the treated samples is provided, using the Leica DCM3D Confocal Microscope reported in Fig. 5.3.

Figure 5.3. Leica DCM3D confocal microscope.

3D Surfaces acquisition setup

After the samples preparation, the 3D surfaces were acquired. For each acquisition, an 8 x 8 mm^2 area was considered and acquired from the center of the sample. According to the Leica DCM3D technical specifications, in the following Table 5.1 are reported the specific parameters used to acquire the surfaces. It is worth to note that a z scan (depth of the surface acquired, starting from the upper peaks) was set to a higher value compared to the expected actual values of the surface roughness parameters described later. This was due to the need to ensure the complete acquisition of the surface points and to compensate possible tilts of the positioned sample under the lens and slight shape defects. Moreover, a speed value of 1x indicates that, within the z scan, every optical sectioning plane was considered to acquire the surface points.

However, for the CP process discussed in Chapter 7, before the 8 x 8 mm^2 area acquisitions, a smaller area of 8 x 2 mm^2 was considered first. This consideration, based on the preliminary goal to gain more rapid information about the surface texture evolution during the process, was dictated by the need to avoid surface damages related to chemical bath residues that might be trapped into the edges of the samples due to the hot mounting. The latter step, necessary for the establishment of the correct chemical polishing process setup, will be discussed in Chapter 7.

Table 5.1. Leica DCM3D measurement setup, use to acquire the 3D surfaces before and after the surface treatments.

Magnification	10x (x-y resolution: 0.94 μm, z resolution: 0.47 μm)
Area	8 x 8 mm^2 (stitching of 1270×950 μm^2 spot areas)
Z scan	600 μm
Speed	1x
Light	Auto

The quantification of the surface evolution after the surface treatments was carried out by means of the investigation of different surface texture parameters, according to the time steps of the different treatments, and performing a comparison before and after the treatment for each sample. According to the ISO 25178-2 and ISO 4287:1997 standards [170, 171], the status of a surface can be described by means of profile and areal texture parameters. The information achievable is related to four main texture parameters groups: *height, spacing, hybrid* and *material-related*. In this work, most of the attention was paid to height parameters, representing the major concern with respect to the discussed surface characteristics of the SLM processed parts. However, an accurate analysis of treatments-induced surface texture represents a key issue in this context, and it needs to be investigated. In the following points are reported the surface texture parameters used in this work, with the definitions and motivations of choice:

- S_a: **arithmetic mean of the absolute of the ordinate values within a definition area (A) (ISO 25178-2).** The mathematical definition and the physical meaning of this parameter are reported in the following Eq. 5.1 and Fig. 5.4. This parameter represents the areal equivalent of the most widespread profile arithmetic roughness (R_a), and it represents the first general indicator of the surface quality. However, it is quite sensitive to isolated spikes and does not provide information on the surface homogeneity or distribution of peaks and valleys with respect to an ideal mean reference plane.

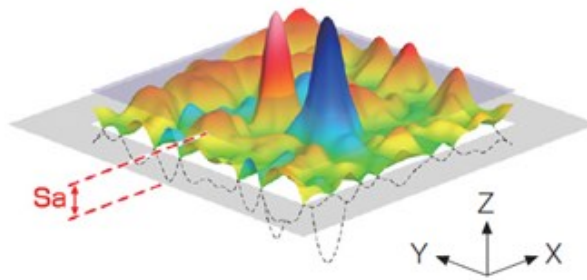$$S_a = \frac{1}{A} \iint_A |Z(x, y)| \, dx \, dy \qquad (5.1)$$

Figure 5.4. Physical meaning of S_a [172].

- S_z: **Maximum height within a definition area (A) (ISO 25178-2).** The mathematical definition and the physical meaning of this parameter are reported in the following Eq. 5.2 and Fig. 5.5. This parameter represents the areal equivalent of the most widespread profile maximum height. (R_z). It is defined as the z distance between the highest peak (S_p) and the deepest valley (S_v) within the considered area. If evaluated in a synergistic way with S_a, it represents a surface quality indicator that defines the worst height-related roughness feature measured on a surface. On the other hand, it is way more sensitive to surface defects and measurement artefacts (i.e. outliers) than S_a.
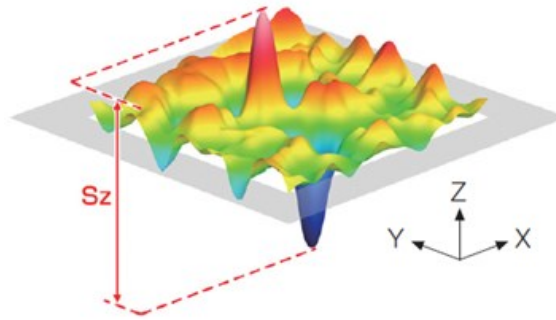
$$S_z = S_p - S_v \qquad (5.2)$$

Figure 5.5. Physical meaning of S_z [172].

- **S_{sk}: Surface Skewness of a defined area (A) (ISO 25178-2).** The mathematical definition and the physical meaning of this parameter are reported in the following Eq. 5.3 and Fig. 5.6. It is defined as the quotient of the mean cube value of the ordinate values and the cube of S_q (root mean square of the areal height distribution, i.e. S_a) within a definition area. It physically represents the symmetry of the peaks and valleys distribution within the considered area and, consequently, is particularly useful to a more comprehensive characterisation of a surface as well as its evolution after a smoothing treatment. In the latter case, it gives information about the effects of a treatment on the peaks and/or on the valleys.

$$S_{sk} = \frac{1}{S_q^3} \left[\frac{1}{A} \iint_A \left(Z(x, y) \right)^3 dx \, d_y \right] \qquad (5.3)$$
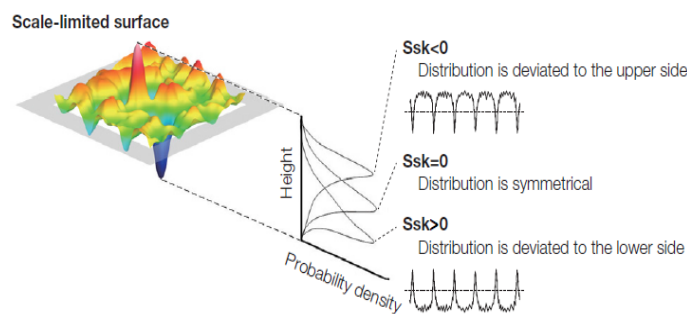
Figure 5.6. Physical meaning of S_{sk} [172].

- **S_{ku}: Surface Kurtosis of a defined area (A) (ISO 25178-2).** The mathematical definition and the physical meaning of this parameter are reported in the following Eq. 5.4 and Fig. 5.7. It is defined as the quotient of the mean quartic value of the ordinate values and the fourth power of S_q within a definition area. It physically provides information about the sharpness of the peaks. Consequently, it is particularly useful to investigate the smoothing effect of a treatment with respect to the removal and/or rounding of the peaks.

$$S_{ku} = \frac{1}{s_q^4}\left[\frac{1}{A}\iint_A \left(Z(x,y)\right)^4 dx\, d_y\right] \tag{5.4}$$
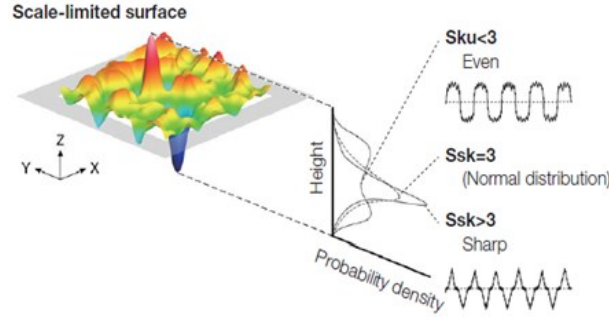

Figure 5.7. Physical meaning of S_{ku} [172].

- **P_{dq}: Root mean square slope of primary profile (ISO 4287:1997).** The mathematical definition and the physical meaning of this parameter are reported in the following Eq. 5.5 and Fig. 5.8. It represents the root mean square of the profile slope dz/dx within the sampling length and, according to literature [173], it is strictly correlated to the brilliance and reflectivity of a surface. It is worth to note that, in this case, the profile version of the slope was considered. Since the aim was to evaluate the brilliance of the surface after a treatment, the areal equivalent of P_{dq}, i.e. S_{dq} (Surface gradient), is not useful because it has a different physical meaning [170]. Moreover, given the random surface texture of the as built SLM surfaces, no filtering operations were carried on the acquired surfaces and profiles. The P_{dq} values reported later for the different surface treatments were measured starting from the extraction of five profiles for each of the two mutual directions identifying the considered samples area. The reported measures were then evaluated by means of the average and standard deviation of the ten values.

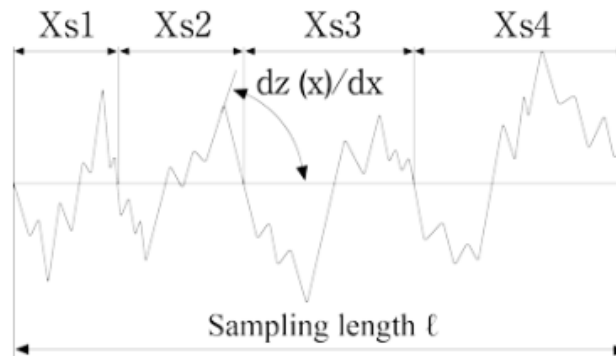$$P_{dq} = \sqrt{\frac{1}{l}\int_0^l \left(\frac{d}{dx}Z(x)\right)^2 dx} \tag{5.5}$$

Figure 5.8. Physical meaning of P_{dq} [172].

It is worth to point out that, before the extraction and analysis of the discussed texture indicators, a series of preliminary operations on the acquired surfaces were necessary in order to avoid the influence of surface artifacts. These operations included tilt and shape correction, as well as filling of missing points caused by internal defects and undercuts that are unavoidable. To carry out these operations, the in-bundle software *Leica Map v7* was used to post-process the acquired data.

5.2.2. Optical Microscopy

Optical Microscopy analyses were carried out on the samples that were subjected to the CO_2 laser re-melting treatment. More specifically, the aim of the analyses was the observation of the microstructure evolution after the treatment for the considered samples and the evaluation of the re-melting depth, as a function of the different process parameters used for the experimental campaign. After the samples preparation for in-section observations, carried out according to the standard metallographic procedure [174], optical macrographs were taken for each of the investigated samples at 200x magnification. To carry out the analyses, a Zeiss Axioplan 2 optical microscope was used, reported in Fig. 5.9. Moreover, the measure of the re-melting depth was carried out for each case considered, performing five measures on the acquired images through the software *ImageJ®,* in order to provide the average and standard deviation values.

Figure 5.9. Zeiss Axioplan 2 Optical Microscope.

5.2.3. SEM-EDS

SEM was used to evaluate qualitatively the real surface morphology evolution occurring for all the investigated surface treatments, as well as for a detailed microstructure analysis for the specific cases of CP and CO_2 LSR treatments. With this aim, an Hitachi TM3000 SEM was employed, reported in Fig. 5.10. The images of the surfaces were acquired at 100x magnification before and after the considered treatments, considering also the different process time steps where present (FBM, CP). Moreover, the SEM is equipped with a SWIFT ED3000 probe for Energy Dispersive X-ray Spectroscopy analysis (EDS), used to analyse the chemical surface composition when needed, i.e. only for the CP case.

Figure 5.10. Hitachi TM3000 Tabletop SEM.

5.2.4. Weight loss

Weight measures were carried out for the treatments in which it is expected to find appreciable changes (FBM, CP). After the samples preparation procedure mentioned above, weight measurements were carried out before and after each step of the investigated treatments. This aspect, besides to provide further support on the results obtained from the other tests, also useful to establish whether if the treatments might induce shifts in dimensional accuracy of the SLM processed parts. Moreover, referring to CP, weight loss measures are also useful to determine the *etch rate*, an output process parameter that provides information about the treatment efficiency regardless of the specific treated area. A detailed description of this parameter is given in Chapter 7.

5.2.5. Chart of the performed tests for the different surface treatments

For sake of clarity, given the different expected influence of the investigated surface treatments based on their nature, the following Table 5.2 reports synthetically al the performed tests. More specifically, according the characterisation tests previously reported, the aim of the chart is to highlight in which case a specific characterisation test was performed.

Table 5.1. Leica DCM3D measurement setup, use to acquire the 3D surfaces before and after the surface treatments.

	Confocal Microscopy	Optical Microscopy	SEM	EDS	Microstructure analysis	Weight loss
FBM	x		x			x
CP	x		x	x		x
CO2 LSR	x	x	x		x	

6. Fluidised Bed Machining

In this Chapter, a detailed description of the preliminary tests carried out with the FBM process is reported. Starting from the description of the experimental setup and the abrasive materials used, the investigated process conditions are also highlighted and motivated. Finally, according to the characterisation methodology presented in Chapter 5, the obtained results are presented and critically analysed.

6.1. Experimental apparatus

The surface finishing preliminary tests were carried out in collaboration with the Combustion Research Institute of the National Research Council (IRC-CNR, Naples, Italy). The reactor used, illustrated in Fig. 6.1, is represented by a Plexiglas column with an inner diameter of 204 mm and a height of 1440 mm. The reactor is composed by two modules: the lower module, with a height of 450 mm, works as a *windbox* and contains ceramic rings that allows the homogeneisation of the gas inlet (air). The upper module, with a height of 970 mm, hosts the abrasive particles and the clamping system for the samples.

Figure 6.1. Experimental apparatus used for the FBM preliminary tests.

Between the two modules, joined by fasteners, a metal bubble caps distributor plate is located, reported in Fig. 6.2. This component allows to hold the abrasive particles in static conditions as well as their fluidisation, once the air inlet is introduced from the bottom of the lower module. The air flow rate inside the reactor was managed by a mass flow-meter (*Bronkhorst El-flow select*) with a maximum flow rate of 200 m^3/h.
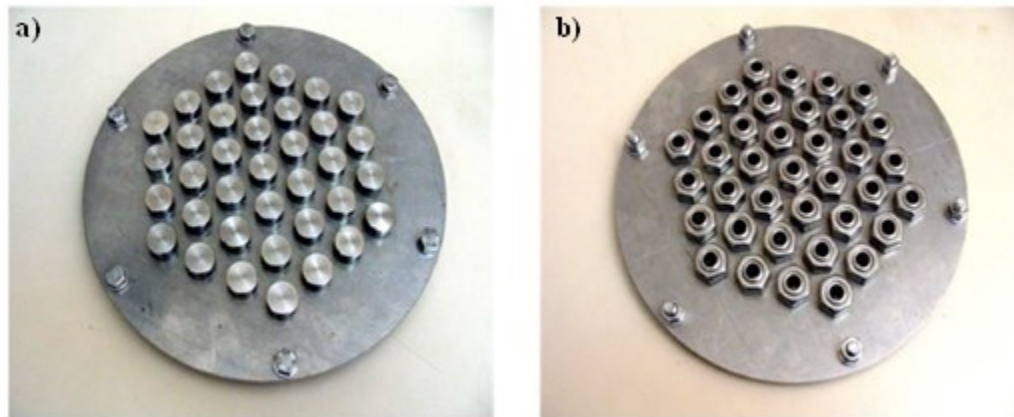

Figure 6.2. Top (a) and bottom (b) view of the metal bubble caps distributor plate.

On one side of the reactor and at the bottom part of the upper module, an electrical motor was linked through a rotating axis partially located inside the reactor, whose rotational speed is controlled by means of an inverter. The axis can rotate at a speed up to 1850 rpm. Considering the middle of the rotating axis portion located inside the fluidisation column, a purposely made samples holder was mounted through a threaded bar. The modified reactor and the samples holder are illustrated in Fig. 6.3a-b respectively. As it will be specified later, this latter configuration was employed in order to carry out the tests in the stationary and rotating sample conditions.
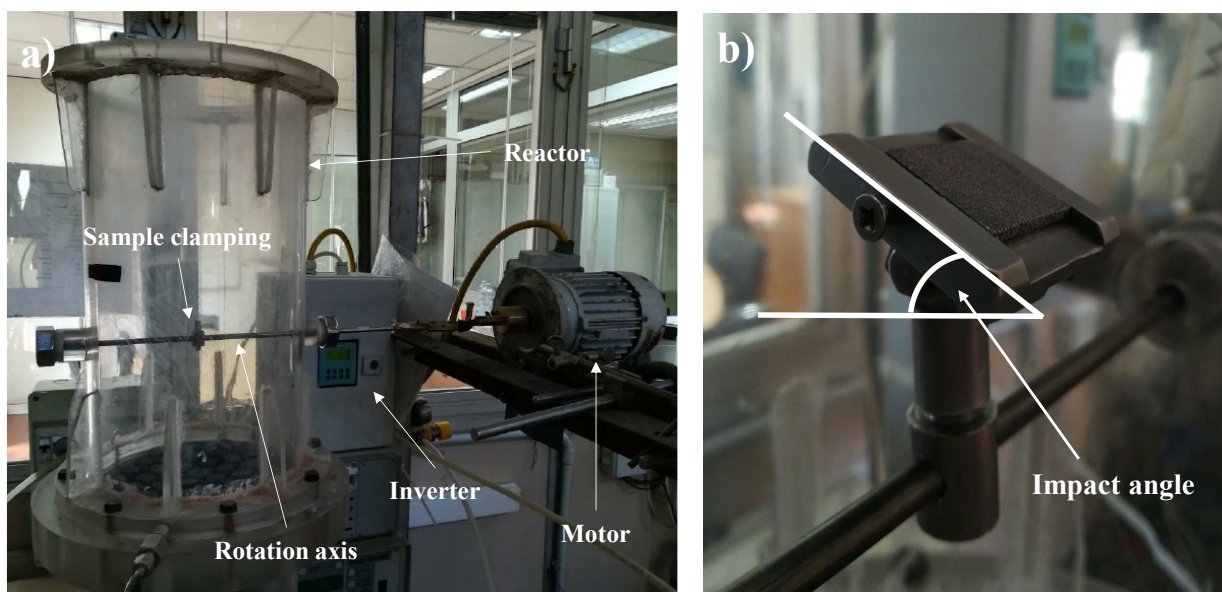

Figure 6.3. Illustration of the experimental apparatus (a), with a detailed magnification of the purposely made samples holder (b).

In order to initiate an experiment, a sample was fixed on the clamping system through a lateral screw. Moreover, the samples holder was designed to carry out the tests considering any impact angle of the substrate exposed to the fluidised abrasives, as illustrated in Fig. 6.3b, with respect to the normal impact condition. It is worth to highlight that, for the stationary sample configuration, the normal impact condition was established for the horizontal position of the sample (i.e. impact angle equal to 0), whereas for the rotating sample configuration the condition is set when the impact angle is equal to 90°.

6.2. Preliminary experimental campaign

The preliminary tests conditions were chosen according to the general process considerations already discussed in Chapter 3, as well as following similar experiments reported in literature. More specifically, regardless of the specific abrasive used, the experimental campaign was composed to by two main tests categories:

- *Stationary sample tests:* In this configuration, according to similar experiments carried out by *Barletta et al.* [139], a bubbling fluidisation regime of the abrasives was investigated, evaluating also the influence of process time and impact angle for different abrasives. Moreover, no external relative motion of the sample with the former was introduced;

- *Rotating sample tests:* The aim of this tests was based on the considerations about the different impact energy sources discussed by *Barletta et al.* [140], as well as to similar experiments conducted by *Atzeni et al.* [135]. In this case, the major impact energy contribution was provided from the external rotational speed imposed to the sample around its axis, since the minimum fluidisation regime was established. As for the stationary sample tests, the influence of the impact angle was investigated while, with respect to the process time, in this case a single-step process was carried out. It is worth to point out that the latter choice was based according to the short process times typically needed in this process configuration, as noted by *Barletta et al.* [140].

6.2.1. Abrasives

The choice of the abrasives used in the experimental campaign was dictated by the need to explore different trade-offs between the main abrasives-related process parameters. About this issue, a general overview of the abrasives properties as a function of their nature is provided by *Carson* [175]. More specifically, the attention was focused on two selection criteria:

- Investigations on the effect of abrasives with high hardness, but low density;
- Investigations on the effect of abrasives with high density, but less hard as the previous ones. In this case, the abrasives shape was also varied as a process parameter.

Based on these considerations, four abrasives were used for the experimental campaign, listed as follows and illustrated by the SEM images reported in Fig. 6.4. Moreover, in Tables 6.1-6.2 the main characteristics of the abrasives are reported.

High hardness abrasives:

- *Silica sand* (Fig.6.4a), with irregular shape and an average particle size of 570 μm;
- *Alumina* (Fig.6.4b), with irregular shape and an average particle size of 650 μm.

High density abrasives:

- *Irregular shaped stainless steel* (Fig.6.4c), with an average particle size of 570 μm;
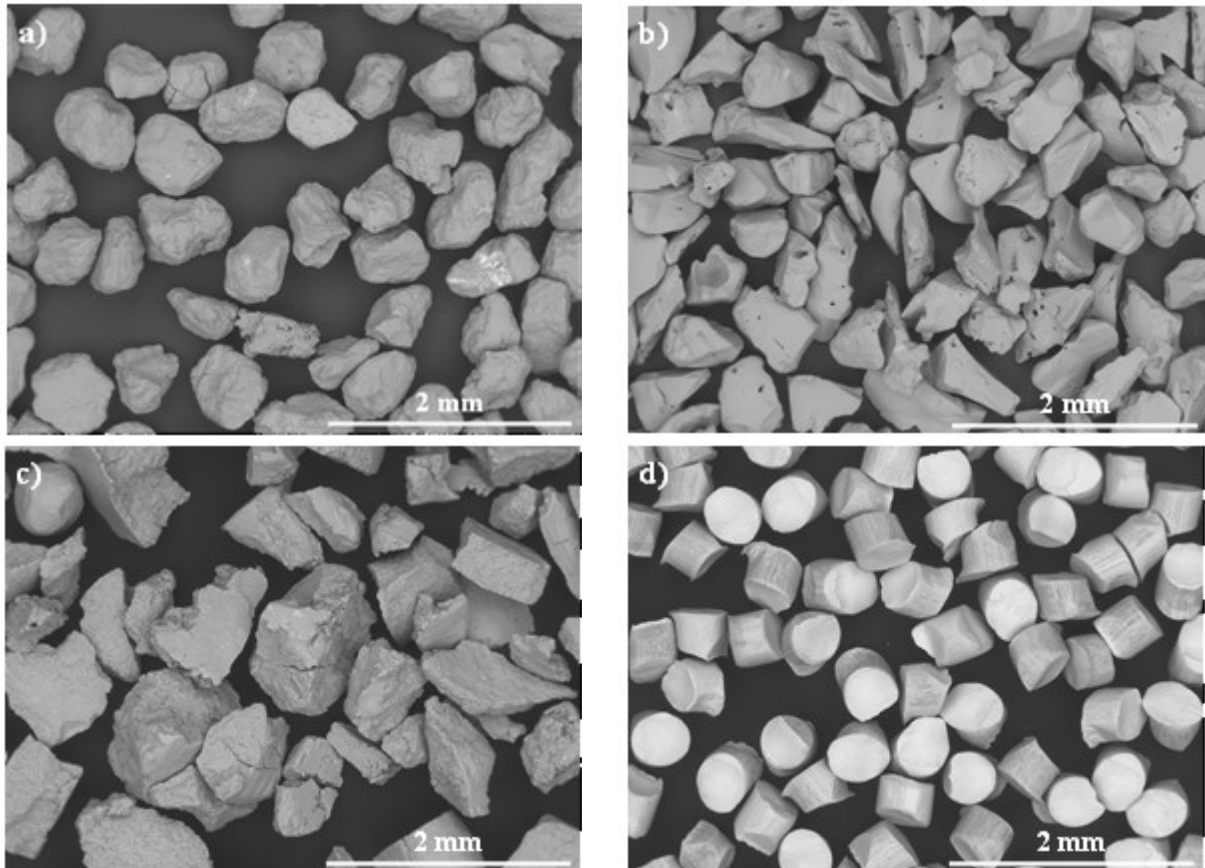- *Cut wire stainless steel* (Fig.6.4d), with an average particle size of 500 μm.

Figure 6.4. SEM images of the abrasives used for the FBM process: (a) irregular shape silica sand, (b) irregular shape alumina, (c) irregular shape stainless steel, (d) cut-wire stainless steel (magnification 40x).

Table 6.1. Chemical composition and main properties of the high hardness abrasives.

Abrasive	Chemical composition (%wt)					Apparent Density $(\frac{Kg}{dm^3})$	Vickers Hardness (HV)
	Al_2O_3	Fe_2O_3	SiO_2	TiO_2	CaO		
Silica sand	--	--	--	--	--	2.57	900
Alumina	99.7	0.035	0.023	0.006	0.025	3.87	2300

Table 6.2. Chemical composition and main properties of the high density abrasives.

Abrasive	Chemical composition (%wt)				Apparent Density $(\frac{Kg}{dm^3})$	Vickers Hardness (HV)
	Fe	C	Si	Mn		
Irregular	96	0.8	0.4	0.35	4.2	500
Cut wire	98	0.55	0.2	0.5	4.5	480

6.2.2. Stationary sample experiments

According to the description mentioned above, in this experimental configuration the impact angle and process time were the main process parameters investigated. Regardless of the specific abrasive used, three impact angles were used, i.e. 0°, 25° and 90. These values were investigated considering the need to evaluate to impact angle extreme conditions (0°, 90°) as well as the impact angle that, according to literature, maximises the contribution of the four substrate-abrasive interaction mechanisms described in Chapter 3 (25°).

Regarding the process time, three steps of 30 min each were considered, giving a total process time of 90 min. Before and after each step (except for the repeatability tests, analysed only before and after the whole treatment), the characterisation procedure described in Chapter 5 was applied. It is necessary to mention that, depending on the specific abrasive used and the reactor dimensions, the superficial gas velocity (U) needed to establish the minimum fluidisation regime (U_{mf}) changes. Therefore, in Tables 6.3-6.5 are reported the operating parameters used for the stationary sample conditions related to the abrasives used.

Table 6.3. FBM process parameters used in the stationary sample condition, considering the silica sand as the fluidised abrasive.

Impact angle (°)	U (m/s)	U_{mf} (m/s)	$U\text{-}U_{mf}$ (m/s)
0	1	0.2	0.8
25	1	0.2	0.8
90	1	0.2	0.8

Table 6.4. FBM process parameters used in the stationary sample condition, considering alumina as the fluidised abrasive.

Impact angle (°)	U (m/s)	U_{mf} (m/s)	$U\text{-}U_{mf}$ (m/s)
0	1.22	0.42	0.8
25	1.22	0.42	0.8
90	1.22	0.42	0.8

Table 6.5. FBM process parameters used in the stationary sample condition, considering stainless steel (irregular, cut wire) as the fluidised abrasive.

Impact angle (°)	U (m/s)	U_{mf} (m/s)	$U\text{-}U_{mf}$ (m/s)
0	1.27	0.47	0.8
25	1.27	0.47	0.8
90	1.27	0.47	0.8

6.2.3. Rotating sample experiments

As previously stated, the rotation of the parts inside the fluidised bed allows to increase the relative speed without the need to use turbulent fluisidation regimes. According to the process conditions described before, in this case the main process parameters investigated for the different abrasives were the impact angle and the rotational speed of the sample. The latter determines a peculiar interaction with the fluidised abrasive, i.e. a process condition in which the tangential speed component of the relative speed is prevalent compared to the others acting on the substrate. Moreover, the tangential speed changes depending on the distance from the rotation axis and the specific impact angle. Therefore, the corresponding rotational speed to apply changes, according to Eq. 6.1, determining also a range of values more than the single.

$$rpm = \frac{v \cdot 60}{(2\pi \cdot b)} \qquad (6.1)$$

Where:

rpm = Rotational speed of the motor axis;

v = Tangential speed calculated at the center of the sample (m/s);

b = Distance between the center of the sample and the center of the motor axis (m).

Based on these considerations, two values of the tangential speed on the surface were investigated, i.e. 1 m/s and 2 m/s, considering a total process time of 30 min. Moreover, in order to identify the real rotational speed of the samples when immersed into the fluidised bed — that represents a considerable inertia component — the actual rpm were controlled using an optical counter. Tables 6.6 – 6.8 illustrates the process parameters used to carry out the rotating sample tests for the different abrasives used and to establish the two different values of tangential speed.

As observable for this process configuration, the 65° impact angle was investigated instead of 0°: based on the results obtained for the latter and using the irregular stainless steel, a clear not uniform effect of the treatment was observed, as illustrated in Fig. 6.5. Referring to the 65° impact angle, it was considered since it represents the opposite angle to 25°, considering in this case the vertical position of the sample as the 0° impact angle, as opposed to the reference used for the stationary sample experiments.

Table 6.5. FBM process parameters used in the rotating sample condition, considering silica sand as the fluidised abrasive (parameters are listed according to Eq. 6.1).

Impact angle (°)	U_{mf} (m/s)	d (mm)	rpm		v (m/s)	
			v = 1	v = 2	v = 1	v = 2
25		43 ± 4.2	222	444	0.911-1.097	1.822 - 2.193
65	0.2	37 ± 9.1	258	516	0.753 – 1.245	1.506 – 2.491
90		32 ± 10	299	597	0.688 – 1.314	1.376 - 2.628

Table 6.6. FBM process parameters used in the rotating sample condition, considering alumina as the fluidised abrasive (parameters are listed according to Eq. 6.1).

Impact angle (°)	U_{mf} (m/s)	d (mm)	rpm		v (m/s)	
			v = 1	v = 2	v = 1	v = 2
25		43 ± 4.2	222	444	0.911-1.097	1.822 - 2.193
65	0.42	37 ± 9.1	258	516	0.753 – 1.245	1.506 – 2.491
90		32 ± 10	299	597	0.688 – 1.314	1.376 - 2.628

Table 6.7. FBM process parameters used in the rotating sample condition, considering stainless steel (irregular, cut wire) as the fluidised abrasive (parameters are listed according to Eq. 6.1).

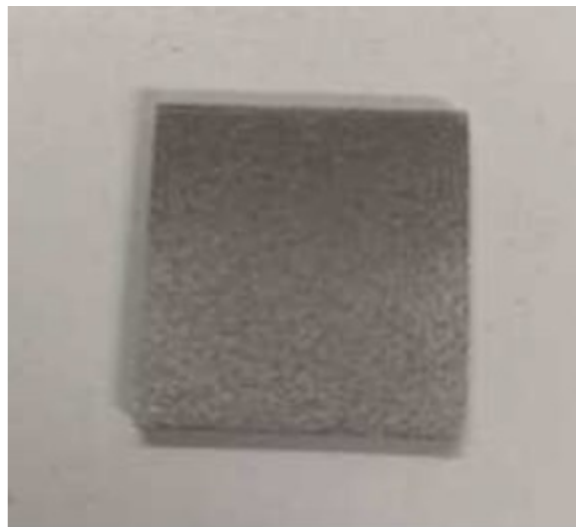| Impact angle (°)	U_{mf} (m/s)	d (mm)	rpm		v (m/s)	
			v = 1	v = 2	v = 1	v = 2
25		43 ± 4.2	222	444	0.911-1.097	1.822 - 2.193
65	0.47	37 ± 9.1	258	516	0.753 – 1.245	1.506 – 2.491
90		32 ± 10	299	597	0.688 – 1.314	1.376 - 2.628

Figure 6.5. Sample treated in rotation conditions and 0° impact angle. Image shows the not uniform effect of the treatment on the upper and lower edges.

6.3. Results and Discussions

6.3.1. Stationary sample experiments

Silica sand

In Fig. 6.6 are reported the time evolutions of the considered surface texture parameters as well as the weight for the different impact angle conditions, while in Fig. 6.7 the 3D surfaces of an untreated sample and the ones treated with the three different impact angles are put in comparison. As a first general observation, it can be noticed that that the samples present a quite different initial surface status, making more difficult a proper evaluation of the actual surface texture. This result is clearly dictated by the phenomena discussed in Chapter 3, promoting a final random surface texture of SLM produced parts.

Regarding the specific experimental conditions reported in this section, the FBM treatment does not promote a consistent surface quality improvement. More specifically, as reported in Tables 6.8 – 6.10, the reduction of S_a and S_z is slight (about 1.5 μm and approx. 150 μm respectively, Fig. 65.6a-b), with the best case represented by the 25° impact angle condition, although comparable results were obtained for the 90° impact angle.

Some specific considerations could be done for S_{sk}: first of all, considering the starting negative values, the initial surface is characterized by more valleys than peaks, the latter mainly represented by the sintered powders attached to the surface. In this context, a clear linear trend can be observed for this parameter (Fig. 6.6c), suggesting that the treatment promotes a partial removal of the sintered powders regardless of the specific impact angle and, therefore, the resulting surface is more asymmetric from the valleys side (S_{sk} decreases). The slight smoothing effect and the partial removal of the sintered powders on the surface were also confirmed by the evolution of S_{ku} and P_{dq} (Fig. 6.6d-e), where for the former a clear trend is not observable due to the slight values change, while the latter experienced more significant reductions for all the impact angles. These results could be justified by the effect of random particles impacts on a random initial surface texture under poor impact energy conditions. More specifically, S_{ku} presents a not clear trend due to the partial remodeling of the surface, leaving almost untouched the underneath surface morphology, while the removal of the sintered powders allows to decrease significantly the average slope of the entire surface.

Although the results related to impact angle were in agreement with the literature about the optimization of the process when angles close to 25° are considered [136], it can be concluded in this case that the process leads to comparable results. About the contribution of the different substrate-particles interactions, taking into consideration the results obtained for the weight (Fig. 6.6f), in these process conditions a slight material removal can be appreciated, while the contribution of plastic deformation-related mechanisms is very low. According with the quantitative results observed by confocal microscopy and weight loss, the SEM images reported in Fig. 6.7 shows that the use of sand as the fluidised abrasive does not promote consistent surface modifications.

Moreover, the images show, for all the samples, the presence of a discrete number of surface defects (darker areas in the images) that were basically not involved in the smoothing process, confirming the poor impact energy transferred from the considered abrasive particles. From the images is also possible to appreciate a partial deformation of the sintered powders that were not detached from the surface, suggesting a not negligible contribution of the micro-peening mechanism.
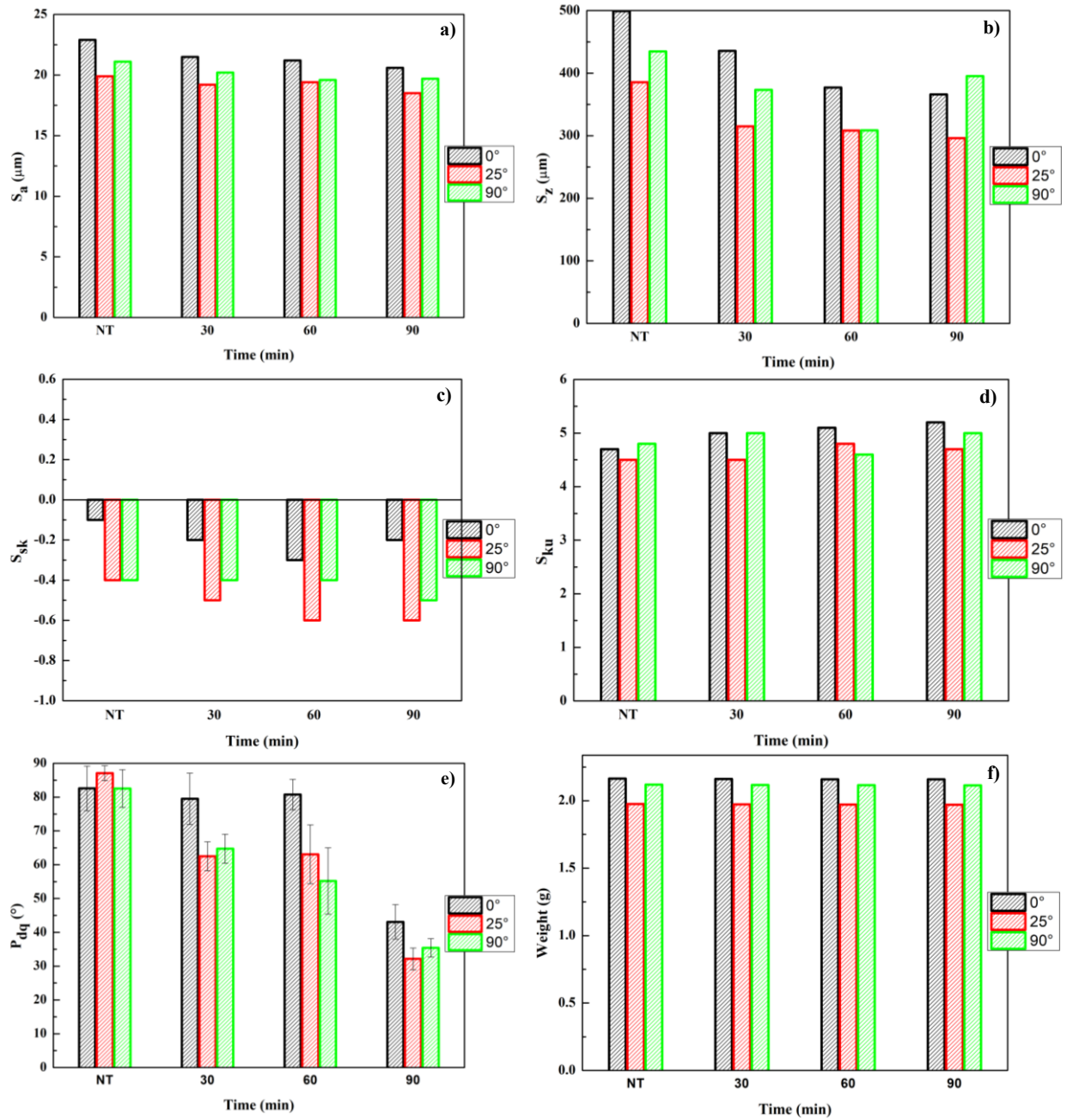
Figure 6.6. Surface texture parameters and weight evolution for the stationary samples tests, using silica sand as the abrasives: (a) S_a, (b) S_z, (c) S_{sk}, (d) S_{ku}, (e) P_{dq} and (f) weight.

Table 6.8. Surface texture and weight values after each step of the FBM, for stationary samples and sand abrasive particles (0° impact angle).

Time (min)	S_a (µm)	S_z (µm)	S_{sk}	S_{ku}	P_{dq} avg (°)	P_{dq} dev.st (±σ) (°)	Weight (g)
0	22.9	499	-0.1	4.7	82.5	6.6	2.164
30	21.5	435	-0.2	5	79.5	7.6	2.161
60	21.2	377	-0.3	5.1	80.7	4.5	2.159
90	20.6	366	-0.2	5.2	43.1	5.1	2.158

Table 6.9. Surface texture and weight values after each step of the FBM, for stationary samples and sand abrasive particles (25° impact angle).

Time (min)	S_a (µm)	S_z (µm)	S_{sk}	S_{ku}	P_{dq} avg (°)	P_{dq} dev.st (±σ) (°)	Weight (g)
0	19.9	385	-0.4	4.5	87.1	2.2	1.976
30	19.2	315	-0.5	4.5	62.5	4.3	1.973
60	19.4	308	-0.6	4.8	63.1	8.7	1.971
90	18.5	296	-0.6	4.7	32.1	3.2	1.97

Table 6.10. Surface texture and weight values after each step of the FBM, for stationary samples and sand abrasive particles (90° impact angle).

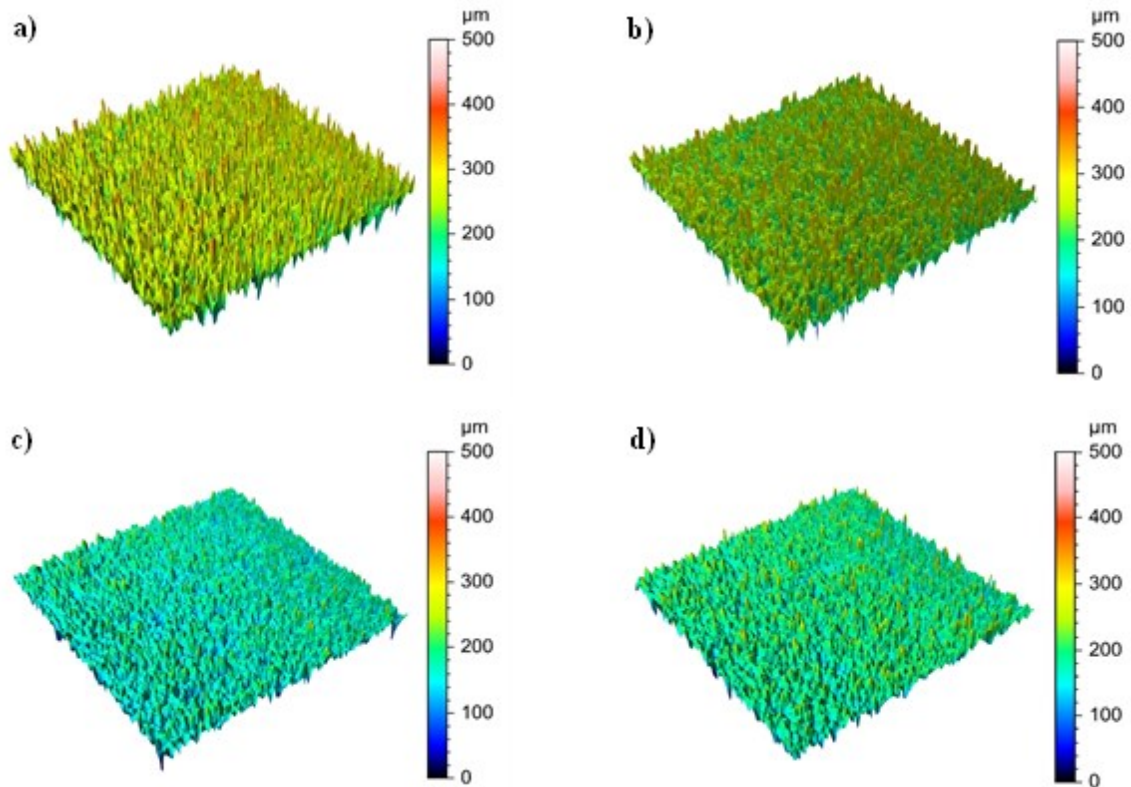| Time (min)	S_a (µm)	S_z (µm)	S_{sk}	S_{ku}	P_{dq} avg (°)	P_{dq} dev.st (±σ) (°)	Weight (g)
0	21.1	434	-0.4	4.8	82.5	5.6	2.119
30	20.2	373	-0.4	5	64.7	4.3	2.116
60	19.6	308	-0.4	4.6	55.2	9.8	2.115
90	19.7	395	-0.5	5	35.4	2.7	2.114

Figure 6.7. Comparison, before and after the whole treatment, between the 3D surfaces of the treated samples under different impact angles: (a) untreated, (b) 0°, (c) 25° and (d) 90°.
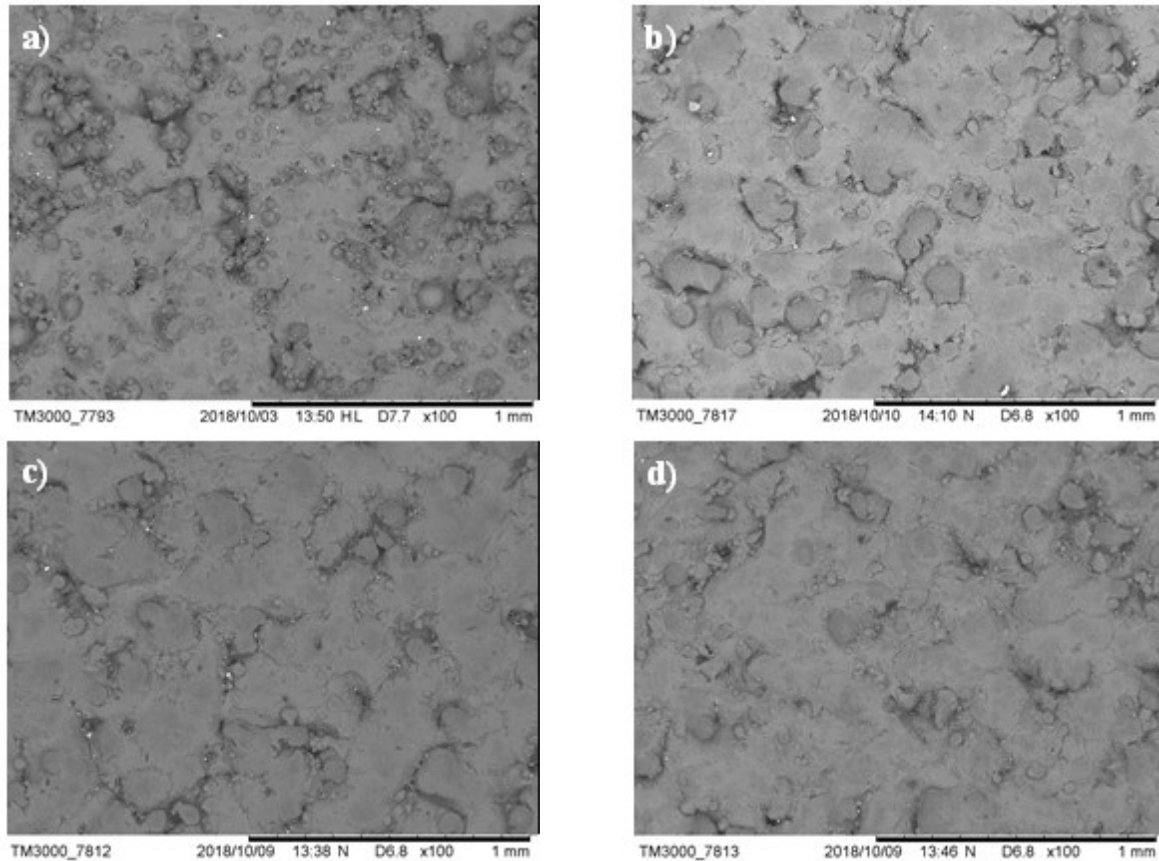
Figure 6.8. Comparison, before and after the whole treatment, between the SEM images of the treated samples under different impact angles: (a) untreated, (b) 0°, (c) 25° and (d) 90° (magnification 100x).

Alumina

According to the tests description and the abrasives characteristics presented above, the aim of the tests carried out by employing alumina as the fluidised abrasive refers to the highest abrasive/substrate hardness ratio condition. In Fig. 6.9 are reported the time evolutions of the surface texture parameters while, in Tables 6.11-13 the actual values measured are reported.

With similar considerations done for the silica sand, the use of a harder abrasive such as alumina does not promote a significant reduction of the surface roughness, as supported the observed values of S_a and S_z that decreases, for the best condition (in this case, 90°), of about 1 μm and 90 μm respectively. It is worth to mention again that the initial values of the parameters related to the untreated surfaces present a remarkable dispersion, due to the SLM mentioned issues and the presence of appreciable defects. This makes more difficult a correct evaluation of the surface improvements determined by the treatment, especially in process conditions, such as the ones presented here and before, that does not induce a completely perceivable change of the investigated parameters.

The similitudes with the investigations reported for the previously case are also observable for the S_{sk} parameter, whose starting negative values decrease even more during the treatment steps. This decrease is quite observable for the 25° impact angle, whereas negligible reductions were observed for the 0° and 90° impact angles. Considering that these results are, again, justified by the slight removal of the sintered powders on the surfaces of the samples, observable by the SEM images reported in Fig. 6.11 and due to low impact energy involved also in this case, the similitudes with the previous experiments are also found for the S_{ku} and P_{dq} parameters.
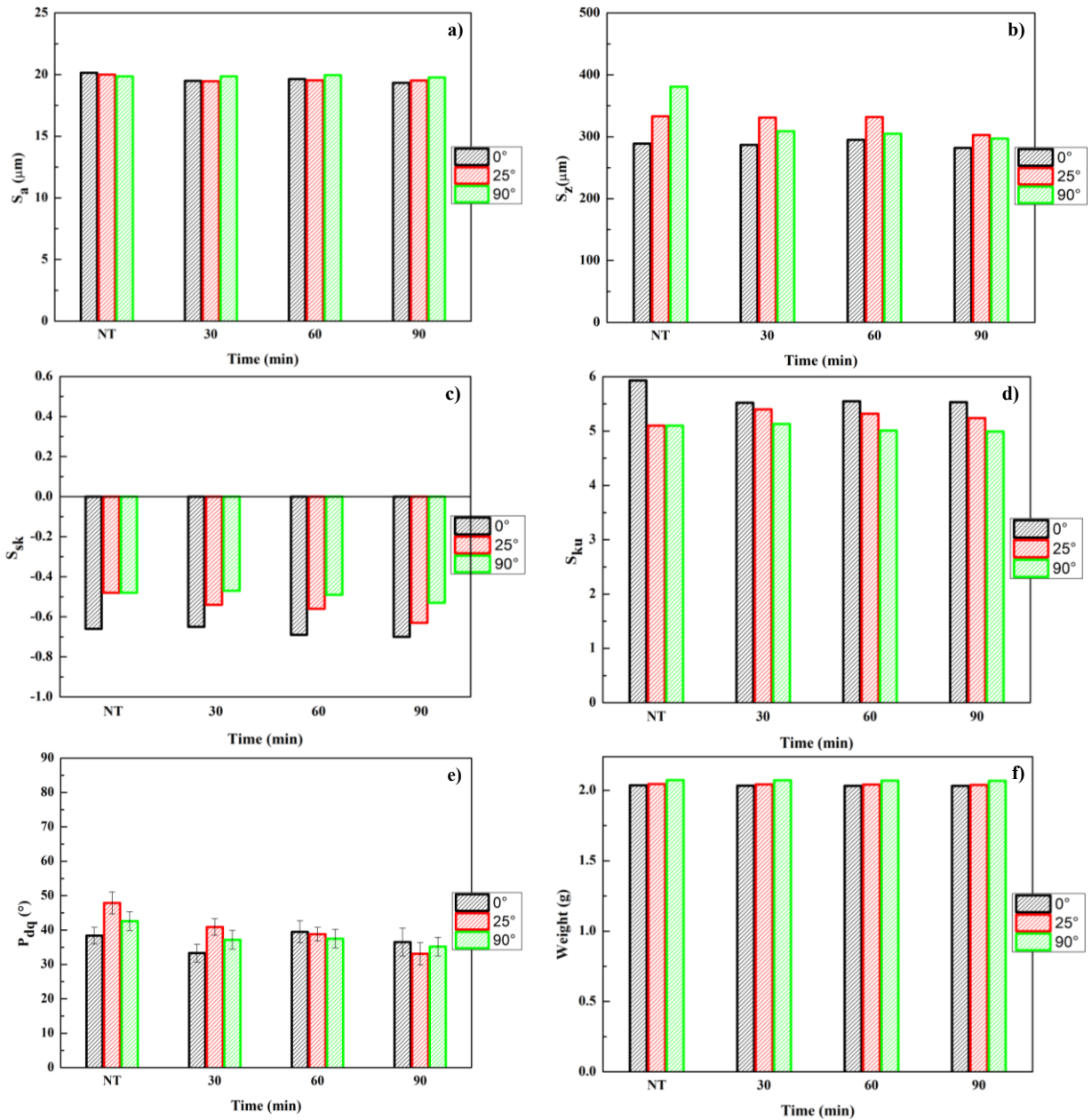
Figure 6.9. Surface texture parameters and weight evolution for the stationary samples tests, using alumina as the abrasives: (a) S_a, (b) S_z, (c) S_{sk}, (d) S_{ku}, (e) P_{dq} and (f) weight.

Based on all the information given by the experimental results, it can be assumed therefore that, under the investigated process conditions, the adoption of a higher abrasive-substrate hardness ratio in FBM is not the best way to achieve the desired significant smoothing effect of the considered samples. Moreover, it can be concluded that, when a stationary sample condition is employed, the hardness of the fluidised abrasive has not a primary effect on the resulting surface modifications, as also visible by the comparison of the acquired 3D surfaces reported in Fig. 6.10.
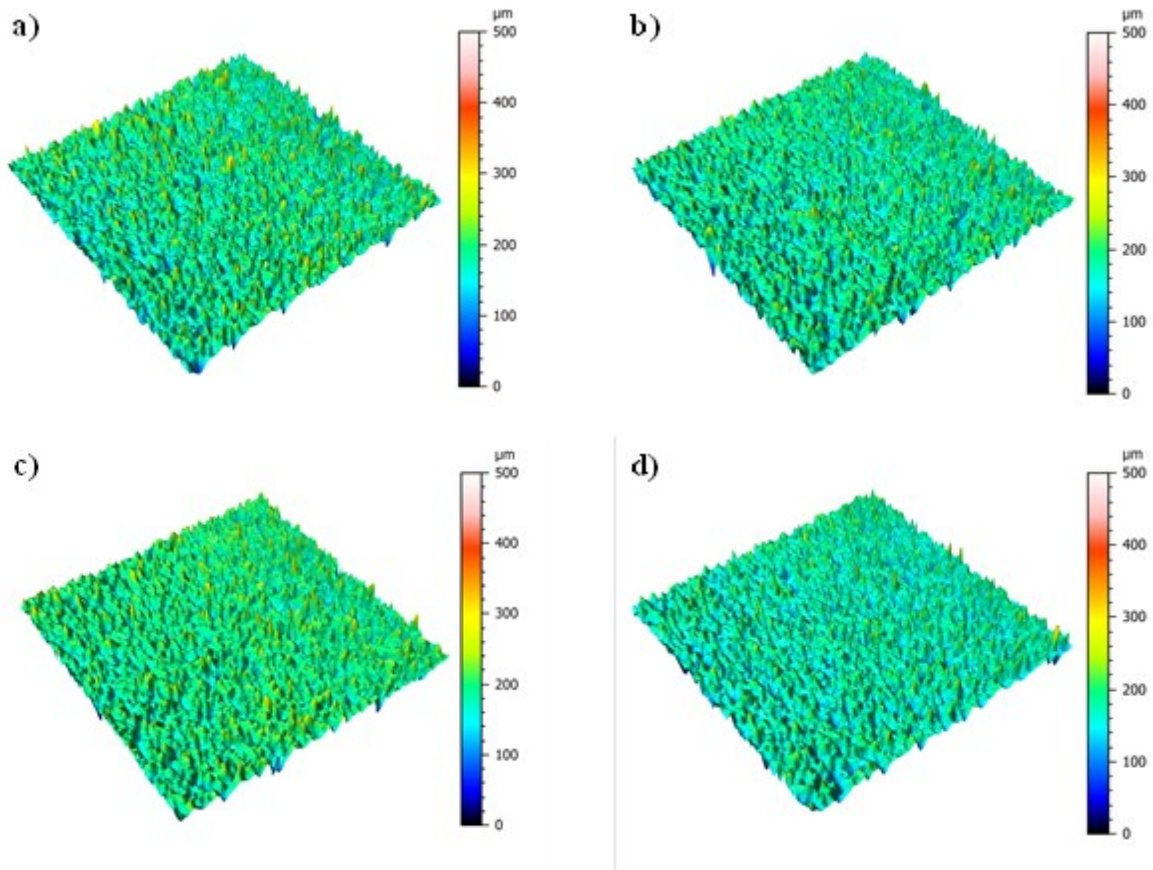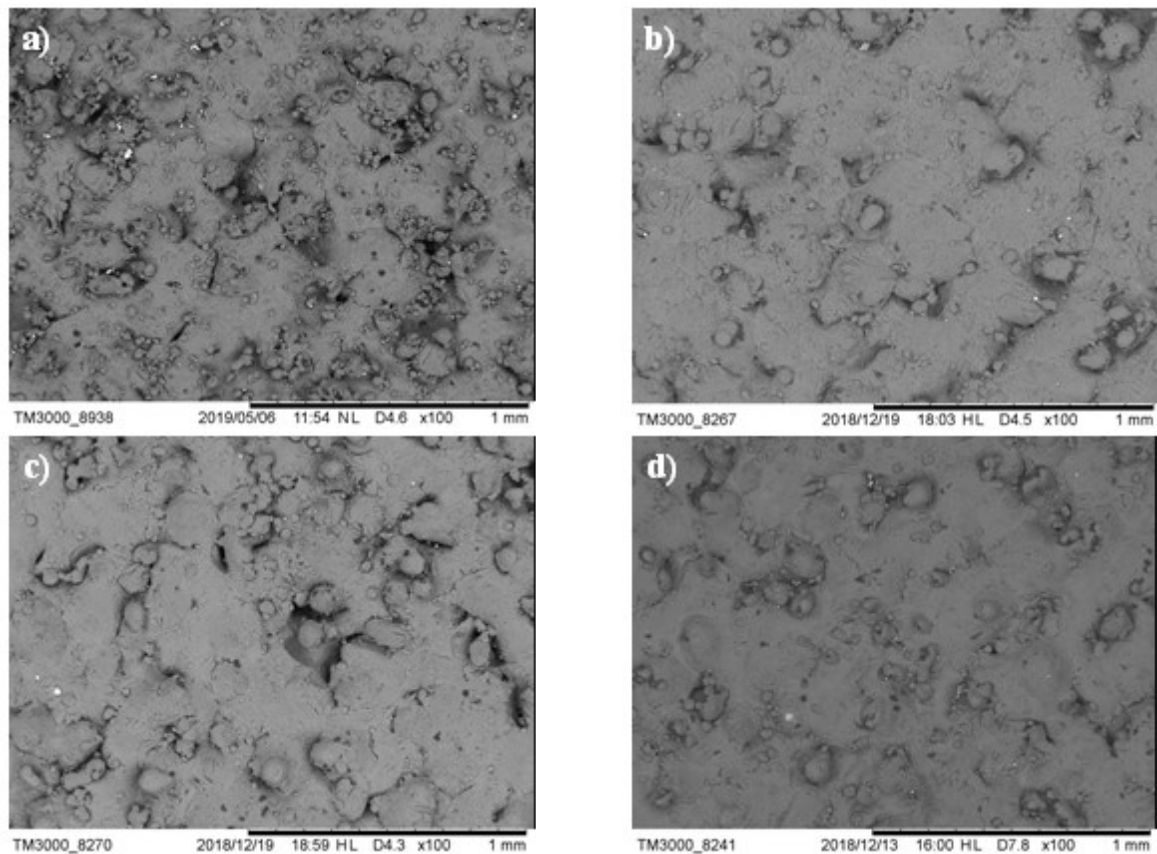
Figure 6.10. Comparison, before and after the whole treatment, between the 3D surfaces of the treated samples under different impact angles: (a) untreated, (b) 0°, (c) 25° and (d) 90°.

Table 6.11. Surface texture and weight values after each step of the FBM, for stationary samples and alumina abrasive particles (0° impact angle).

Time (min)	S_a (μm)	S_z (μm)	S_{sk}	S_{ku}	P_{dq} avg (°)	P_{dq} dev.st (±σ) (°)	Weight (g)
0	20.1	289	-0.66	5.93	38.4	2.4	2.036
30	19.4	287	-0.65	5.52	33.3	2.6	2.034
60	19.6	295	-0.69	5.55	39.5	3.2	2.032
90	19.3	282	-0.7	5.53	36.5	4	2.032

Table 6.12. Surface texture and weight values after each step of the FBM, for stationary samples and alumina abrasive particles (25° impact angle).

Time (min)	S_a (μm)	S_z (μm)	S_{sk}	S_{ku}	P_{dq} avg (°)	P_{dq} dev.st (±σ) (°)	Weight (g)
0	20	333	-0.48	5.1	47.9	3.2	2.045
30	19.4	331	-0.54	5.4	40.9	2.4	2.043
60	19.5	332	-0.56	5.32	38.8	2	2.041
90	19.5	303	-0.63	5.24	33.1	3.3	2.039

Table 6.13. Surface texture and weight values after each step of the FBM, for stationary samples and alumina abrasive particles (90° impact angle).

Time (min)	S_a (µm)	S_z (µm)	S_{sk}	S_{ku}	P_{dq} avg (°)	P_{dq} dev.st (±σ) (°)	Weight (g)
0	19.8	381	-0.48	5.1	42.6	2.725	2.074
30	19.8	309	-0.47	5.13	37.2	2.725	2.072
60	19.9	305	-0.49	5.01	37.5	2.725	2.07
90	19.7	297	-0.53	4.99	35.2	2.725	2.069

Figure 6.11. Comparison, before and after the whole treatment, between the SEM images of the treated samples under different impact angles: (a) untreated, (b) 0°, (c) 25° and (d) 90° (magnification 100x).

Irregular stainless steel

As stated before, this case refers to a different condition in which the abrasives density was privileged with respect to hardness, increasing therefore the impact energy transferred to the surface. However, for the stationary samples condition and for the process parameters investigated, this factor does not seem to contribute significantly on the surface improvements, as observable by the time evolution of the surface texture parameters reported in Fig. 6.12. More specifically, it can be observed that, except for the best case represented by the 90° impact angle, for the other two impact angles the parameters remains basically unchanged. On the other hand, similarly to the high hardness abrasives experiments, the surface parameter that experiences the most appreciable reduction is P_{dq}, as also reported in Tables 6.14-6.16.

Still considering the best case, also S_{sk} undergoes a significant reduction towards more negative values, with a similar trend observed for the two previous cases. Moreover, it is worth to note that, regardless of the impact angle, the weight loss is negligible in any case investigated.

All these results confirms, like for the previous cases, the 90° impact angle condition as the best case. This outcome could be explained considering that, in this sample position, the interaction between the particles and substrate is optimised for the material removal by means of prevalent shear stresses, promoting a smoothing effect mainly by the removal of the peaks represented by the sintered powders on the surface (S_{sk}, P_{dq} decrease). However, the low impact energy transferred from the abrasive to the substrate due to the considered fluidisation regime, determined the low overall contribution of both plastic deformation and material removal. These considerations are justified by the general observation of the surface texture parameters and the resulting 3D surfaces reported in Fig. 6.13, as well as the actual morphology evolution observed from the SEM images reported in Fig. 6.14.
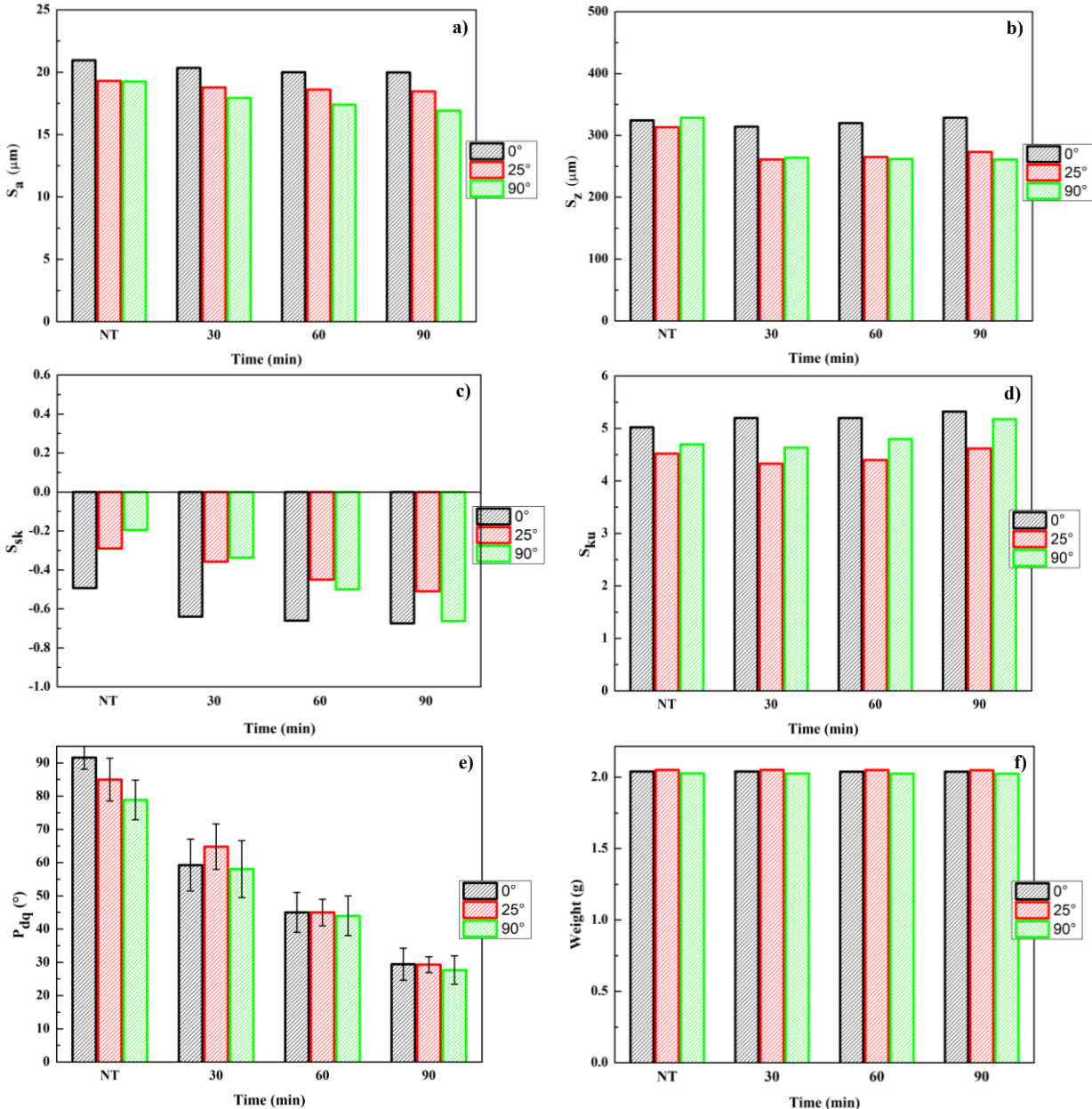

Figure 6.12. Surface texture parameters and weight evolution for the stationary samples tests, using irregular shape stainless steel as the abrasives: (a) S_a, (b) S_z, (c) S_{sk}, (d) S_{ku}, (e) P_{dq} and (f) weight.
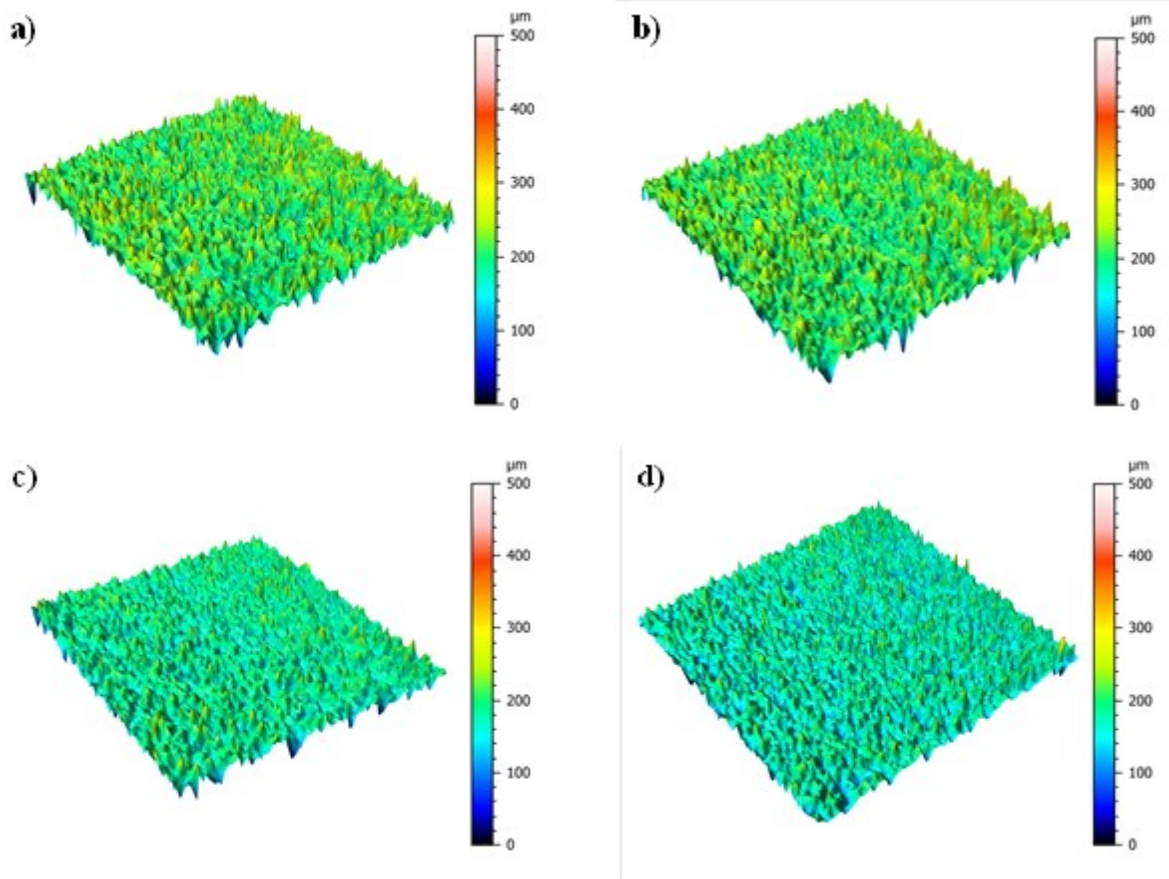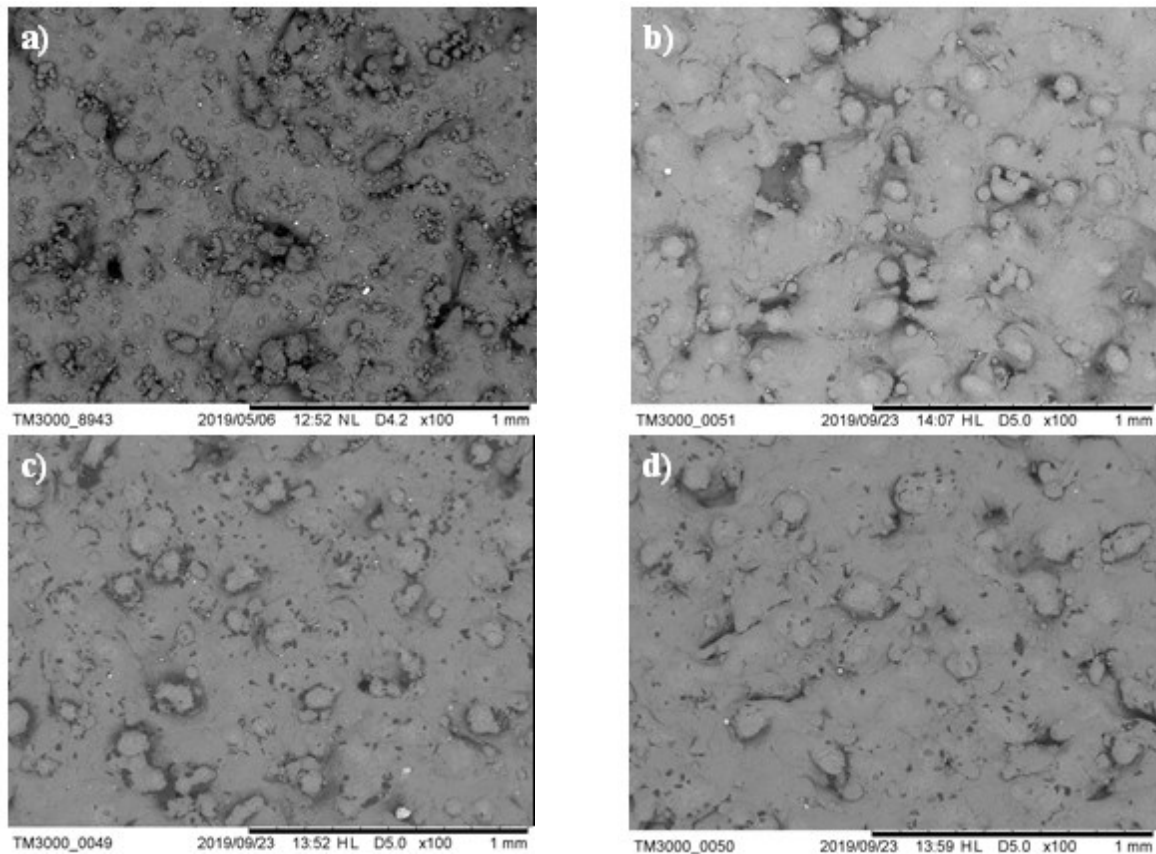
Figure 6.13. Comparison, before and after the whole treatment, between the 3D surfaces of the treated samples under different impact angles: (a) untreated, (b) 0°, (c) 25° and (d) 90°.

Table 6.14. Surface texture and weight values after each step of the FBM, for stationary samples and irregular shape stainless steel abrasive particles (0° impact angle).

Time (min)	S_a (µm)	S_z (µm)	S_{sk}	S_{ku}	P_{dq} avg (°)	P_{dq} dev.st (±σ) (°)	Weight (g)
0	20.9	324	-0.49	5.02	91.6	3.5	2.040
30	20.3	314	-0.64	5.2	59.2	7.8	2.039
60	20	320	-0.66	5.2	45	6	2.039
90	19.9	328	-0.67	5.32	29.4	4.8	2.039

Table 6.15. Surface texture and weight values after each step of the FBM, for stationary samples and irregular shape stainless steel abrasive particles (25° impact angle).

Time (min)	S_a (µm)	S_z (µm)	S_{sk}	S_{ku}	P_{dq} avg (°)	P_{dq} dev.st (±σ) (°)	Weight (g)
0	19.3	313	-0.29	4.52	84.9	6.4	2.052
30	18.7	261	-0.35	4.33	64.7	6.8	2.050
60	18.6	265	-0.45	4.4	45	4	2.049
90	18.4	273	-0.51	4.62	29.2	2.3	2.049

Table 6.16. Surface texture and weight values after each step of the FBM, for stationary samples and irregular shape stainless steel abrasive particles (90° impact angle).

Time (min)	S_a (µm)	S_z (µm)	S_{sk}	S_{ku}	P_{dq} avg (°)	P_{dq} dev.st (±σ) (°)	Weight (g)
0	19.2	328	-0.19	4.69	78.8	5.9	2.027
30	17.9	263	-0.33	4.63	58	8.5	2.026
60	17.4	262	-0.5	4.8	44	6	2.025
90	16.9	261	-0.66	5.18	27.6	4.2	2.024

Figure 6.14. Comparison, before and after the whole treatment, between the SEM images of the treated samples under different impact angles: (a) untreated, (b) 0°, (c) 25° and (d) 90° (magnification 100x).

Cutwire stainless steel

Based on the surface texture parameters evolution reported in Fig. 6.15, it can be assumed that the second shape investigated for stainless steel abrasive particles did not influence in an appreciable way the smoothing effect of the treatment. However, comparing these results with the previous case, a clear dependency of the result from the impact angle can be highlighted since the best case is represented, again, by the 90° impact angle condition.

Regardless of the specific starting values observed, this result is due to the previous considerations about the shear stresses imposed in this specific process condition. Another clear experimental outcome is the very low fraction of impact energy transferred to the substrates under the fluidisation regime established, regardless of the specific properties of the abrasives. This result is confirmed also in this case and clearly observable by the diagrams reported in Fig. 6.15, as well as the actual values reported in Tables 6.17-19.

Moreover, the slight smoothing effect of the fluidised abrasives under stationary samples conditions has been confirmed also in this case by considering the acquired 3D surface reported in Fig. 6.16 and the SEM images reported in Fig. 6.17. As a confirm of the observed variations of the surface texture indicators, from the analysis of the SEM images, including this case, it can be concluded that the actual effect of the investigated process conditions is only the partial removal of the sintered powders attached to surface. Therefore, the FBM treatment under static conditions of the samples does not promote the desired surface modifications with respect to the process time, impact angle and abrasives.
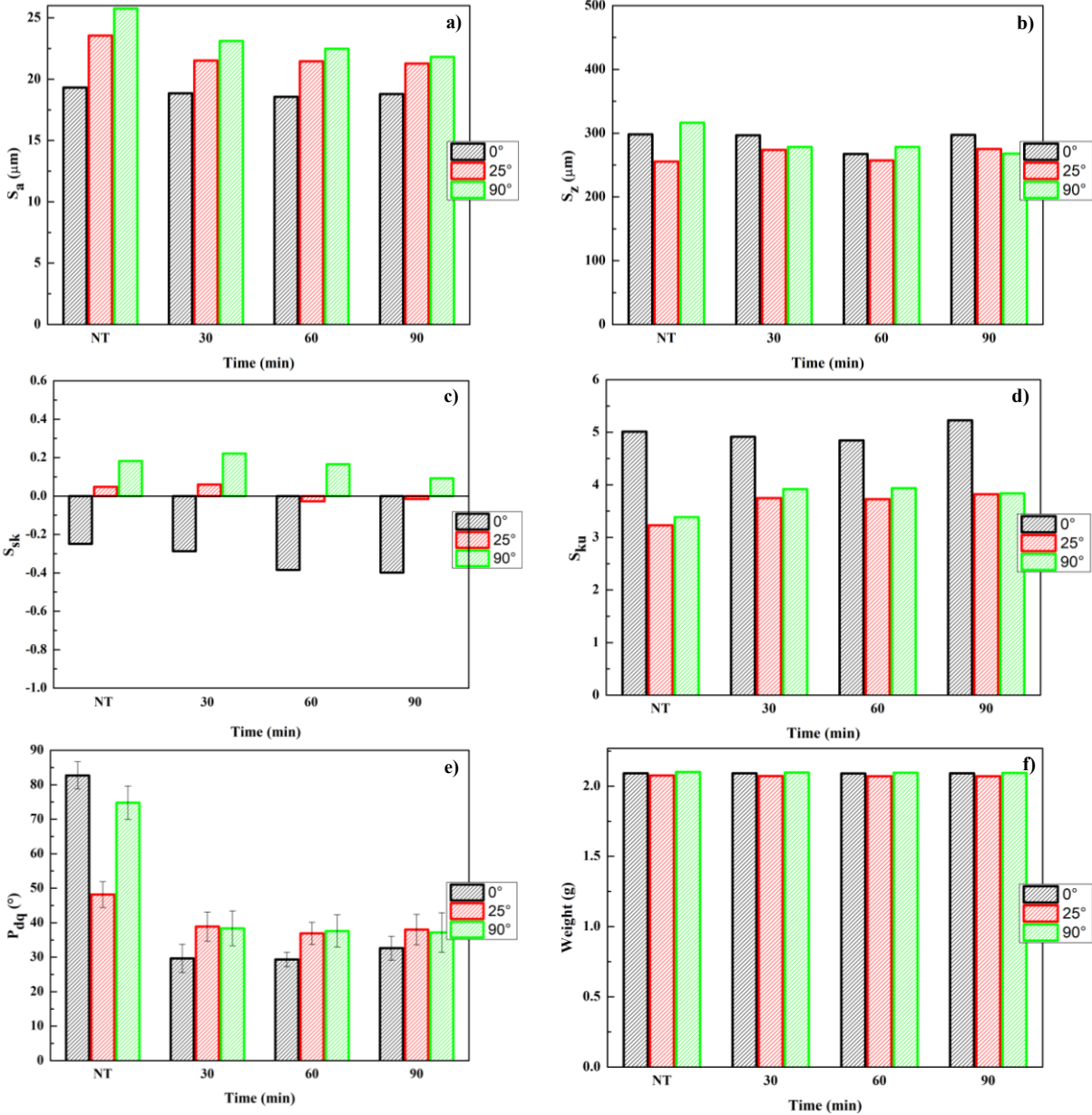

Figure 6.15. Surface texture parameters and weight evolution for the stationary samples tests, using cutwire stainless steel as the abrasives: (a) S_a, (b) S_z, (c) S_{sk}, (d) S_{ku}, (e) P_{dq} and (f) weight.
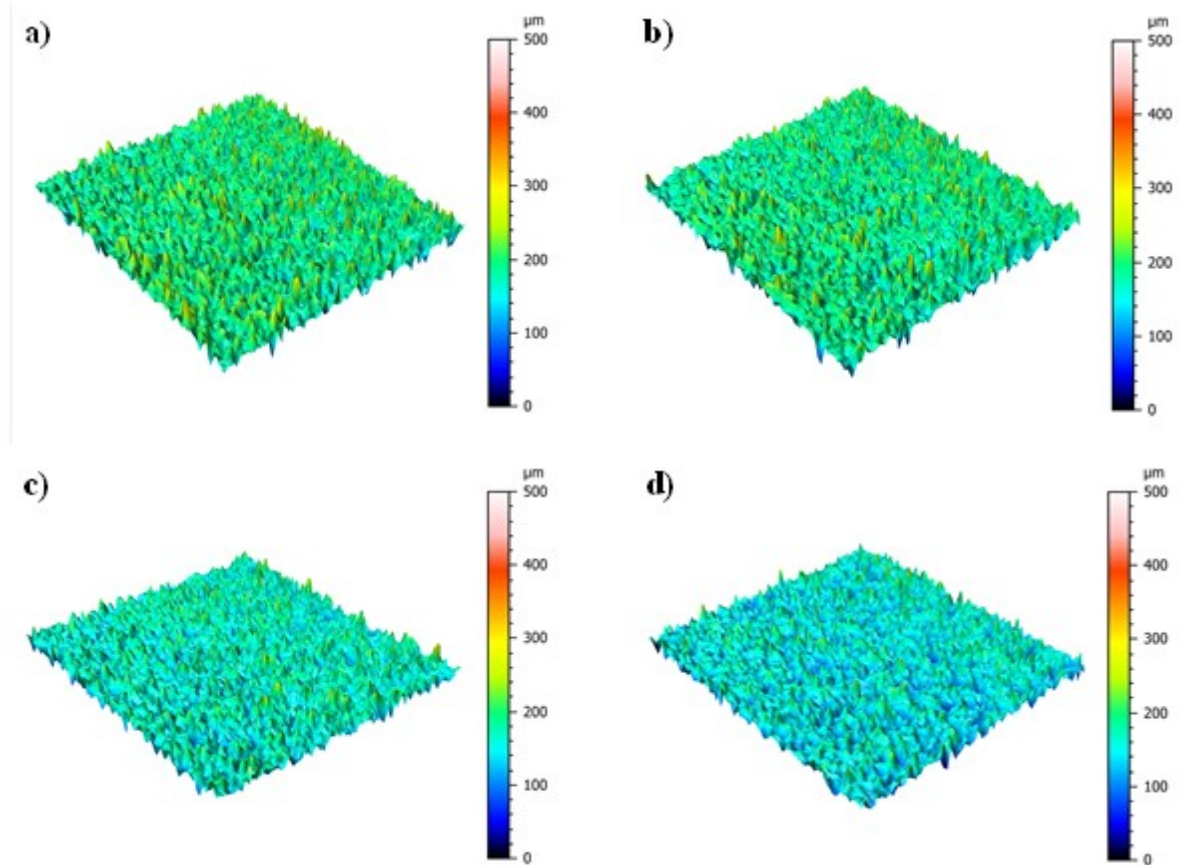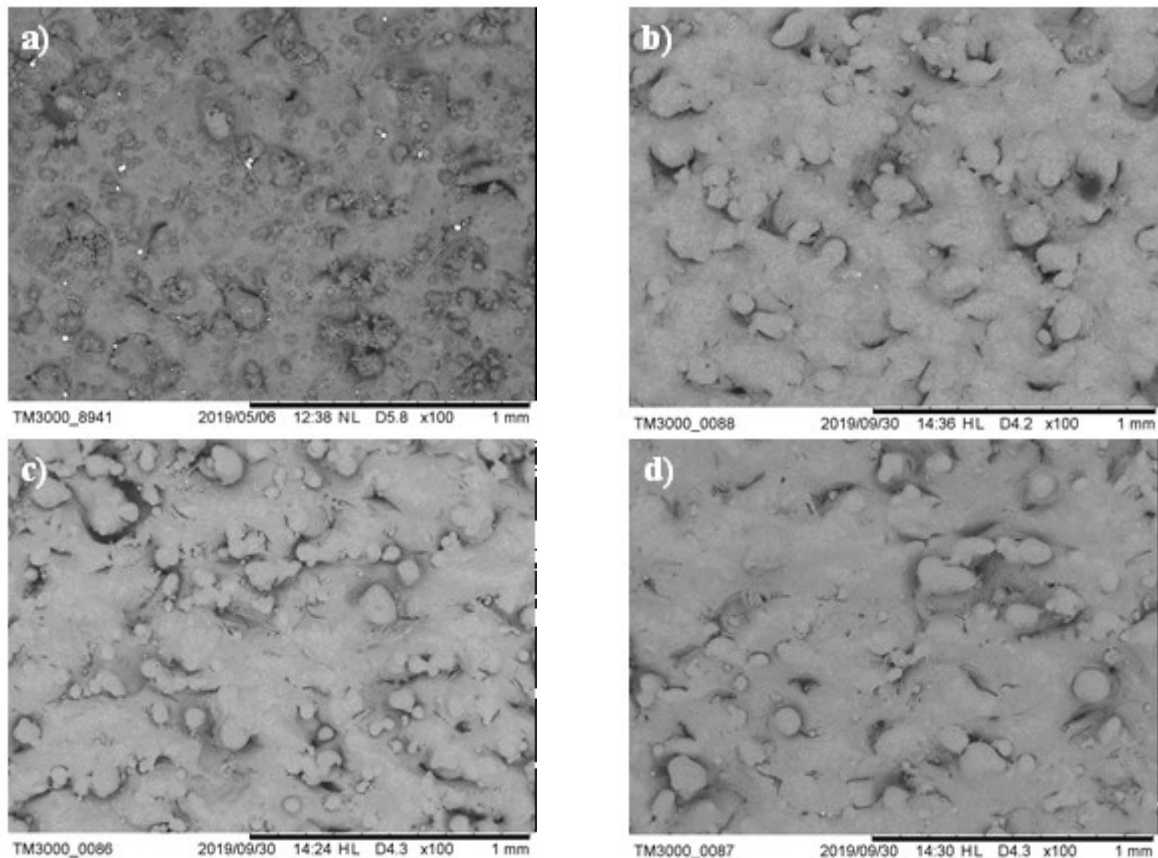
Figure 6.16. Comparison, before and after the whole treatment, between the 3D surfaces of the treated samples under different impact angles: (a) untreated, (b) 0°, (c) 25° and (d) 90°.

Table 6.17. Surface texture and weight values after each step of the FBM, for stationary samples and cutwire stainless steel abrasive particles (0° impact angle).

Time (min)	S_a (µm)	S_z (µm)	S_{sk}	S_{ku}	P_{dq} avg (°)	P_{dq} dev.st (±σ) (°)	Weight (g)
0	19.3	298	-0.24	5.01	82.7	3.9	2.091
30	18.8	296	-0.28	4.91	29.6	4.1	2.091
60	18.5	267	-0.38	4.84	29.3	2	2.090
90	18.7	297	-0.39	5.22	32.6	3.4	2.091

Table 6.18. Surface texture and weight values after each step of the FBM, for stationary samples and cutwire stainless steel abrasive particles (25° impact angle).

Time (min)	S_a (µm)	S_z (µm)	S_{sk}	S_{ku}	P_{dq} avg (°)	P_{dq} dev.st (±σ) (°)	Weight (g)
0	23.5	255	0.04	3.23	48.1	3.7	2.075
30	21.5	273	0.06	3.75	38.8	4.2	2.072
60	21.4	257	-0.03	3.72	36.9	3.2	2.070
90	21.2	275	-0.02	3.82	38	4.4	2.071

Table 6.19. Surface texture and weight values after each step of the FBM, for stationary samples and cutwire stainless steel abrasive particles (90° impact angle).

Time (min)	S_a (μm)	S_z (μm)	S_{sk}	S_{ku}	P_{dq} avg (°)	P_{dq} dev.st (±σ) (°)	Weight (g)
0	25.7	316	0.18	3.38	74.7	4.8	2.101
30	23.1	278	0.22	3.92	38.3	5	2.096
60	22.4	278	0.16	3.93	37.6	4.6	2.095
90	21.8	268	0.09	3.83	37.1	5.7	2.094

Figure 6.17. Comparison, before and after the whole treatment, between the SEM images of the treated samples under different impact angles: (a) untreated, (b) 0°, (c) 25° and (d) 90° (magnification 100x).

6.3.2. Rotating sample experiments

Silica sand

Considering the lowest value of the average relative tangential speed of 1 m/s, Fig. 6.18 illustrates the time evolution of the investigated surface texture parameters. From the observations of the results, it can be concluded that — in comparison with the stationary sample tests conducted with the silica sand — the surface improvements are comparable. This result could be justified considering that the superficial speed acting on the surface: whether if it belongs to the sample or the abrasives, is not too different in absolute value. This leads, considering both the diagrams in Fig. 6.18 and the actual values reported in Tables 6.20-22, to reduction of the surface roughness S_a of approximately 1,7 μm for the 65° and 90° impact angles, while the 25° condition leads to a

poorer reduction of 0,4 μm. Same considerations are valid for S_z. Moreover, the slightly appreciable smoothing effect is also observable from the trends of the S_{sk}, S_{ku} and P_{dq} parameters. This result is fully supported by both the 3D surfaces acquired, reported in Fig. 6.19, and the SEM images reported in Fig. 6.20. Similarly to the previous cases, in the latter images the presence of a several defects can be observed. As discussed before, these defects (craters) makes more difficult a proper analysis of surface improvements. However, it can be observed that the treatment promotes an appreciable removal of the small sintered powders attached to the surface although, considering the non-optimal energetic conditions, more specific considerations about the contribution of the different substrate-abrasive interaction mechanisms would not be reliable.
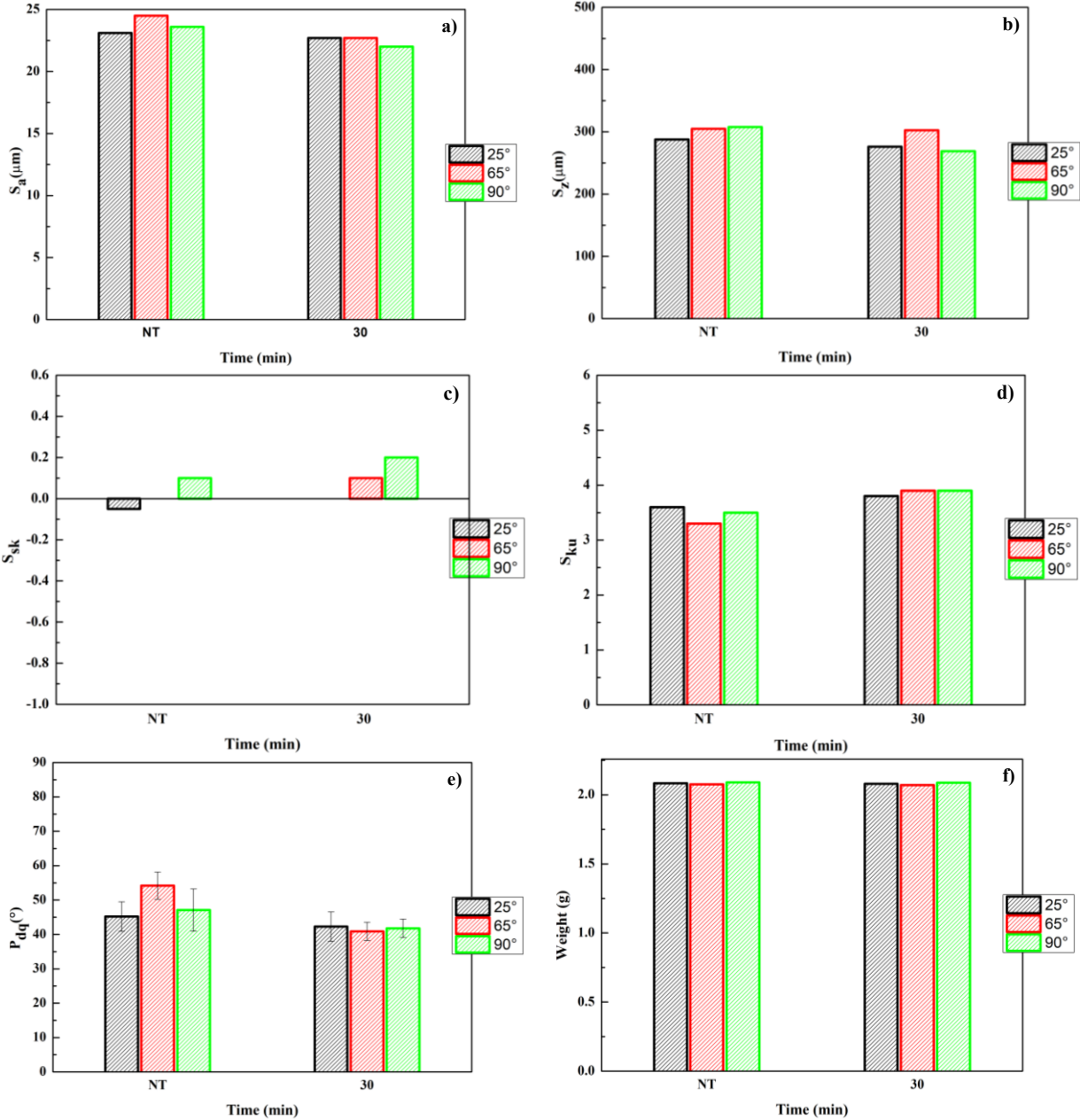

Figure 6.18. Surface texture parameters and weight evolution for the rotating samples (v = 1 m/s) tests, using silica sand as the abrasives: (a) S_a, (b) S_z, (c) S_{sk} (= 0 if not reported), (d) S_{ku}, (e) P_{dq} and (f) weight.
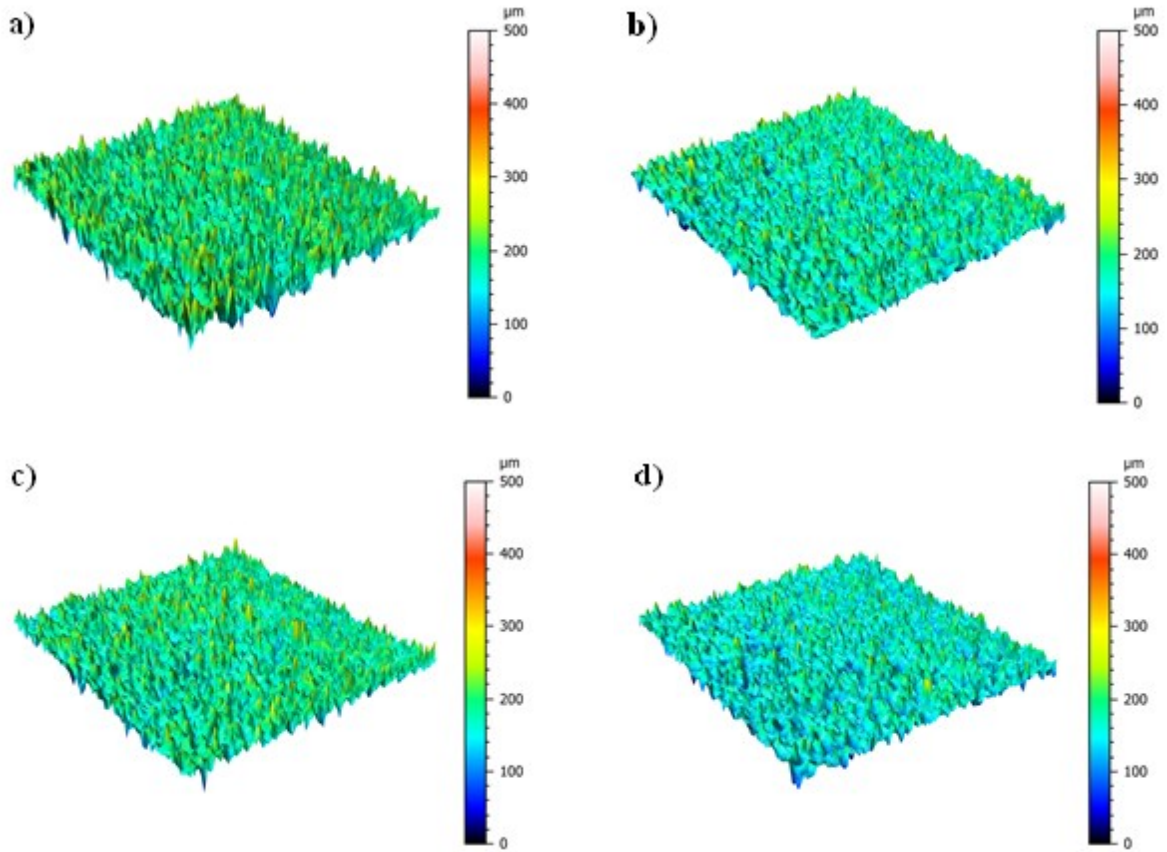
Figure 6.19. Comparison, before and after the whole treatment, between the 3D surfaces of the treated samples under different impact angles: (a) untreated, (b) 25°, (c) 65° and (d) 90°.

Table 6.20. Surface texture and weight values after each step of the FBM, for rotating samples and silica sand abrasive particles (25° impact angle, average tangential speed v = 1 m/s).

Time (min)	S_a (μm)	S_z (μm)	S_{sk}	S_{ku}	P_{dq} avg (°)	P_{dq} dev.st (±σ) (°)	Weight (g)
0	23.1	287	-0.05	3.6	45.2	4.3	2.083
30	22.7	276	0	3.8	42.3	4.3	2.080

Table 6.21. Surface texture and weight values after each step of the FBM, for rotating samples and silica sand abrasive particles (65° impact angle, average tangential speed v = 1 m/s).

Time (min)	S_a (μm)	S_z (μm)	S_{sk}	S_{ku}	P_{dq} avg (°)	P_{dq} dev.st (±σ) (°)	Weight (g)
0	24.5	304	0	3.3	54.2	3.9	2.075
30	22.7	302	0.1	3.9	40.9	2.6	2.070

Table 6.22. Surface texture and weight values after each step of the FBM, for rotating samples and silica sand abrasive particles (90° impact angle, average tangential speed v = 1 m/s).

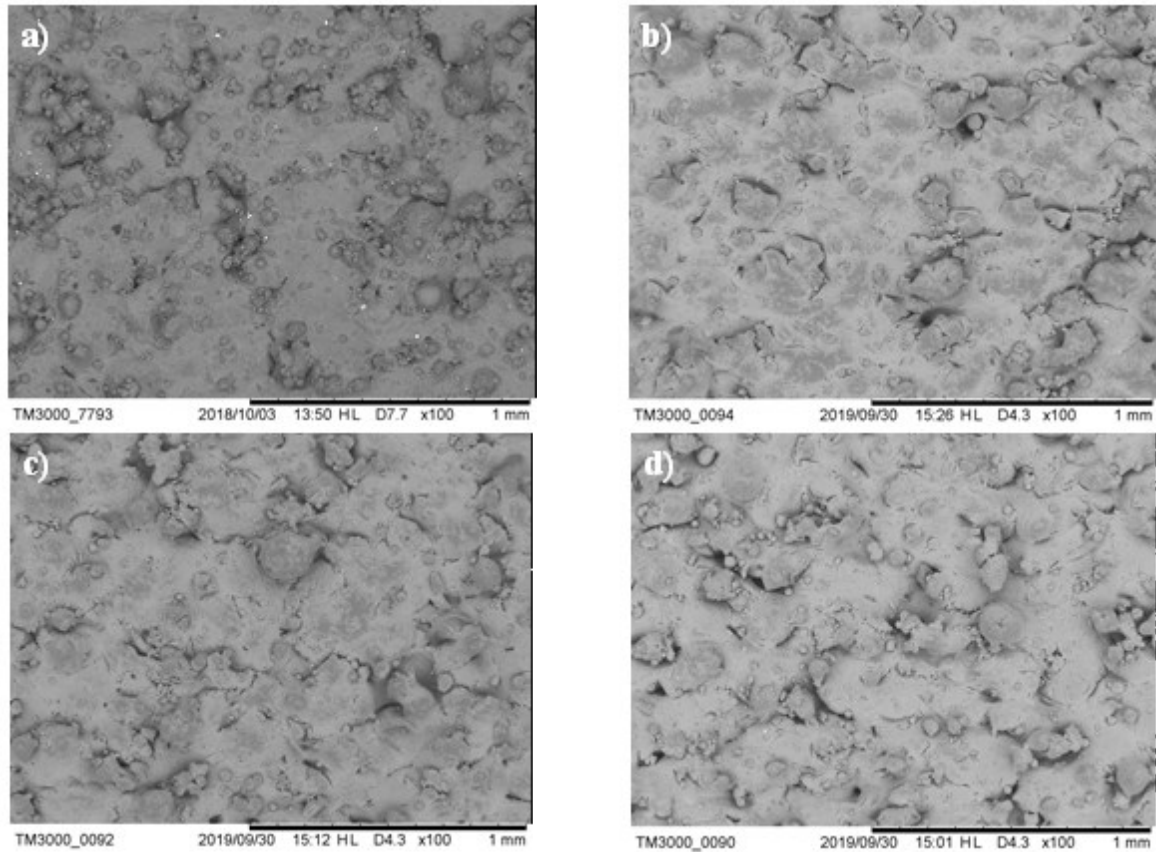| Time (min)	S_a (μm)	S_z (μm)	S_{sk}	S_{ku}	P_{dq} avg (°)	P_{dq} dev.st (±σ) (°)	Weight (g)
0	23.6	307	0.1	3.5	47.1	6.1	2.091
30	22	268	0.2	3.9	41.8	2.6	2.087

Figure 6.20. Comparison, before and after the whole treatment, between the SEM images of the treated samples under different impact angles: (a) untreated, (b) 25°, (c) 65° and (d) 90° (magnification 100x).

In comparison with the results obtained for v = 1 m/s, different considerations can be drawn when considering the higher value of 2 m/s. As expectable, the higher relative speed between the sample and the abrasive particles promotes a greater smoothing effect. The results obtained, also in this case, are reported in terms of time evolution of surface texture parameters in Fig. 6.21, as well as in terms of actual values in Tables 6.23-25 and 3D surfaces in Fig. 6.22. From a quantitative point of view, it can be observed that the reduction of S_a is almost doubled for all the investigated impact angles. Similar considerations could be done for the S_z parameter, whose reduction is considerably more appreciable compared to the previous case. In this context, the impact angles of 25° and 65° provide the higher reductions of about 30 μm and 50 μm respectively. In terms of surface symmetry and brilliance after treatment, the analysis of S_{sk} and S_{ku} suggests a more prominent texture from the peaks side. However, considering the slight change of the actual values, a clear trend could not be observed given the random nature of the surface and the slight effect of the treatment. On the other hand, the notable reduction of P_{dq} compared to the previous case indicates that, despite the latter consideration, the material removal effect of the treatment increased. This result can be easily observed from the comparison of the SEM images obtained for the two values of the superficial tangential speed investigated, where for the 2 m/s experimental condition the results are illustrated in Fig. 6.23.

In order to provide the main experimental outcomes from the comparison between stationary and rotating samples FBM conditions using silica sand abrasives, it can be concluded that the results achievable depends primarily on the impact energy provided to the substrate, i.e. higher surface improvements are obtainable when higher relative speed between substrate and abrasives are adopted. This observation is also confirmed by the analysis of the two different values of the

average tangential speed applied in the rotating sample condition. However, the comparison between the two experimental conditions highlighted also the role played by the abrasive. More specifically, considering the trade-off between density and hardness of the silica sand, for the process conditions investigated does not represent the best abrasive material to use. Therefore, based on the obtained results, the following experiments discussed were carried out in order to find the optimum combination of abrasives characteristics and process conditions, following the same guideline adopted for the stationary samples condition.
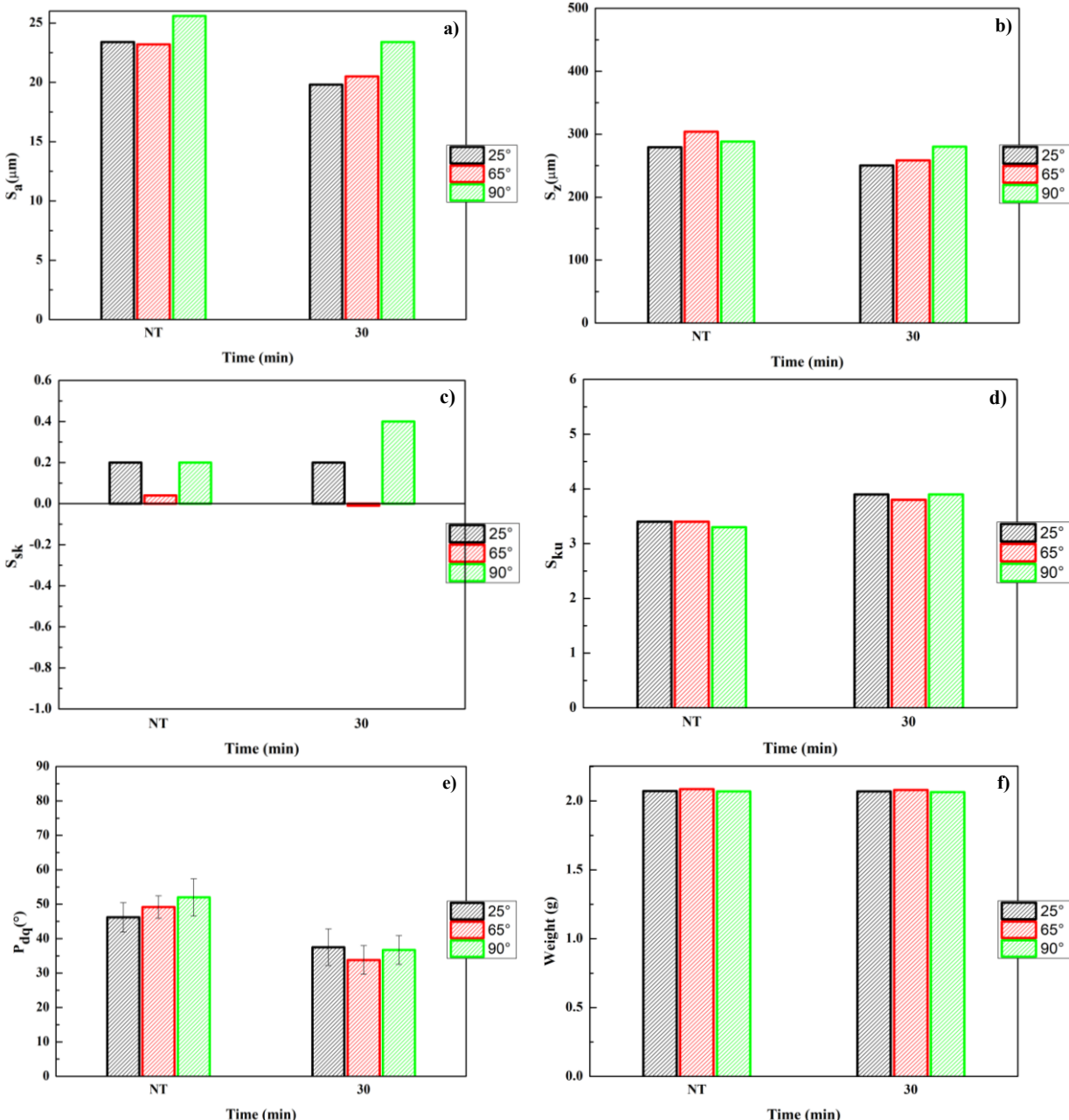
Figure 6.21. Surface texture parameters and weight evolution for the rotating samples ($v = 2$ m/s) tests, using silica sand as the abrasives: (a) S_a, (b) S_z, (c) S_{sk} (= 0 if not reported), (d) S_{ku}, (e) P_{dq} and (f) weight.
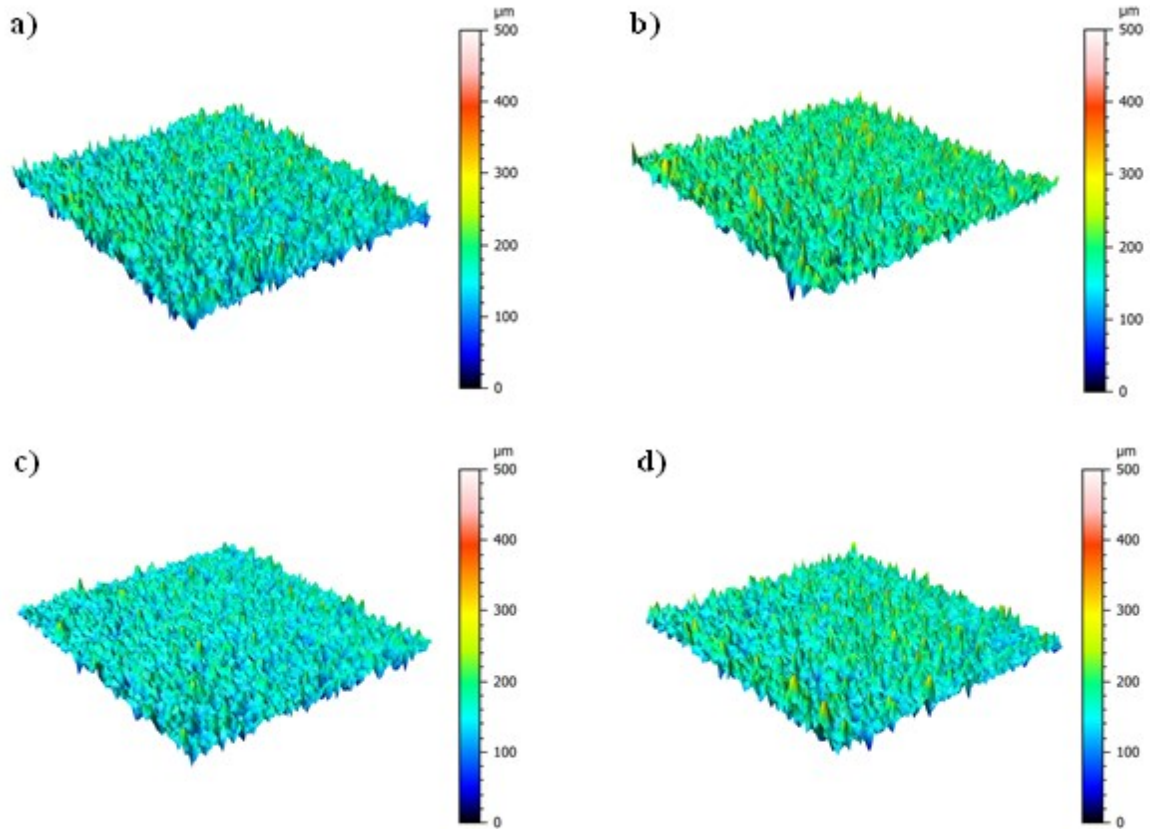
Figure 6.22. Comparison, before and after the whole treatment, between the 3D surfaces of the treated samples under different impact angles: (a) untreated, (b) 25°, (c) 65° and (d) 90°.

Table 6.23. Surface texture and weight values after each step of the FBM, for rotating samples and silica sand abrasive particles (25° impact angle, average tangential speed v = 2 m/s).

Time (min)	S_a (μm)	S_z (μm)	S_{sk}	S_{ku}	P_{dq} avg (°)	P_{dq} dev.st (±σ) (°)	Weight (g)
0	23.4	279	0.2	3.4	46.2	4.26	2.073
30	19.8	250	0.2	3.9	37.5	5.3	2.070

Table 6.24. Surface texture and weight values after each step of the FBM, for rotating samples and silica sand abrasive particles (65° impact angle, average tangential speed v = 2 m/s).

Time (min)	S_a (μm)	S_z (μm)	S_{sk}	S_{ku}	P_{dq} avg (°)	P_{dq} dev.st (±σ) (°)	Weight (g)
0	23.2	304	0.04	3.4	49.2	4.26	2.073
30	20.5	258	-0.01	3.8	33.8	5.3	2.070

Table 6.25. Surface texture and weight values after each step of the FBM, for rotating samples and silica sand abrasive particles (90° impact angle, average tangential speed v = 2 m/s).

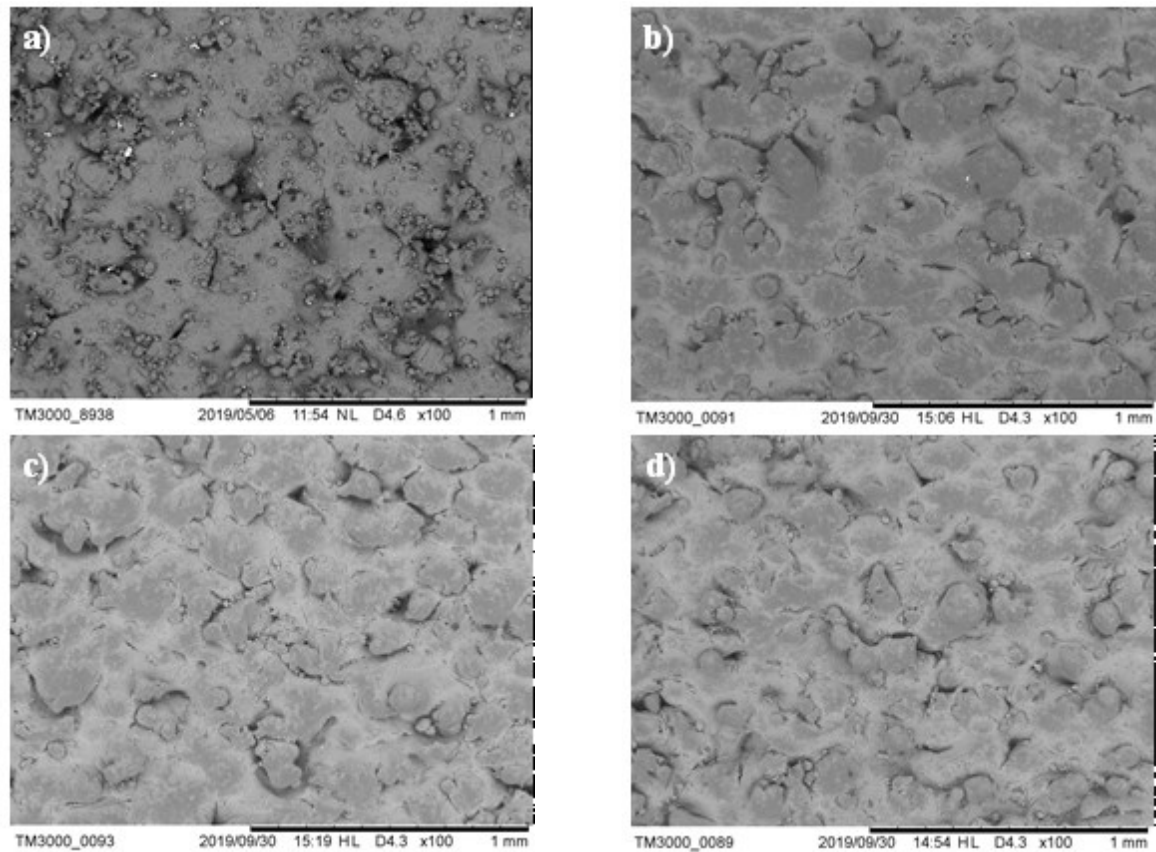| Time (min)	S_a (μm)	S_z (μm)	S_{sk}	S_{ku}	P_{dq} avg (°)	P_{dq} dev.st (±σ) (°)	Weight (g)
0	25.6	288	0.2	3.3	52	5.41	2.070
30	23.4	280	0.4	3.9	36.7	4.17	2.065

Figure 6.23. Comparison, before and after the whole treatment, between the SEM images of the treated samples under different impact angles: (a) untreated, (b) 25°, (c) 65° and (d) 90° (magnification 100x).

Alumina

The obtained results for the experiments conducted with alumina abrasive particles and an average tangential speed of 1 m/s are reported in Fig. 6.24 in terms of surface texture parameters evolution, and in Tables 6.26-28 in terms of actual values measured. The results suggest that, as for the previous cases when silica sand was used, the process efficiency improvements associated with the use of alumina are slightly appreciable. Compared to the same process conditions with abrasive sand, even the more than doubled hardness of the abrasive do not lead to appreciable variations and trends in the surface texture parameters over the whole process. Furthermore, in the investigated process conditions, the influence of the specific impact angle cannot be distinguished clearly. These considerations observable and justified by the 3D surfaces reported in Fig. 6.25 and the SEM images reported in Fig. 6.26, the latter showing the partial removal of the small sintered powders but not a significant morphology modification. Therefore, in agreement with the observations reported previously about the impact energy associated with the process conditions, even in this case it can be concluded that the relative speed imposed between the substrate and the fluidised particles is not sufficient alone to guarantee a proper smoothing effect. As also stated before, this consideration makes more difficult proper evaluations of the influence of the different process parameters.
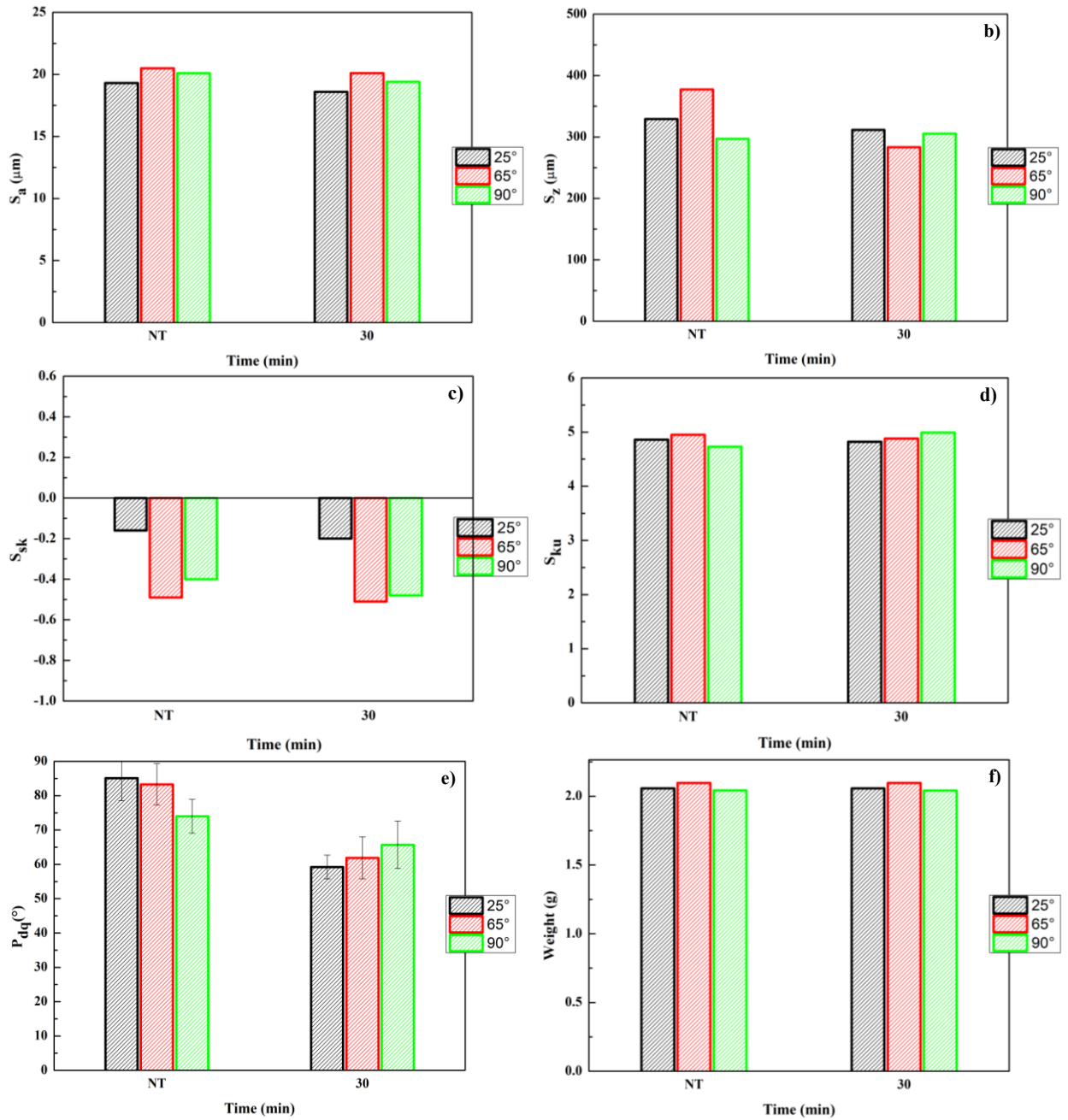
Figure 6.24. Surface texture parameters and weight evolution for the rotating samples (v = 1 m/s) tests, using alumina as the abrasives: (a) S_a, (b) S_z, (c) S_{sk}, (d) S_{ku}, (e) P_{dq} and (f) weight.
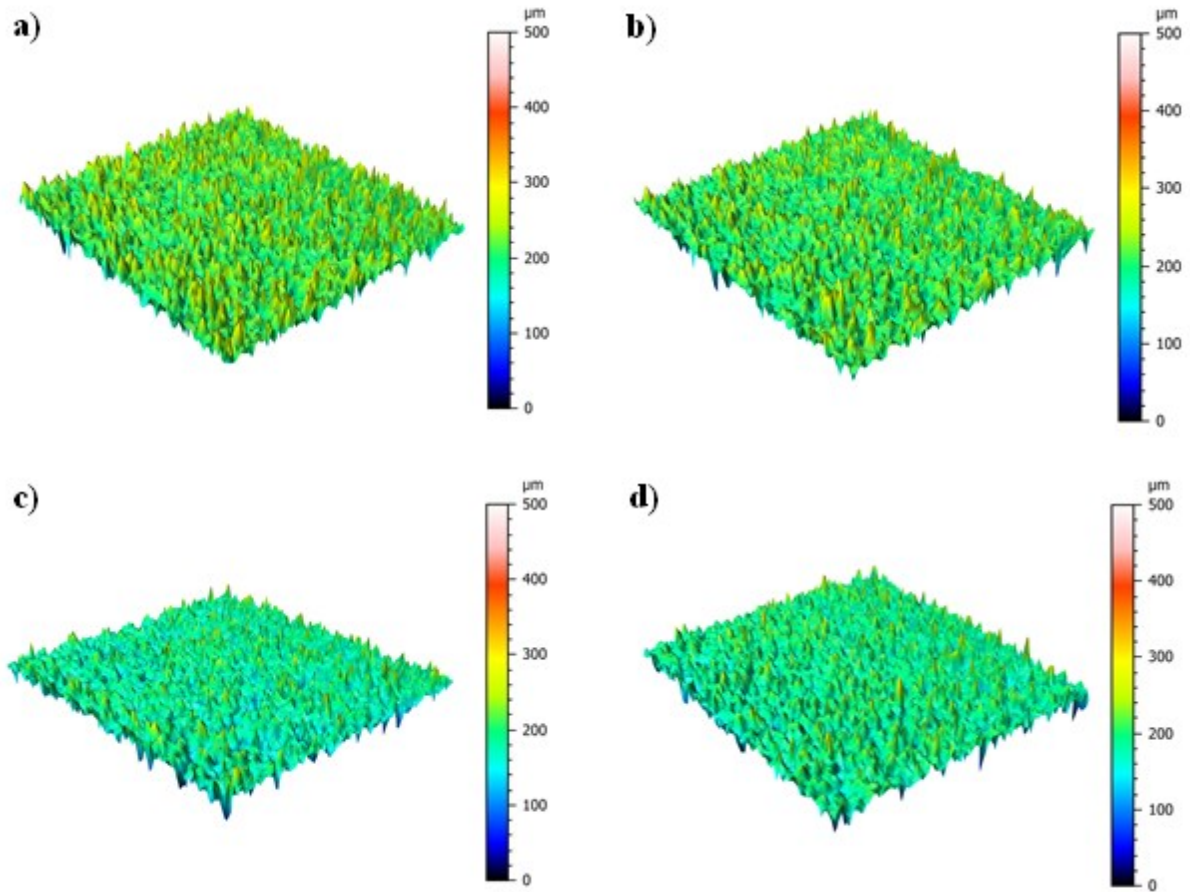
Figure 6.25. Comparison, before and after the whole treatment, between the 3D surfaces of the treated samples under different impact angles: (a) untreated, (b) 25°, (c) 65° and (d) 90°.

Table 6.26. Surface texture and weight values after each step of the FBM, for rotating samples and alumina abrasive particles (25° impact angle, average tangential speed $v = 1$ m/s).

Time (min)	S_a (μm)	S_z (μm)	S_{sk}	S_{ku}	P_{dq} avg (°)	P_{dq} dev.st (±σ) (°)	Weight (g)
0	19.3	329	-0.16	4.86	85.1	6.58	2.058
30	18.6	311	-0.2	4.82	59.2	3.44	2.057

Table 6.27. Surface texture and weight values after each step of the FBM, for rotating samples and alumina abrasive particles (65° impact angle, average tangential speed $v = 1$ m/s).

Time (min)	S_a (μm)	S_z (μm)	S_{sk}	S_{ku}	P_{dq} avg (°)	P_{dq} dev.st (±σ) (°)	Weight (g)
0	20.5	377	-0.49	4.95	83.3	6.02	2.097
30	20.1	283	-0.51	4.88	61.9	6.06	2.097

Table 6.28. Surface texture and weight values after each step of the FBM, for rotating samples and alumina abrasive particles (90° impact angle, average tangential speed $v = 1$ m/s).

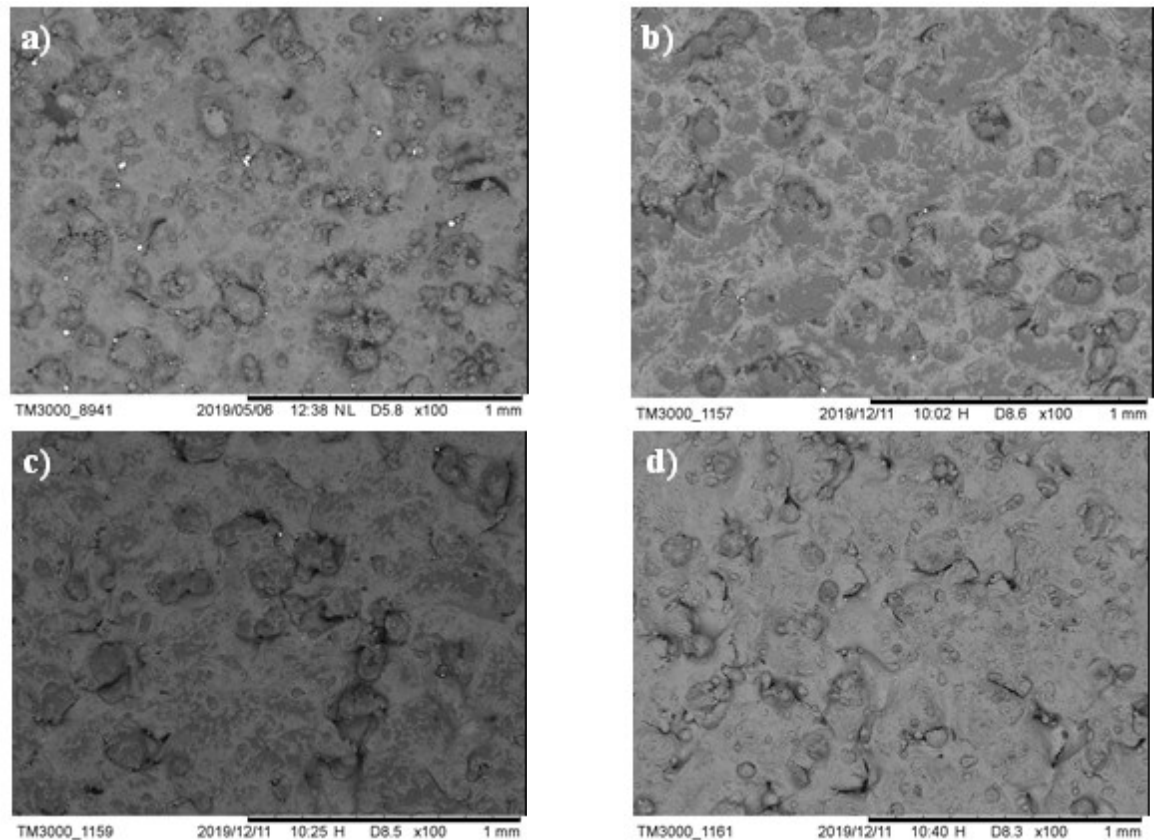| Time (min)	S_a (μm)	S_z (μm)	S_{sk}	S_{ku}	P_{dq} avg (°)	P_{dq} dev.st (±σ) (°)	Weight (g)
0	20.1	297	-0.4	4.73	74	4.94	2.043
30	19.4	305	-0.48	4.99	65.7	6.93	2.042

Figure 6.26. Comparison, before and after the whole treatment, between the SEM images of the treated samples under different impact angles: (a) untreated, (b) 25°, (c) 65° and (d) 90° (magnification 100x).

A further confirm of these considerations comes from the results obtained when the tangential speed was increased from 1 m/s to 2 m/s. Similarly to the conclusions drawn for the case of silica sand, the surface roughness reduction becomes more appreciable, as observable from the graphs reported in Fig. 6.27. Still considering the comparison between the two abrasives, for higher superficial tangential speed a more clear influence of the impact angle emerge again. More specifically, the 25° impact angle condition represents again the best case referring to this process parameter, as observable by the remarkable S_a reduction reported in Tables 6.29-31. However, referring to the other surface texture parameters, the same conclusions could be drawn in comparison with the case of tangential speed of 1 m/s.

In conclusion, with the aim to provide some general considerations of the results obtained for the investigated process conditions, it can be assumed that abrasives in which the trade-off between density and hardness is favorable to the latter are not suitable when minimum fluidisation or bubbling regimes are considered. This result was proved by considering both the stationary and rotating sample configurations, as well as from the comparison between two abrasives, both with higher hardness compared to the substrate.
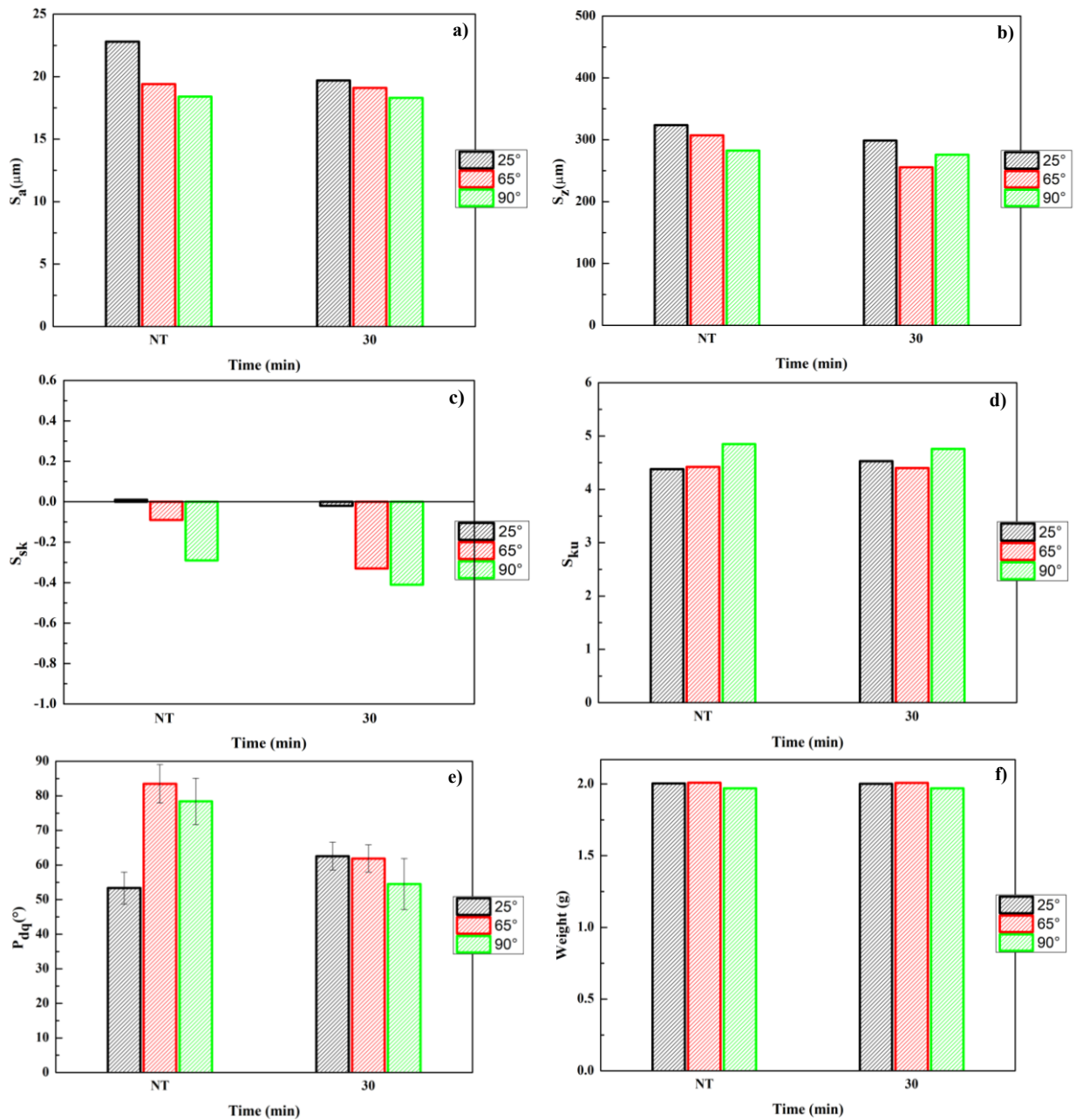
Figure 6.27. Surface texture parameters and weight evolution for the rotating samples (v = 2 m/s) tests, using alumina as the abrasives: (a) S_a, (b) S_z, (c) S_{sk}, (d) S_{ku}, (e) P_{dq} and (f) weight.
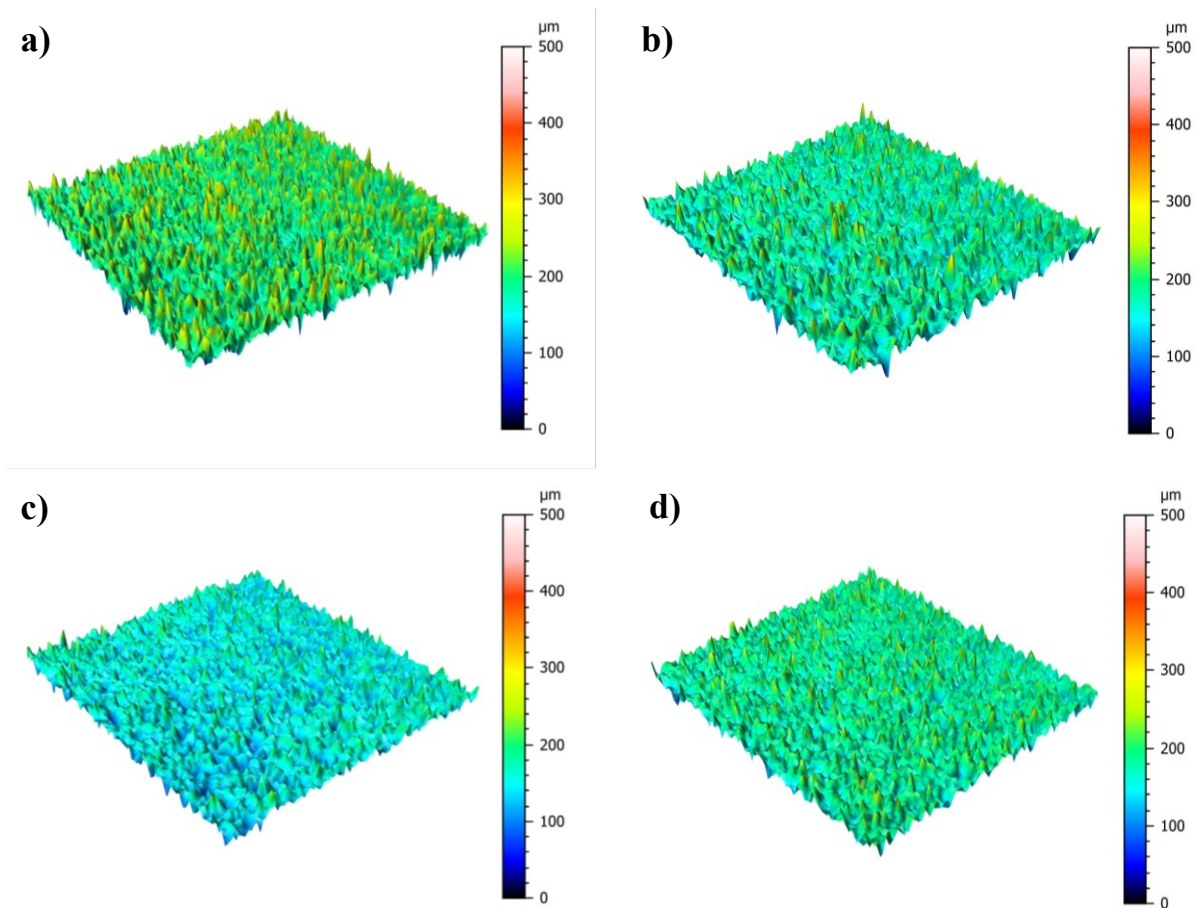
Figure 6.28. Comparison, before and after the whole treatment, between the 3D surfaces of the treated samples under different impact angles: (a) untreated, (b) 25°, (c) 65° and (d) 90°.

Table 6.29. Surface texture and weight values after each step of the FBM, for rotating samples and alumina abrasive particles (25° impact angle, average tangential speed v = 2 m/s).

Time (min)	S_a (µm)	S_z (µm)	S_{sk}	S_{ku}	P_{dq} avg (°)	P_{dq} dev.st (±σ) (°)	Weight (g)
0	22.8	323	0.01	4.38	53.3	4.62	2.004
30	19.7	298	-0.02	4.53	62.5	4.04	2.001

Table 6.30. Surface texture and weight values after each step of the FBM, for rotating samples and alumina abrasive particles (65° impact angle, average tangential speed v = 2 m/s).

Time (min)	S_a (µm)	S_z (µm)	S_{sk}	S_{ku}	P_{dq} avg (°)	P_{dq} dev.st (±σ) (°)	Weight (g)
0	19.4	307	-0.09	4.42	83.5	5.57	2.009
30	19.1	255	-0.33	4.4	61.9	3.93	2.008

Table 6.31. Surface texture and weight values after each step of the FBM, for rotating samples and alumina abrasive particles (90° impact angle, average tangential speed v = 2 m/s).

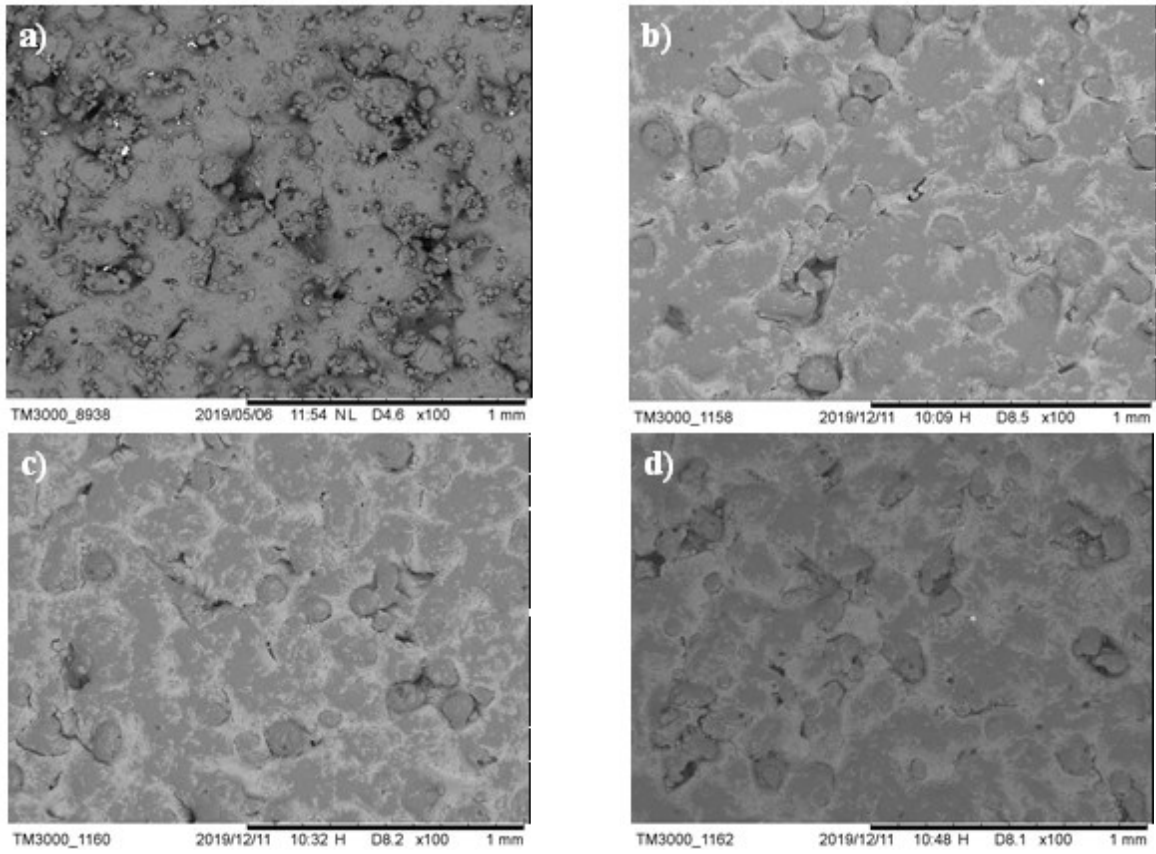| Time (min)	S_a (µm)	S_z (µm)	S_{sk}	S_{ku}	P_{dq} avg (°)	P_{dq} dev.st (±σ) (°)	Weight (g)
0	18.4	282	-0.29	4.85	78.4	6.72	1.97
30	18.3	276	-0.41	4.76	54.5	7.4	1.97

Figure 6.29. Comparison, before and after the whole treatment, between the SEM images of the treated samples under different impact angles: (a) untreated, (b) 25°, (c) 65° and (d) 90° (magnification 100x).

Irregular stainless steel

As observable from the results reported in Fig. 6.30 about the surface texture parameters as well as the 3D surfaces reported in Fig 6.31, the experimental outcome in this case is that the adoption of abrasive particles with higher density leads to notable improvements for the smoothing process, remarkable in the rotating sample process configuration even for the lower value of average tangential speed (v = 1 m/s). More specifically, it can be noted that, for the best case of 25° impact angle, S_a decreases of about 10 μm, whereas for the 65° and 90° impact angles the reduction of S_a decreases of about 3 μm and 1,5 μm respectively. With similar considerations, S_z presents the same reduction trend, quantified by the actual values measured and reported in Tables 6.29-31.

On the other hand, a notable difference in the treatment effects can be observed, still in comparison with the previous experiments results, about the influence of the abrasive impacts on S_{sk}. Since the parameter evolution is characterised by a significant decrease to more negative values, which is the highest for the 25° impact angle, this result can be justified by the quite higher shear stresses imposed on the surface due to the higher kinetic energy possessed by the fluidised particles. As a result, the surfaces treated under this condition experience a deeper surface morphology modification, as observable from the SEM images reported in Fig. 6.32.

These modifications can be related to a greater removal of the sintered particles on the surface and, given the more effective impacts, also to a partial plastic deformation of the underlying surface. However, these effects are not sufficient to modify the deep valleys of the original surface, leading to a preferential treatment effect on the peaks side. It is worth to note that, for the abrasives used in this case, a more clear influence of the impact angle emerged, although it was already confirmed for the previously discussed results.

Moreover, the major contribution of the plastic deformation involved for higher density abrasives such as the stainless steel used in this case, can be justified by taking into consideration also the relatively low weight loss compared to the quantified surface roughness reduction, as reported in Tables 6.29-31. Accordingly, the considerations about the contribution of the plastic deformation and material removal mechanisms are in agreement with the trend observed for P_{dq}, whose reduction is also greater compared to the previous cases.

About the evolution of S_{ku}, it is characterised by a more defined trend, i.e. an increase observed in general for all the investigated impact angles. However, considering the presence of defects that alter the quantified surface improvements — a consideration valid for all the surface texture parameters — and the less sensitivity of this parameter with respect to roughness scale, there is a major difficulty in drawing clear conclusions, as also stated in the previous cases.
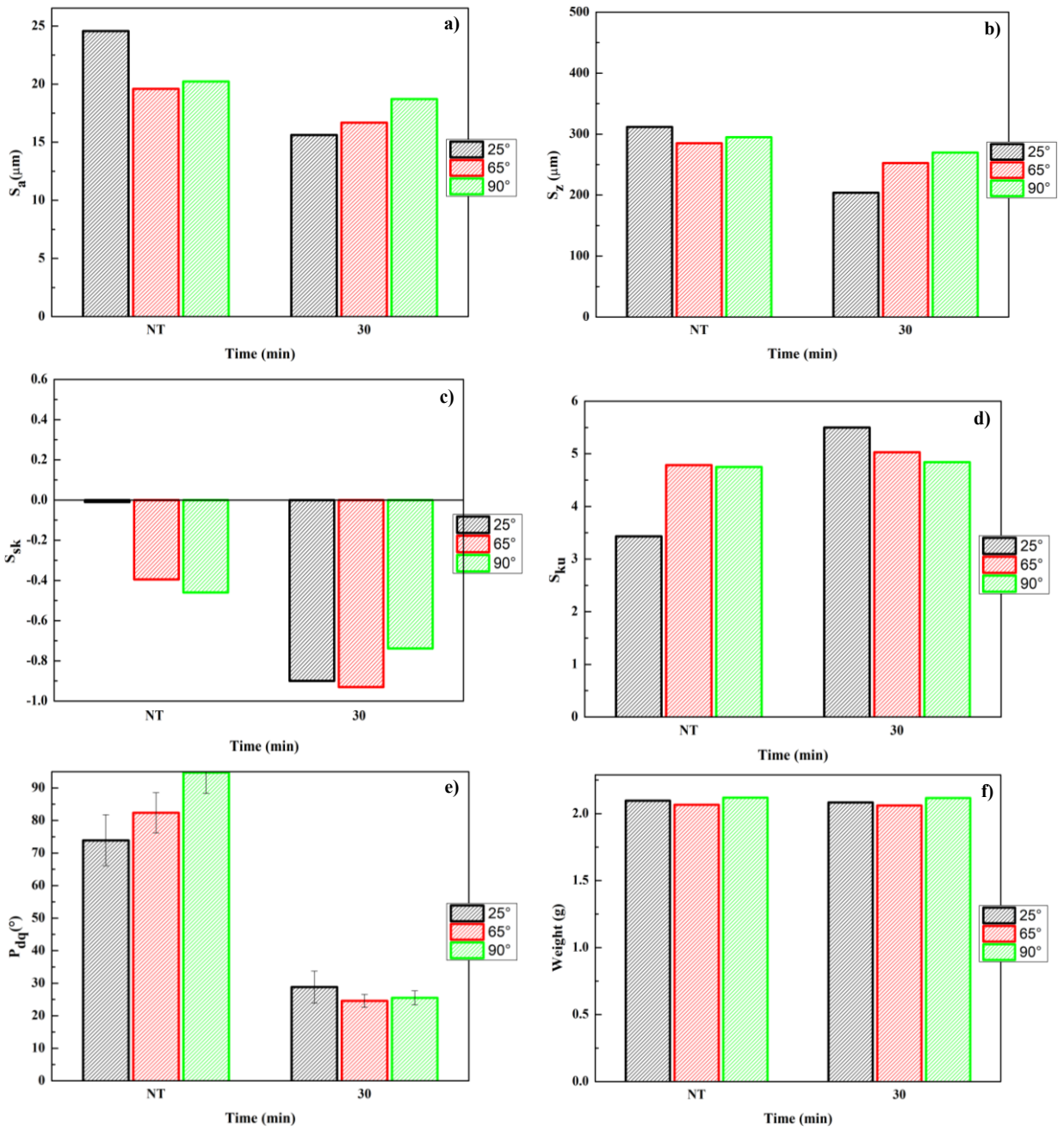
Figure 6.30. Surface texture parameters and weight evolution for the rotating samples (v = 1 m/s) tests, using irregular shape stainless steel as the abrasives: (a) S_a, (b) S_z, (c) S_{sk}, (d) S_{ku}, (e) P_{dq} and (f) weight.
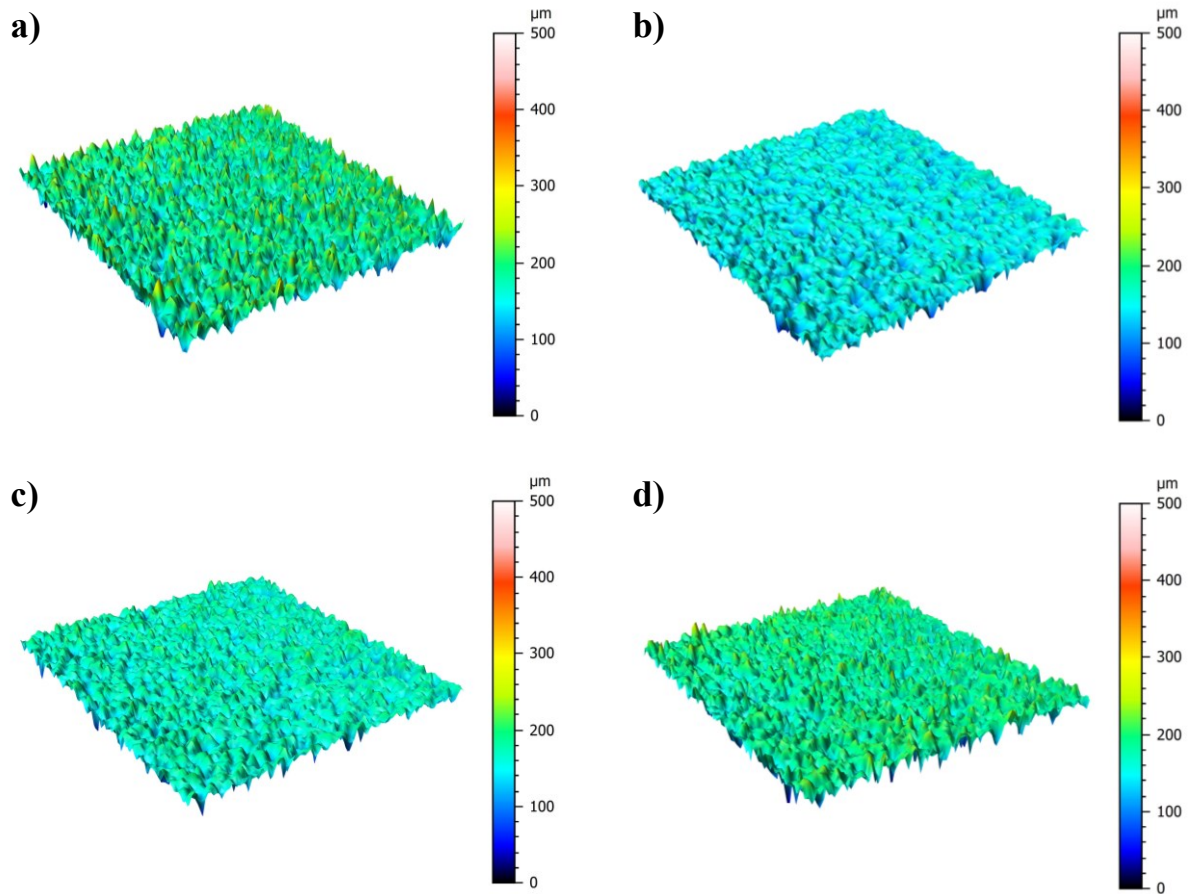
Figure 6.31. Comparison, before and after the whole treatment, between the 3D surfaces of the treated samples under different impact angles: (a) untreated, (b) 25°, (c) 65° and (d) 90°.

Table 6.29. Surface texture and weight values after each step of the FBM, for rotating samples and irregular shape stainless steel abrasive particles (25° impact angle, average tangential speed v = 1 m/s).

Time (min)	S_a (µm)	S_z (µm)	S_{sk}	S_{ku}	P_{dq} avg (°)	P_{dq} dev.st (±σ) (°)	Weight (g)
0	24.5	311	-0.01	3.43	73.9	7.8	2.096
30	15.6	203	-0.9	5.4	28.8	4.9	2.083

Table 6.30. Surface texture and weight values after each step of the FBM, for rotating samples and irregular shape stainless steel abrasive particles (65° impact angle, average tangential speed v = 1 m/s).

Time (min)	S_a (µm)	S_z (µm)	S_{sk}	S_{ku}	P_{dq} avg (°)	P_{dq} dev.st (±σ) (°)	Weight (g)
0	19.6	285	-0.39	4.78	82.3	6.1	2.065
30	16.6	252	-0.93	5.03	24.5	1.9	2.060

Table 6.31. Surface texture and weight values after each step of the FBM, for rotating samples and irregular shape stainless steel abrasive particles (90° impact angle, average tangential speed v = 1 m/s).

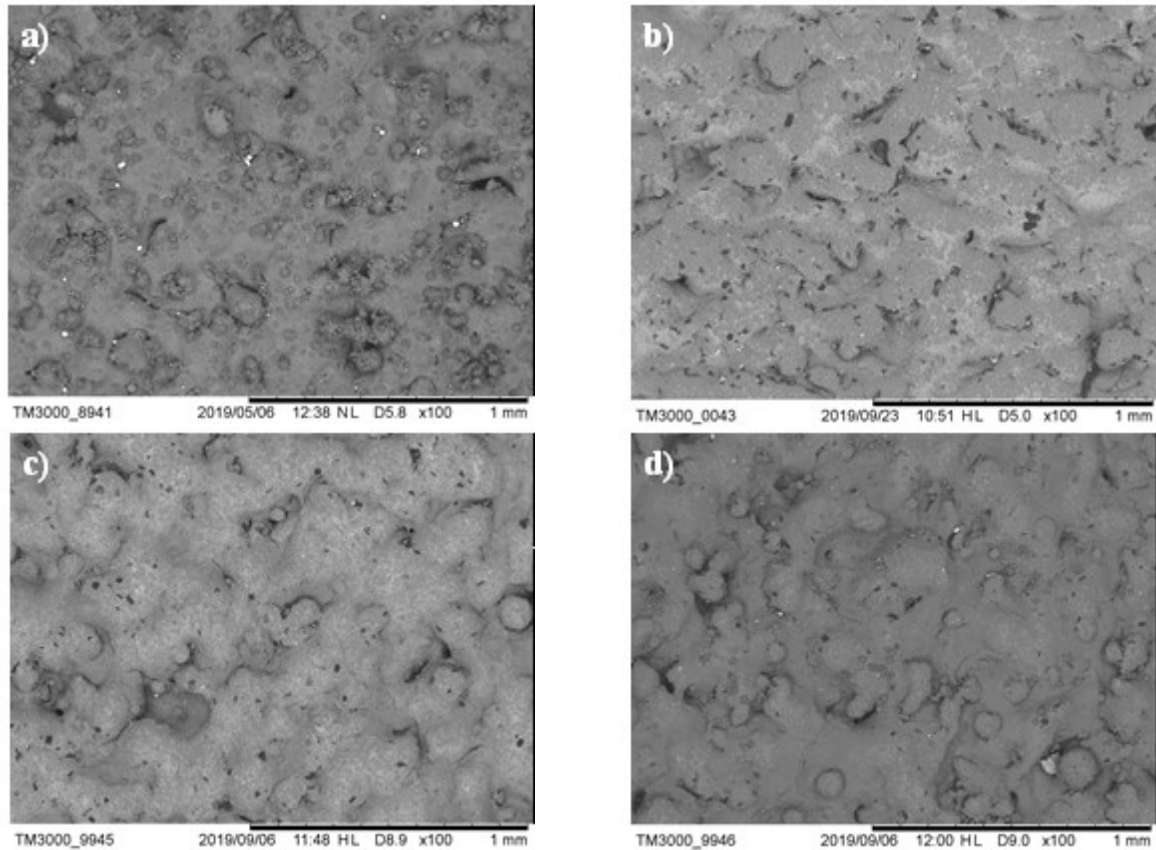| Time (min)	S_a (µm)	S_z (µm)	S_{sk}	S_{ku}	P_{dq} avg (°)	P_{dq} dev.st (±σ) (°)	Weight (g)
0	20.2	295	-0.46	4.75	94.7	6.3	2.117
30	18.7	269	-0.73	4.84	25.5	2.1	2.112

107

Figure 6.32. Comparison, before and after the whole treatment, between the SEM images of the treated samples under different impact angles: (a) untreated, (b) 25°, (c) 65° and (d) 90° (magnification 100x).

More appreciable surface improvements are observable from the tests in which the higher value of tangential speed (v = 2 m/s) was adopted. In this case, according to the time evolution of the surface texture parameters reported in Fig. 6.30, the 3D surfaces reported in Fig. 6.31 and the actual values reported in Tables 6.32-34, the surface roughness reduction is more consistent.

For the best case, confirmed again as the 25° impact angle condition, S_a decreases from 24.8 μm to 6.1 μm, whereas for the 65 ° and 90° impact angles the reductions of this parameter are still consistent but in a minor degree. Similar conclusions could be drawn for the other parameters and the weight loss, in comparison with the v = 1 m/s condition. Moreover, the SEM images reported in Fig. 6.32 provides a confirm of the quantified surface improvements, highlighting also the presence of several defects that, according to the observations done for the previous case, alters significantly the actual values measured. Therefore, it would be a proper assumption to consider the real roughness values as lower than the effectively measured ones.

However, according the 3D surface acquired for the 25° impact angle condition (Fig. 6.31b), a not homogeneous smoothing effect was highlighted. This result, physically illustrated also in Fig. 6.33, is mainly dictated by the locally different tangential speed values acting on the surface, depending on the punctual distance from the rotation axis (Eq. 6.1).

This consideration, reported schematically in Fig. 6.34, implies another effect on the resulting shear stresses applied to the surface in the rotating samples process configuration. More specifically, given the samples inclination with respect to the main axial direction of the fluidised abrasive, the particles directed through the lower area of the sample performs a longer path on the surface compared to the ones directly impacting on the upper side. This phenomenon could lead to a greater dissipation energy of the abrasives through simple rolling, hampering the use of that

energy for pure shear stresses that proved to be more effective with respect to the surface smoothing. The implications of these aspects are illustrated more clearly in Fig. 6.35, reporting the detailed SEM images of the different areas of the sample treated in the best case condition. From the latter, it can observed the presence of shear bands on the treated surface, whose intensity decreases when moving from the upper to the middle and lower areas of the sample.

Based on this premise, a proper FBM strategy could lead to more homogeneous results. Therefore, at the end of this Chapter are reported the results of further tests carried out on the best case, evaluating the effect of two process strategies that takes into consideration the rotation sense of the sample as well as the process time spent for the single rotation verse.
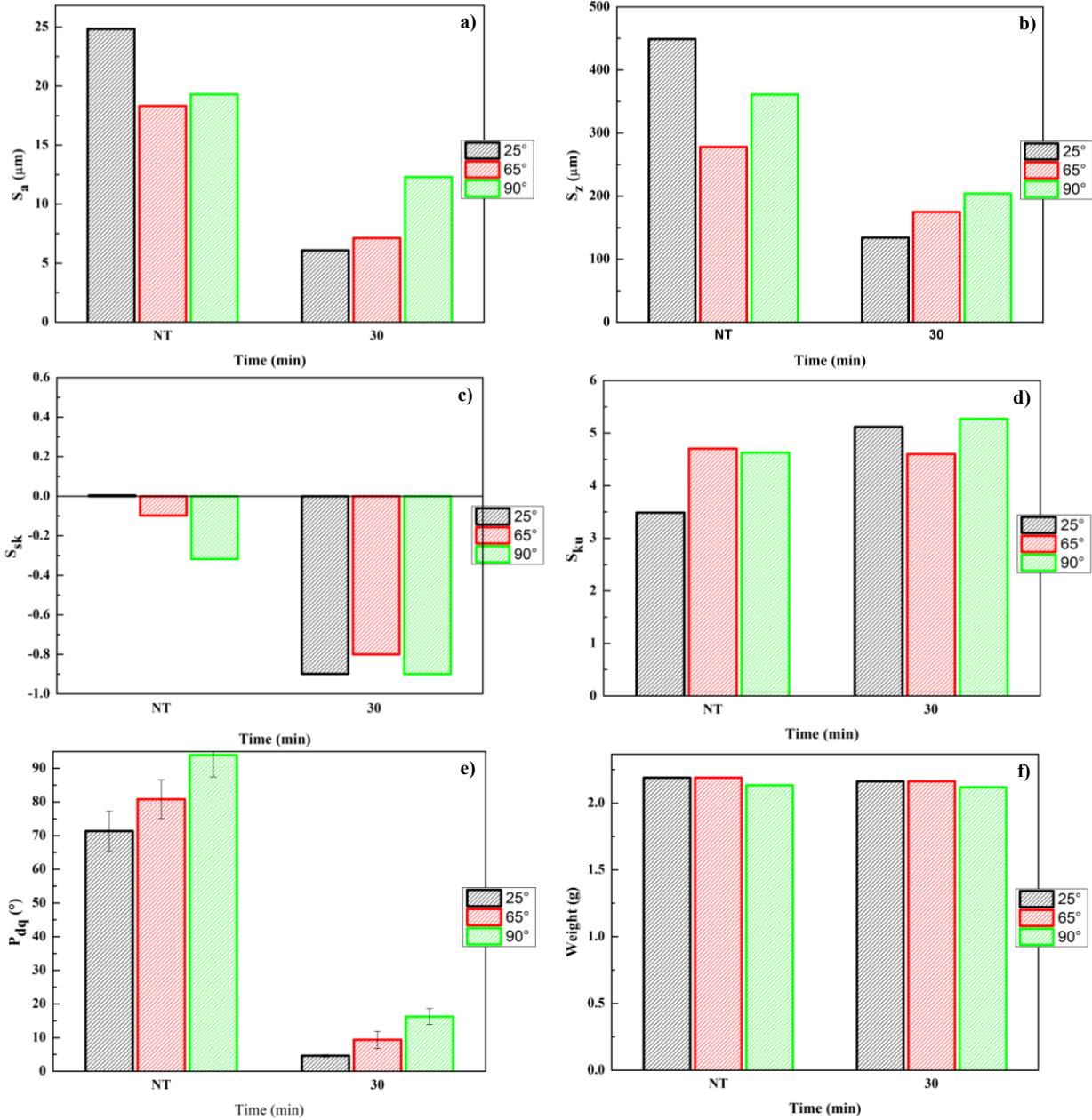

Figure 6.30. Surface texture parameters and weight evolution for the rotating samples ($v = 2$ m/s) tests, using irregular shape stainless steel as the abrasives: (a) S_a, (b) S_z, (c) S_{sk}, (d) S_{ku}, (e) P_{dq} and (f) weight.
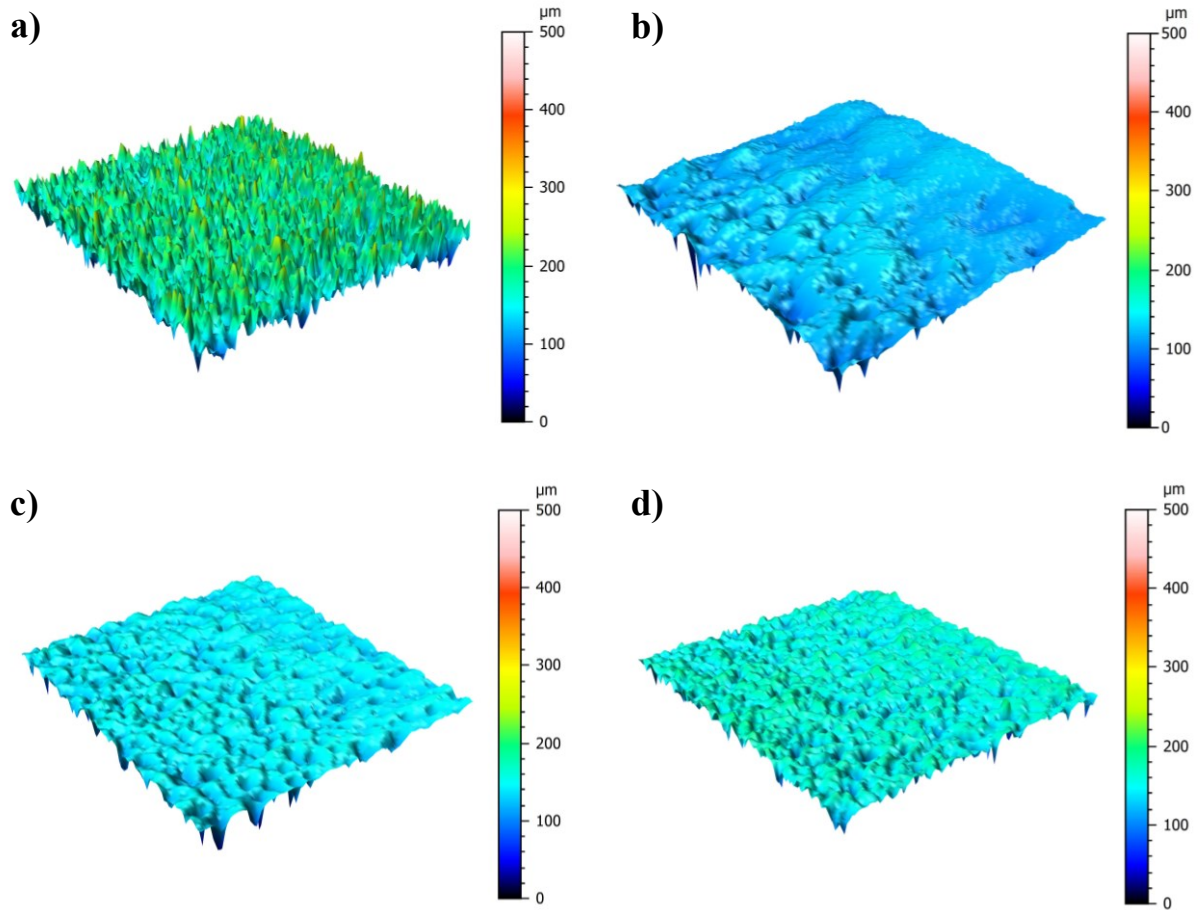
Figure 6.31. Comparison, before and after the whole treatment, between the 3D surfaces of the treated samples under different impact angles: (a) untreated, (b) 25°, (c) 65° and (d) 90°.

Table 6.32. Surface texture and weight values after each step of the FBM, for rotating samples and irregular shape stainless steel abrasive particles (25° impact angle, average tangential speed v = 2 m/s).

Time (min)	S_a (µm)	S_z (µm)	S_{sk}	S_{ku}	P_{dq} avg (°)	P_{dq} dev.st (±σ) (°)	Weight (g)
0	24.8	448	0	3.48	71.3	5.9	2.190
30	6.1	134	-0.89	5.11	4.60	0.3	2.162

Table 6.33. Surface texture and weight values after each step of the FBM, for rotating samples and irregular shaped stainless steel abrasive particles (65° impact angle, average tangential speed v = 2 m/s).

Time (min)	S_a (µm)	S_z (µm)	S_{sk}	S_{ku}	P_{dq} avg (°)	P_{dq} dev.st (±σ) (°)	Weight (g)
0	18.3	278	-0.1	4.7	80.8	5.7	2.190
30	7.1	175	-0.8	4.6	9.3	2.5	2.162

Table 6.34. Surface texture and weight values after each step of the FBM, for rotating samples and irregular shape stainless steel abrasive particles (90° impact angle, average tangential speed v = 2 m/s).

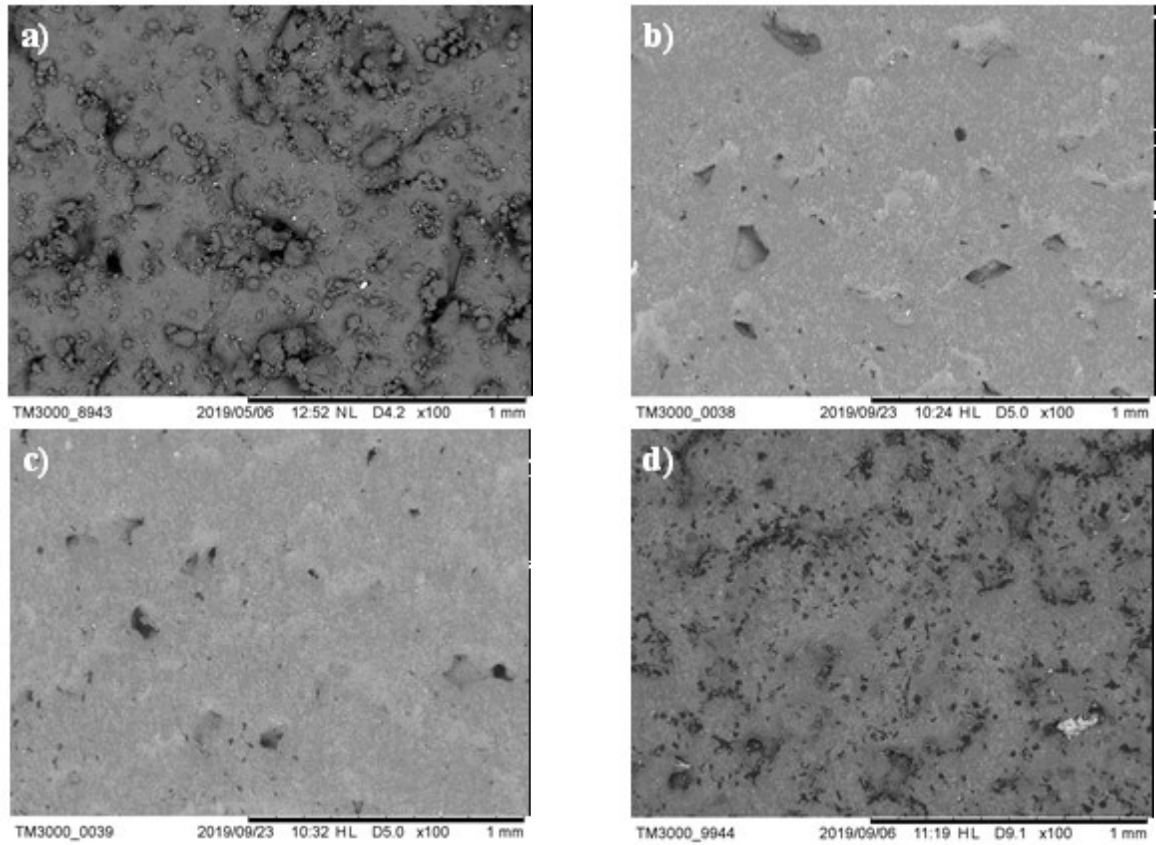| Time (min)	S_a (µm)	S_z (µm)	S_{sk}	S_{ku}	P_{dq} avg (°)	P_{dq} dev.st (±σ) (°)	Weight (g)
0	19.3	361	-0.31	4.63	93.9	6.4	2.134
30	12.2	204	-0.9	5.27	16.2	2.3	2.119

Figure 6.32. Comparison, before and after the whole treatment, between the SEM images of the treated samples under different impact angles: (a) untreated, (b) 25°, (c) 65° and (d) 90° (magnification 100x).
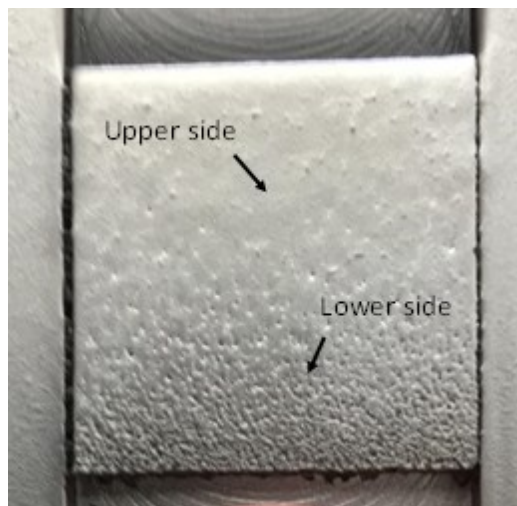

Figure 6.33. Illustration of the non-homogeneous surface finish of sample treated with irregularly shaped stainless steel abrasive particles, with a 25° impact angle in rotating configuration (v = 2 m/s).
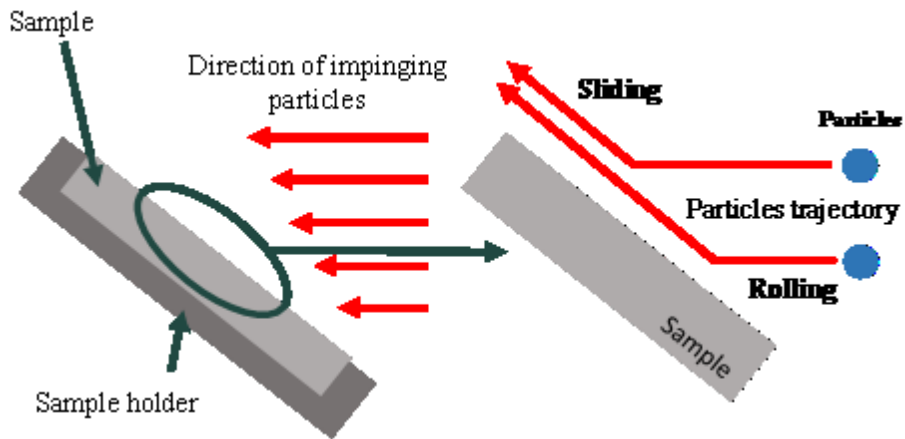
Figure 6.34. Illustration of the different shear stresses acting on the top and bottom areas of the sample illustrated in Fig. 5.33.
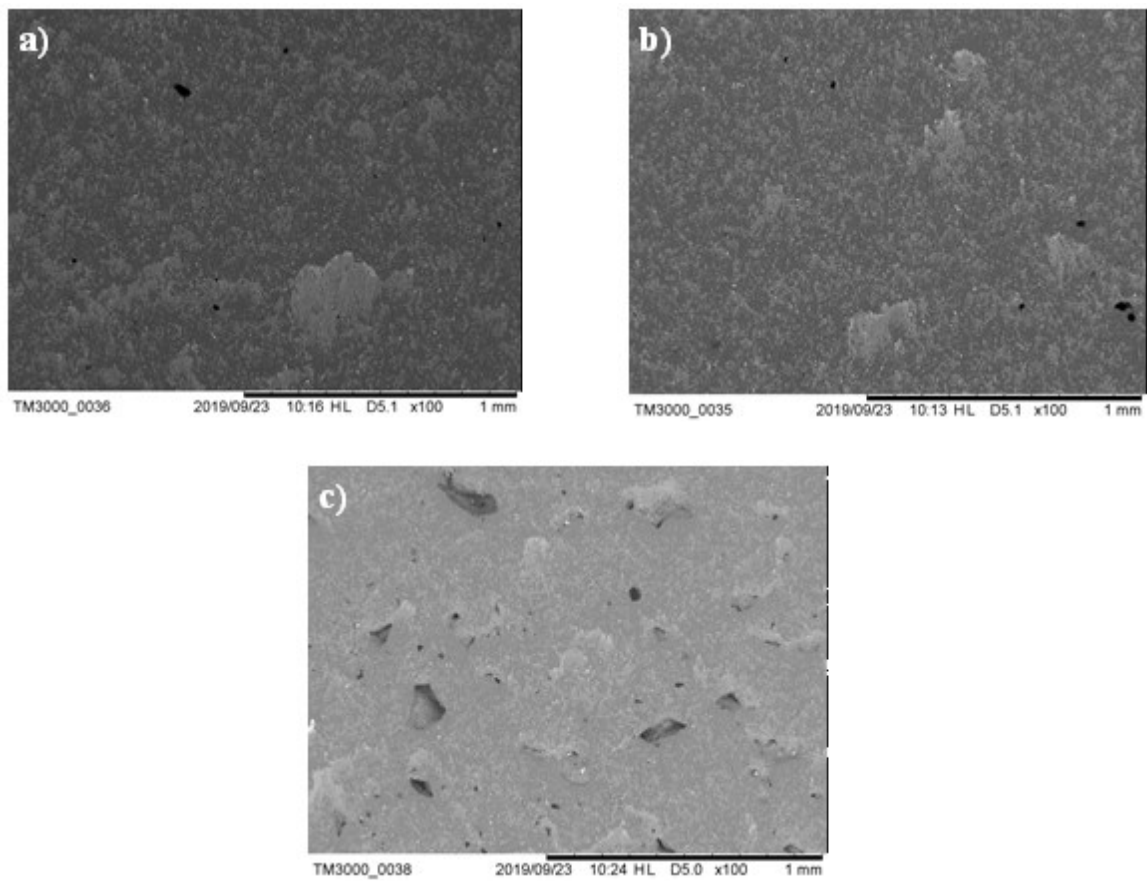

Figure 6.35. SEM images of the different areas of the sample treated at 25° (v = 2 m/s) impact angle. (a) Upper, (b) middle and (c) lower area (magnification: 100x).

In Fig. 6.36 are reported the trends of the surface texture parameters observed for the experiments carried out with the cutwire abrasives and a tangential speed of 1 m/s. In first analysis, it can be observed that the surface roughness reductions achieved in this case are lower compared to the irregular stainless steel abrasives but, at the same time, more consistent than the high hardness abrasives. This result is confirmed by the actual values reported in Tables 6.35-6.37 in which, as a further confirm of the previous observations, the 25° impact angle represents again the best case. Concerning the surface parameters trends, similar conclusions can be drawn in comparison with the previous case except for a variation of S_{sk} to more positive values, indicating a more uniform effect of the treatment on the peaks and valleys. On the other hand, a not well defined trend for S_{ku} and a consistent reduction of P_{dq} are were observed in this case.

However, it can be noted that the shape of the abrasives has a remarkable influence on the process efficiency. As also confirmed by the 3D surfaces and the SEM images reported in Fig. 6.37 and Fig. 6.38 respectively, the cutwire abrasives promoted lesser surface modifications. More specifically, the treatment promoted the same consistent removal of the sintered powders on the surface observed for the irregular abrasives, especially for the 25° impact angle but, at the same time, the morphology lying underneath was less affected.

The influence of the abrasive shape to this result can be associated to the extremely lower number of cutting edges for the cutwire shape. This implies a considerably higher probability that the impacts on the surface will not induce indentations (i.e. only rolling will take place) but rather more plastic deformation of the substrate. Based on this premise, the impacts of the abrasive will remove a minor number of sintered particles and, consequently, will modify in a lesser degree the underlying morphology.

It is worth to highlight that this result seems to be not in agreement with the abrasives effect observed by *Atzeni et al.* [135]. In their experiments, the cut wire abrasive promoted the highest surface roughness reductions, but considering abrasive particles with greater size, different dimensions of the FBM reactor, different SLM process parameters and a different surface characterization approach. Therefore, the results reported in this work are difficult to be properly compared with the ones reported in literature.

However, considering that the FBM with stainless steel represents a process condition for which a comparison with literature exists, the agreement of the more global process trends could be noted. For instance, it can be seen by the comparison with the data reported from *Atzeni et al.* [135] that the FBM process promotes significant roughness reductions when stainless steel is used, as also clearly visible in this work, and the trends for the surface texture parameters (for areas in this work, for profiles in literature) are very similar. At the same way, the irregular shape stainless steel promoted very similar results that are also in agreement in terms of final roughness value.
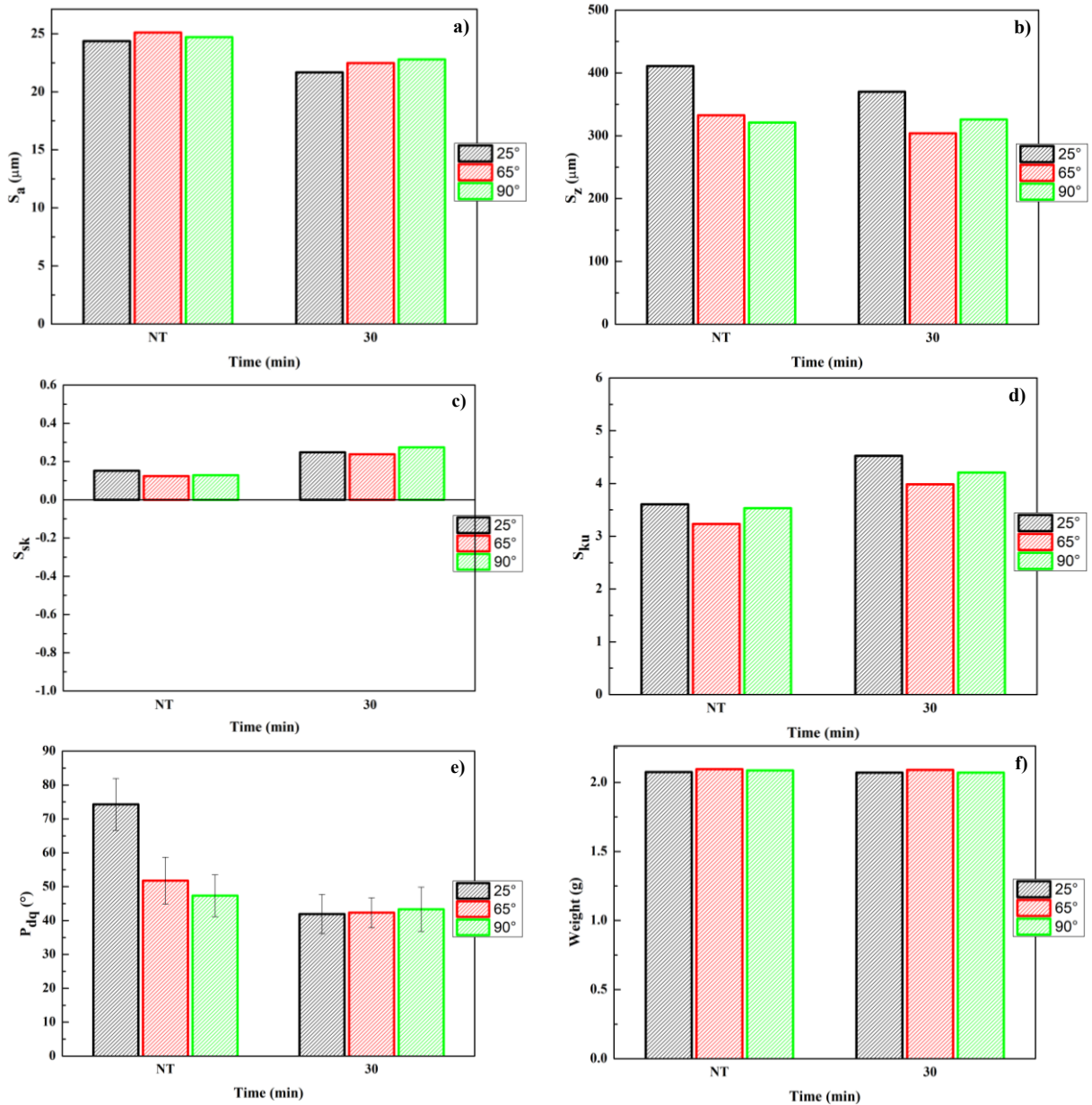
Figure 6.36. Surface texture parameters and weight evolution for the rotating samples (v = 1 m/s) tests, using cutwire stainless steel as the abrasives: (a) S_a, (b) S_z, (c) S_{sk}, (d) S_{ku}, (e) P_{dq} and (f) weight.
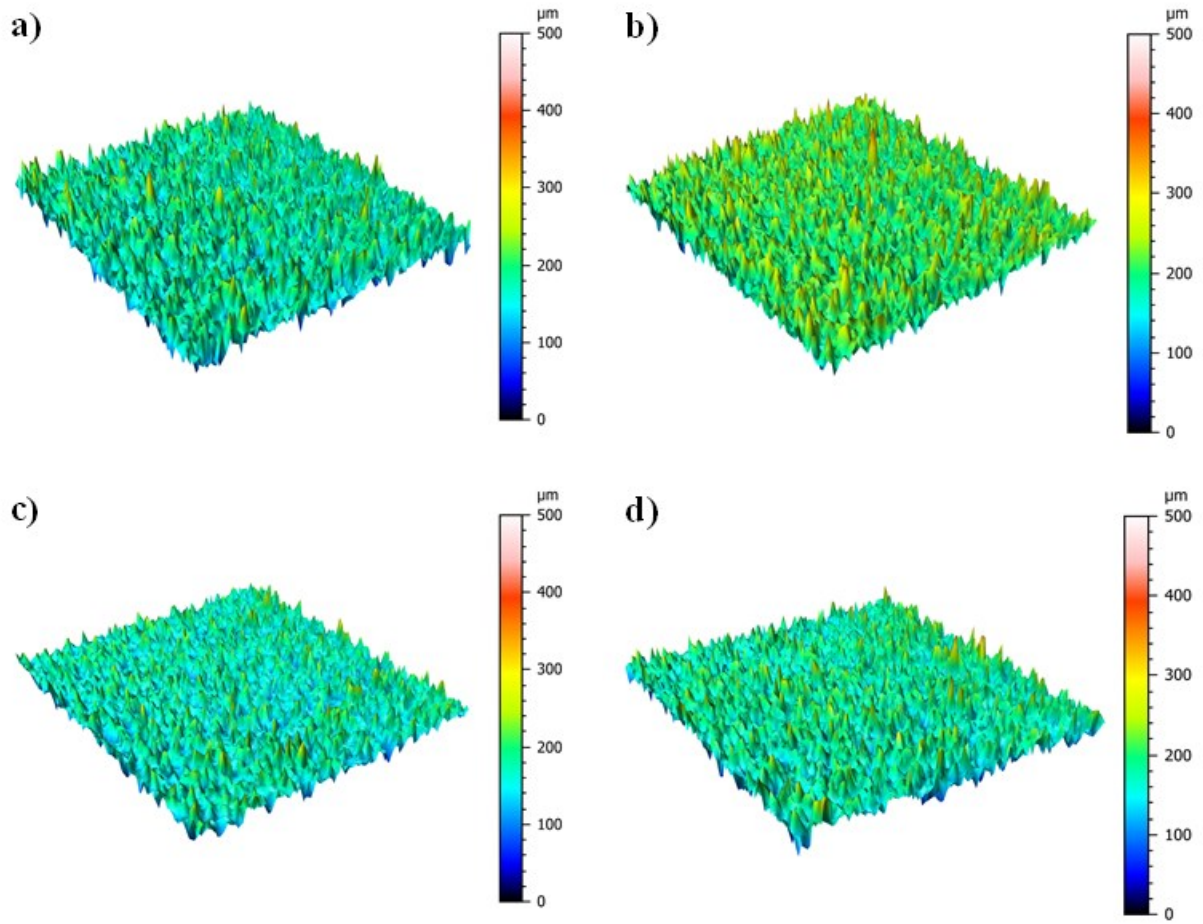
Figure 6.37. Comparison, before and after the whole treatment, between the 3D surfaces of the treated samples under different impact angles: (a) untreated, (b) 25°, (c) 65° and (d) 90°.

Table 6.35. Surface texture and weight values after each step of the FBM, for rotating samples and cutwire shaped stainless steel abrasive particles (25° impact angle, average tangential speed v = 1 m/s).

Time (min)	S_a (μm)	S_z (μm)	S_{sk}	S_{ku}	P_{dq} avg (°)	P_{dq} dev.st (±σ) (°)	Weight (g)
0	24.3	411	0.15	3.60	74.2	7.6	2.074
30	21.6	370	0.24	4.52	41.9	5.7	2.070

Table 6.36. Surface texture and weight values after each step of the FBM, for rotating samples and cutwire shaped stainless steel abrasive particles (65° impact angle, average tangential speed v = 1 m/s).

Time (min)	S_a (μm)	S_z (μm)	S_{sk}	S_{ku}	P_{dq} avg (°)	P_{dq} dev.st (±σ) (°)	Weight (g)
0	25.1	332	0.12	3.23	51.7	6.8	2.096
30	22.4	304	0.23	3.98	42.3	4.3	2.091

Table 6.37. Surface texture and weight values after each step of the FBM, for rotating samples and cutwire shaped stainless steel abrasive particles (90° impact angle, average tangential speed v = 1 m/s).

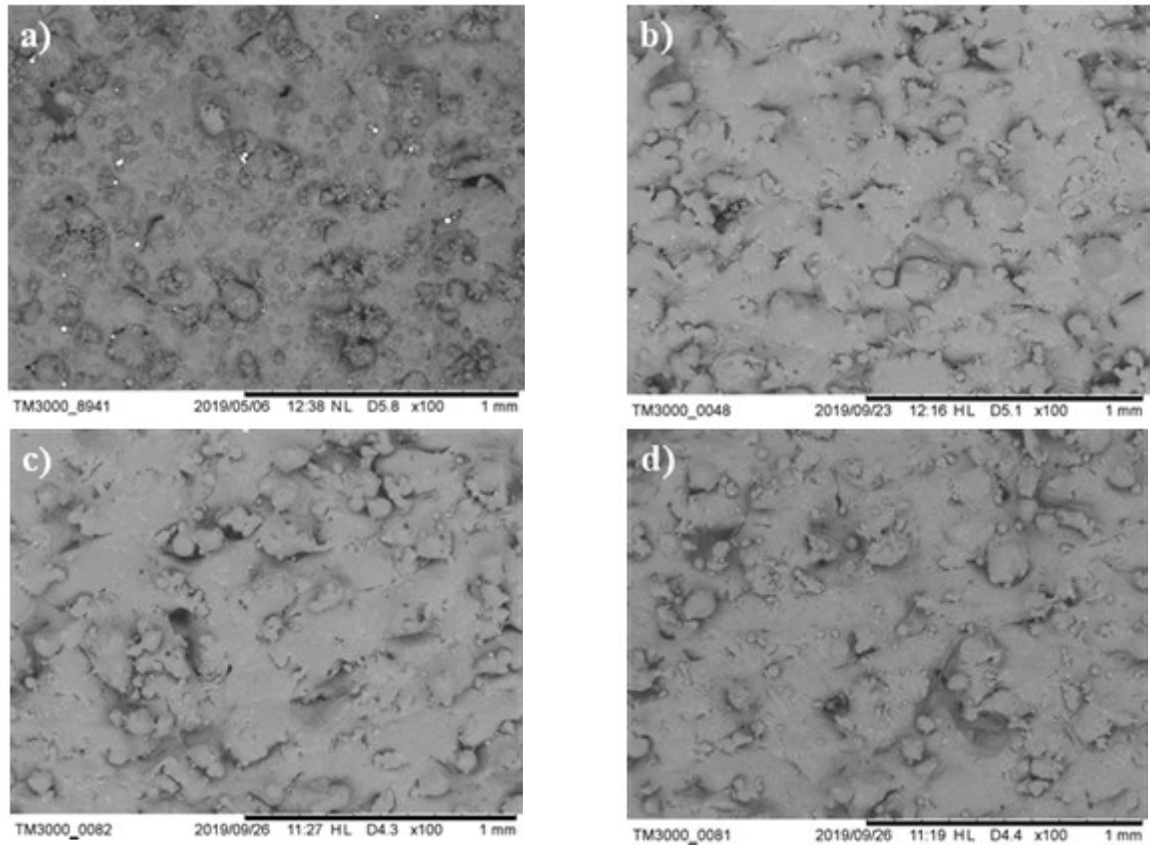| Time (min)	S_a (μm)	S_z (μm)	S_{sk}	S_{ku}	P_{dq} avg (°)	P_{dq} dev.st (±σ) (°)	Weight (g)
0	24.7	321	0.12	3.53	47.3	6.20	2.087
30	22.8	329	0.27	4.20	43.3	6.52	2.071

Figure 6.38. Comparison, before and after the whole treatment, between the SEM images of the treated samples under different impact angles: (a) untreated, (b) 25°, (c) 65° and (d) 90° (magnification 100x).

The effects of the abrasive shape change observed by the comparison between the irregular and cutwire particles becomes more evident when the tangential speed applied to the surface increased to 2 m/s. As for all the rotating sample experiments reported in this Chapter, the increase of tangential speed is beneficial also in this case. Furthermore, the aforementioned minor efficiency of the cutwire abrasive particles is confirmed again, as observable by the evolution of the surface texture parameters reported in Fig. 6.39 and the actual values reported in Tables 6.38-5.40. Consequently, the confirm of all the mentioned aspects is found also from the 3D surfaces reported in Fig. 5.40 as well as the SEM images reported in Fig. 6.41.

It is worth to assume, based on all the considerations done for the high density abrasives, that the latter characteristic is way more beneficial for the smoothing process efficiency, compared to the hardness property. Moreover, it can be also noted that abrasives shape possesses a notable influence on the achievable results, because it is responsible for the establishing of the different surface-abrasive interaction mechanisms that promotes a major contribution of rolling (plastic deformation) mechanisms rather than sliding (material removal). As a result, the number of detached sintered powders is reduced, resulting in a less smooth surface compared to the one subjected to the interaction with the irregularly shaped abrasive particles.

Finally, the influence of the impact angle with the case of the cutwire abrasive provides a further confirm of the best case represented by the 25°.
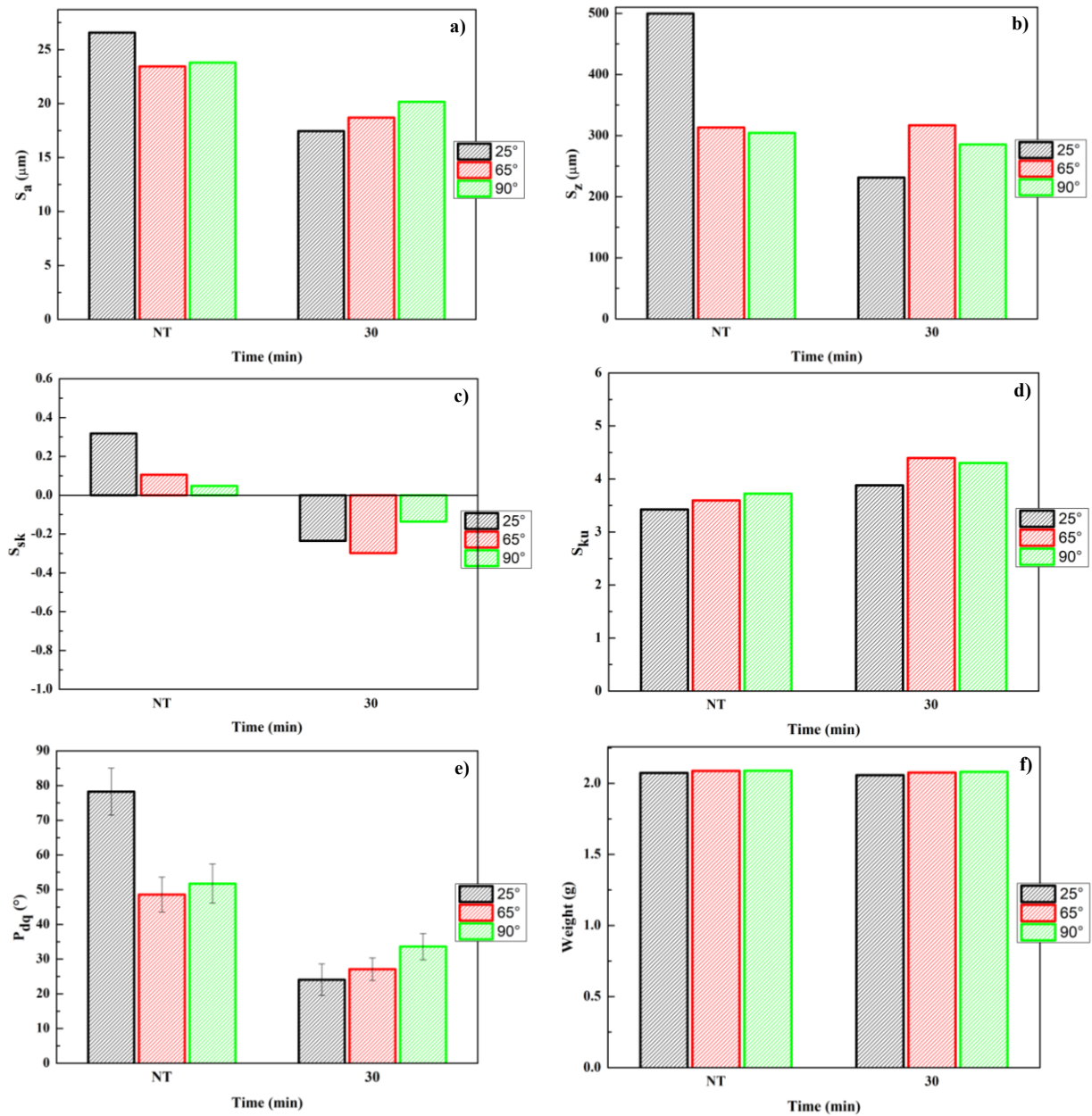
Figure 6.39. Surface texture parameters and weight evolution for the rotating samples (v = 2 m/s) tests, using cutwire stainless steel as the abrasives: (a) S_a, (b) S_z, (c) S_{sk}, (d) S_{ku}, (e) P_{dq} and (f) weight.
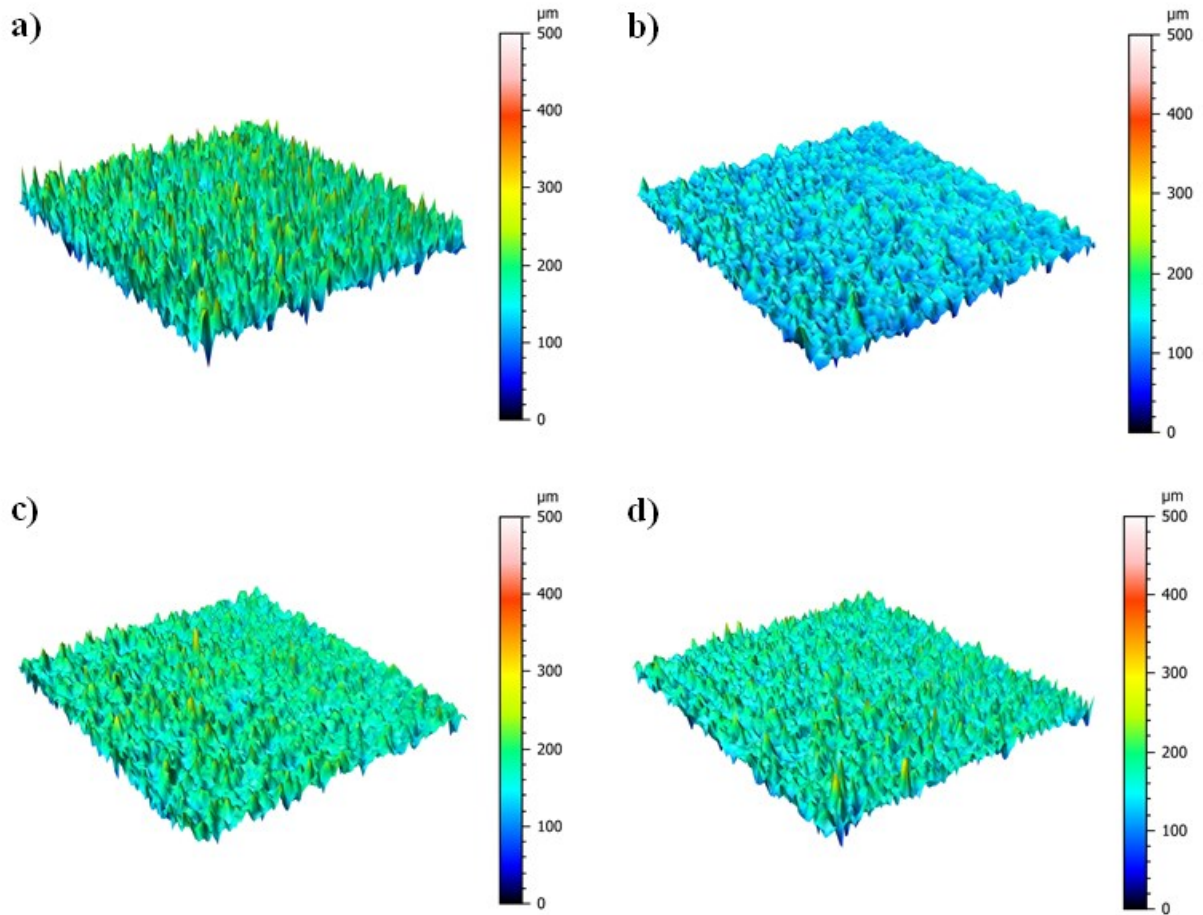
Figure 6.40. Comparison, before and after the whole treatment, between the 3D surfaces of the treated samples under different impact angles: (a) untreated, (b) 25°, (c) 65° and (d) 90°.

Table 6.38. Surface texture and weight values after each step of the FBM, for rotating samples and cutwire shaped stainless steel abrasive particles (25° impact angle, average tangential speed v = 2 m/s).

Time (min)	S_a (µm)	S_z (µm)	S_{sk}	S_{ku}	P_{dq} avg (°)	P_{dq} dev.st (±σ) (°)	Weight (g)
0	26.5	499	0.31	3.42	78.2	6.7	2.074
30	17.4	231	-0.23	3.87	24.0	4.5	2.057

Table 6.39. Surface texture and weight values after each step of the FBM, for rotating samples and cutwire shaped stainless steel abrasive particles (65° impact angle, average tangential speed v = 2 m/s).

Time (min)	S_a (µm)	S_z (µm)	S_{sk}	S_{ku}	P_{dq} avg (°)	P_{dq} dev.st (±σ) (°)	Weight (g)
0	23.4	313	0.10	3.59	48.5	5	2.088
30	18.7	316	-0.29	4.39	27.1	3.2	2.077

Table 6.40. Surface texture and weight values after each step of the FBM, for rotating samples and cutwire shaped stainless steel abrasive particles (90° impact angle, average tangential speed v = 2 m/s).

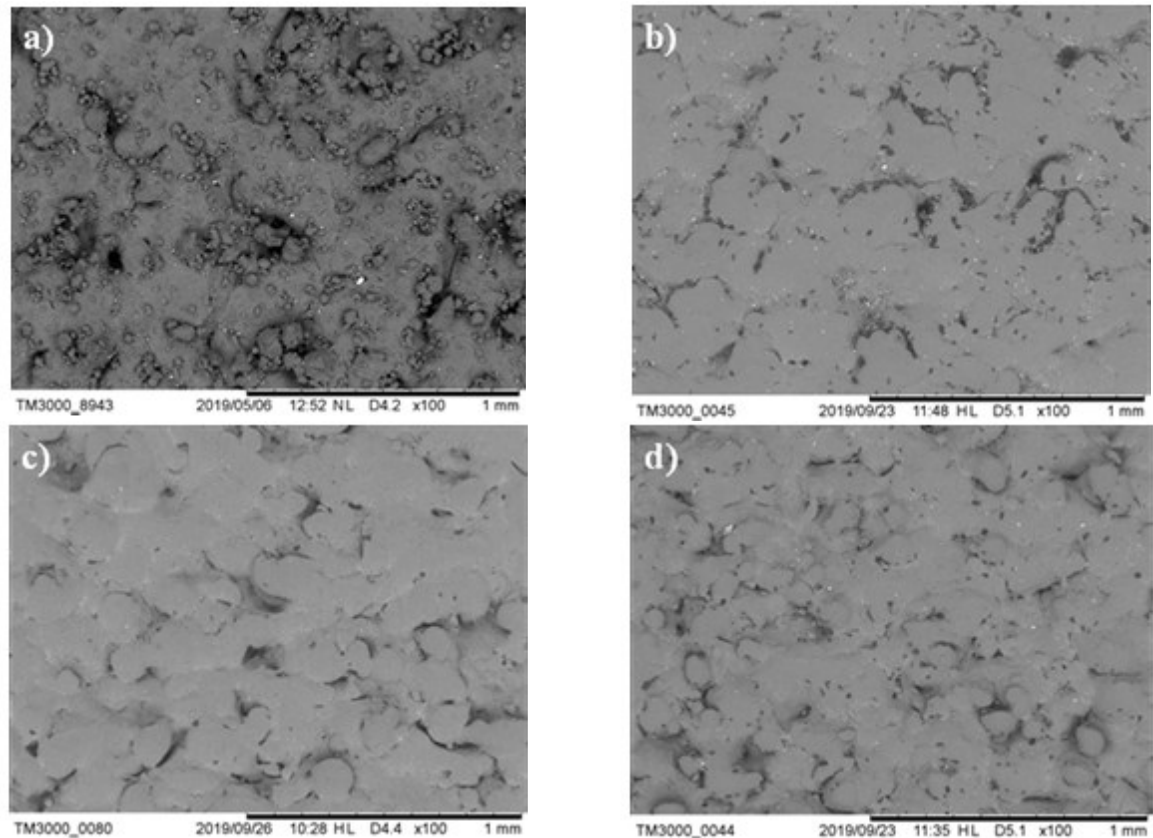| Time (min)	S_a (µm)	S_z (µm)	S_{sk}	S_{ku}	P_{dq} avg (°)	P_{dq} dev.st (±σ) (°)	Weight (g)
0	23.8	304	0.04	3.72	51.7	5.6	2.090
30	20.1	285	-0.13	4.3	33.6	3.7	2.082

Figure 6.41. Comparison, before and after the whole treatment, between the SEM images of the treated samples under different impact angles: (a) untreated, (b) 25°, (c) 65° and (d) 90° (magnification 100x).

6.3.3. Further experiments on the best case

From the results reported in the previous subparagraphs, the best case in terms of surface roughness improvement was obtained for the process conditions related to the sample reported in Fig. 6.33, i.e.:

- Rotating sample (v = 2 m/s);
- Impact angle: 25°;
- Abrasive: irregular stainless steel;
- Process time: 30 min.

However, it was also highlighted the not homogeneous treatment effects on the exposed surface. It is worth to remind that this was the reason why the 0° impact angle was not investigated in the rotating sample tests (practically, very similar to the 90° condition in the stationary sample tests). Therefore, another important outcome is that, whenever the shear conditions are established and the impact energy involved is sufficient to promote significant surface modifications, a not homogeneous surface will result from the treatment in the investigated conditions. It is also worth to note that this experimental evidence was not possible for the high hardness abrasives, given the low surface modifications due to the low impact energy involved.

Based on all these premises, two further tests were carried out in order to compensate this issue. These tests refers to the possibility of surface improvement through the application of a proper process strategy. With this aim, two conditions were tested according to the sample illustration reported in Fig. 6.33:

- With the same process conditions reported above, a second step of treatment was carried out by turning the sample upside down. Therefore, the total process time was 60 min (30 min in one verse, 30 min in the opposite);
- In a second case, the 30 min process time was considered as the sum of alternating steps of 5 min for each side of the sample (i.e. upper and lower).

Moreover, in order to evaluate the differences in the considered areas, the same 8 x 8 mm² area acquired by means of confocal microscopy was divided in two sub-areas related to the upper and lower side of the sample. As a further comparison, the actual values of the surface texture parameters were evaluated for the considered areas as well as the total area.

Fig. 6.42 illustrates the surface resulting from the first FBM strategy adopted, whose actual values also reported in Table 5.41. Results suggests an improved surface uniformity, however a sort of pattern can be easily noted.

The latter result is probably caused by the plastic deformation of the surface, in conditions in which two fronts are "crushing" one in front of another. On the other hand, the values reported in Table 6.41 suggests an improvement of the surface quality but with appreciable differences in the values of the surface parameters. It is worth to note that this result was the reason why the second process strategy was considered, based on the hypothesis that the two plastic deformation fronts given by the consistent shear stresses (as discussed previously) can be balanced if the time step adopted for the smoothing of each side of the sample is lowered. In the latter case, Fig. 6.43 illustrates the results obtained, quantified also by the actual values reported in Table 6.42, suggesting a further surface improvement compared to the previous more time-consuming strategy.
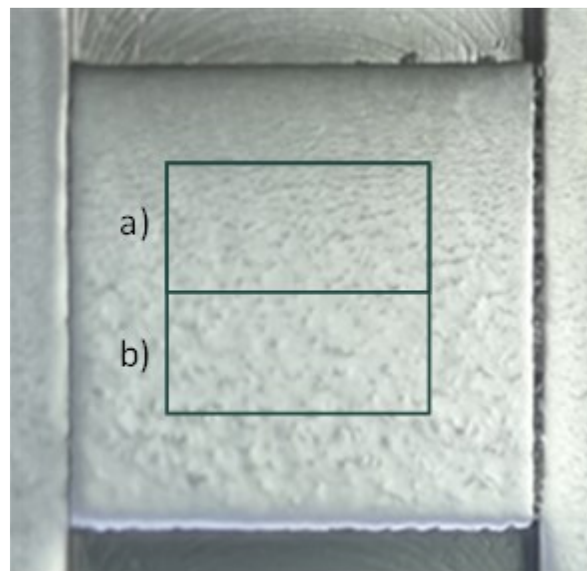

Figure 6.42. Illustration of the result obtained from the adoption of two process steps of 30 min for the upper (a) and lower (b) sides of the sample.

Table 6.41. Surface texture parameters obtained after the treatment with the adoption of the two process steps of 30 min for the upper (a) and lower (b) sides of the sample.

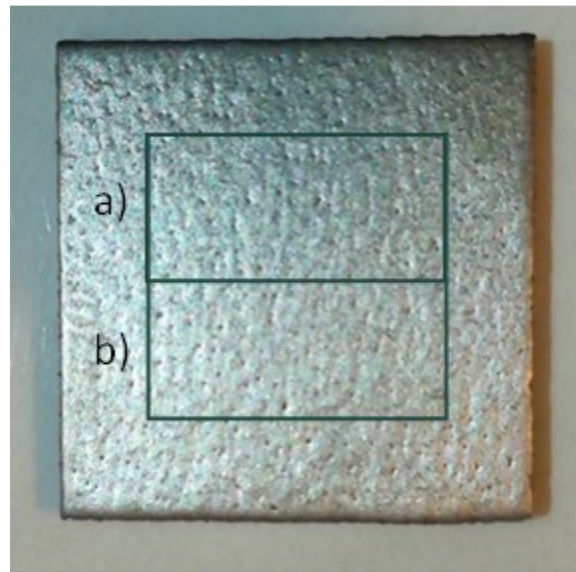|	S_a (µm)	S_z (µm)	S_{sk}	S_{ku}	P_{dq} avg (°)	P_{dq} dev.st (±σ) (°)
Upper side	5,1	58,3	0,26	3,0	4,3	0,2
Lower side	6,3	54,4	0,48	3,4	5,4	0,1
Total area	5,7	64,3	0,46	3,5	4,9	0,5

Figure 6.43. Illustration of the result obtained after 30 min of treatment, divided into alternating steps of 5 min for each side of the sample.

Table 6.42. Surface texture parameters obtained after 30 min of treatment, divided into alternating steps of 5 min for each side of the sample.

	S_a (µm)	S_z (µm)	S_{sk}	S_{ku}	P_{dq} avg (°)	P_{dq} dev.st (±σ) (°)
Upper side	4,9	84,0	-0,93	6,0	4,3	0,2
Lower side	4,8	77,4	-1,10	6,7	5,4	0,1
Total area	4,9	77,0	-0,81	5,4	4,9	0,5

6.4. Conclusions

Based on the experimental results observed for the FBM process conditions and parameters investigated, the following conclusions can be drawn:

- A preliminary consideration about the initial surface status of the treated samples is necessary: given the random surface texture caused by the presence of a sintered powders layer, the measured surface texture parameters can vary in a considerable way. In addition, the presence of surface defects, more likely caused by lack of fusion, leads to a less reliable quantification of the surface improvements given by the FBM process. This consideration is valid especially for the treatment conditions in which the surface modifications are slight;

- In relation to the surface treatment, a first experimental outcome is related to the implications of the process configuration on the resulting surface-abrasives interaction mechanisms: for all the investigated abrasives, it was found that the rotating sample configuration, especially for an average tangential speed of 2 m/s, provides the highest surface texture improvements. Regardless of the specific abrasive, this outcome suggests the need to establish process conditions that enhance shear-based abrasive interactions with the surface of the sample;

- With this premise and according to the theoretical considerations reported in literature [136], the impact angle has a remarkable influence on the achievable results. More specifically, it was found that the 25° angle leads to the best results for the rotating sample configuration, whereas the 90° impact angle represents the best case for the stationary sample configuration. This result would be expectable considering the proximity of the values with respect to the process configurations investigated (90° in stationary sample condition is closer to 25° in the rotating condition). To the best knowledge of the author, there are no data in literature reporting the influence of the impact angle on the process efficiency, both in stationary and rotating sample;

- The surface improvements are highly dependent on the abrasive particles properties. More specifically, it was observed that abrasives with higher density (stainless steel), given the higher impact energy possessed, led to quite appreciable results compared to abrasives in which hardness is the privileged property (silica sand, alumina). It is worth to highlight that, at the best knowledge of the author, there is lack in literature data about the use of high hardness abrasives in FBM of metal AM parts.

- Based on the two investigated abrasive shapes for the stainless steel abrasives, an irregular shape is preferred to the cutwire, given the lower impact energy dissipation through shear observed in the latter case, probably caused by a lower number of cutting edges. This aspect hamper the removal of the sintered powders on the sample surface, leading to a lesser reduction in surface roughness. However, compared to the results reported in literature, based on similar experiments conducted by *Atzeni et al* [135], the results are not in agreement about the effects of the particles shape. This result could be justified by the lower abrasives size adopted in this work, as well as by the different surface characterization approach, the different impact angles used and the different process parameters used to produce the SLM samples;

- The combination of the previous points leads to the best case condition investigated, in which a remarkable surface roughness reduction was achieved (S_a decrease up to the 80%). A quite appreciable surface improvement was confirmed also by the other surface texture parameters, except for S_{ku} for which a clear trend could not be observed. Moreover, it was also observed that the treatment leads to more negative values of S_{sk}, suggesting the need for further process improvements in order to improve the symmetry of the treated surfaces;

- In the rotating sample process configuration, a not uniform smoothing effect was observed, caused by the different shear stresses as a function of punctual distance of the sample from the rotation axis. Based on this premise, it was proved that a proper machining strategy could address this issue, promoting a more uniform smoothing effect and a further roughness reduction compared to the minimum value achieved in a single process step. In this context, it was also proved that alternating the direction of the process with short time steps provides the best results.

7. Chemical polishing

In this Chapter, a detailed description of the experimental setup used for the CP process of AlSi10Mg samples made by SLM technology is reported. Moreover, a detailed description of the investigated experimental conditions is provided, as well as the presentation and discussion of the obtained results.

As previously discussed, CP consists in dipping parts into purposely made polishing solutions, with controlled conditions in terms of bath composition, temperature and stirring. This finishing technique might represent one of the best options for the smoothing of complex AM parts, also with narrow features such as lattice structures and internal channels that would be difficult to access even with the previously presented FBM process.

To remind the main benefits of this process, it is worth to remember the absence of physical tools (besides the polishing solution itself), the absence of residual stresses and the suitability for very complex parts. On the other hand, the main drawbacks are related to the use of chemical solutions that are not environmental-friendly (and therefore difficult and costly for the end of life disposal) and the need to use high temperatures in order to achieve satisfactory results in terms of etch rate and roughness reduction.

7.1. Experimental apparatus and preliminary tests

The scheme of the process and the physical apparatus are reported in Fig. 7.1. The equipment is represented by a thermostatic bath that hosts a Teflon graduated beaker, in which the chemical polishing solutions and the samples were placed. The thermostatic bath is able to control the temperature of the chemical solution by controlling the temperature of the water surrounding the beaker (max. temperature: 150 °C, resolution: $\pm$ 0,1 °C), as well as the stirring conditions. The continuous stirring of the solution, carried out by means of a magnetic anchor immersed in the chemical bath, allowed to reduce problems related to the saturation of the bath itself close to the samples due to the formation of reactions products during the process. For a safe use of all the equipment, the whole setup was placed under a chemical hood in order to prevent the exposure of the operator to acid vapors.
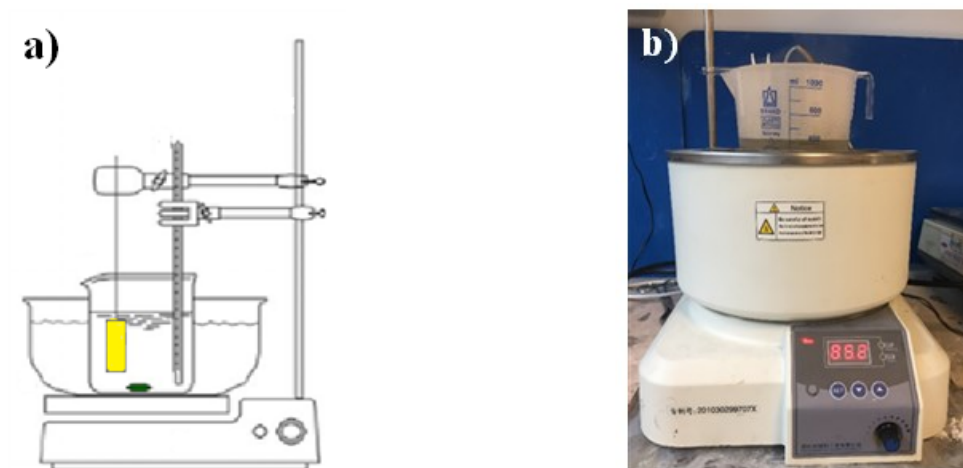

Figure 7.1. Scheme of the CP process (a) and experimental setup used (b).

Regarding the samples, a teflon clamping system was used in order to avoid contamination of the polishing solution and to preserve the system itself. Moreover, considering the need to evaluate the amount of mass dissolved per unit time and the surface roughness reduction only on one side of the samples, each one of them was hot mounted in an acid proof resin, after an accurate cleaning by means of ultrasonic bath in ethanol and drying. Fig. 7.2 illustrates, as an example, one of the hot mounted samples.
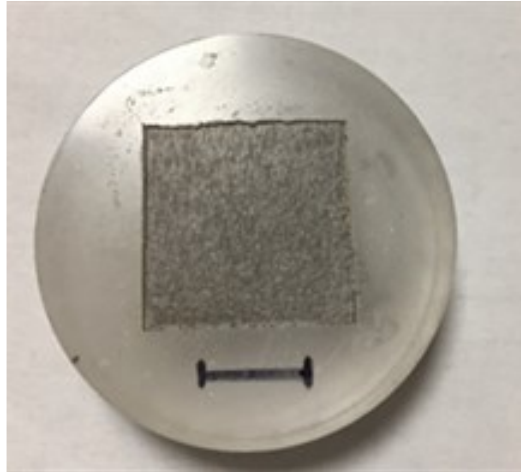

Figure 7.2. Example of a hot mounted sample for the CP experiments.

According to the theoretical background of CP for Aluminum alloys presented in Chapter 3, the process studied and tuned for the considered material was carried out in two fundamental stages:

i) Chemical Machining: this first stage is responsible for the major roughness reduction during the whole process. In principle, it is linked to the more widespread chemical machining process used to reduce the weight of Aluminum sheets for aeronautic use and to obtain holes on very thin sheets (0,035÷3 mm);

ii) Chemical Brightening: being the second and final stage, it accounts for the further reduction of roughness and an improvement of the surface symmetry and brilliance [176].

7.1.1. Chemical Machining

In order to justify the choice of the acid bath used for this stage, it is essential to point out some aspects related to the microstructure of the SLM processed AlSi10Mg alloy. To this aim, a preliminary analysis was carried out on a sample before the treatment by means of the observation of the microstructures along the building direction of the SLM process and its orthogonal direction, the latter identifying the scanning strategy adopted. The optical macrographs reported in Fig. 7.3 illustrates the microstructure for the considered directions respectively. In the first case, it is possible to appreciate the presence of the melt pools and their stratification due to the building of the sample, while the second one points out the linear scanning strategy adopted for the process, with a rotation of the scanning vectors for each layer.
Moreover, the SEM image reported in Fig. 7.4 describes the microstructure at the inside the single melt pool-scale: from this observation, the darker phase is represented by the Aluminum matrix, whose fine grains are surrounded by a brighter phase resulting from a grain boundaries segregation

process due to the high cooling rates involved in the SLM process. This microstructure is justified by the high Silicon content (12,5 % wt), that forms and eutectic phase with Aluminum at 570 °C [177]. The SEM micrographs show also the presence of spherical shape defects, typically ascribable to gas inclusions.
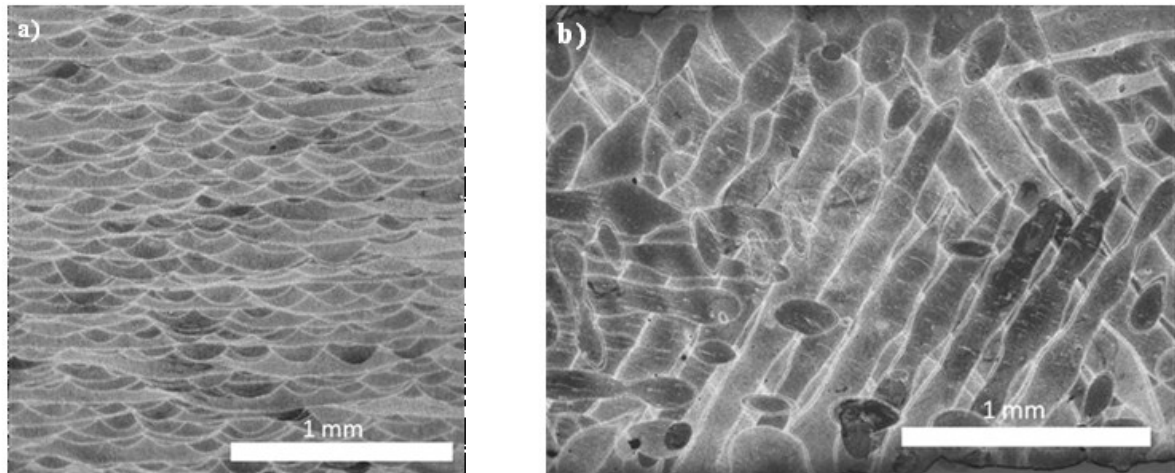

Figure 7.3. Optical macrographs of the SLM processed AlSi10Mg alloy, in parallel (a) and orthogonal (b) direction with respect to building direction (magnification 50x).
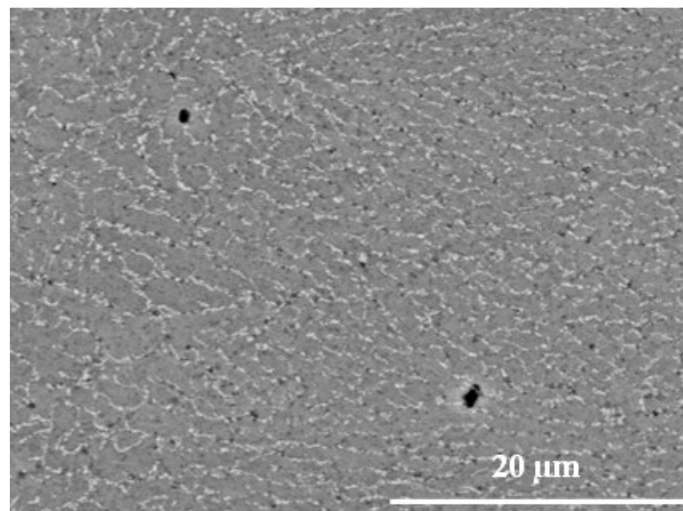

Figure 7.4. SEM image of the SLM processed AlSi10Mg alloy, indicating the microstructure inside a single melting pool. The darker phase represents the Aluminum fine grains, surrounded by a brighter Silicon-rich eutectic phase (magnification 4000x).

Considering all these aspects, the acid solution for the Chemical Machining stage was formulated with the aim to etch as more equally as possible all the alloy elements. After a series of preliminary tests and according to the literature [178], the established chemical bath was composed by 20 ml of Hydrofluoridric acid (HF), 50 ml of Nitric acid (HNO$_3$) and distilled water as balance for 1 l of solution. The presence of HF is due to the need to etch the Silicon, a non-metal that is resistant almost all the other acids, and the Aluminum at the same time. HNO$_3$, on the other hand, has the role to promote the formation of a thin oxide layer on the surface that, alternating with the etching performed by HF, could guarantee a more uniform smoothing

treatment [176]. More specifically, the mechanisms involved during the Chemical Machining step can be summarised as follows:

- $2Al + 6HNO_3 \rightarrow Al_2O_3 + 6NO_2 + 3H_2O$ (Aluminum passivation due to HNO₃)

- $Al_2O_3 + 6HF \rightarrow 2AlF_3 + 3H_2O$ (Aluminum dissolution due to HF)

- $Si + 4HNO_3 \rightarrow SiO_2 + 4NO_2 + 2H_2O$ (silicon passivation due to HNO₃)

- $SiO_2 + 4HF \rightarrow SiF_4 + 2H_2O$ (silicon dissolution due to HF)

To conduct the experiments, the samples were dipped into the solution already brought to the fixed temperature and stirring conditions. The positioning of the samples inside the acid bath was meant to consider the tangential flow of the solution as the preferential component acting on the surface, in order to maximize the dispersion of the dissolution products away from the sample.

Three values of the acid bath temperature and process time were investigated based on the considerations reported in literature and already discussed in Chapter 3 [145], i.e. 45 °C, 65 °C and 85 °C, with process times of 105 min for the first case and 75 mins for the other two respectively. Following the characterisation setup described in chapter 5, the effects of the Chemical Machining step were investigated every 15 min in terms of surface roughness parameters and weight loss, while morphology evolution investigations by means of SEM were considered only after the whole process.

Before any treatment step, the samples were accurately cleaned by brushing in a 4% vol aqueous solution of acetic acid — in order to ensure the removal of the insoluble dissolution products on the surfaces — and then cleaned in an ultrasonic bath of distilled water and dried.

7.1.2. Chemical Brightening

According to literature, in order to achieve the best results from the Chemical Brightening of Aluminum alloys it is necessary to perform the process at temperatures equal or higher to 85 °C [176]. Regarding the acid bath composition, it was formulated starting from the already commercially available Phosbrite® solution: reminding again the high Silicon content in the alloy used to manufacture the samples, the Phosbrite® was modified with the addition of HF. More specifically, the bath composition used was the following:

- 154 ml of Phosphoric acid (H₃PO₄);
- 34 ml of Sulphuric acid (H₂SO₄);
- 12 ml of HF;
- 12 ml of HNO₃;
- 0,106g of CuSO₄

As for the previous stage, three values of bath temperature were considered for the experimental campaign, i.e. 85°C, 90°C, 95 °C. The total treatment time was set to 7,5 min, according to considerations reported in literature about the need to perform the Chemical Brightening in short process times [176].

About the characterisation of the process results, analyses were carried out every 2,5 min of treatment. In order to evaluate the repeatability of the results, the process conditions that gave the best results were repeated two times for each of the two CP stages, but still considering the reduced acquired surface by means of confocal microscopy. Moreover, to compare the results as a function of the acquisition area, with respect to the general surface quantitative characterisation

established in this work, two further experiments were carried out for the best case related to the individual Chemical Machining and Brightening stages. It is worth to note that, in the latter case, the results were not investigated after each machining time-step, but just at the end of the treatment.

7.2. Results and Discussions

7.2.1. Chemical Machining

In Fig. 7.5a are reported the weight loss trends of the chemical machined samples, as a function of the bath temperature. Results show that, regardless of the specific condition, these trends are descending and linear but with a higher slope for the 85 °C bath temperature, which is comparable otherwise for the lower ones. This result, as widely discussed before, is expectable in relation to the accelerated process kinetics as the whole process temperature rises. The weight loss dependency on the bath temperature is quantitatively more visible in the histogram reported in Fig. 7.5b, that shows the percentage weight loss per unit area, calculated as the average from each time-step. For the 85 °C bath temperature condition, the weight loss is about the 0,82% and it decreases down to the 0,55% and 0,30% for the 65 °C and 45 °C conditions respectively.
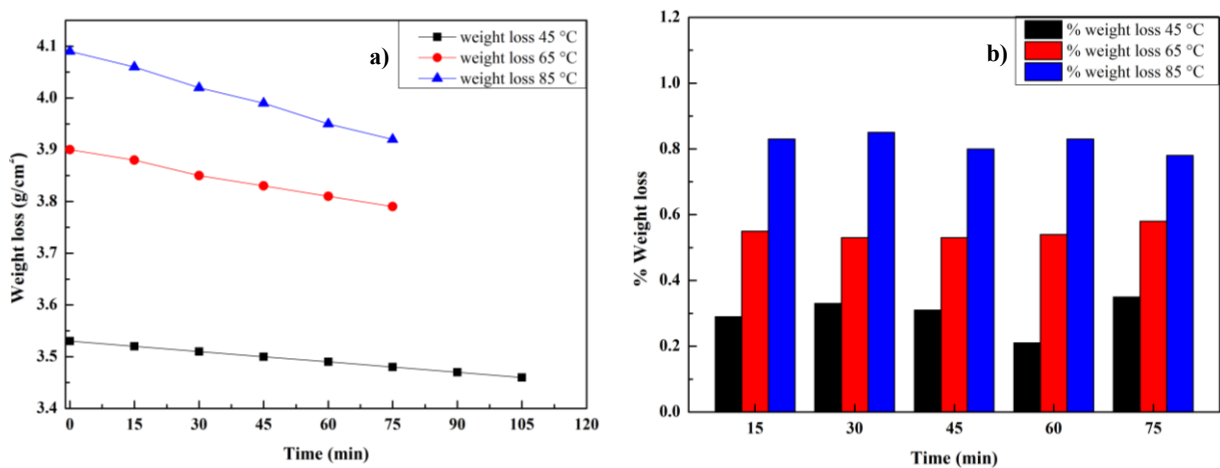

Figure 7.5. Weight loss trends for the chemical machined samples as a function of the bath temperature. Results are illustrated in terms of each process time-step (a) and in terms of percentage reduction at the end of the process (b).

As a better descriptor index of the process speed and efficiency, the results obtained were also evaluated in terms of *etch rate*, defined in Eq. 7.1, in which the m_i indicates the mass of the sample at the time t_i and A represents the real area exposed to the process. This parameter describes in a more reliable way the process trends since it takes into account the different areas of the samples given by the not closely controlled dimensional accuracy of the SLM process. Results in terms of etch rate are also reported quantitatively in Fig. 7.6 suggesting that, for a fixed process temperature, the etch rate remains practically constant all over the process times investigated, while an increase of the bath temperature, according to the observations on the weight loss, leads to an increase up to one order of magnitude. Therefore, the average etch rate increases from $6,2 \cdot 10^{-4}$ g/cm^{2}min for the 45 °C bath temperature, up to $1,5 \cdot 10^{-3}$ g/cm^{2}min and $2,2 \cdot 10^{-3}$ g/cm^{2}min for the 65/85 °C conditions respectively. This result is justified by the same observation done previously about the process kinetics but also with a physical issue related to the formation of bubbles close to the

immersed samples during the process carried out at 45 °C. This phenomenon clearly indicates that the lowest bath temperature value investigated is not sufficient to promote the stability of the reactions system discussed above, giving also rise to the large difference between the etch rate of this specific condition compared to the 65/85 °C temperature conditions, in which no formation of bubbles was observed.

$$Etch\ Rate = \frac{m_i - m_{i-1}}{A(t_i - t_{i-1})}\ \left(\frac{g}{cm^2 min}\right) \tag{7.1}$$
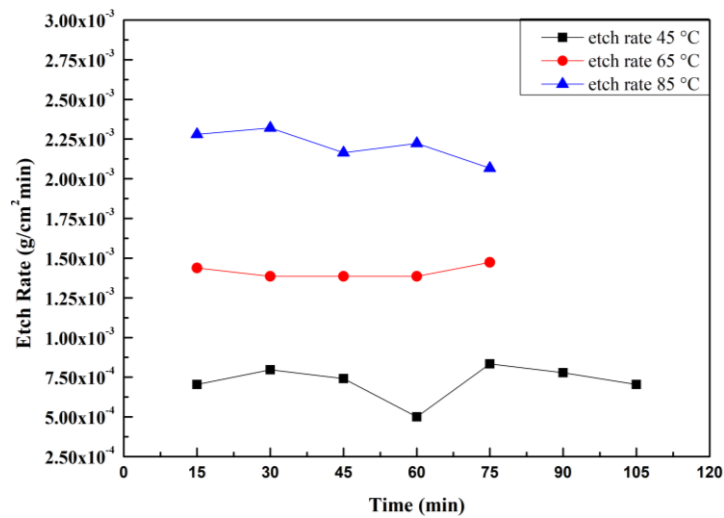

Figure 7.6. Etch rate trends for the chemical machined samples as a function of the bath temperature.

The considerations done for the results in terms of weight loss and etch rate find support also from the surface texture parameters evolution. It was already stated and observed in the previous Chapter that the surface roughness of the samples used present significant differences, expressed in a remarkable dispersion of values of all the considered surface parameters.

The results are illustrated in the graphs reported in Fig. 7.7a-e. As stated before, the first experimental outcome is that the best results achievable for this step were obtained for the 85 °C bath temperature condition. In this case, S_a decreases down to 10 μm at the end of the treatment, representing the best case compared to the 65 °C and 45 °C cases, for which the final S_a are 15 μm and approximately unchanged, respectively. Similar considerations could be done for S_z, decreasing of about 100 μm, but in this case both for the 65 °C and 85 °C bath temperatures.

It is worth to note that the best finishing effect was observed for the first 45 min of treatment: this result is most likely due to the high initial roughness of the samples, promoting therefore the different anodic layer stability phenomenon discussed in Chapter 3.

Different considerations needs to be done for the S_{sk} parameter evolution, whose behavior is clearly different with respect to the different bath temperatures and the initial values. For the lowest bath temperature condition, the trend indicates a slight variation with process time, supporting the observations done before about the limited improvement of the surface in this process condition. For a 65 °C bath temperature, the response changes and indicates a preferential smoothing effect on the peaks side rather than the valleys, since S_{sk} tends to decrease further of about 0,2 points from the starting value of -0,3. The best case is observed again for the 85 °C bath temperature condition, since the final S_{sk} value approaches to -0.1 with a starting value of -0.8: this result

clearly indicates that, for the highest bath temperatures, Chemical Machining improves considerably the symmetry of the surface. Similarly, it is possible to discuss the trends observed for the S_{ku} parameter: the best process condition is represented again by the highest bath temperature, with a decrease of kurtosis down to approximately 2,9 from an initial value of 4,3. Viceversa, the 45 °C/65 °C bath temperature conditions seems not to contribute significantly to the reduction of the sharpness of the peaks.

Finally, as observed from the results obtained with the FBM treatment, P_{dq} is confirmed again as one of the most sensitive roughness parameters that further supports the primary effect of the bath temperature on the process efficiency. The greatest reduction was observed for the 85 °C bath temperature condition, with a minimum value of 10°, whilst the 45/65 °C bath temperature conditions the slope was reduced down to 15°. As observed for S_a and S_z, the major effects in terms of finishing were observed within the first 45 min of the process.

For sake of clarity, in Tables 7.1 – 7.3 are reported all the values measured for the different surface roughness parameters for each chemical machining step and bath temperatures, while Fig. 7.8a-d illustrates the comparison of the 3D surfaces acquired before and at the end of the treatments as a function of the bath temperature.
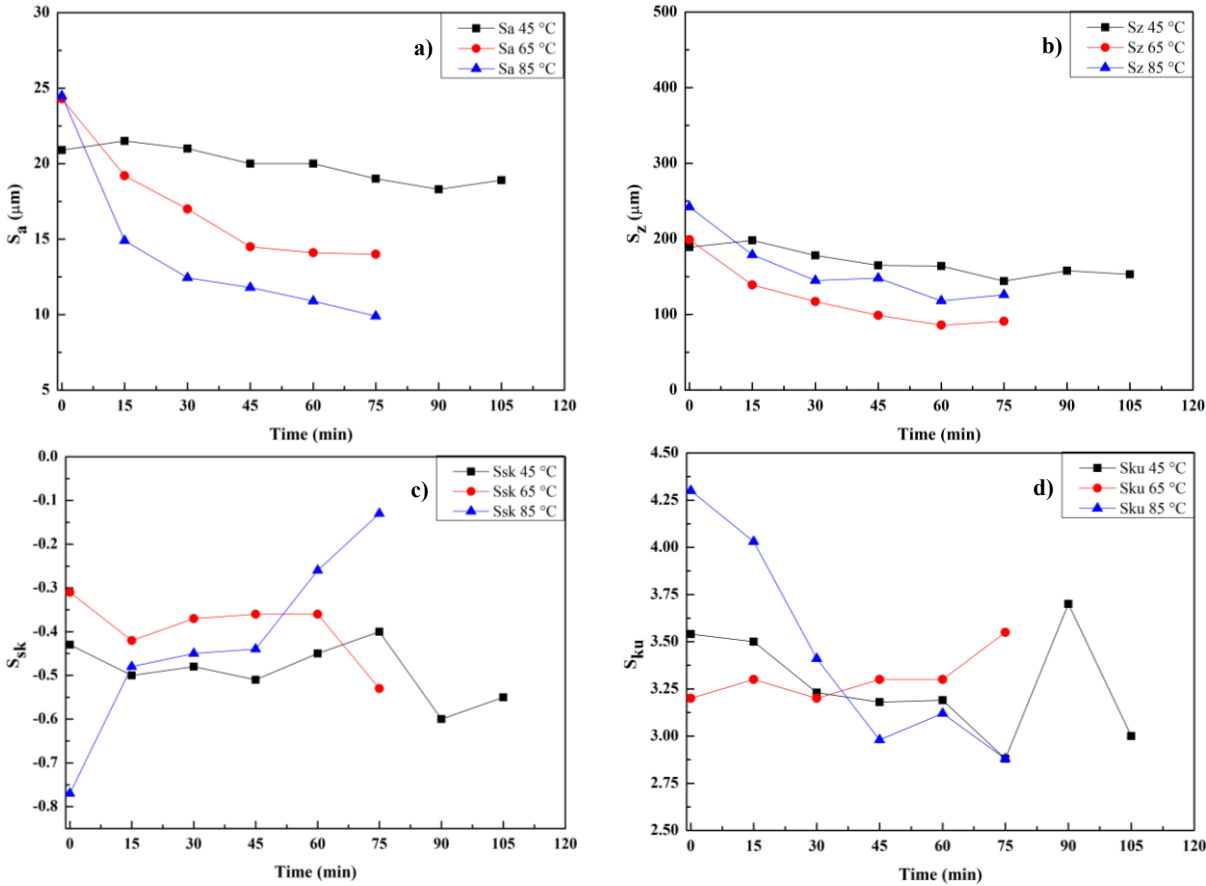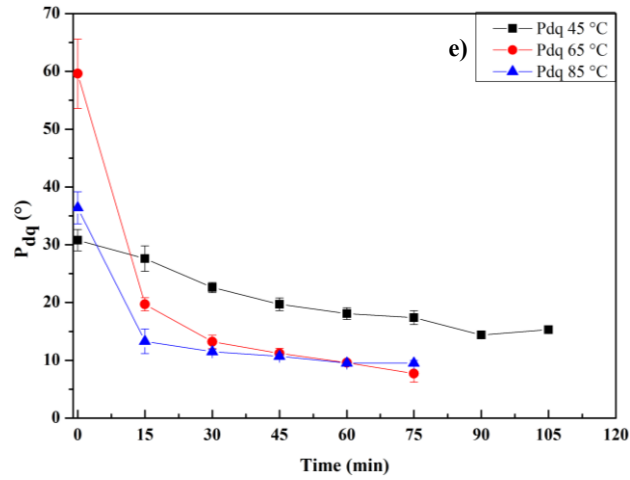
Figure 7.7. Time evolution of the investigated surface roughness parameters for the chemical machining step, as a function of the bath temperature. (a) Sa, (b) Sz, (c) Ssk, (d) Sku, (e) Pdq.

Table 7.1. Surface roughness parameters before and after Chemical Machining (bath temperature: 45 °C).

Time (min)	S_a (µm)	S_z (µm)	S_{sk}	S_{ku}	P_{dq} avg (°)	P_{dq} st.dev (±σ) (°)
0	21.0	189	-0.43	3.54	32.9	1.8
15	21.6	198	-0.50	3.51	25.1	2.2
30	21.1	178	-0.49	3.23	21.8	0.9
45	20.0	165	-0.52	3.18	19.7	1.1
60	20.0	165	-0.46	3.20	18.2	1.0
75	19.0	145	-0.40	2.88	16.2	1.2
90	18.3	158	-0.63	3.71	14.9	0.7
105	18.9	153	-0.55	3.04	15.7	0.6

Table 7.2. Surface roughness parameters before and after Chemical Machining (bath temperature: 65 °C).

Time (min)	S_a (µm)	S_z (µm)	S_{sk}	S_{ku}	P_{dq} avg (°)	P_{dq} st.dev (±σ) (°)
0	24.3	242	-0.31	3.21	52.7	6.0
15	19.2	179	-0.42	3.31	18.4	1.2
30	17.0	145	-0.37	3.19	13.2	1.2
45	14.5	148	-0.37	3.33	10.4	0.9
60	14.1	118	-0.37	3.29	9.3	0.4
75	14.0	126	-0.54	3.54	9.0	1.5

Table 7.3. Surface roughness parameters before and after Chemical Machining (bath temperature: 85 °C).

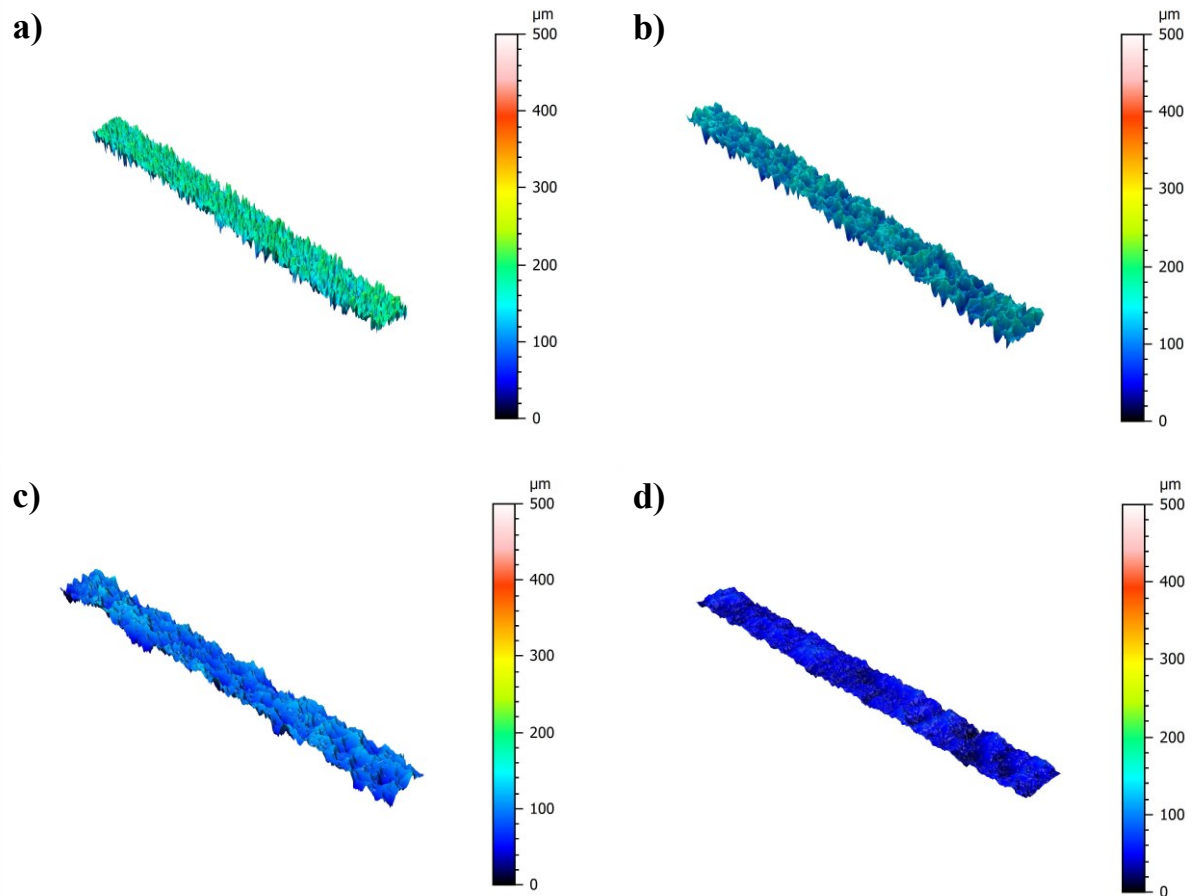| Time (min)	S_a (µm)	S_z (µm)	S_{sk}	S_{ku}	P_{dq} avg (°)	P_{dq} st.dev (±σ) (°)
0	24.5	199	-0.78	4.30	33.3	2.8
15	15.0	139	-0.49	4.04	13.8	2.1
30	12.4	117	-0.45	3.42	11.2	0.4
45	11.2	100	-0.44	2.99	10.4	0.4
60	10.9	87	-0.27	3.13	9.4	0.2
75	10.0	91	-0.13	2.89	9.3	0.5

Figure 7.8. Comparison of the 3D surfaces before Chemical Machining (a) and after chemical machining at 45 °C (b), 65 °C (c) and 85 °C (d).

Before the analysis of the effects of the second process stage, as discussed before, the repeatability of the Chemical Machining stage was investigated. Considering first the same 8 x 2 mm^2 areas acquired for the previous experiments, Table 7.4 reports the values of the surface roughness parameters measured. Based on the results, it can be clearly seen that the process possesses a satisfactory degree of repeatability, even considering the different initial surface status of the samples, showing comparable surface improvements as measured for the first experiment.

Table 7.4. Surface roughness parameters before and after each repeatability test for the best condition of Chemical Machining (bath temperature: 85 °C).

Experiment	Time (min)	S_a (µm)	S_z (µm)	S_{sk}	S_{ku}	P_{dq} avg (°)	P_{dq} st.dev (±σ) (°)
1	0	19.1	199	-0.44	4.30	33.3	2.8
	75	9.95	91.2	-0.13	2.89	9.3	0.5
2	0	21	185	-0.21	3.41	36.4	2.6
	75	9.22	78.1	-0.08	2.86	8.75	0.2
3	0	21.1	206	-0.23	3.38	31.9	2.5
	75	8.98	91.5	-0.13	3.01	9.68	0.3

As introduced in the previous section of this Chapter, the process repeatability was also evaluated with respect to the predefined acquisition area of 8 x 8 mm^2. This step was possible considering that there was no need to evaluate the surface evolution for each time-step, but in this case the results were quantified only before and after the whole treatment in the best process condition. Fig. 7.9 illustrates, as an example, the 3D surfaces acquired before and after Chemical Machining for one of the two experiments. Moreover, the full data sets measured for two experiments, in terms of surface roughness parameters values, weight loss and etch rate, are reported in Tables 7.5-7.6, in comparison with the results obtained from the first experiment.

Apart from the weight loss and etch rates that shows a very good agreement, results clearly indicates a dependency of some texture parameters values from the dimensions of the acquired area. More specifically, S_z and S_{sk} seem to be not in agreement with the previous measures. However, considering the bigger area acquired, the higher values of S_z and the more negative values of S_{sk} at the end of the treatment suggests the presence of a residual texture, representing a fingerprint of the Chemical Machining process. In fact, the relative motion of the stirred acid solution against the immersed surface could promote a not homogeneous smoothing condition, leaving some traces related to the impinging flux on the peaks and valleys of the original surface texture. As a result, the maximum distance between peaks and valleys, as well as their symmetry, could be altered and more easily detectable if a greater portion of the treated surface is observed. Moreover, the final S_a, S_{ku} and P_{dq} values shows again a good agreement with the previous experiments. All these results could be well supported considering the observation of the pictures of the actual samples, reported again before and after the best Chemical Machining condition in Fig 7.10, clearly showing that the first step of the chemical polishing process leaves a notable fingerprint on the treated sample.
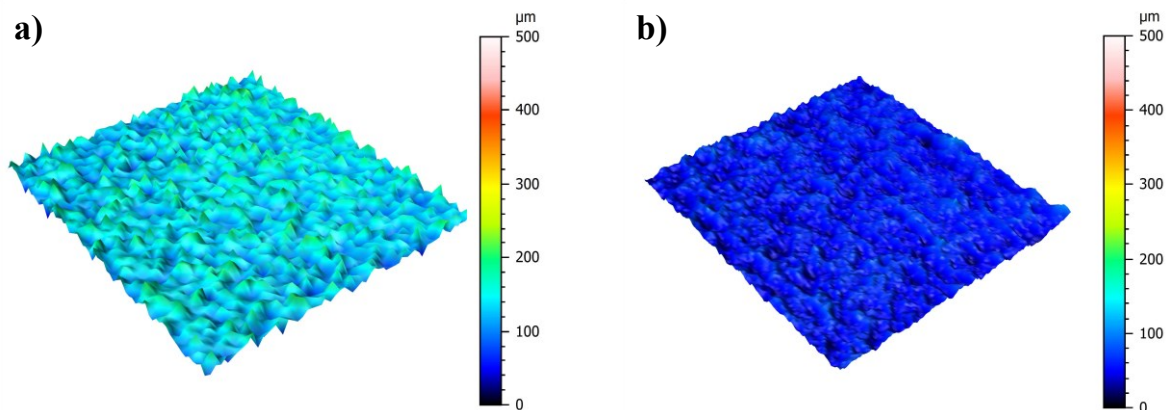

Figure 7.9. Comparison between the 3D surfaces acquired before (a) and after Chemical Machining at 85 °C (b), considering an 8 x 8 mm^2 area used for the repeatability tests.

Table 7.5. Surface roughness parameters values of the repeatability experiments for the Chemical Machining, as a function of an 8 x 8 mm^2 acquisition area.

Experiment	Time (min)	S$_a$ (μm)	S$_z$ (μm)	S$_{sk}$	S$_{ku}$	P$_{dq}$ avg (°)	P$_{dq}$ st.dev (±σ) (°)
1 (8 x 2 mm^2)	0	19.1	199	-0.44	4.30	33.3	2.8
	75	9.95	91.2	-0.13	2.89	9.3	0.5
2 (8 x 8 mm^2)	0	23	230	0.25	3.4	45	3.5
	75	9.2	135	-0.25	3.1	8.4	2.3
3 (8 x 8 mm^2)	0	21.3	228	0.12	3.6	41	6.6
	75	7.5	120	-0.34	3.2	6	1.5

Table 7.6. Weight loss and etch rate values of the repeatability experiments for Chemical Machining, as a function of an 8 x 8 mm^2 acquisition area.

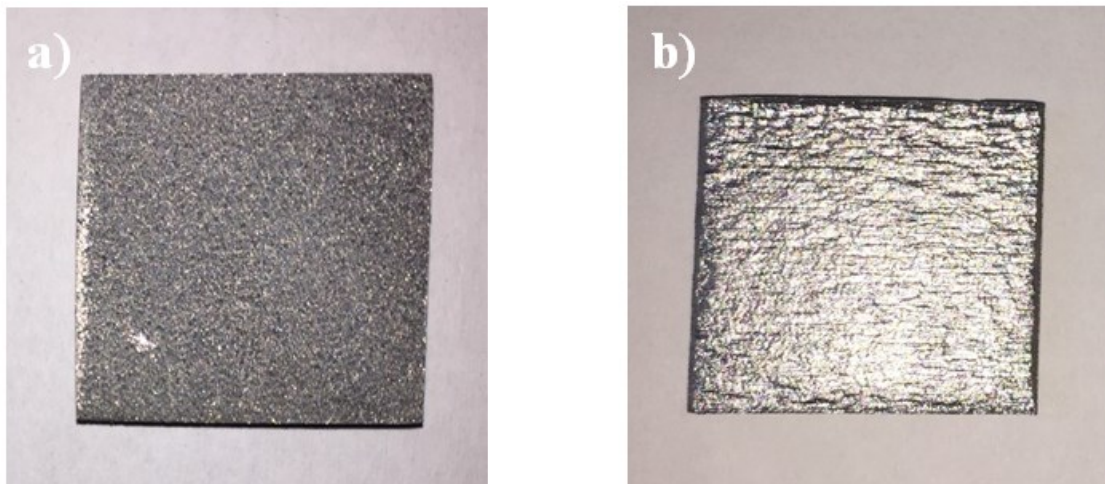| Experiment	Time (min)	Weight loss (%)	Etch rate ($\frac{g}{cm^2 \cdot min}$)
1 (8 x 2 mm^2)	0	0.82	2.21·10^{-3}
	75		
2 (8 x 8 mm^2)	0	0.96	1.92·10^{-3}
	75		
3 (8 x 8 mm^2)	0	0.95	1.83·10^{-3}
	75		

Figure 7.10. Images of a sample before (a) and after (b) Chemical Machining (85 °C bath temperature).

Finally, from a more detailed observation provided by means of SEM and reported in Fig. 7.11, it can be also noticed that after the chemical machining process the resulting surface is characterised by the emerging of melt pools. The latter, before the treatment, were laying underneath a sintered powders layer, whose presence is due to the balling effect, as described in Chapter 2. This result clarifies also the need to employ the Brightening stage, as also well stated by *Jacquet* [145]. Moreover, the presence of a residual texture, represented on a micro scale by a series of melt pools, justifies the results obtained in terms of final surface roughness and the different values obtained from the repeatability experiments as a function of the acquired area.
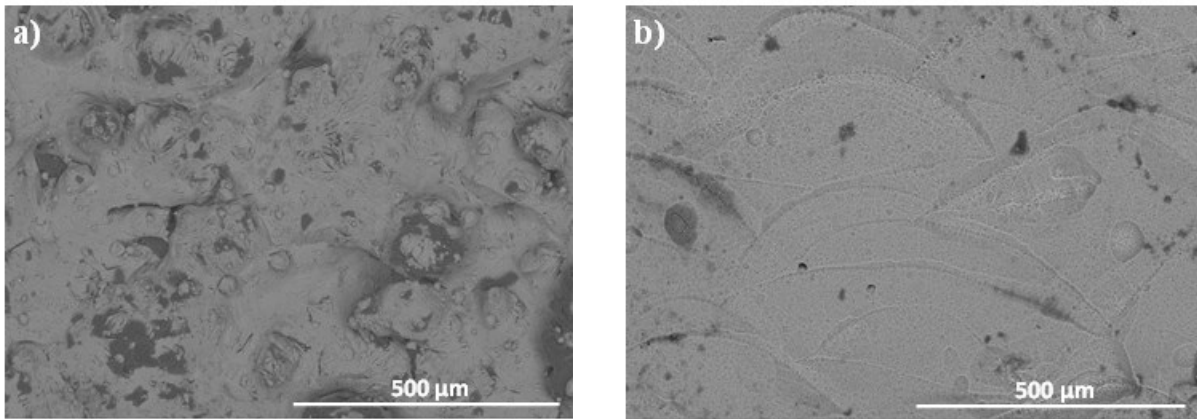
Figure 7.11. SEM Images of a sample before (a) and after (b) Chemical Machining (85 °C bath temperature).

7.2.2. Chemical Brightening

The results obtained for this stage, carried out on the samples that were already chemical machined with a 85 °C bath temperature, are shown qualitatively as 3D surfaces for the 95 °C bath temperature condition in Fig. 7.12 (in this case, 3D surfaces for the 85 °C and 90 °C are not reported, due to inappreciable differences). Quantitative results are reported in terms of time evolution of the surface texture parameters in Fig 7.13a-e and actual values in Tables 7.7-7.9, as a function of the acid bath temperature. Like for the previous case, results were investigated considering first a 8 x 2 mm^2 acquired area by means of confocal microscopy and, subsequently, repeatability was also evaluated considering an 8 x 8 mm^2 area.

It is worth to note that, given the very slow kinetics involved, measures of weight loss and etch rate were not carried out for this process step. By the observation of the collected data, it can be clearly seen that the brightening is not particularly effective for a bath temperature of 85 °C, since the quantified surface improvements are very slight and characterized even by a worsening after 5 min of treatment. Similar considerations are valid for the treatment step carried out at 90 °C. The best result is indeed achieved for the 95 °C bath temperature condition, in which the surface roughness improvements becomes very appreciable since the first 2,5 minutes of treatment. More specifically, the latter condition returns a final S_a value of 6,8 µm against the 10 µm reached at the end of the chemical machining step, as well as a greatly reduced S_z value from 90 µm to 52 µm. Furthermore, S_{ku} and P_{dq} values are greatly reduced of about one point and 6.6° respectively, with final values of 2.6 and 3.3. The symmetry of the surface, in agreement with the other parameters, was improved reaching a final value practically equal to 0, indicating a very high symmetry degree. From a general point of view, the obtained results imply a strong selective behavior of the acid bath at the highest temperature, with respect to the residual asperities of the surface rather than the valleys, the former due to the previous process step. This mechanism, described in literature [179] and reported schematically in Fig. 7.14, assumes that the precipitation of corrosion products in the valleys, that contributes for a further viscosity increase of the solution, determines lower mass transfer phenomena from the surface to the solution itself. These aspects, in addition to the higher anodic film stability in the valleys discussed previously, implies that the smoothing effect of the treatment is higher on the peaks.
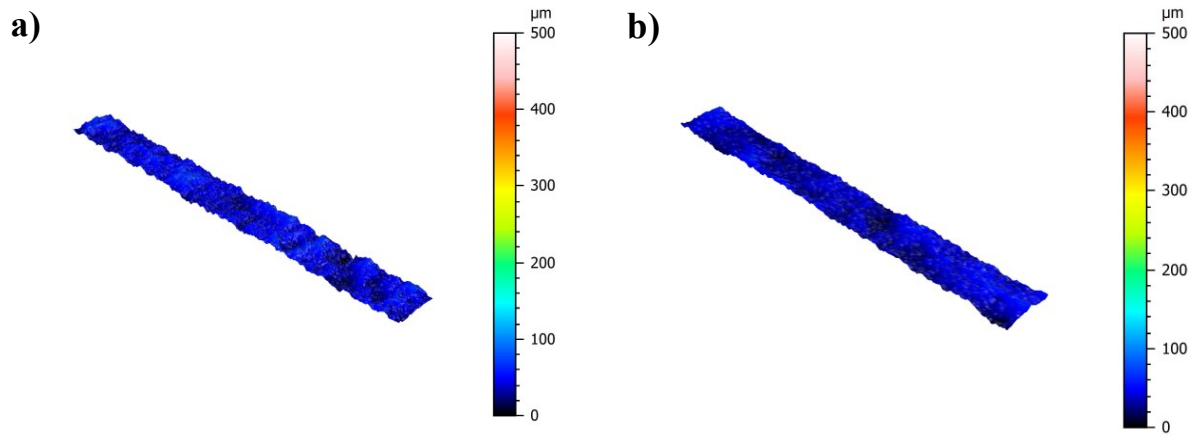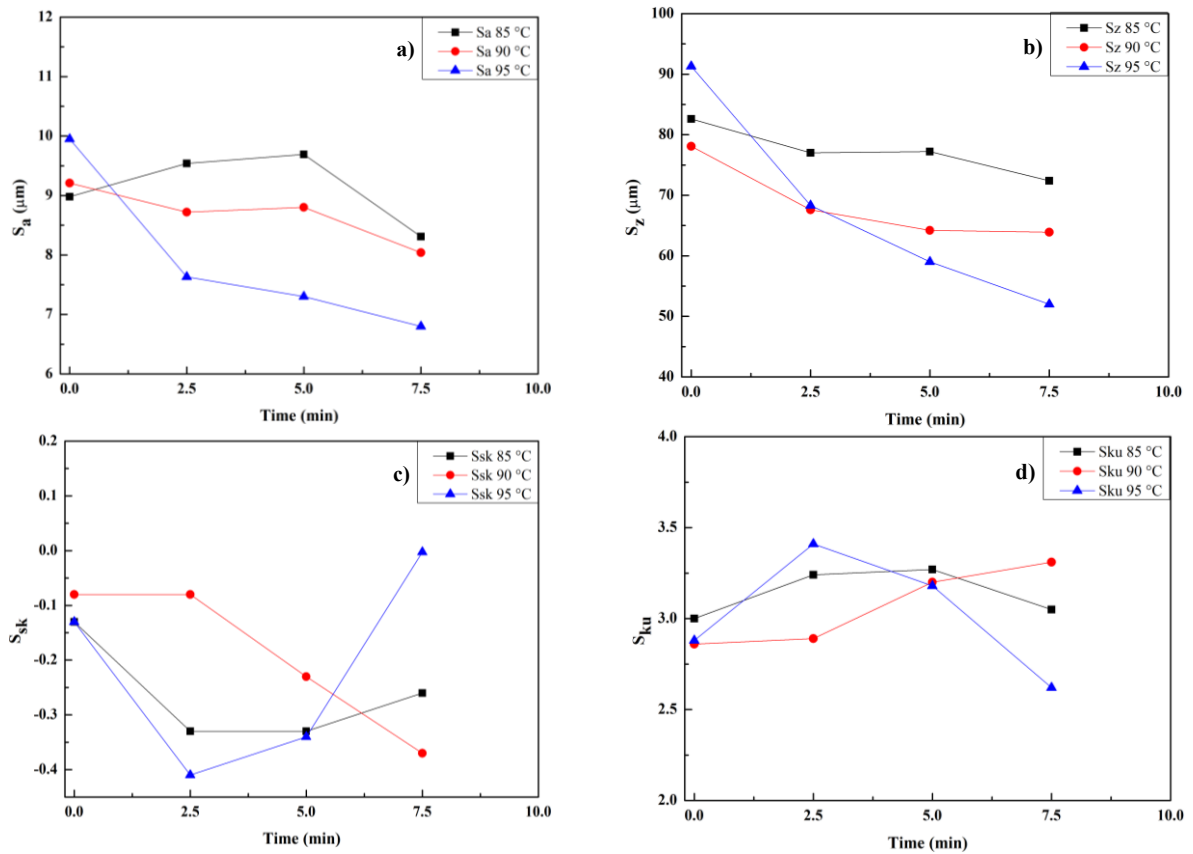
Figure 7.12. Comparison between the 3D surfaces acquired before (a) and after the chemical brightening step at 95 °C (b).
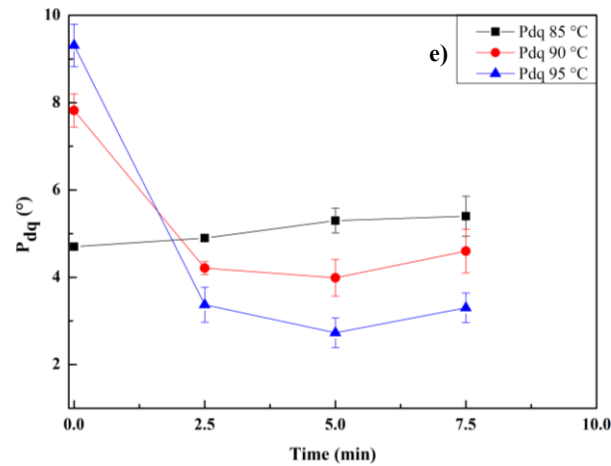
Figure 7.13. Time evolution of the investigated surface roughness parameters for the Chemical Brightening stage, as a function of the bath temperature. (a) Sa, (b) Sz, (c) Ssk, (d) Sku, (e) Pdq.

Table 7.7. Surface roughness parameters before and after Chemical Brightening (bath temperature: 85 °C). Time 0 refers to the sample right after the Chemical Machining.

Time (min)	S_a (µm)	S_z (µm)	S_{sk}	S_{ku}	P_{dq} avg (°)	P_{dq} st.dev (±σ) (°)
0	8.99	82.7	-0.13	3.01	4.7	0.05
2.5	9.55	77.1	-0.33	3.24	4.9	0.04
5	9.69	77.2	-0.33	3.27	5.3	0.28
7.5	8.32	72.4	-0.27	3.05	5.4	0.46

Table 7.8. Surface roughness parameters before and after Chemical Brightening (bath temperature: 90 °C). Time 0 refers to the sample right after the Chemical Machining.

Time (min)	S_a (µm)	S_z (µm)	S_{sk}	S_{ku}	P_{dq} avg (°)	P_{dq} st.dev (±σ) (°)
0	9.21	78.1	-0.08	2.86	7.8	0.38
2.5	8.72	67.6	-0.08	2.90	4.2	0.16
5	8.81	64.2	-0.23	3.20	4.0	0.42
7.5	8.04	63.9	-0.37	3.31	4.6	0.51

Table 7.9. Surface roughness parameters before and after Chemical Brightening (bath temperature: 95 °C). Time 0 refers to the sample right after the Chemical Machining.

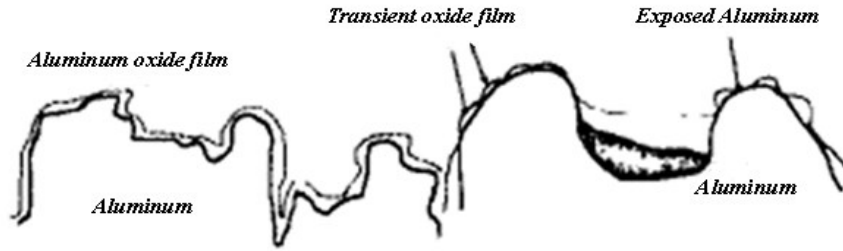| Time (min)	S_a (µm)	S_z (µm)	S_{sk}	S_{ku}	P_{dq} avg (°)	P_{dq} st.dev (±σ) (°)
0	9.96	91.3	-0.13	2.89	9.3	0.50
2.5	7.64	68.3	-0.41	3.41	3.4	0.41
5	7.30	59.1	-0.34	3.18	2.7	0.35
7.5	6.80	52.0	0.00	2.62	3.3	0.35

Figure 7.14. Schematization of selective smoothing effect of the peaks occurring in the chemical brightening process of Aluminum [179].

Considering the best brightening condition, the obtained results are also in good agreement with the ones observed for the repeatability tests considering first the 8 x 2 mm^2 acquisition area, whose results are reported in Table 7.10 and, as for the previous stage, considering also an 8 x 8 mm^2 acquisition area. For the latter case, with the aim to compare the results obtained for the best chemical brightening experiment, the actual surface texture parameters are compared and reported in Table 7.11, while Fig. 7.16 shows, as an example, the surface improvement before and after the Chemical Brightening step for one of the two repeatability experiments. Similarly to the previous process step, it can be assumed that also the chemical brightening process presents a satisfactory degree of stability and repeatability, besides the further surface improvement compared to the chemical machined surface.

Table 7.10. Surface roughness parameters before and after each repeatability test for the best condition of Chemical Brightening (bath temperature: 95 °C). Time 0 refers to the previously chemical machined samples.

Experiment	Time (min)	S_a (μm)	S_z (μm)	S_{sk}	S_{ku}	P_{dq} avg (°)	P_{dq} st.dev ($\pm\sigma$) (°)
1	0	9.95	91.2	-0.13	2.89	9.3	0.5
	7.5	6.80	52.0	0.00	2.62	3.3	0.35
2	0	9.22	78.1	-0.08	2.86	8.75	0.2
	7.5	7.3	68	-0.06	2.91	4.0	0.5
3	0	8.98	91.5	-0.13	3.01	9.68	0.3
	7.5	6.7	73	-0.07	2.87	3.9	1.1

The surface improvements achieved after the chemical brightening finds confirm also from the results obtained by means of SEM analysis. Fig. 7.17 shows the comparison, on a higher magnification, between the same sample after each CP stage. Images clearly shows that the brightening step contributed to remove the residual asperities from the previous stage, as well as to remove any trace of the naturally present melt pools. Consequently, the resulting surface appears more flat and homogeneous. On a macroscale, same considerations can be drawn from the visual inspection of an actual sample before and after Chemical Brightening, as illustrated in Fig. 7.18, that shows a more smooth and brilliant surface.
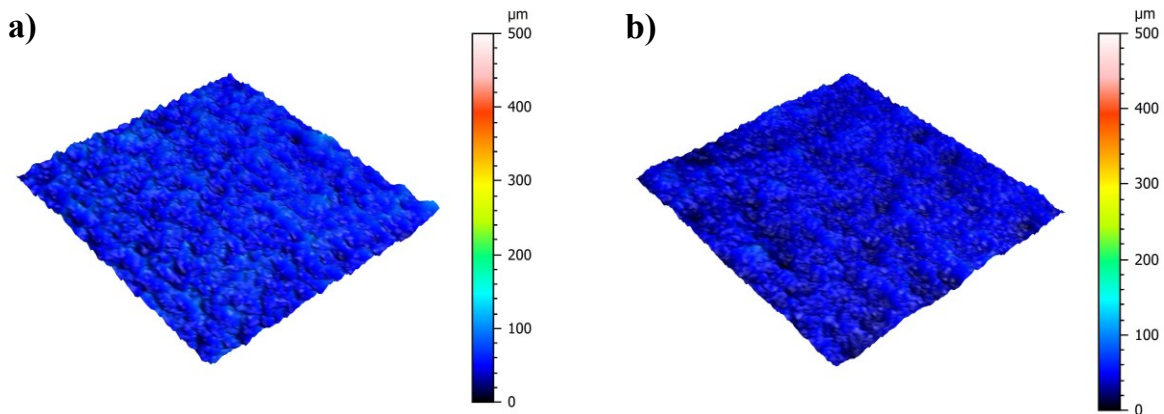
Figure 7.15. Comparison between the 3D surfaces acquired before (a) and after a repeatability experiment of the chemical brightening step at 95 °C (b), considering an 8 x 8 mm^2 area.

Table 7.11. Surface roughness parameters values of the repeatability experiments for the best Chemical Brightening condition (bath temperature 95 °C), as a function of an 8 x 8 mm^2 acquisition area (time 0 refers to the previously chemical machined samples).

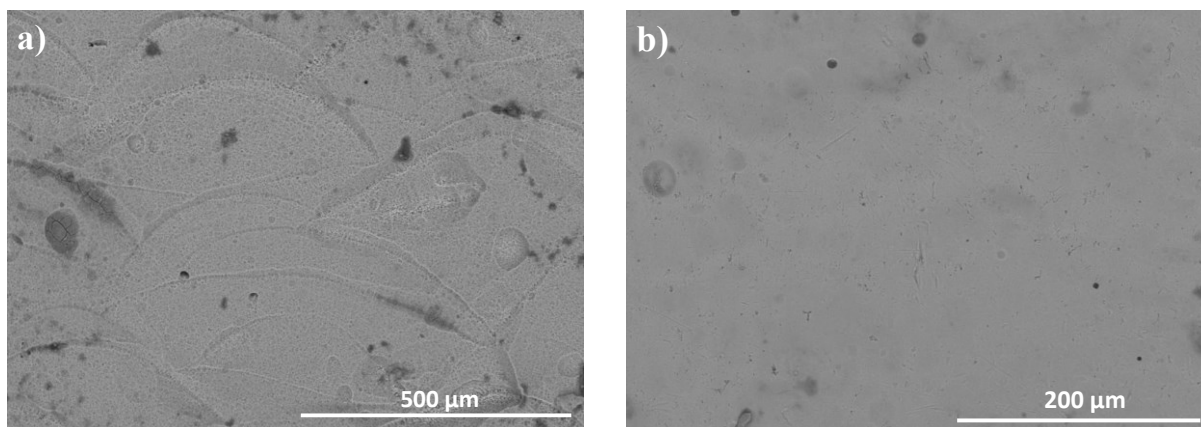| Experiment	Time (min)	S_a (µm)	S_z (µm)	S_{sk}	S_{ku}	P_{dq} avg (°)	P_{dq} st.dev (±σ) (°)
1 (8 x 2 mm^2)	0	9.95	91.2	-0.13	2.89	9.3	0.5
	7,5	6.80	52.0	0.00	2.62	3.3	0.35
2 (8 x 8 mm^2)	0	9.2	135	-0.25	3.4	8.4	2.3
	7,5	7.7	63	-0.08	2.82	4.2	0.6
3 (8 x 8 mm^2)	0	7.5	120	-0.34	3.2	6	1.5
	7,5	6.7	57	-0.02	2.75	3.2	0.2

Figure 7.16. SEM images comparison of a sample treated with: Chemical Machining at 85 °C (a - magnification 400x) and Chemical Machining at 85 °C plus Chemical Brightening at 95 °C (b - magnification 500x).
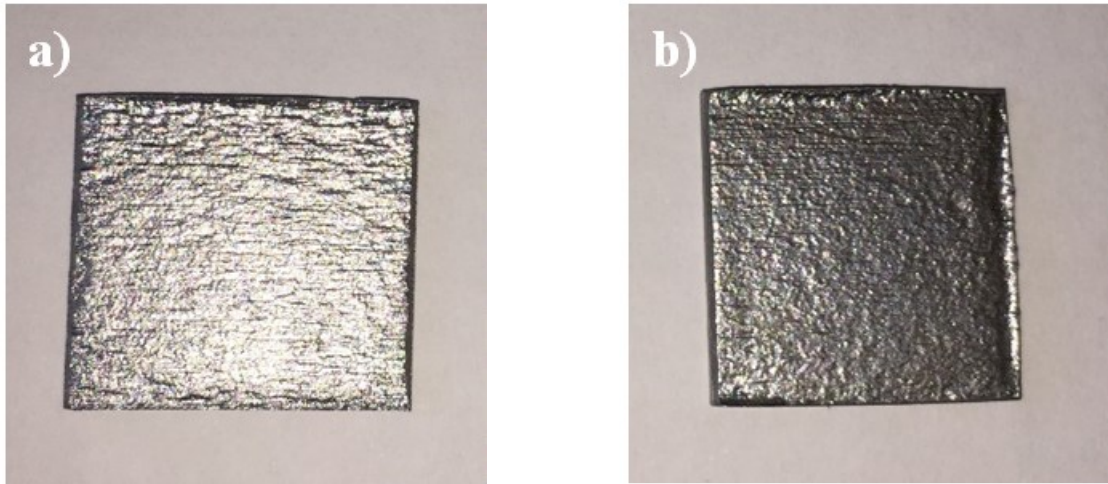
Figure 7.17. Images of a sample before (a) and after (b) the chemical Brightening (95 °C bath temperature).

Finally, as specified in chapter 5, EDS analysis was carried out on the samples before and after the whole CP process in order to evaluate the influence on the resulting chemical composition of the surface. In Table 7.12 is reported the comparison between the chemical compositions of a sample in the above mentioned conditions. Results suggests that the investigated treatments does not alter significantly the original alloy composition on the surface, indicating therefore that the whole process performed also the smoothing effect in very uniform conditions, without appreciable de-alloying effects.

Table 7.12. Comparison of the surface chemical composition, carried out by means of EDS analysis, for a sample before and after CP.

Element [% wt]	Before treatment	After chemical machining + chemical brightening
Aluminum	86.503	88.229
Silicon	12.626	11.200
Magnesium	0.871	0.570

7.3. Conclusions

Based on the experimental results and the investigated process parameters, the following conclusions can be drawn for the CP process applied to AlSi10Mg alloy samples made by SLM technology:

- As observed with the experimental results obtained for the FBM treatment, the initial surface status of the used samples is quite different in terms of the investigated surface texture parameters. This aspect implies a less precise knowledge of the exact surface reference for the subsequent treatments;

- In relation to the investigated process conditions, the best CP results are achievable at high bath temperatures, as proved for both the Chemical Machining and Brightening stages with the best cases of 85 °C and 95 °C respectively. This result is mainly due to the accelerated kinetics of the dissolution/passivation reactions occurring on the immersed surface. As

observed by the confocal microscopy analyses for the best processes conditions, the Chemical Machining process is able to reduce S_a by the 60% and S_z by the 46%. These parameters can be further decreased of approx. 30% and 60% respectively considering also the Chemical Brightening process;

- The symmetry and brilliance of the surface is quite improved, as observed by the S_{sk} values tending to zero and the significantly reduced values of P_{dq} and S_{ku};

- The greatest surface improvements, for both the CP stages, were achieved within the first 45 min and 2,5 min respectively. This result is most probably due to the initial high surface roughness, determining the higher anodic film stability in the valleys that promotes a greater effect of the Chemical Machining step, as well as a higher solution viscosity that implies a preferential smoothing effect of the peaks during the Chemical Brightening step. The combination of these factors, according also to literature, enhances the major roughness reduction during the first machining step and the improvement of surface symmetry and brilliance during the second.

- As observed by means of SEM-EDS analyses, the surface improvements given by the CP process are in agreement with the quantitative analysis carried out by means of confocal microscopy. Moreover, the Chemical Machining stage is responsible for the elimination of the sintered powders layer on the surface, letting the underlaying melt pools to emerge, whose trace is also completely removed by Chemical Brightening.

- As also proved by SEM-EDS analysis, in terms of chemical composition of the surface, the CP does not induce appreciable changes, not promoting therefore de-alloying effects and performing a sufficiently homogeneous smoothing effect on the material, even considering the different phases present in the considered alloy.

- For both the process step investigated, the obtained results proved that the CP treatment is quite stable and repeatable, even considering the appreciable differences of the initial surface status of the samples mentioned above. The repeatability of the results was proved for the 8 x 2 mm^2 acquired area — considered in first instance in order to avoid the degradation of the surface during the intermediate process time-steps in the hot mounted condition — as well as for the 8 x 8 mm^2 acquisition area used for the general characterization method used in this work;

- Finally, it is worth to mention that, at the best knowledge of the author, the studied CP process applied to AlSi10Mg parts made through SLM represents a fully novel work, considering the absence of available data in literature for the specific case here investigated.

8. CO₂ Laser surface re-melting

According to the theoretical background reported in Chapter 3, a detailed discussion of the experimental setup and campaign for the CO₂ laser re-melting is reported in this Chapter. Moreover, a detailed explanation of the experimental approach is provided, as well as a critical analysis of the obtained results and the main experimental outcomes.

8.1. Experimental apparatus

The CO_2 LSR experiments were carried out by means of the Rofin DC-012 CO_2 laser reported in Fig. 8.1. The main technical specifications of the laser are reported in Table 8.1 [180]. To carry out the experiments, the samples were clamped on a steel vice and supported beneath by an Aluminum bar, in order to avoid distortions of the sample subjected to the heat input. The latter was also used as a heat sink, allowing the excess heat dispersion of the sample.

Figure 8.1. Rofin DC-015 CO_2 laser.

Table 8.1. Rofin DC-015 laser characteristics and stage-related parameters [180].

Source wavelength	10.6 μm
Laser beam quality (M²)	1.05
Max. power	1.5 kW
Beam focus	200 μm
Laser mode	Continuous/pulsed wave
x-y stage speed	0÷5000 mm/min
Shielding gas	Argon

In relation to the process setup, the focus position was initially considered at the top surface of the sample. Therefore, considering the texture of the latter, the focus was positioned right over the peaks of the surface. Moreover, the scanning strategy adopted to re-melt the samples surface was linear and bi-directional. Fig. 8.2 illustrates the scanning vectors applied to the surface of a typical sample, as well as the considered width of the re-melted area, i.e. 10 mm. The latter was considered

in order to acquire the defined area by means of confocal microscopy, i.e. 8 x 8 mm^2, as already discussed in Chapter 5.
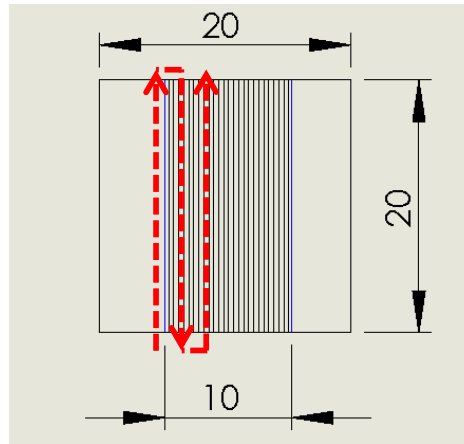

Figure 8.2. Schematic illustration of a sample, the LSR scanning strategy and the re-melting width.

8.2. Experimental campaign

Compared to the previously discussed surface treatments, LSR represents a process with a higher maturity level. More specifically, the critical process parameters that affects significantly the LSR efficiency are already identified. In addition to the more ease of changing the process parameters (no material or machine constructive features changes are needed), a more methodological experimental approach was feasible in this case.

With this premise, the experimental campaign can be synthesised in the following points, assumed that the main process parameters to investigate were the laser power, the beam scanning speed and the overlap between the single laser tracks (OV%):

- **Preliminary tests:** this step was carried out in order to establish the influence of the single process parameter value adopted. Moreover, another process parameter considered at this step was the shielding gas pressure, since it determines the turbulence of material in the molten state and, consequently, an induced surface roughness upon solidification. The outcome of these experiments, not reported in this work, allowed to define the factors and their respective levels for the next experimental step;

- **Design of Experiments (DoE) tests:** The determined process parameters sets, according to a 3^3 full factorial DoE, is reported in Table 8.2, while Table 8.3 reports the complete list of the carried out tests. Other parameters considered in the previous step, such as shielding gas pressure, were fixed to the optimal values investigated, whereas the laser focus was initially positioned on the peaks of the surface, as stated before.

  Concerning the relationship between the input parameters and the experimental outputs — the latter represented by the surface texture parameters discussed in Chapter 5 — the process effects were analysed by means of the software *Design Expert® 11*. In first instance, the collected data were analysed using the *Response Surface Method (RSM)* [181] that allows to observe multiple input-output correlations, providing therefore a more comprehensive and quick view of the process effects. Moreover, given the surface generation by means of a fitting model, it gives also the possibility to find experimental

conditions that provides better results for a given output, i.e. a process predictive model can be identified. Subsequently, the results were statistically analysed through the A*nalysis of Variance (ANOVA)* and the *externally studentised residuals plot* vs. each Run. Considering the former, the statistical significance of the terms (i.e. process parameters) of the applied model was evaluated through the analysis of different descriptors such as the *adjusted determination coefficient (Adj R^2)*, the *p-value* with a confidence interval (C.I.) of 95% and the *Adequate precision* [181]. Moreover, the resulting model was reported for each output as a coded equation (i.e. the coefficients are related to the established process parameter level, defined as -1, 0 and +1 for the low, mid and high level respectively).

On the other hand, the externally studentised residual analysis allowed to observe the presence of outliers as well as the presence of unexpected trends related to uncontrolled process conditions. Moreover, the externally studentised residual analysis could also provide indications about the importance of a chosen output parameter for a given process.

Table 8.2. Process parameters considered for the DoE tests.

	Power (W)	Scanning speed (mm/min)	OV %	Focus position (mm)	Shielding gas pressure (bar)
Level 1	350	500	50		
Level 2	450	750	65	0 (on surface)	0.2
Level 3	550	1000	80		

Table 8.3. Complete list of the DoE tests.

Run	Power (W)	Scanning speed (mm/min)	OV%
1	550	750	50
2	450	500	80
3	550	750	80
4	550	500	65
5	350	1000	50
6	450	1000	50
7	550	1000	80
8	450	500	65
9	350	1000	65
10	550	500	80
11	550	1000	50
12	450	750	50
13	350	750	80
14	350	500	80
15	350	750	65
16	450	750	65
17	450	1000	80
18	450	750	80
19	450	1000	65
20	550	1000	65
21	350	500	65
22	350	500	50
23	450	500	50
24	350	750	50
25	350	1000	80
26	550	500	50
27	550	750	65

Furthermore, the DoE tests step was concluded with the evaluation of the process repeatability for the most significant experimental conditions. More specifically, the tests were repeated two times for the process parameters related to the best case observed and the minimum/maximum values of energy density per unit area investigated. The latter can be easily calculated to the following Eq. 8.1 [182]:

$$E = \frac{P}{\emptyset \cdot V} \qquad (8.1)$$

Where E is the areal energy density (J/mm^2), P represents the laser power input (W) and V represents the laser scanning speed (mm/s). According to this equation, the areal energy density levels investigated for the aforementioned repeatability experiments were calculated and reported in the following Table 8.4. It is worth to note that although E refers to a single laser track, since it does not consider the overlap between the tracks, it still represents a useful indicator to correlate with the experimental results, representing therefore an operative outcome;

Table 8.4. Areal energy density levels investigated for the DoE repeatability tests.

E (J/mm^2)	
Min	105
Best case	180
Max	330

- **Defocused beam tests:** Considering the best case obtained from the DoE campaign, in this step the effects of the beam defocusing were investigated. The aim of these tests was to evaluate the effect of the focal position shift above the surface, since the other verse would increase the microstructure alteration of the base material. About the actual value of the laser spot in the different defocusing levels, this represents an unknown parameter given the unavailability of information about the laser beam geometry of the considered machine. On the other hand, it is expected that an increase of the laser spot occurs when the focus is shifted above the peaks of the surface.

  Moreover, as discussed later, the main scope of these tests was to make the laser treatment less sensitive to the surface asperities due to the sintered powders, an experimental outcome observed from the results of the previous step. Concerning the levels of defocusing, a total distance of 3 mm above the surface was considered, divided into three steps of 1 mm each taking as a reference the focal position of the previous experimental steps. Finally, the campaign was concluded by means of repeatability tests carried out for each defocusing step.

8.3. Results and Discussions

8.3.1. DoE tests

In Fig. 8.3-8.7 are reported, for each test of the DoE, the actual values of the different surface texture parameters before (NT) and after the treatment. As well stated in the results and discussions of the previously investigated treatments, the initial surface status of the samples is, again, quite different.

Concerning the effects of LSR, the best results were achieved when the combination of the highest power level (550 W) and low to medium scanning speed (500-750 mm/min) values were adopted within the considered process window. With respect to the overlap between the tracks, the best results were achieved for the highest value adopted (80%). These considerations are practically shown by means of the best cases, represented by Run 3, Run 10 and Run 27. Among the latter three, Run 3 gives the highest surface improvements for all the investigated texture parameters. The actual values of the measured surface texture parameters are reported in Table 8.5. Based on all the results, the main experimental outcome of the DoE tests is that the major surface improvements were achieved when moving towards the highest areal energy density values within the investigated process window.
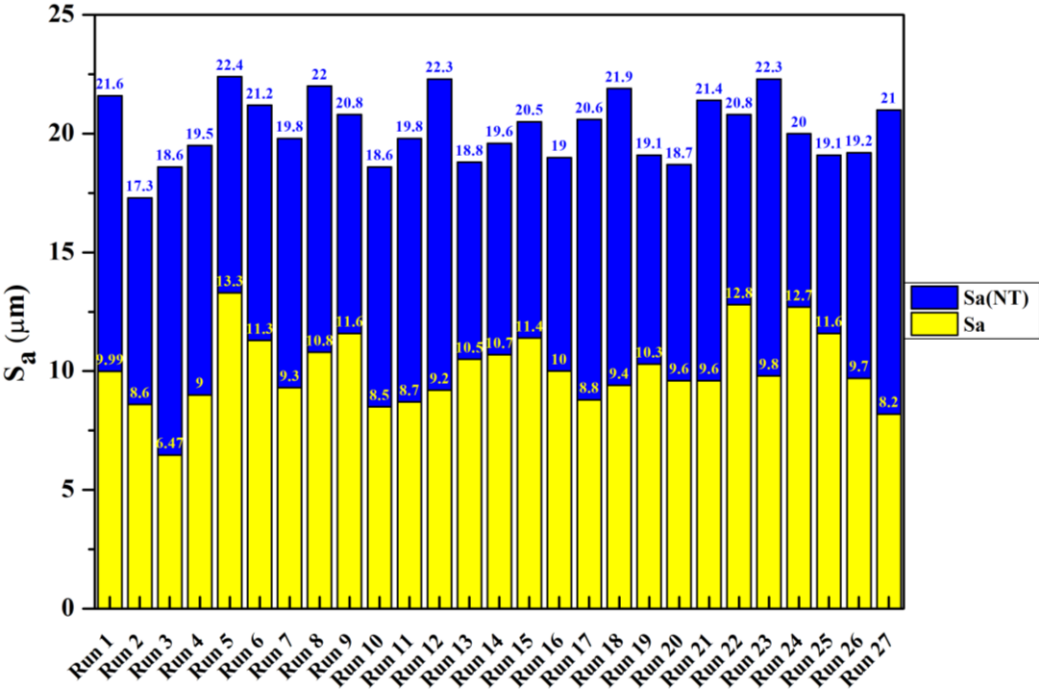
Figure 8.3. Evolution of S_a for the considered DoE tests (NT = not treated).
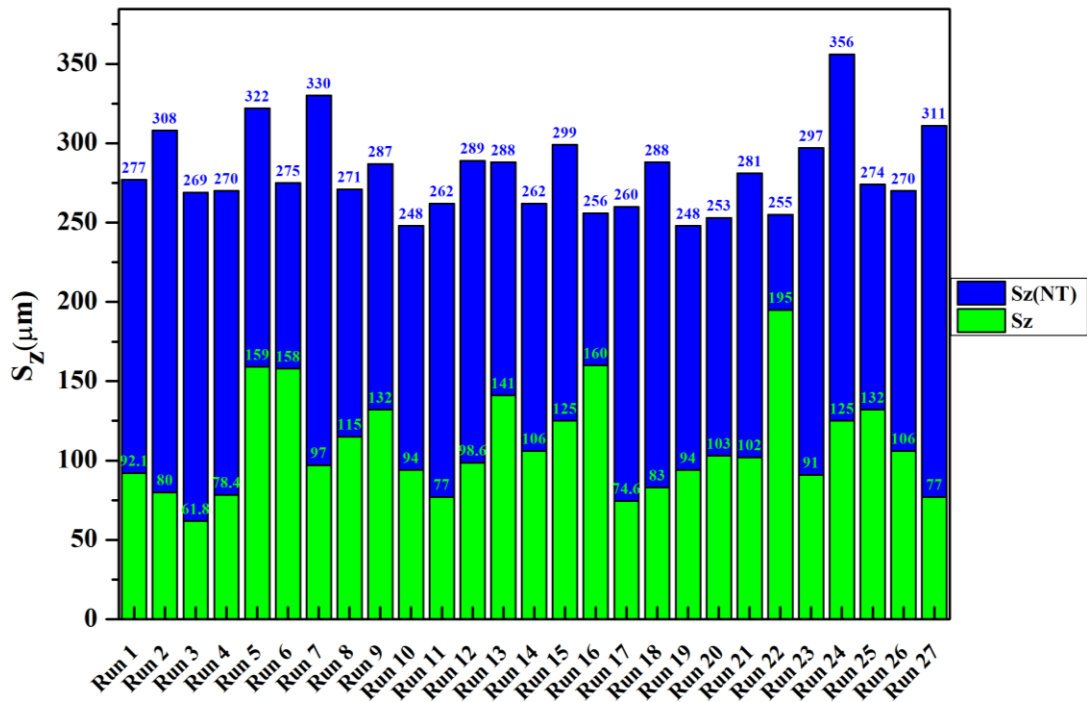
Figure 8.4. Evolution of S_z for the considered DoE tests (NT = not treated).
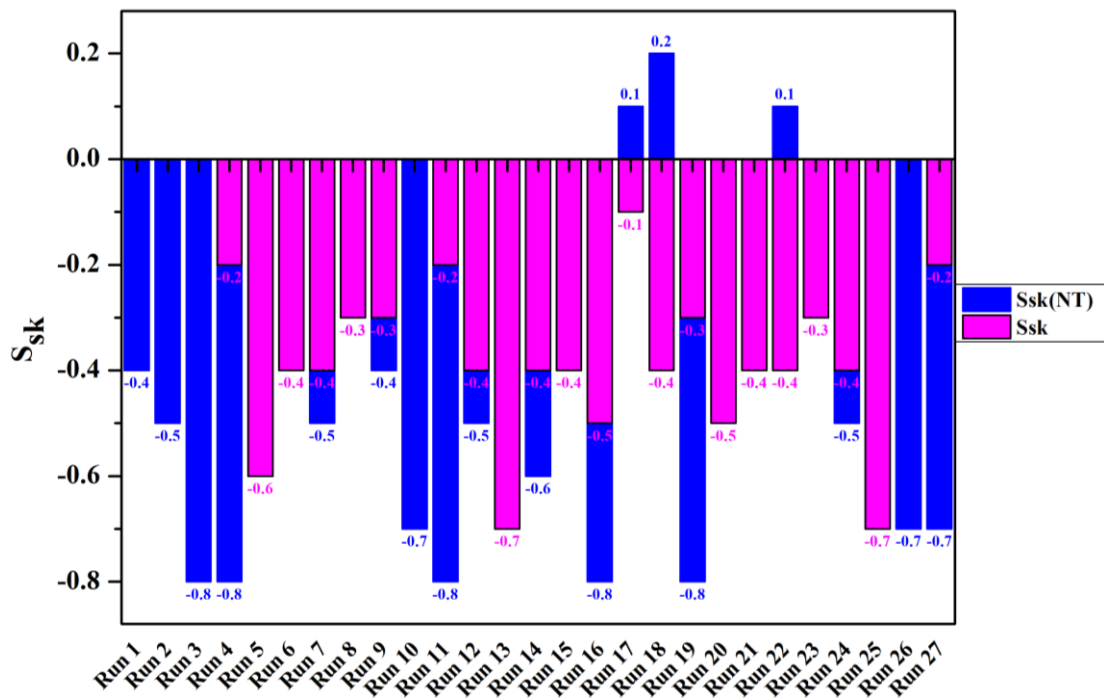
Figure 8.5. Evolution of S_{sk} (if not reported, S_{sk} = 0) for the considered DoE tests (NT = not treated).
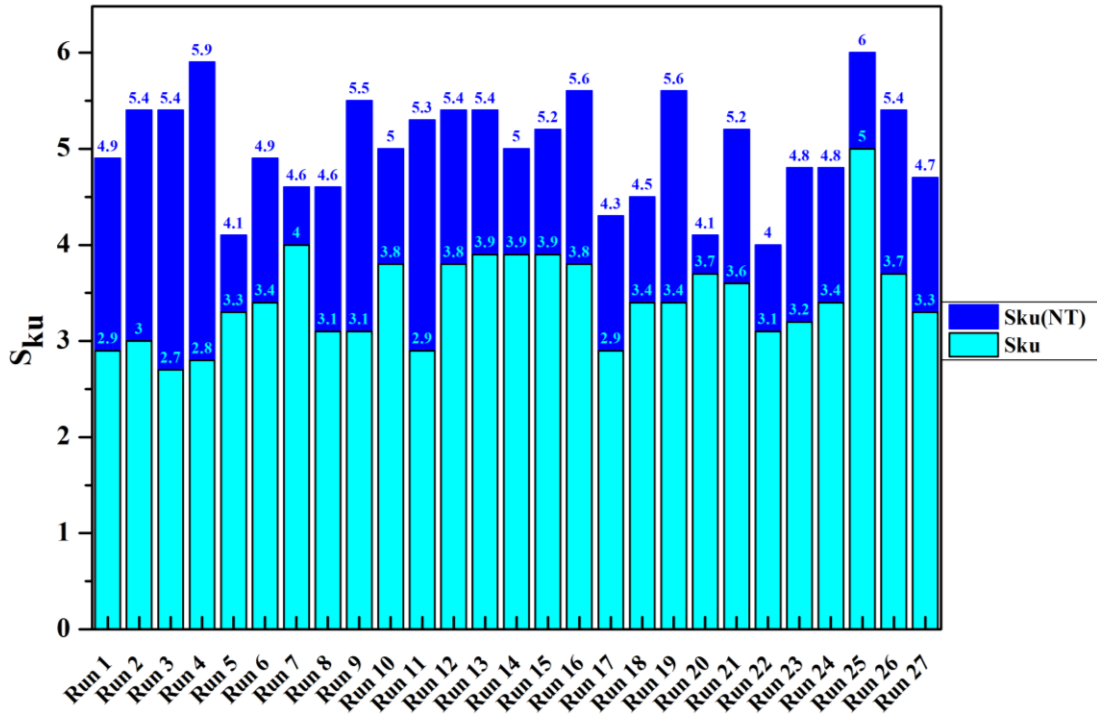
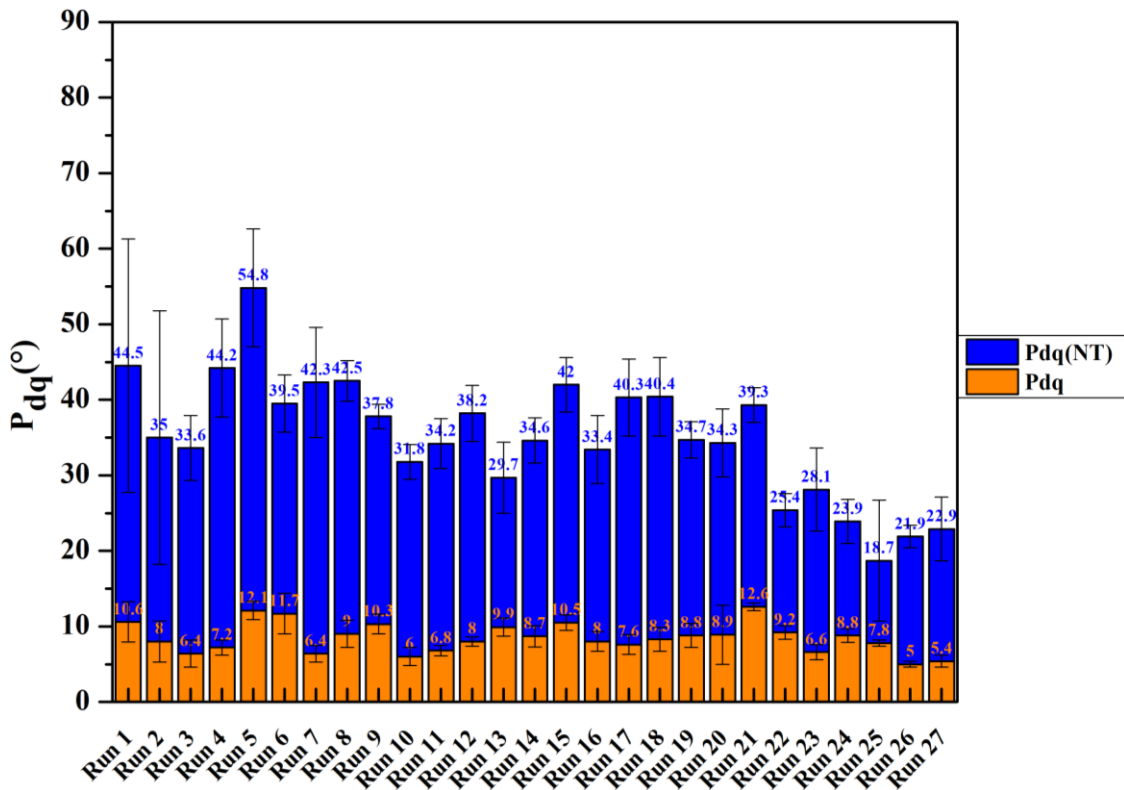**Figure 8.6.** Evolution of S_{ku} for the considered DoE tests (NT = not treated).

Figure 8.7. Evolution of P_{dq} for the considered DoE tests (NT = not treated).

Table 8.5. Actual surface texture parameters measured for the DoE tests.

Run	S_a (NT) (μm)	S_z (NT) (μm)	S_{sk} (NT)	S_{ku} (NT)	P_{dq} avg. (NT) (°)	P_{dq} dev. st. ($\pm\sigma$) (NT) (°)	S_a (μm)	S_z (μm)	S_{sk}	S_{ku}	P_{dq} avg. (°)	P_{dq} dev. st. ($\pm\sigma$) (°)
1	21.6	277	-0.4	4.9	44.5	16	9.99	92.1	0	2.9	10.6	2.6
2	17.3	308	-0.5	5.4	35	16	8.6	80	0	3	8	2.7
3	18.6	269	-0.8	5.4	33.6	4.3	6.47	61.8	0	2.7	6.4	1.8
4	19.5	270	-0.8	5.9	44.2	6.5	9	78.4	-0.2	2.8	7.2	1
5	22.4	322	-0.1	4.1	54.8	7.8	13.3	159	-0.6	3.3	12.1	1.2
6	21.2	275	-0.1	4.9	39.5	3.8	11.3	158	-0.4	3.4	11.7	2.7
7	19.8	330	-0.5	4.6	42.3	7.3	9.3	97	-0.4	4	6.4	1.1
8	22	271	-0.3	4.6	42.5	2.7	10.8	115	-0.3	3.1	9	1.8
9	20.8	287	-0.4	5.5	37.8	1.6	11.6	132	-0.3	3.1	10.3	1.3
10	18.6	248	-0.7	5	31.8	2.3	8.5	94	0	3.8	6	1.2
11	19.8	262	-0.8	5.3	34.2	3.3	8.7	77	-0.2	2.9	6.8	0.7
12	22.3	289	-0.5	5.4	38.2	3.7	9.2	98.6	-0.4	3.8	8	0.6
13	18.8	288	-0.4	5.4	29.7	4.7	10.5	141	-0.7	3.9	9.9	1.2
14	19.6	262	-0.6	5	34.6	3	10.7	106	-0.4	3.9	8.7	1.4
15	20.5	299	0	5.2	42	3.6	11.4	125	-0.4	3.9	10.5	1
16	19	256	-0.8	5.6	33.4	4.5	10	160	-0.5	3.8	8	1.3
17	20.6	260	0.1	4.3	40.3	5.1	8.8	74.6	-0.1	2.9	7.6	1.3
18	21.9	288	0.2	4.5	40.4	5.2	9.4	83	-0.4	3.4	8.3	1.6
19	19.1	248	-0.8	5.6	34.7	2.4	10.3	94	-0.3	3.4	8.8	1.6
20	18.7	253	-0.4	4.1	34.3	4.5	9.6	103	-0.5	3.7	8.9	3.9
21	21.4	281	-0.4	5.2	39.3	2.3	9.6	102	-0.4	3.6	12.6	0.5
22	20.8	255	0.1	4	25.4	2.2	12.8	195	-0.4	3.1	9.2	0.9
23	22.3	297	0	4.8	28.1	5.5	9.8	91	-0.3	3.2	6.6	1
24	20	356	-0.5	4.8	23.9	2.9	12.7	125	-0.4	3.4	8.8	0.9
25	19.1	274	-0.7	6	18.7	8	11.6	132	-0.7	5	7.8	0.4
26	19.2	270	-0.7	5.4	21.9	1.5	9.7	106	0	3.7	5	0.4
27	21	311	-0.7	4.7	22.9	4.2	8.2	77	-0.2	3.3	5.4	0.8

This result was also confirmed by means of the 3D surfaces reported in Fig. 8.8 and the SEM images reported in Fig. 8.9, in which a comparison between an untreated surface and Run 3 is illustrated. The comparison includes also the DoE tests related to the minimum areal energy density (Run 5) as well as the maximum (Run 10) reported in Table 8.4. As expected, Run 3 and Run 10 presents very similar results, given the only slight difference in the scanning speed as the process parameter, as already highlighted by the evolution of the surface texture parameters reported before.

On the other hand, a very appreciable difference is highlighted with Run 5: given the reduced overlap between the re-melting tracks and the Gaussian distribution of the laser, the treatment determines the formation of a residual texture given by some un-melted areas of the single tracks, given also the low power and high speed. This effect is also clearly observable by the remarkable decrease of S_{sk} towards more negative values with respect to the untreated surface.

As a general further outcome, the evolution of all the surface texture parameters is compatible with a consistent surface improvement, i.e. the strong reduction of S_a, S_z, S_{ku}, P_{dq} and the tendency of S_{sk} to 0 in the best cases.
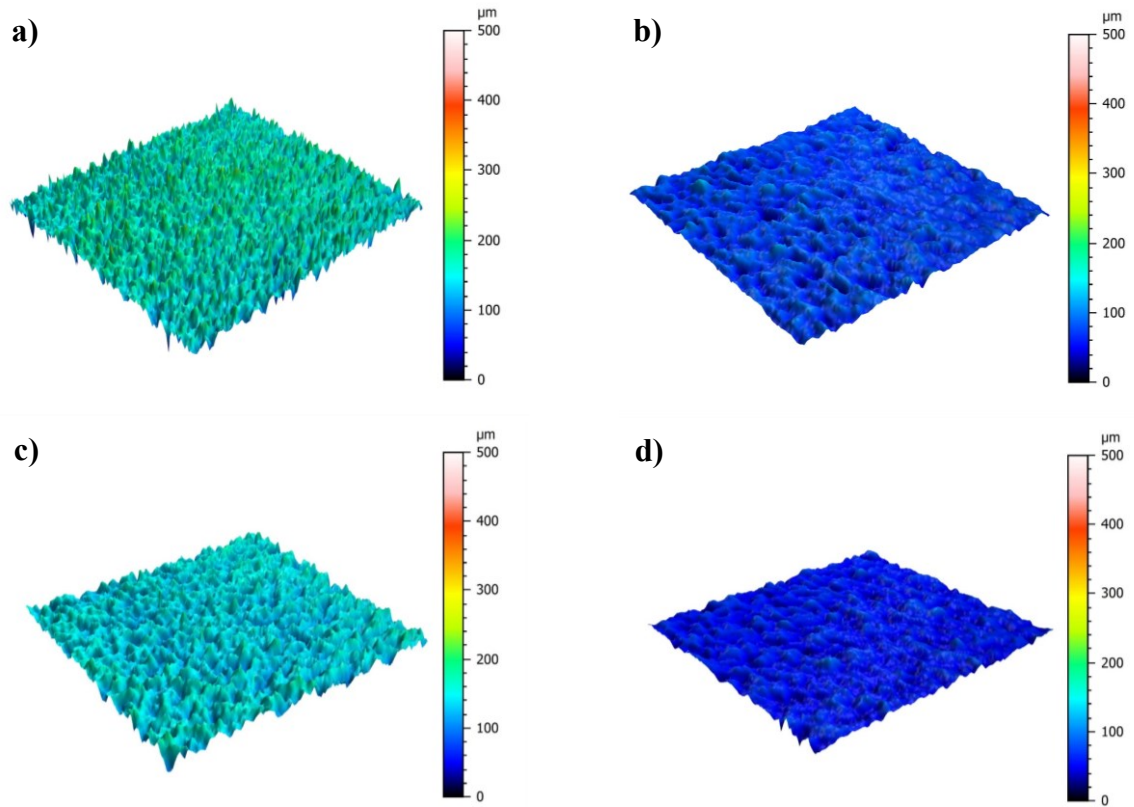
Figure 8.8. Comparison between the 3D surfaces of an untreated sample (a) and Run 3 (b), Run 5 (c) and Run 10 (d).
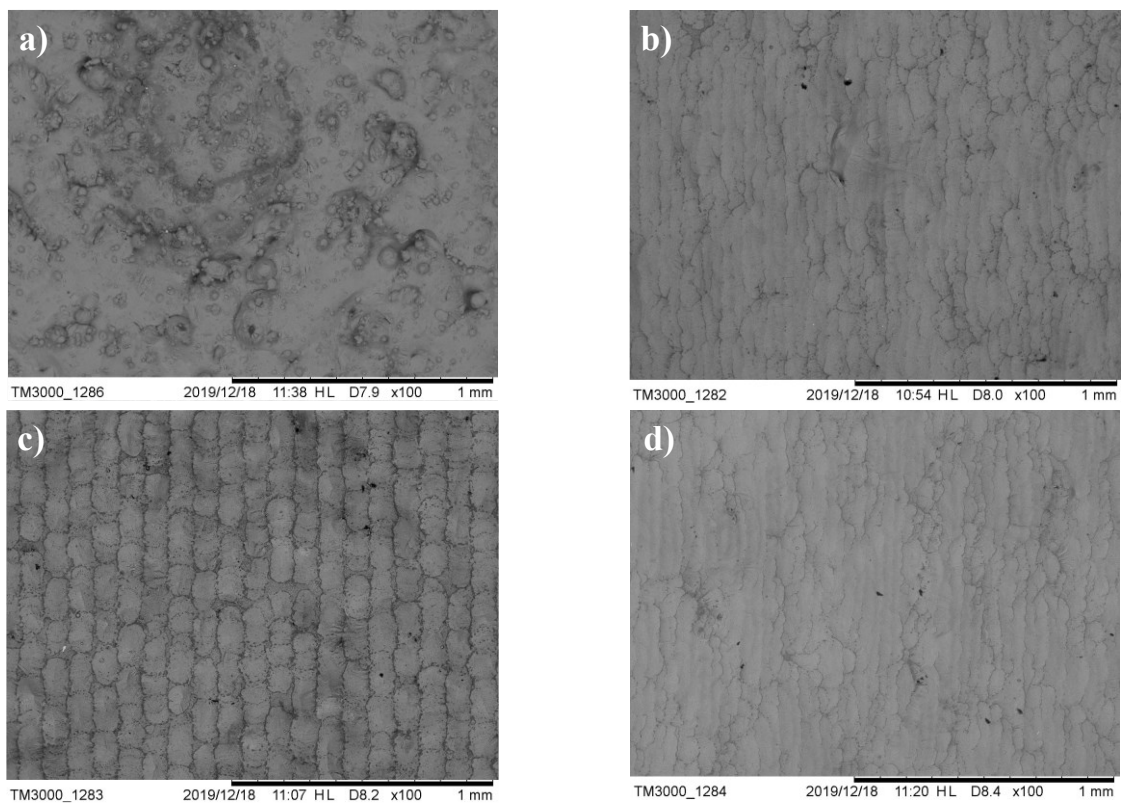

Figure 8.9. Comparison between the SEM images of an untreated sample (a) and Run 3 (b), Run 5, (c) and Run 10 (d).

Concerning the results analysis through the RSM, in the following Figures are reported the extrapolated surfaces according to each texture parameter as well as the factors and levels considered for the DoE tests. According to the statistical analysis — whose results are reported later — a linear model resulted as the best fitting between the actual and predicted values. However, several measured points were outside the surface based on the predicted values from the model (red dots refers to actual measured values above the predicted ones, whereas white points are related to actual measured values below the predicted ones).

This result could be justified by the mathematical ease of the linear model that, therefore, does not take into account other important process parameters such as focus position, as well as some physical phenomena occurring during the treatment and the dispersion of the initial values of the surface texture parameters.

In relation to the latter, the interaction of the laser source with the specific texture of the surface could represent the most significant issue. More specifically, the effect of the provided heat input on the random surface texture could depend on the relative distance of the laser focus from the individual peaks and valleys. Therefore, given the combination of high energy densities involved and the high dispersion of S_a and S_z values, the surface modification behavior might be different with respect of the most prominent peaks, whose exposure to the heat input and subsequent laser absorption is different in comparison with the valleys.
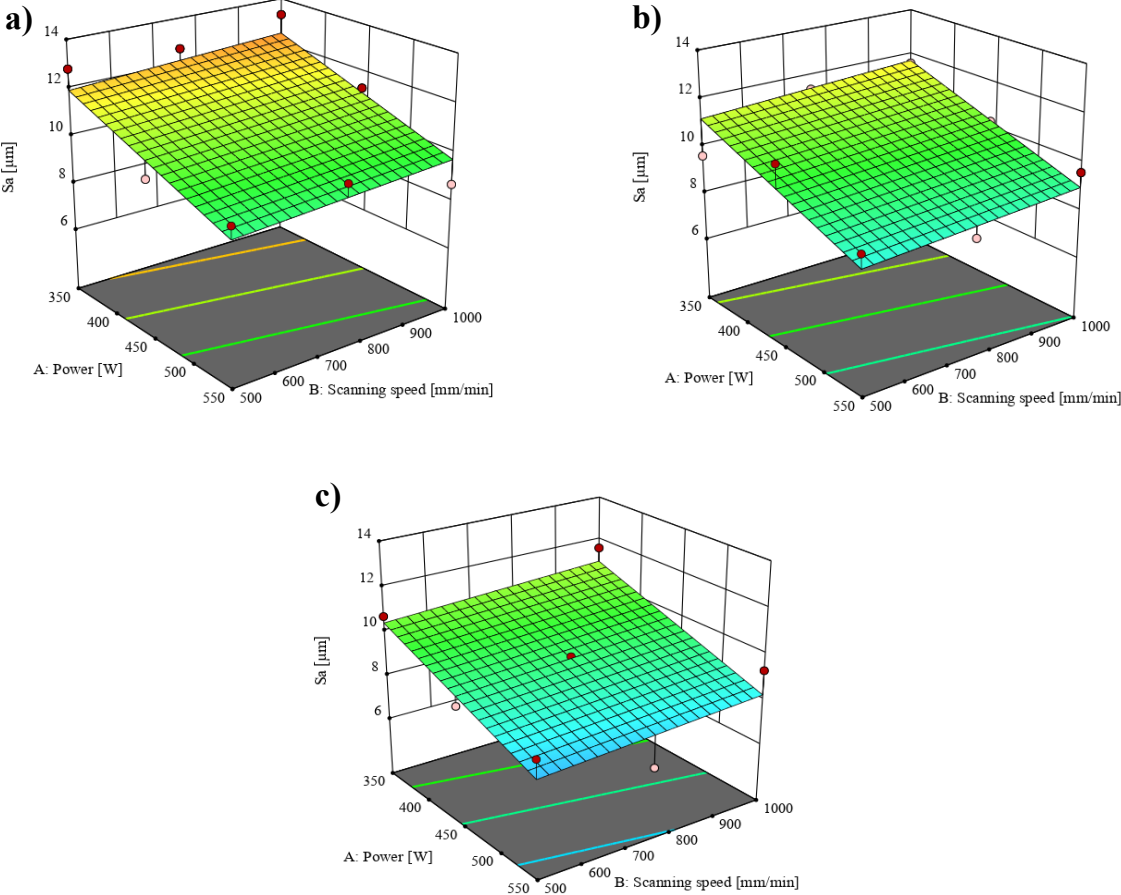
Figure 8.10. RSM illustration of S_a evolution, as a function of laser power and scanning speed for: (a) OV 50%, (b) OV 65% and (c) OV 80%.
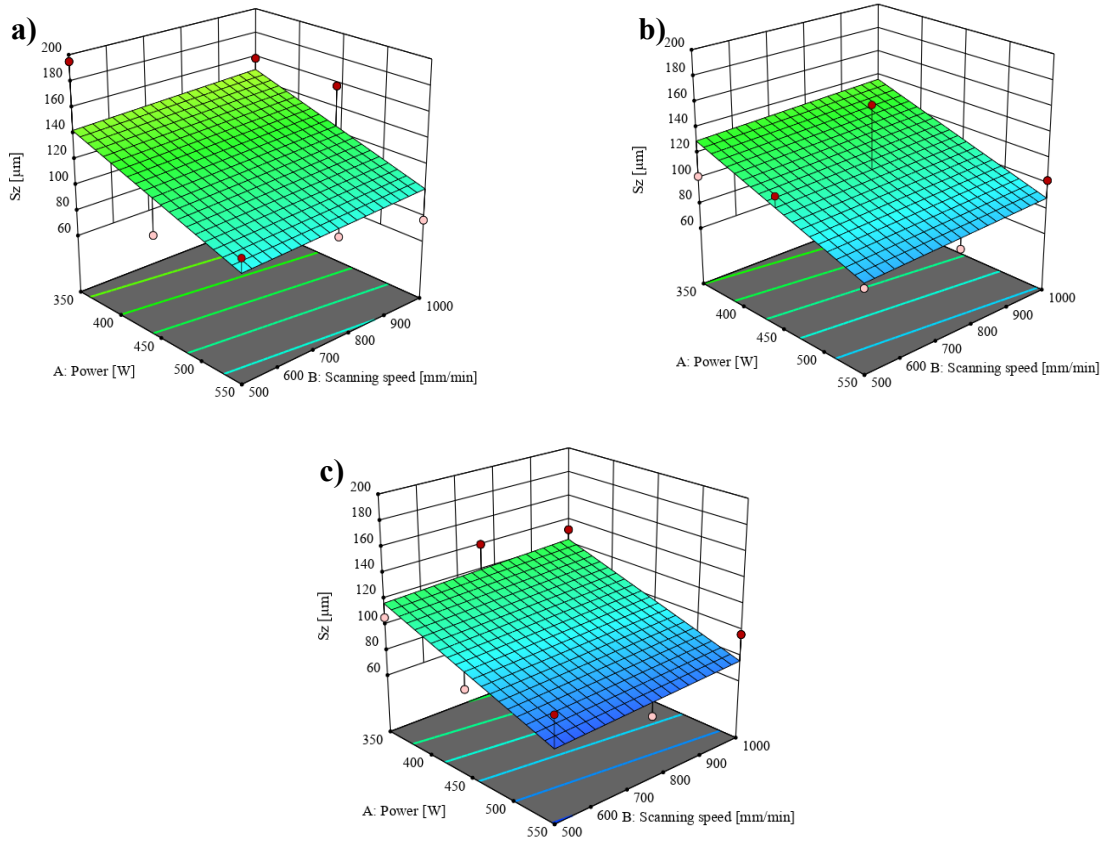
Figure 8.11. RSM illustration of S_z evolution, as a function of laser power and scanning speed for: (a) OV 50%, (b) OV 65% and (c) OV 80%.
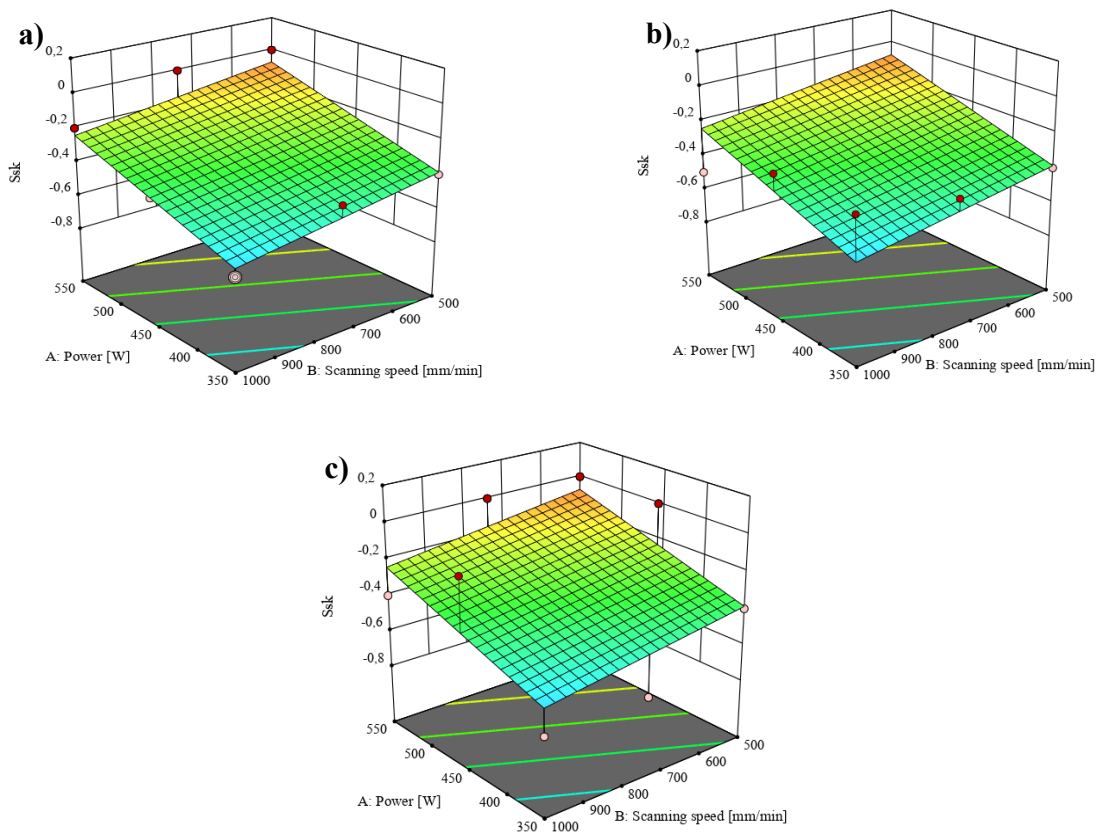

Figure 8.12. RSM illustration of S_{sk} evolution, as a function of laser power and scanning speed for: (a) OV 50%, (b) OV 65% and (c) OV 80%.
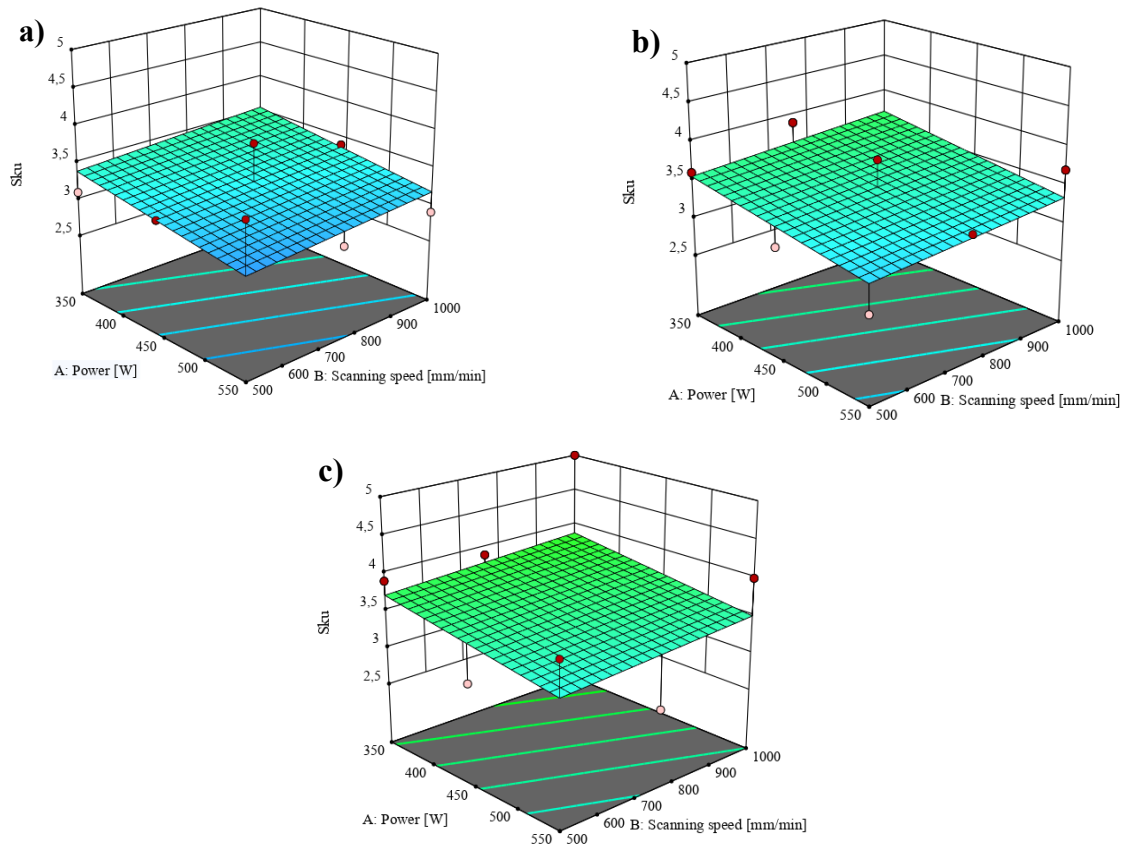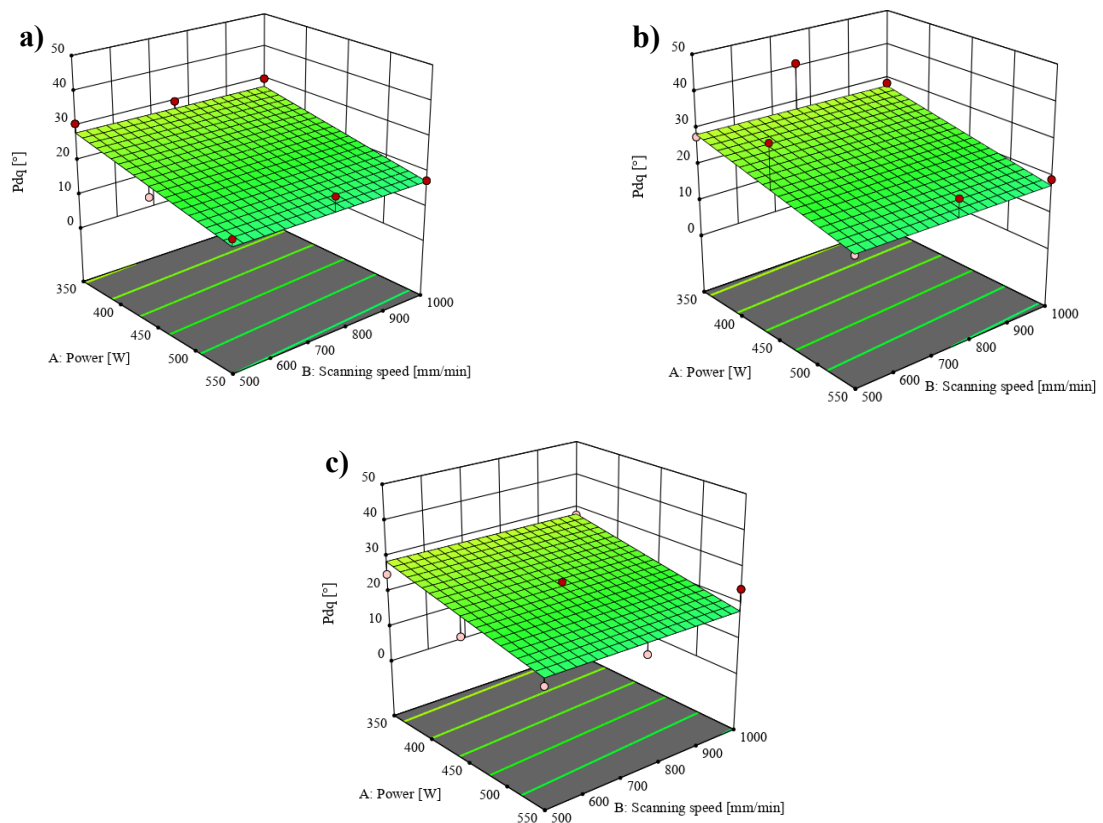
Figure 8.13. RSM illustration of S_{ku} evolution, as a function of laser power and scanning speed for: (a) OV 50%, (b) OV 65% and (c) OV 80%.

Figure 8.14. RSM illustration of P_{dq} evolution, as a function of laser power and scanning speed for: (a) OV 50%, (b) OV 65% and (c) OV 80%.

The dependency of the laser absorption from the random surface texture features of the samples could also justify the statistical analysis results obtained. In first instance, the linear fitting model was chosen according to the *maximum to minimum output ratio* between the actual values, reported in the following Tables 8.6-10. The ratio — automatically provided from Design Expert 11® — represents a first criterion for the linear model selection, suggesting its feasibility for ratios lower than 10. From the following Tables it can be observed that the max/min ratio values are always lower than the aforementioned limit, except for S_{sk} for which this parameter is not calculable, given the presence of zero values.

In the Tables are also reported the statistic descriptors used to evaluate the model validity and input process parameters significance, for each of the investigated surface texture parameters. From the results, it can be easily observed that most of the input (process parameters) and output (surface texture parameters) model terms are statistically significant, the latter not strongly correlated to the former according the Adj R^2 values (for the best case, represented by S_a, a value of 0,70 was obtained).

However, in relation to the output, S_{ku} does not represent a statistically significant surface texture indicator, as observable from all the descriptors obtained from the ANOVA analysis. Despite the reductions observed after the treatment in Fig. 8,6, this result can be justified considering that S_{ku} is not sensitive to the roughness scale compared to the other parameters (i.e., surfaces with different roughness values could possess the same S_{ku}) and, therefore, it is difficult to control. This consideration was proved, in first instance, by the almost null value of Adj R^2 and the high p-values — greater than the 0,05 threshold value — for all the input process parameters (Table 8.9). The poor statistical significance of S_{ku} was proved also by means of the adequate precision whose value — unlike the other surface texture parameters — is quite near the limit value of 4. This result suggests that the values could be significantly affected by noise.

On the other hand, in relation to the input model terms, another general outcome is that the scanning speed is not a statistically significant process parameter, according to the p-values observed for each surface texture parameter, except S_{sk}. However, it can be easily concluded that this parameter, affecting E in a direct way, cannot be excluded from the ANOVA models.

Still concerning the input process parameters, from the Tables it can be also concluded that, except for S_a and S_z, OV% does not represent a statistically significant process parameter. In first instance, this result could be easily explained for S_{ku} and P_{dq}. For the former, the reason is due to the poor statistical significance of the surface texture parameter itself, as discussed above. For the latter, the poor significance of the OV% could be justified considering that the reduction of P_{dq} is mainly promoted by the melting of the sintered powders on the surface, a mechanism that depends mainly from the laser power and the scanning speed. On the other hand, different considerations are needed for S_{sk}: despite the discussed influence of OV% on this parameter, as shown from the actual values in Table 8.5 and the SEM images in Fig. 8.9, the different starting values affects significantly the surface response to the treatment. More specifically, from Fig. 8.5 can be observed that if the starting values of S_{sk} are close to 0 or slightly positive, the resulting values after the treatment are quite negative. Vice versa, if the starting values are negative, the LSR effect is to bring S_{sk} closer to 0 as a function of the provided heat input. Based on this result, a proper statistical significance of S_{sk} with respect to OV% is therefore difficult.

Table 8.6. Values of the **s**tatistical descriptors used to evaluate the correlation and significance of the process parameters with respect to S_a.

		S_a				
max/min ratio	**Adj R²**	**p-value**				**Adeq. Precision**
		model	**Power**	**Scanning speed**	**OV%**	
2,04	0,71	<0,0001	<0,0001	0,1754	0,0009	14,8

Table 8.7. Values of the **s**tatistical descriptors used to evaluate the correlation and significance of the process parameters with respect to S_z.

		S_z				
max/min ratio	**Adj R²**	**p-value**				**Adeq. Precision**
		model	**Power**	**Scanning speed**	**OV%**	
3,15	0,44	0,0009	0,0003	0,568	0,0327	8,65

Table 8.8. Values of the **s**tatistical descriptors used to evaluate the correlation and significance of the process parameters with respect to S_{sk}.

		S_{sk}				
max/min ratio	**Adj R²**	**p-value**				**Adeq. Precision**
		model	**Power**	**Scanning speed**	**OV%**	
n.d.	0,45	0,0008	0,0002	0,0295	1	8,15

Table 8.9. Values of the **s**tatistical descriptors used to evaluate the correlation and significance of the process parameters with respect to S_{ku}.

		S_{ku}				
max/min ratio	**Adj R²**	**p-value**				**Adeq. Precision**
		model	**Power**	**Scanning speed**	**OV%**	
1,85	0,08	0,169	0,1046	0,4635	0,1629	4,75

Table 8.10. Values of the **s**tatistical descriptors used to evaluate the correlation and significance of the process parameters with respect to P_{dq}.

		P_{dq}				
max/min ratio	**Adj R²**	**p-value**				**Adeq. Precision**
		model	**Power**	**Scanning speed**	**OV%**	
2,52	0,42	0,0012	0,0003	0,2166	0,1418	8,64

All the results obtained, as well as the considerations done about the statistical significance of the linear model chosen to fit the actual data, were also in agreement with the ones observed from the externally studentised residuals analysis. According to the plots reported in Fig. 8.15-19, the results obtained for the different surface texture parameters investigated suggest the proper fitting of the linear model, considering the random dispersion of the residuals around the horizontal axis. This indicates also the absence of trends that might be due to uncontrolled experiments conditions and operator errors. However, for the case of S_{ku} —whose poor statistical significance was already proved before — an outlier was observed for Run 25 (the residual was greater than 3). The latter result confirms the control difficulty of this parameter for the considered surfaces, in agreement with the model significance descriptors reported in Table 8.9.

In conclusion of the statistical analysis of the collected data, the reported Eqs. 8.2-5 represents the coded equations adopted for the CO_2 LSR process for the investigated surface texture parameters, highlighting the impact of each input process parameter through the related coefficient. It is worth to note that the terms related to the interactions between the process parameters were removed from the models, since they were not statistically significant (i.e. the p-values were greater than 0,05). Moreover, considering that S_{ku} was also not a statistically significant output, the related equation is not reported.
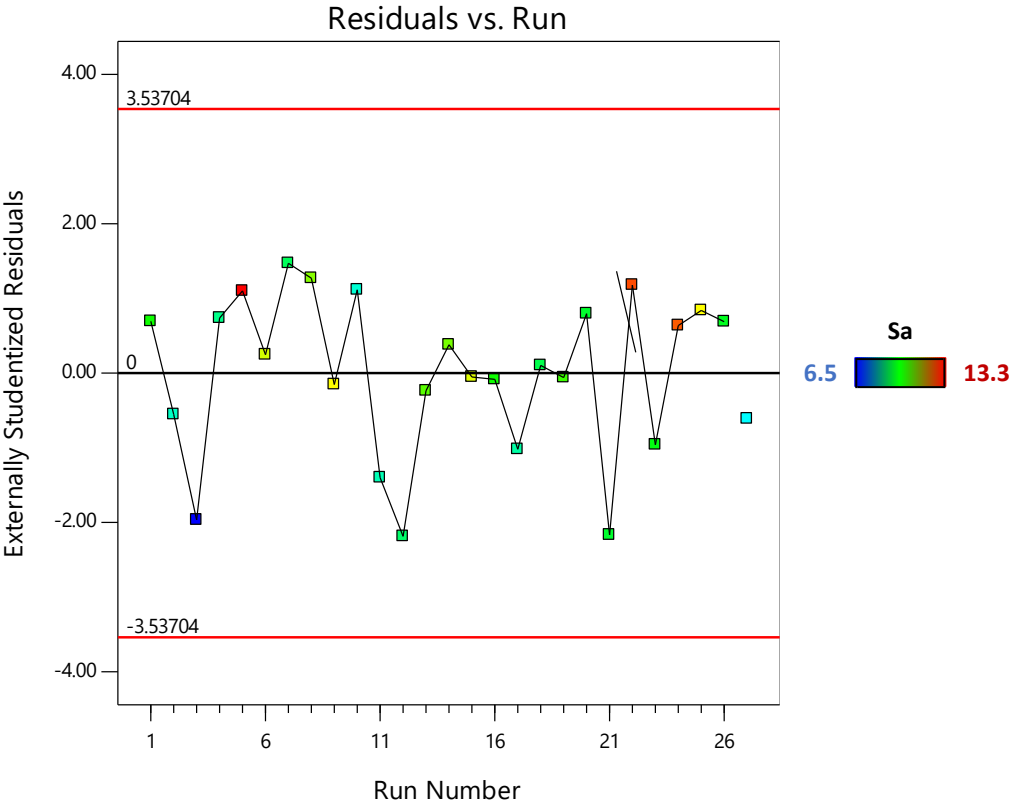
Figure 8.15. Externally studentised residuals of S_a (color points are related to the actual parameter values).
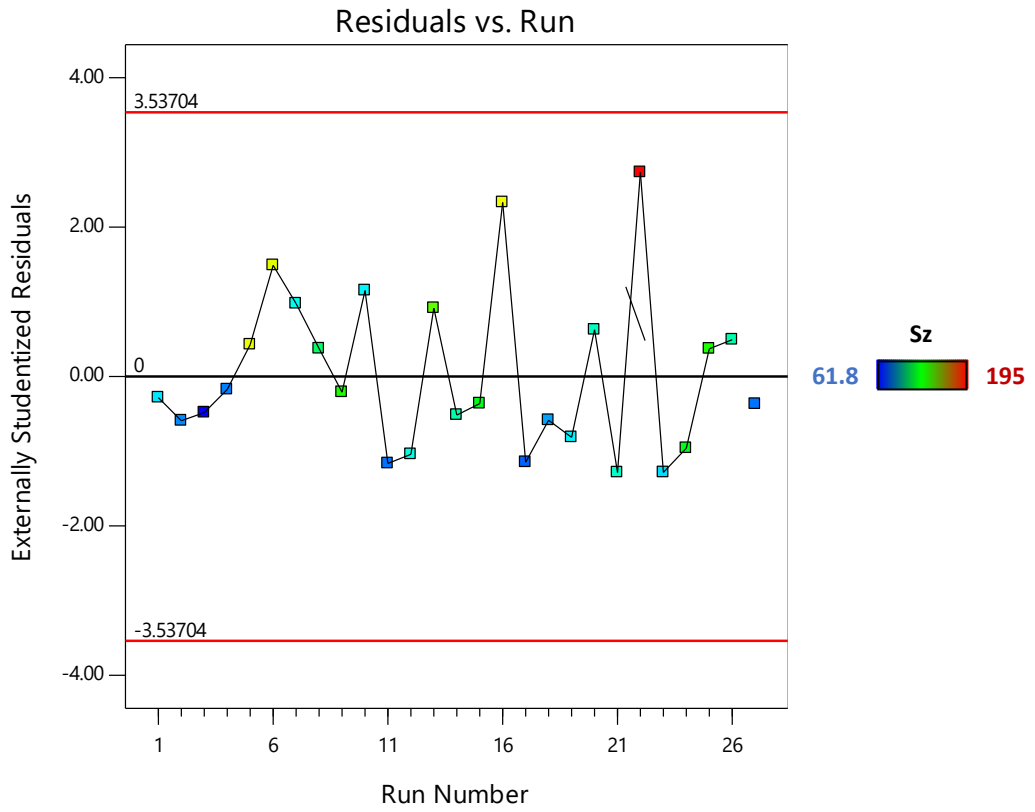
Figure 8.16. Externally studentised residuals of S_Z (color points are related to the actual parameter values).
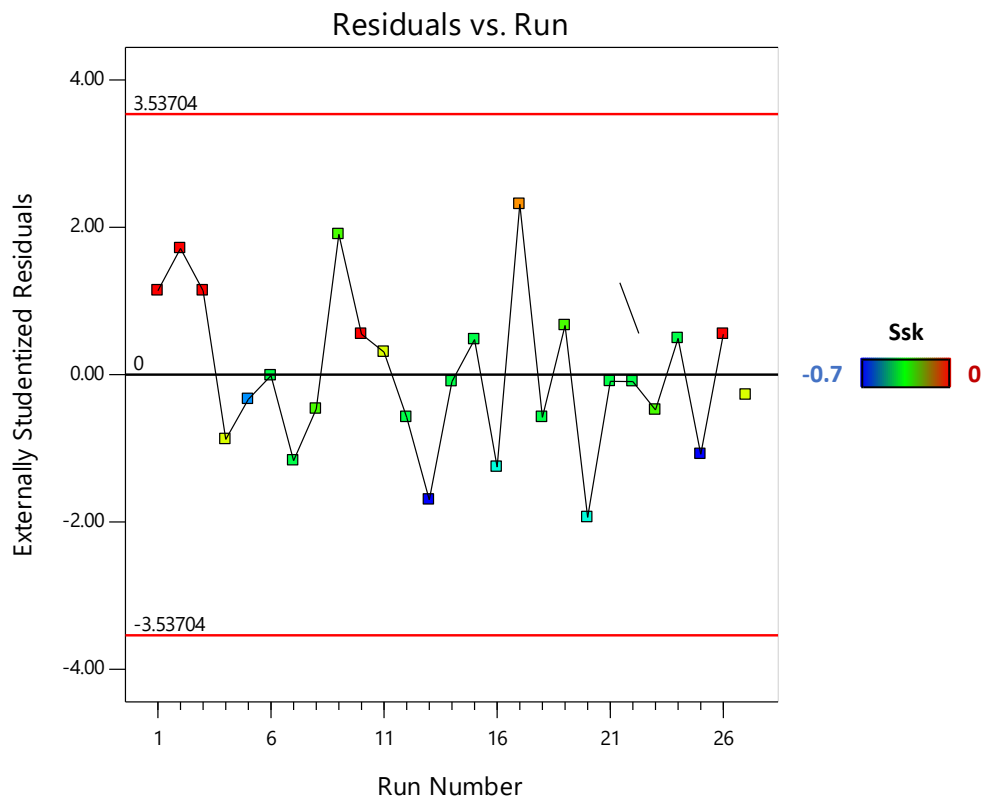
Figure 8.17. Externally studentised residuals of S_{sk} (color points are related to the actual parameter values).
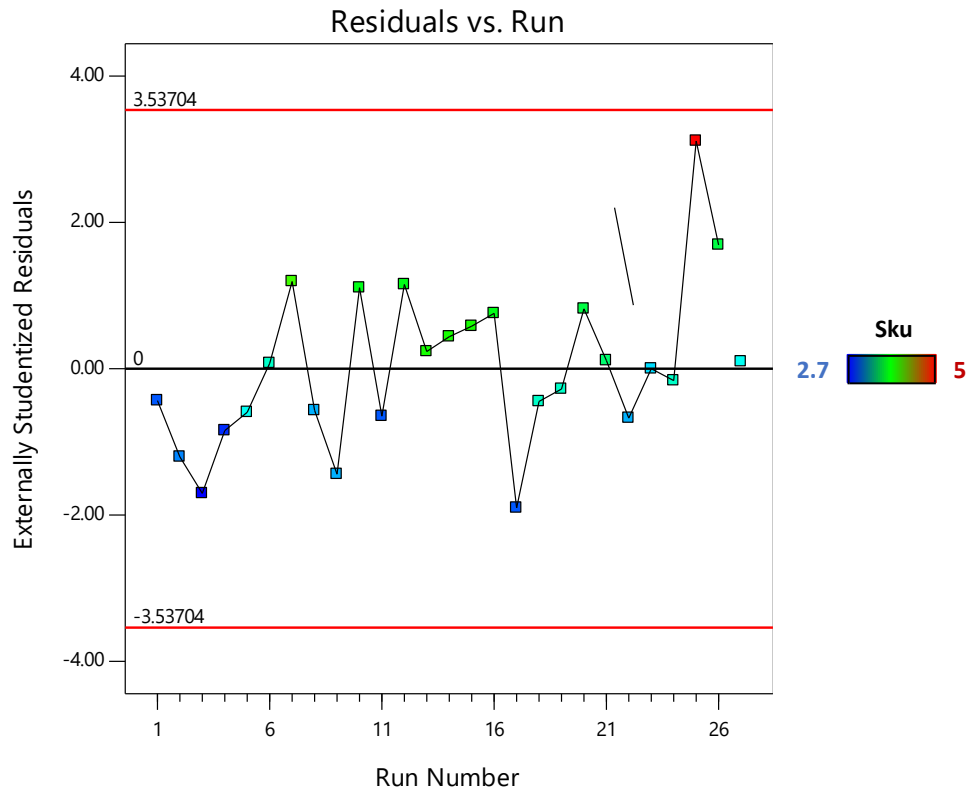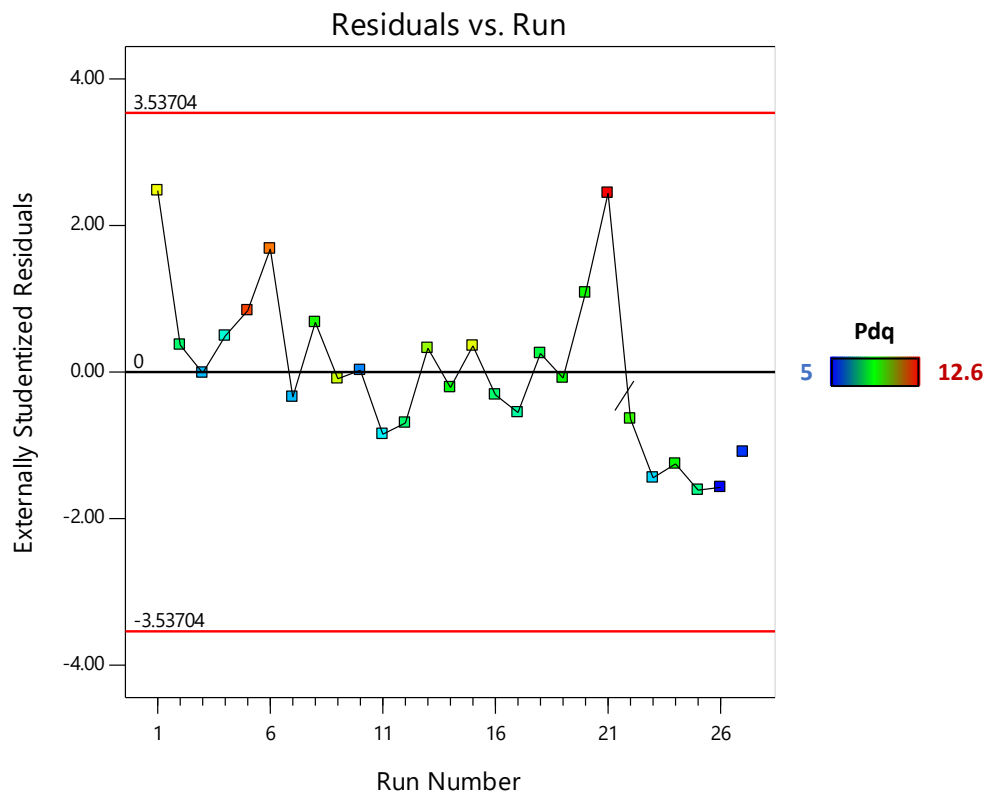
Figure 8.18. Externally studentised residuals of S_{ku} (color points are related to the actual parameter values).

Figure 8.19. Externally studentised residuals of P_{dq} (color points are related to the actual parameter values).

$$S_a = 10{,}07 - 1{,}37 \, Power + 0{,}28 \, Scanning \, speed - 0{,}27 \, OV\% \qquad (8.2)$$

$$S_z = 110 - 23{,}9 \, Power + 3{,}29 \, Scanning \, speed - 12{,}91 \, OV\% \qquad (8.3)$$

$$S_{sk} = -0{,}3 + 0{,}16 \, Power - 0{,}08 \, Scanning \, speed + 0 \, OV\% \qquad (8.4)$$

$$P_{dq} = 8{,}47 - 1{,}51 \, Power + 0{,}45 \, Scanning \, speed - 0{,}54 \, OV\% \qquad (8.5)$$

According to the experimental campaign description reported in the previous section, the DoE tests stage was concluded with the repeatability tests.

The results of the surface texture parameters are reported in Fig. 8.20 -8.25, illustrating the comparison of the results investigated for Run 3, Run 5 and Run 10. The first outcome related to this experimental step is the notable dispersion of the surface texture parameters for the treated surfaces under a given process parameter set (i.e. Run), result that is in agreement with the previous considerations about the not controlled interaction phenomena between the laser and the random powder-related features of the original surfaces. On the other hand, the same results confirm the surface morphology evolution trend discussed previously, as a function of E. More specifically, a confirm of the similar results achievable through the process conditions related to Run 3 and Run 10 was highlighted, as well as the less (but more stable) surface improvement effects of the process conditions related to Run 5.
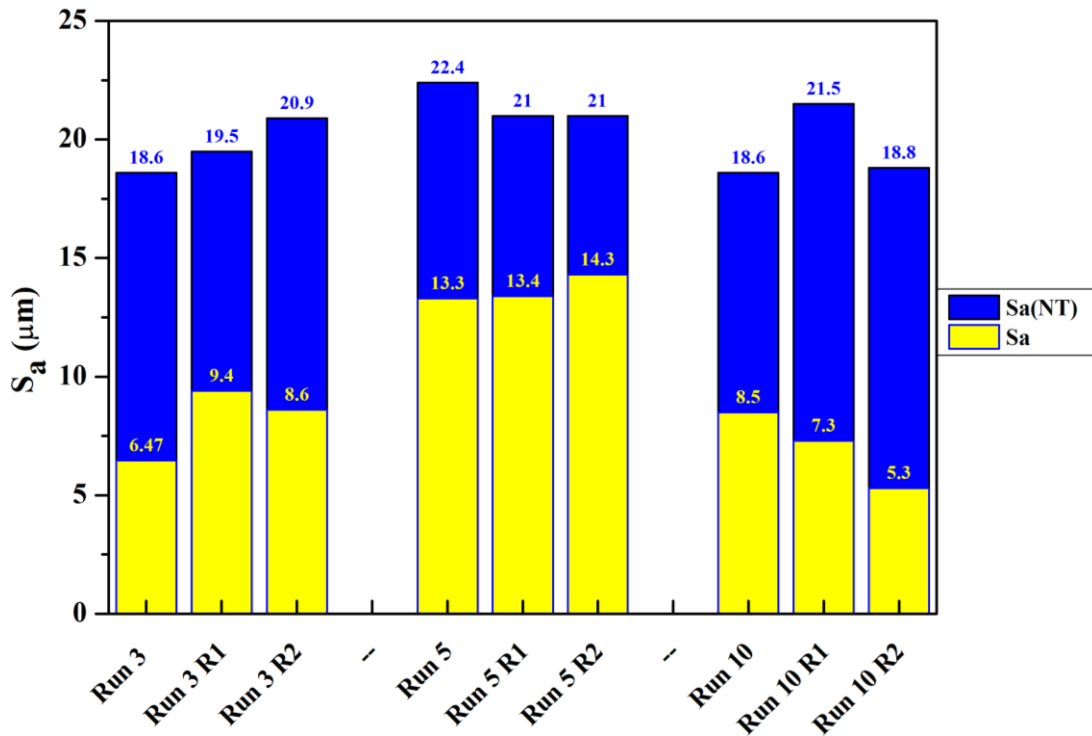
Figure 8.20. Evolution of S_a for the DoE repeatability tests on Run 3, Run 5 and Run 10 (NT = not treated).
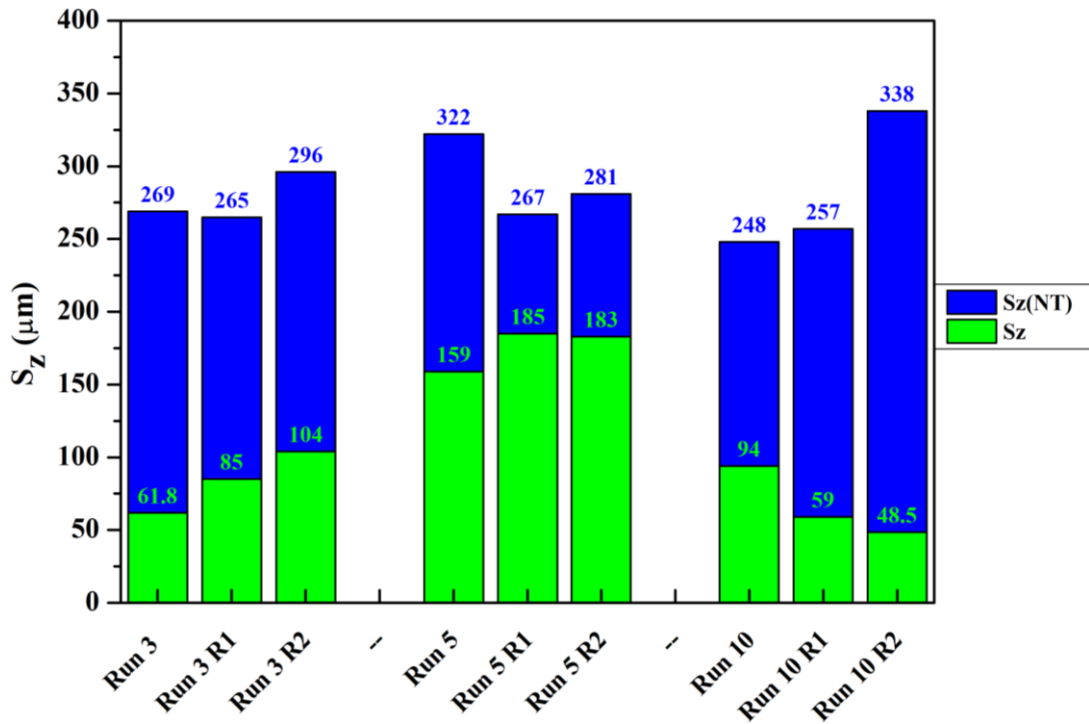
Figure 8.21. Evolution of S_z for the DoE repeatability tests on Run 3, Run 5 and Run 10 (NT = not treated).
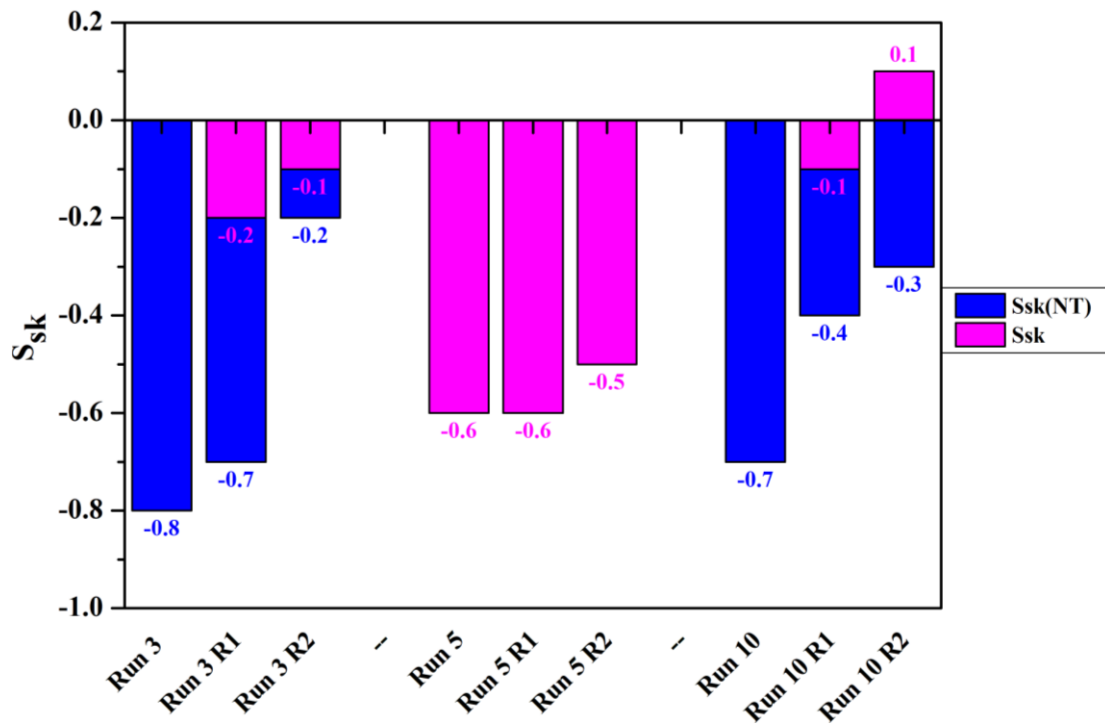

Figure 8.22. Evolution of S_{sk} (if not reported, $S_{sk} = 0$) for the DoE repeatability tests on Run 3, Run 5 and Run 10 (NT = not treated).
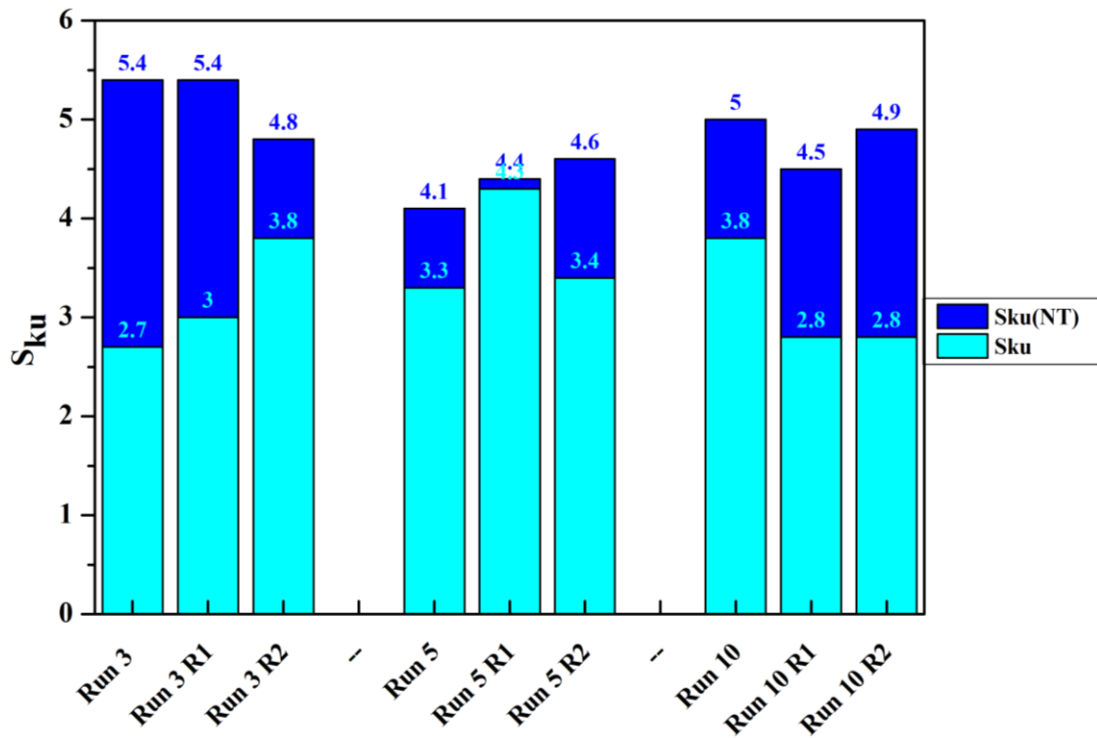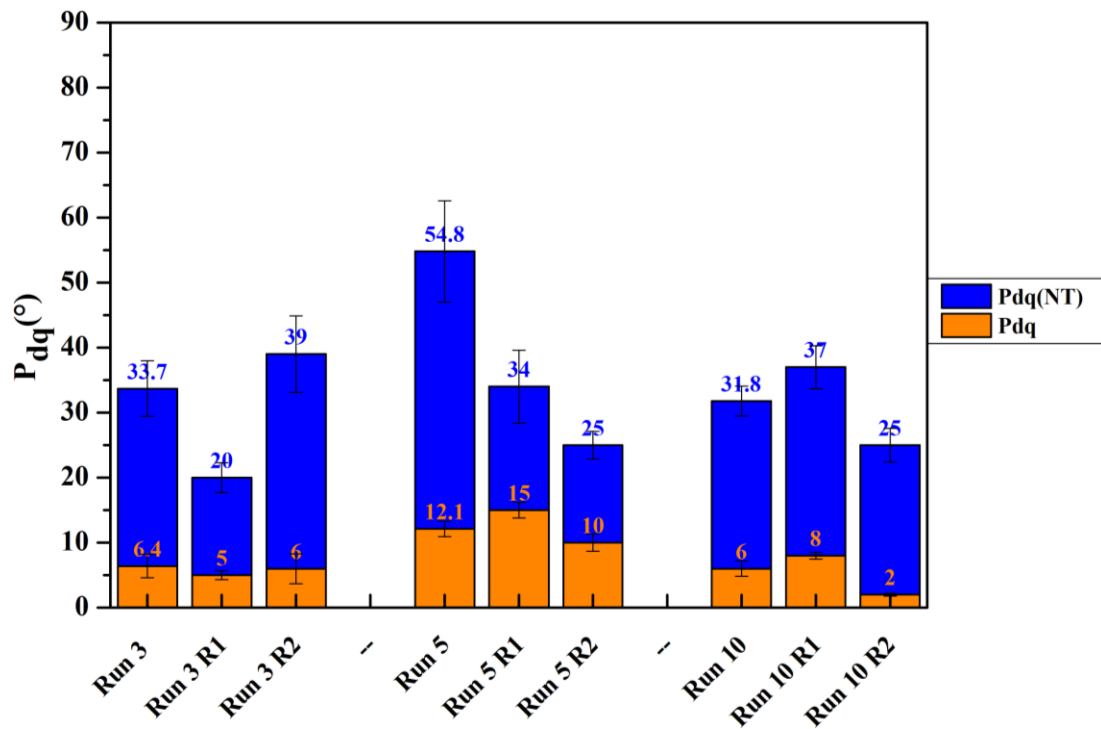
Figure 8.23. Evolution of S_{ku} for the DoE repeatability tests on Run 3, Run 5 and Run 10 (NT = not treated).

Figure 8.24. Evolution of P_{dq} for the DoE repeatability tests on Run 3, Run 5 and Run 10 (NT = not treated).

According to the appearance of the actual treated samples reported in Fig. 8.25, the agreement with the results quantified and reported above can be observed. However, surface oxidation can be also appreciated on some treated samples (Run 5, Run 10). This result is clearly due to a low shielding gas pressure, whose value was originally set to 0,2 bar, in order to minimise the turbulence of the molten surface under the effect of the gas flux. Therefore, given the high sensitivity of the surface under the investigated process conditions, the shielding gas should be carefully considered for further investigations.

Moreover, the investigation of other process parameters is also dictated by the need to further optimise the surface quality and the process stability, considering for instance the high dispersion of S_a for a given process condition.

For sake of clarity, in Table 8.11 are reported the maximum variations of S_a for the process conditions related to the repeatability tests, highlighting the major data dispersion for the high energy density-related process parameters. With this premise, the aim of the defocused beam tests was to analyse the influence of this parameter on the resulting surface quality, given the wider heat input distribution when the laser focus is set above the surface. Furthermore, it is expected that an increase of the laser focus distance from the peaks of the surface, should determine a reduced sensitivity of the laser-surface interactions with respect to the different peaks and valleys heights, as observed previously from the remarkable difference of S_a and S_z between the different samples used for the DoE experimental campaign.

Table 8.11. Maximum S_a dispersion observed for the repeatability tests of Run 3, Run 5 and Run 10.

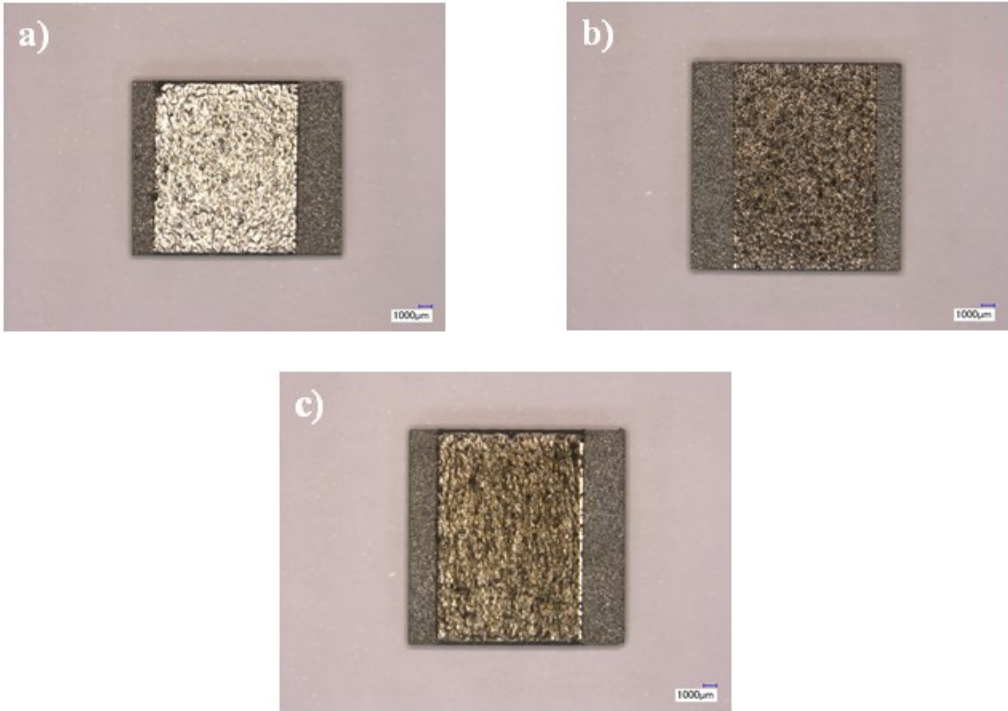| Run	S_a max. dispersion (μm)
3	3
5	< 1
10	3,2

Figure 8.25. Illustration of the re-melted surfaces: (a) Run 3, (b) Run 5 and (c) Run 10.

8.3.2. Defocused beam experiments

According to the previous results, Run 3 was considered as the best case for which the focal position was investigated as a further process parameter. Starting from the reference condition in which the laser focus is set on the surface peaks, the maximum shift considered was 3 mm, investigating the effects of this parameter by means of a 1 mm shift step.

Given the aforementioned dispersion of the starting values of the texture parameters, in Fig. 8.26-8.30 illustrates the evolution of the surface texture parameters as a function of the focal position (F + x mm above surface) as well as considering the repeatability of the achievable results (Rx) compared to Run 3. The results are also reported in terms of 3D acquired surfaces in Fig. 8.31, whereas the actual values measured are reported in Table 8.12. Besides some isolated outlying values that might result from the initial dispersion of the texture parameters, a beneficial effect of the laser focus shift can be observed. More specifically, a linear descending trend can be observed for S_a and S_z, whose further reduction becomes remarkable with respect to the highest focal position shift investigated (+3 mm). However, considering the evolution of S_{sk}, S_{ku} and P_{dq}, there is no experimental evidence of their improvement with respect to Run 3 without defocusing the laser beam.

In addition to the morphology evolution information provided by the SEM images in Fig. 8.32, the obtained results could be justified by a more localised re-melting effect on the surface peaks and a more uniform heat input provided due to a greater laser spot acting on the surface.
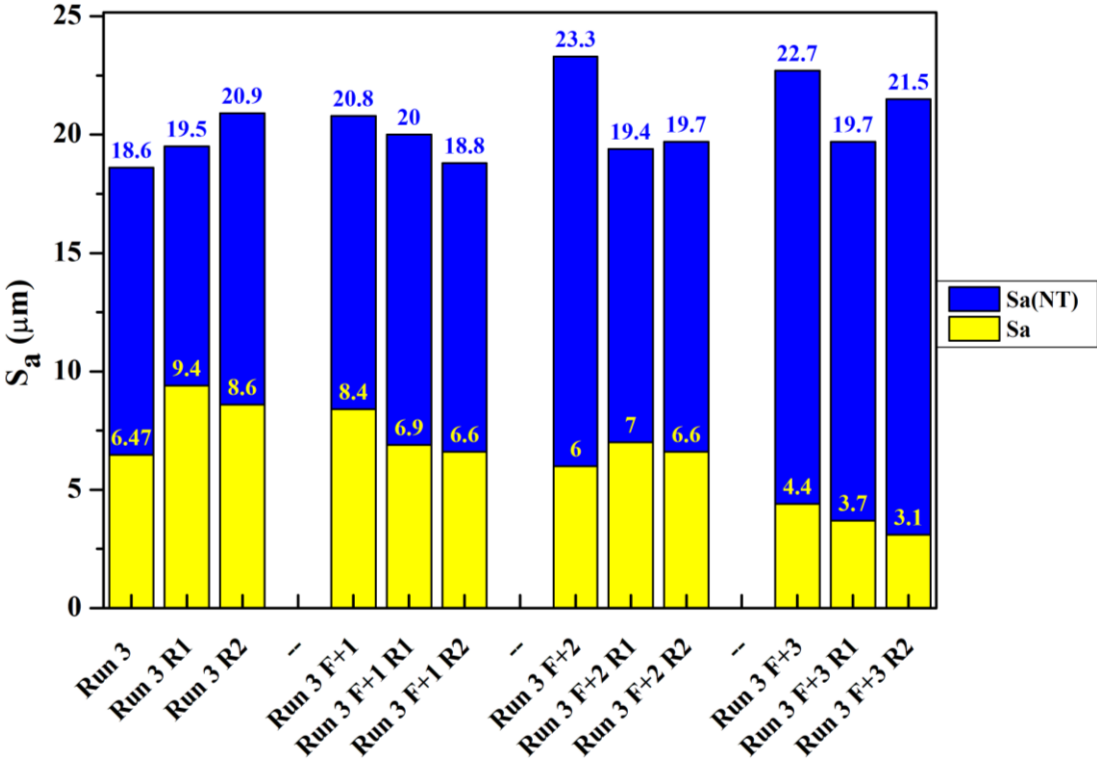

Figure 8.26. Evolution of S_a for the defocused beam tests on Run 3, Run 5 and Run 10 (NT = not treated). The diagram includes the repeatability tests.
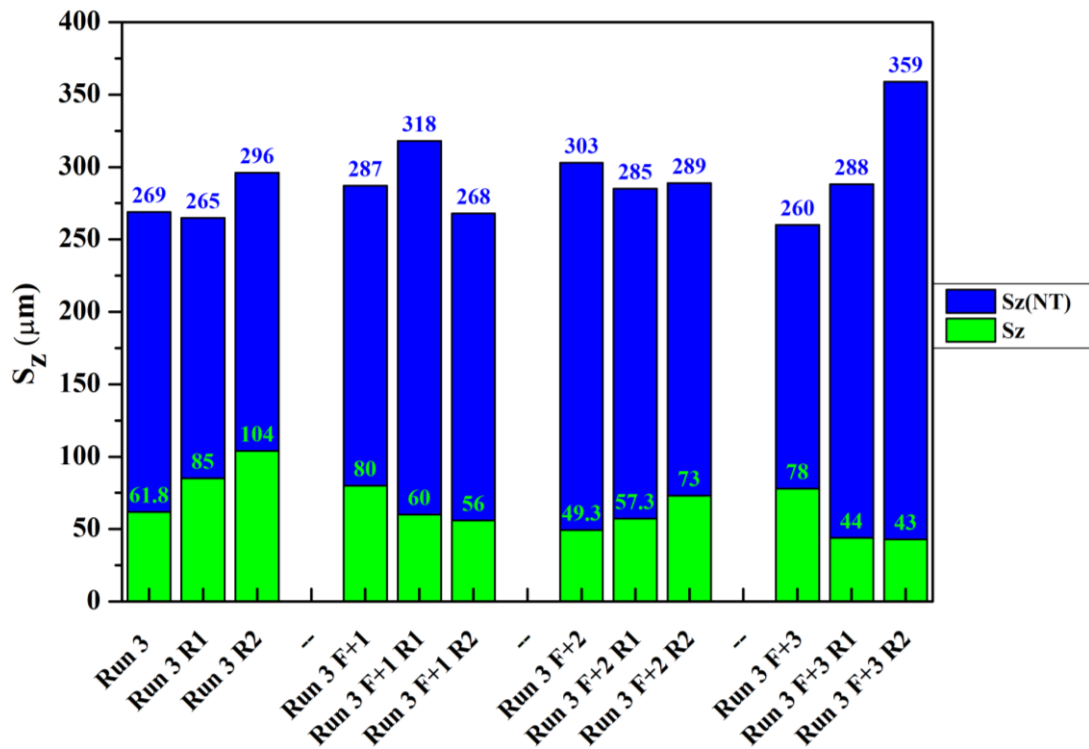
Figure 8.27. Evolution of S_Z for the defocused beam tests on Run 3, Run 5 and Run 10 (NT = not treated). The diagram includes the repeatability tests.
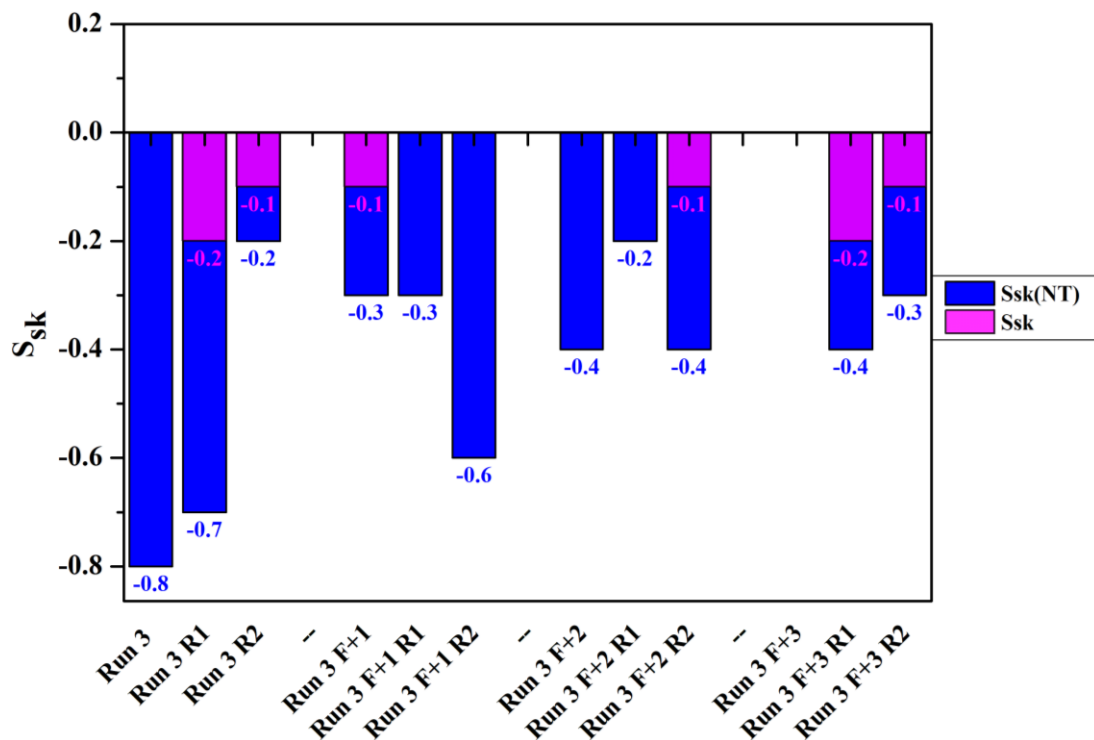

Figure 8.28. Evolution of S_{sk} (if not reported, S_{sk} = 0) for the defocused beam tests on Run 3, Run 5 and Run 10 (NT = not treated). The diagram includes the repeatability tests.
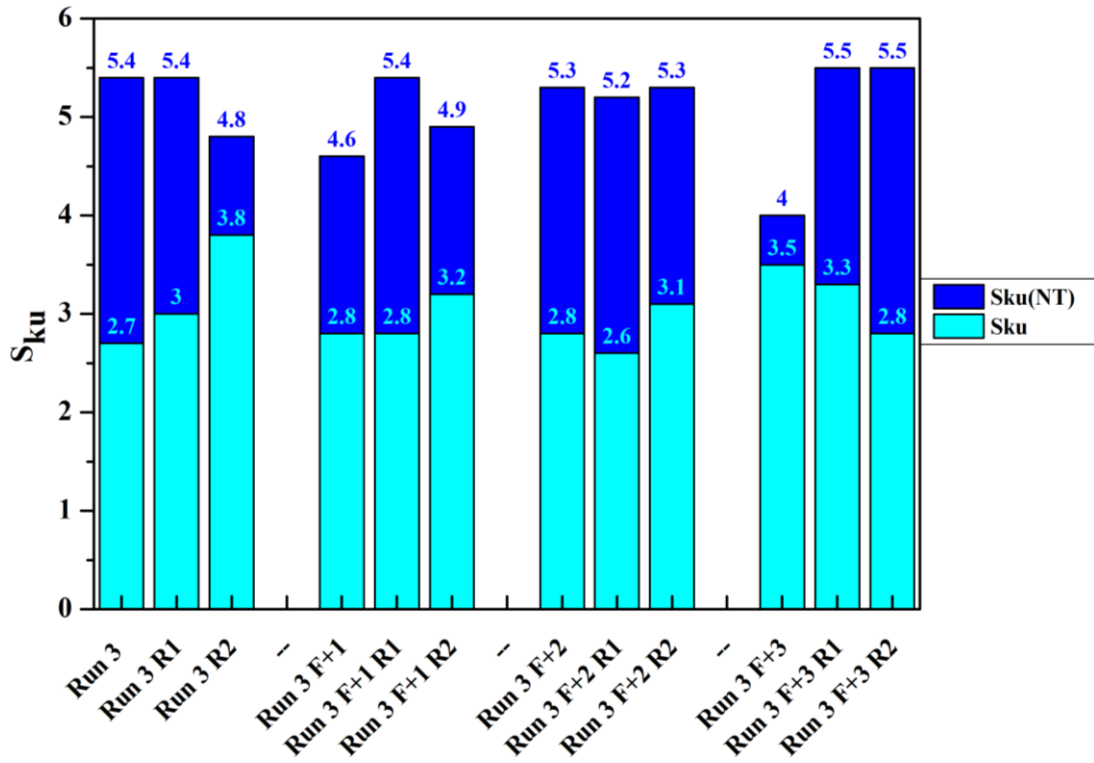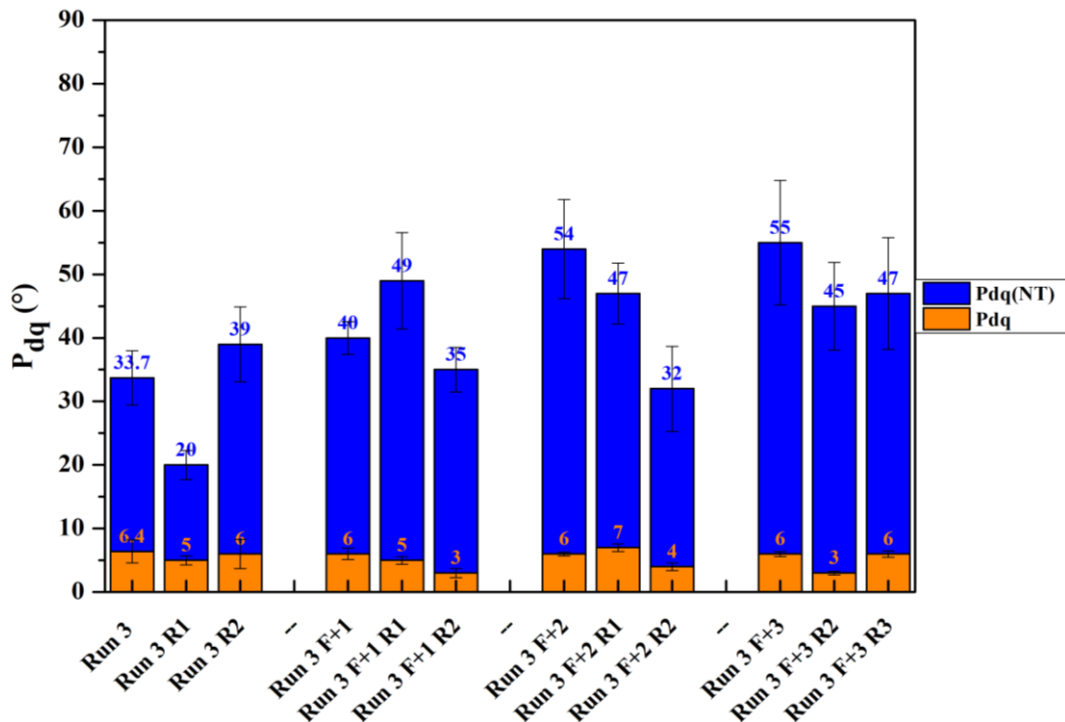
Figure 8.29. Evolution of S_{ku} for the defocused beam tests on Run 3, Run 5 and Run 10 (NT = not treated). The diagram includes the repeatability tests.

Figure 8.30. Evolution of P_{dq} for the defocused beam tests on Run 3, Run 5 and Run 10 (NT = not treated). The diagram includes the repeatability tests.
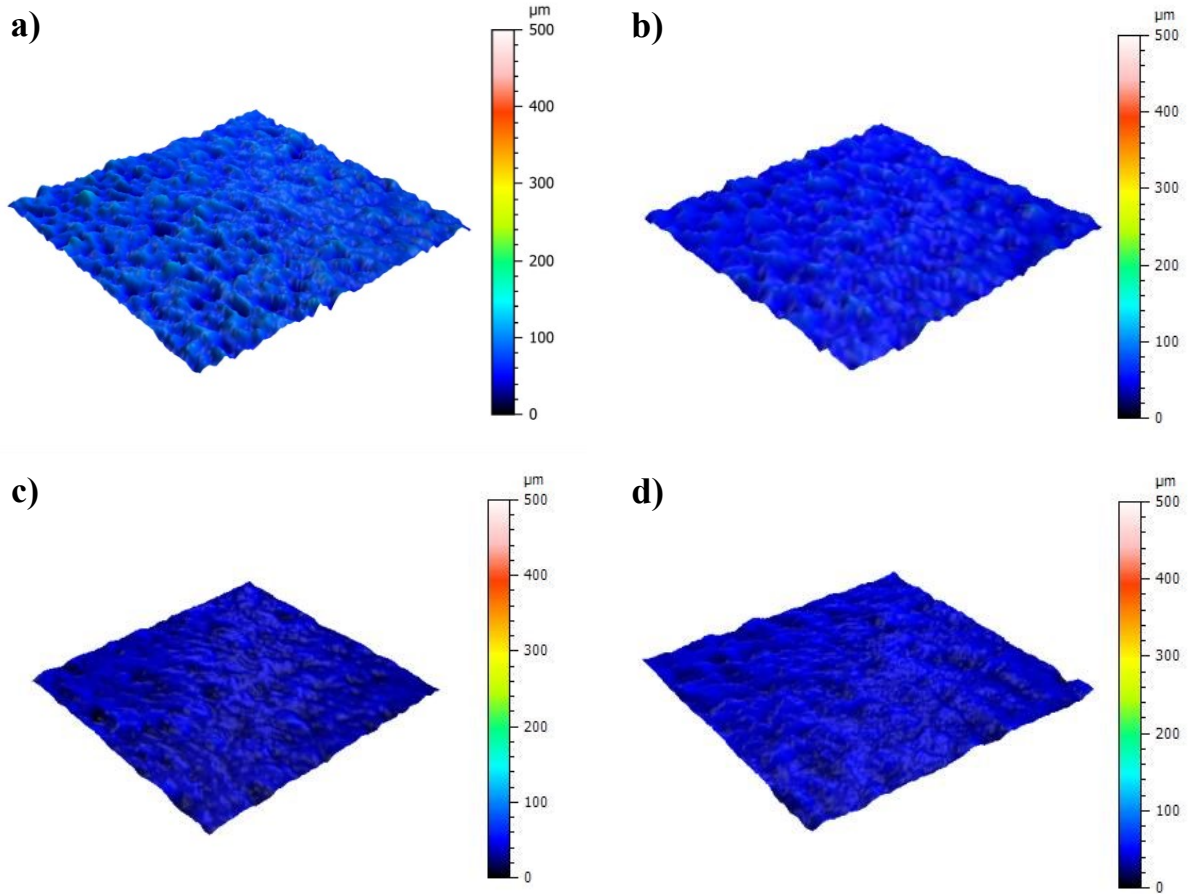
Figure 8.31. Comparison between the 3D surfaces of Run 3 (a), Run 3 F+1 (b), Run 3 F+2 (c) and Run 3 F+3 (d).

Table 8.12. Values of the surface texture parameters measured for the defocused beam experiments, with repeatability information.

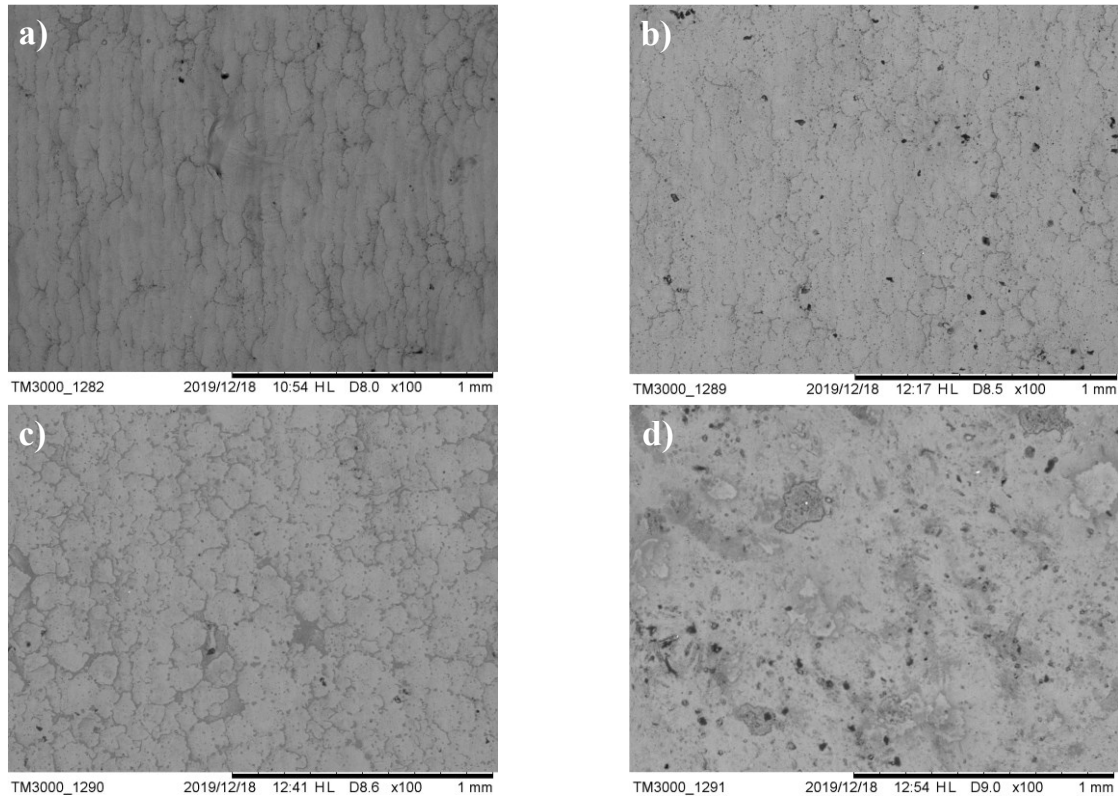|	S_a (NT) (µm)	S_z (NT) (µm)	S_{sk} (NT)	S_{ku} (NT)	P_{dq} avg. (NT) (°)	P_{dq} dev. st. (±σ) (NT) (°)	S_a (µm)	S_z (µm)	S_{sk}	S_{ku}	P_{dq} avg. (°)	P_{dq} dev. st. (±σ) (°)
Run 3	18.6	269	-0.8	5.4	33.7	4.2	6.47	61.8	0	2.7	6.4	1.8
Run 3 R1	19.5	265	-0.7	5.4	20	2.3	9.4	85	-0.2	3	5	0.7
Run 3 R2	20.9	296	-0.2	4.8	39	5.9	8.6	104	-0.1	3.8	6	2.3
Run 3 F+1	20.8	287	-0.3	4.6	40	2.6	8.4	80	-0.1	2.8	6	0.9
Run 3 F+1 R1	20	318	-0.3	5.4	49	7.6	6.9	60	0	2.8	5	0.6
Run 3 F+1 R2	18.8	268	-0.6	4.9	35	3.5	6.6	56	0	3.2	3	0.7
Run 3 F+2	23.3	303	-0.4	5.3	54	7.8	6	49.3	0	2.8	6	0.3
Run 3 F+2 R1	19.4	285	-0.2	5.2	47	4.8	7.2	57.3	0	2.6	7	0.6
Run 3 F+2 R2	19.7	289	-0.4	5.3	32	6.7	6.68	73	-0.1	3.1	4	0.6
Run 3 F+3	22.7	260	0	4	55	9.8	4.45	78	0	3.5	6	0.4
Run 3 F+3 R1	19.7	288	-0.4	5.5	45	6.9	3.72	44	-0.2	3.3	3	0.3
Run 3 F+3 R2	21.5	359	-0.3	5.5	47	8.8	3.12	43	-0.1	2.8	6	0.5

Figure 8.32. Comparison between the SEM images of Run 3 (a) and Run 3 F+1 (b), Run 3 F+2 (c) and Run 3 F+3 (d).

Furthermore, with the aim to compare the process stability in the defocused beam condition, in Table 8.8 are reported the maximum dispersions of S_a for Run 3 and the investigated focus shifts. The results demonstrate the expected decreased sensitivity of the process with respect to the different heights of the peaks and valleys by means of the dispersion reduction compared to the DoE tests.

Table 8.13. Maximum S_a dispersion measured for the defocused beam tests for Run 3.

	S_a max. dispersion (µm)
Run 3	3
Run F+1	1,8
Run 3 F+2	0,4
Run 3 F+3	1,3

On the other hand, two main drawbacks were observed in the defocused beam experiments, i.e. the remarkable surface oxidation for the highest focus shift and the overmelting of the samples edges, as illustrated in Fig. 8.32. This result is justified by the OV% increase when the laser spot is defocused above the surface. This effect counteracts also the E decrease due to the greater spot diameter, implying also that the increase of the tracks overlap represents also a contribution of the surface improvements observed. For the 3 mm focus shift case, the strong oxidation might be caused by the greater distance of the laser head from the molten surface, making the shielding gas pressure even less effective compare to the previous DoE experiments, in which the oxidation issue was already observed. The further increase of the overlap between the tracks leads to the

overmelting at the edges of the samples, given the reduced heat dissipation in that specific zone. Moreover, the overmelting of the edges was more appreciable when the laser focus shift was increased, proving that the resulting E value might be even greater compared to Run 3. Based on these considerations, some further investigations should be considered in order to find the best combination of focal position and OV% that leads to a mitigation of the observed issues as well as the surface improvements measured in comparison with the DoE tests.
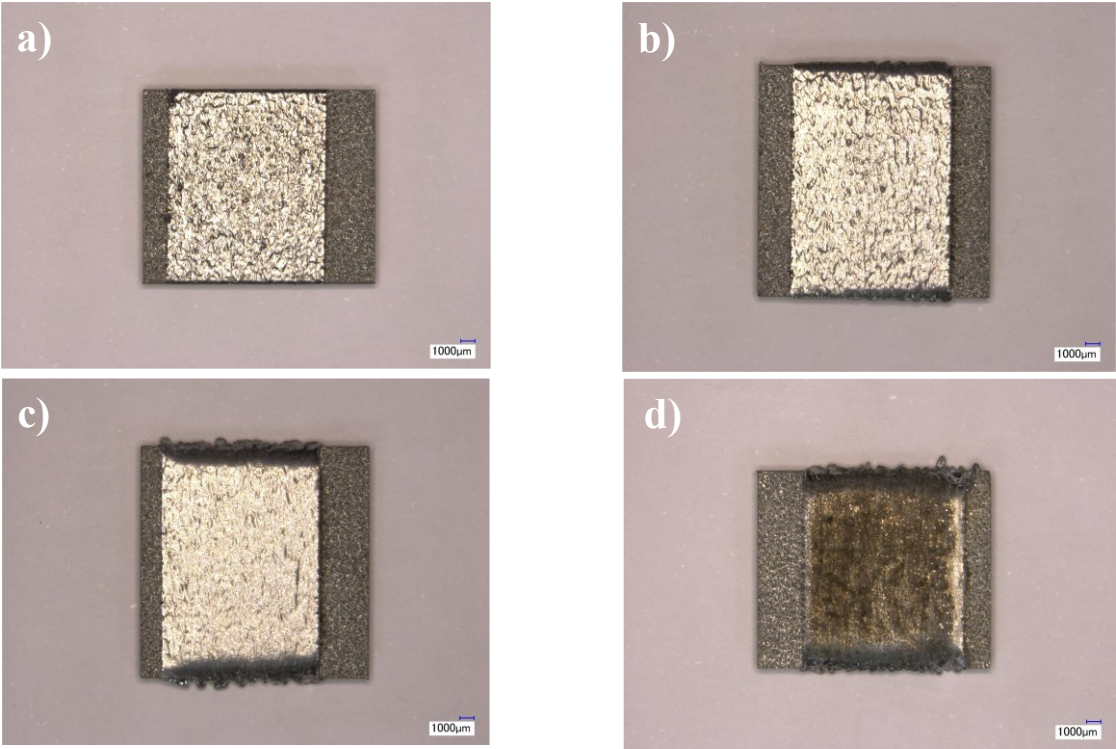
Figure 8.32. Illustration of the re-melted surfaces: (a) Run 3, (b) Run 3 F+1, (c) Run 3 F+2 and (d) Run 3 F+3.

8.4. Microstructure analysis results

The microstructure analysis after CO_2 LSR was carried out on the same process conditions presented previously, for which the repeatability tests were considered. Therefore, Run 3, Run 5 and Run 10 were considered for the DoE tests, as well as the samples treated with the three laser focus shifts, considering the process parameters set related to Run 3 (i.e. Run 3 F+1, Run 3 F+2 and Run 3 F+3).

8.4.1. DoE tests

In Fig. 8.33 are reported the optical macrographs of the considered DoE tests samples. As a general observation, the re-molten zone at the top surface (RZ) is clearly distinguishable in all the cases, highlighted by the presence of the new melt pools generated during the treatment over the existing ones in the base material (BM) processed by SLM. It is worth to note that the latter are clearly visible only in Fig. 8.29b, whereas in Fig. 8.29a-c the microstructure of the base material was observed in the scanning strategy direction (i.e. in a parallel plane to the single layer of the sample). This result is due to the fact that the building direction of the samples was not always parallel to the laser re-melting tracks. Moreover, as a function of the high percentage overlap between the re-melting tracks and the Gaussian power density distribution of the CO_2 laser beam, a Heat Affected Zone (HAZ) is clearly visible, as expectable, at the interface between the RZ and the BM, as well as at the edges of the melt pools produced by re-melting.

These process conditions lead also to different microstructures inside the new melt pools, whose grain size is significantly altered (i.e., coarser) by the multiple re-melting and re-heating of the material imposed by the highly overlapped re-melting tracks. The results of the in-section observations supports well the ones observed for the surface roughness improvements. More specifically, it can be seen that a similar surface morphology was obtained for Run 3 and Run 10 process conditions, whereas a wavy surface was produced when adopting the process parameters related to Run 5. The latter result justifies also the observed trend for the S_{sk} parameter, whose values were more negative after the treatment compared to Run 3 and Run 10.

Furthermore, the similarity of the process conditions of the latter is also confirmed by the comparable re-melting depth measured with respect to the more shallow value observed for Run 5, as reported in Table 8.13. On the other hand, the measured values of re-melting depth are not compatible with a proper evaluation of micro-hardness properties, since the distance between the different regions is very narrow.

For a further microstructure comparison between the investigated samples, it is worth to note that in the case of Run 10 — whose process parameters are related to the highest E value (330 J/mm^2) and OV% (80%) — the presence of some spherical defects in the lower region of the re-molten zone can be appreciated. According to [103], these defects could be ascribable to gas inclusions, whose formation may take place following different mechanisms, such as gas absorption from the outside environment, nucleation and coalescence from some gaseous nuclei already present in the SLM processed material as well as the vaporization of low melting point alloy elements. However, it is reasonable to assume that the melting pool is more susceptible to gas inclusions for higher energy densities imposed to the material during LSR, given the greater gas solubility of the molten metal under higher temperature.
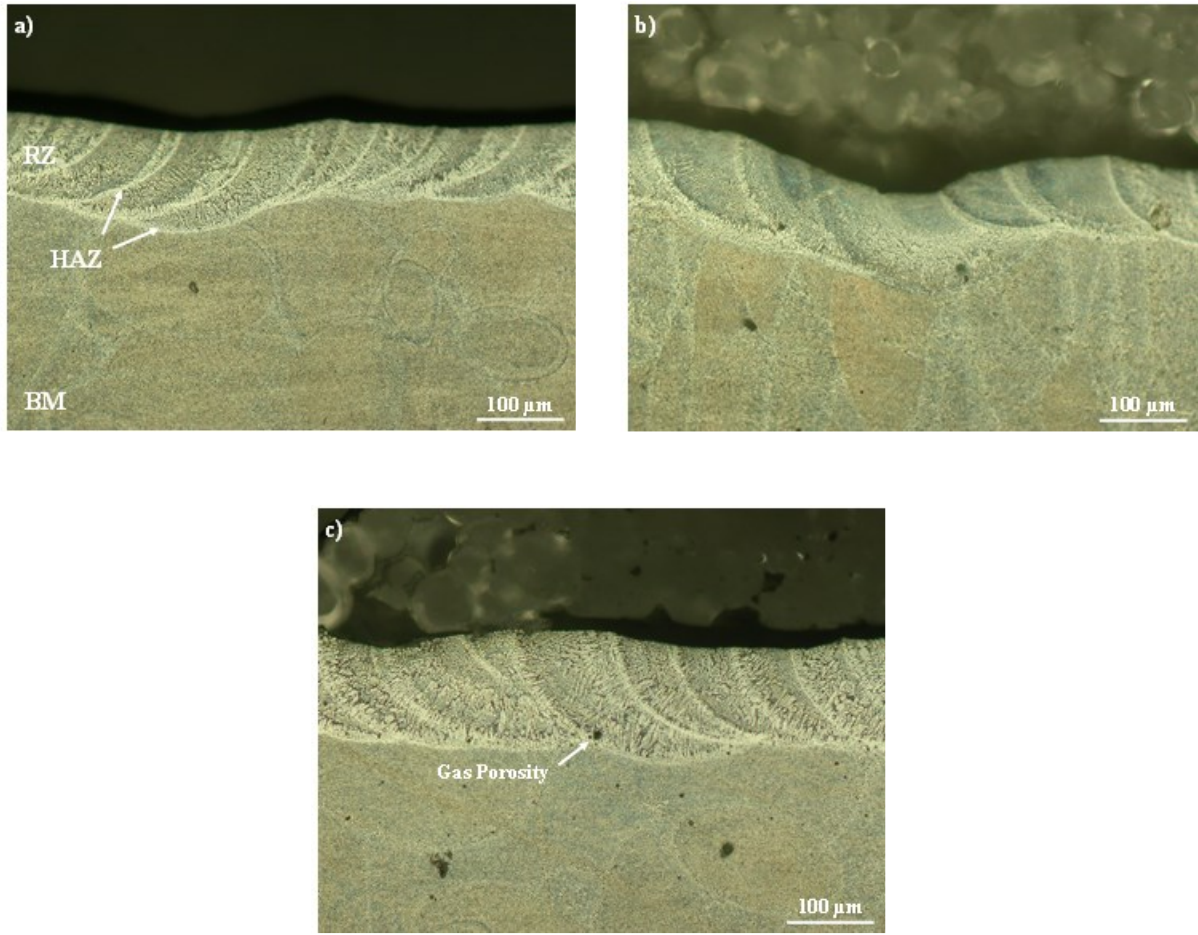
Figure 8.33. Optical macrographs illustrating the microstructure evolution after re-melting for the DoE tests: (a) Run 3, (b) Run 5 and (c) Run 10 (magnification 200x). In (a), the indications of the Base Material (BM), the Re-molten Zone (RZ) and the Heat Affected Zone (HAZ) are reported.

Table 8.13. Re-melting depth measures for the considered DoE tests.

	Re-melting depth avg. (μm)	Re-melting depth st. dev. (±σ) (μm)
Run 3	113	9,8
Run 5	84	13,3
Run 10	115	11,3

A more detailed observation of the microstructure features of the treated samples is provided by the SEM images reported in Fig. 8.34, illustrating the details of the different grain structures observed for the areas identified in the previous macrographs. Starting from the microstructure of the BM (lower area of Fig. 8.34a), whose characteristics have been already discussed in Chapter 7, the different microstructure of the HAZ at the interface with the re-melting pool is clearly visible (upper area of Fig. 8.34a and Fig. 8.34b). More specifically, a coarser cellular microstructure can be appreciated, as well as the preferential orientation of the grains towards the temperature gradient imposed by the re-melting laser beam. This result can be easily explained considering the location of this material portion between the RZ and the BM: since the former experiences a higher cooling rate, the cooling of the HAZ material is forced towards the maximum heat dissipation direction, i.e. the laser axis direction that represents the shorter path between the cold BM and the

fast cooling RZ material. For the latter, the cellular dendritic microstructure (upper area of Fig. 8.34c and Fig. 8.34d) presents coarser grains compared to the BM, but equiaxed compared to the HAZ. This result, as expectable, is caused by the higher cooling rate of the material on the free surface as well as to the aforementioned multiple re-heating cycles imposed by the adjacent re-melting tracks. Therefore, a proper investigation of the induced grains size and structure under the different process conditions is not possible by analyzing solely the reported data, since they are not related to a single re-melting track.

However, considering that for all the investigated samples the distinction between the different microstructures regions is the same, in Fig. 8.31 are reported in comparison the different microstructures in the RZ for the DoE tests samples observed. From the SEM images it can be observed that, in general, the surface treatment led to a growth of the dendrites of the grain boundary eutectic phase caused by the high Si content. This result, that was also greatly affected from the aforementioned multiple re-heating cycles, might lead to a decrease in mechanical properties, for which further analyses are needed.
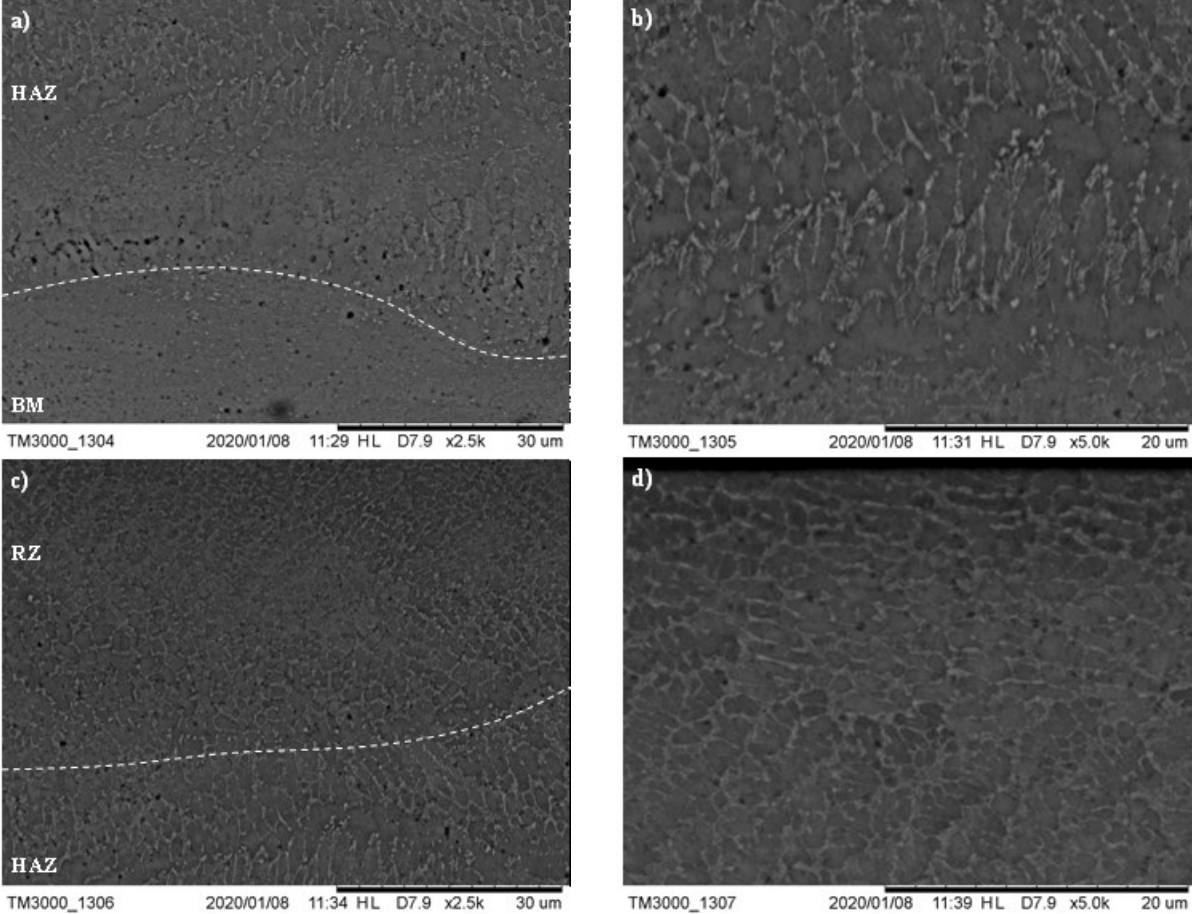

Figure 8.34. SEM images of the different microstructure regions observed after re-melting (Run 3): (a) BM-HAZ interface (2500x), (b) higher magnification of the HAZ reported in (a) (5000x), (c) HAZ-RZ interface (2500x) and (d) higher magnification of RZ reported in (c) (5000x).
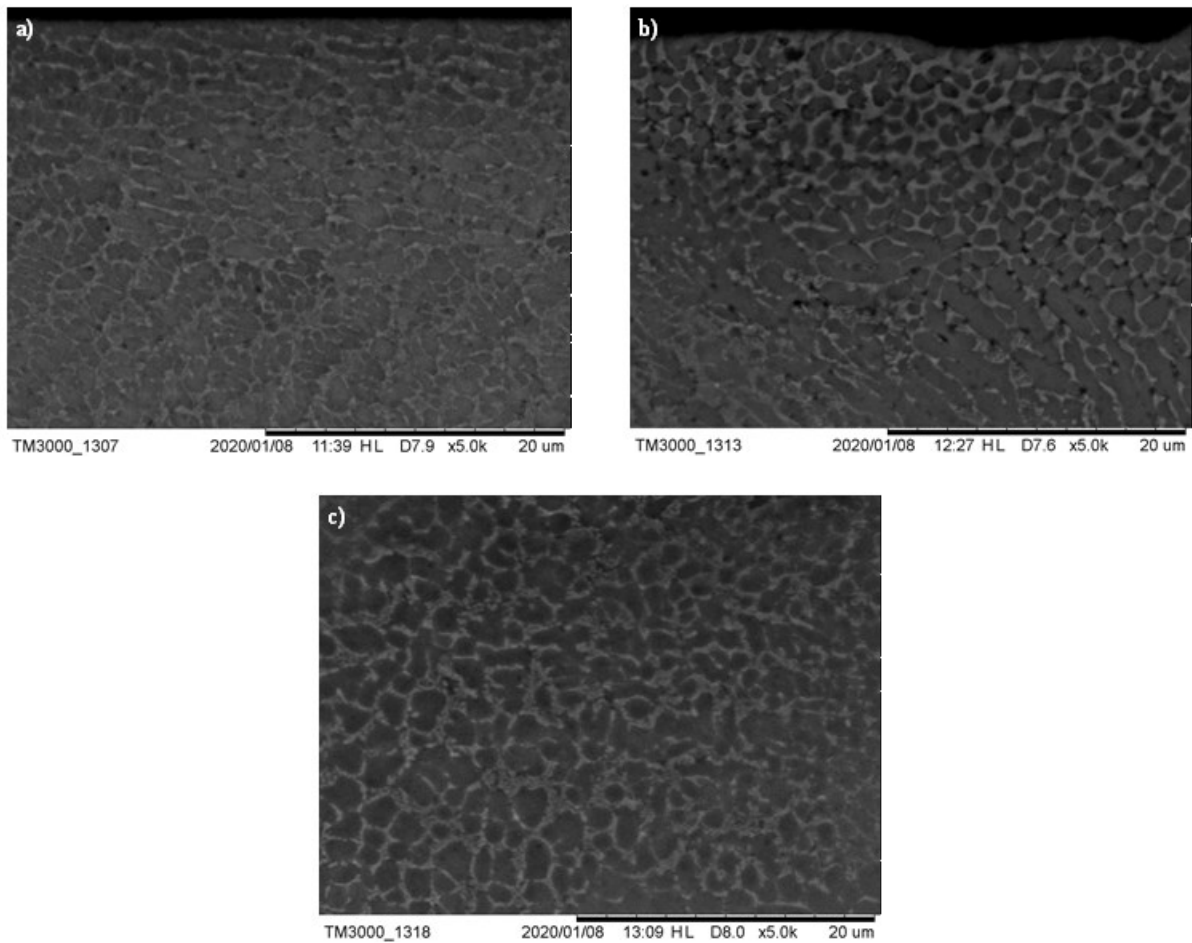
Figure 8.35. Comparison between the microstructures in the re-molten zone for the considered DoE tests: (a) Run 3, (b) Run 5 and (c) Run 10.

8.4.2. Defocused beam tests

In Fig. 8.36 are reported in comparison the optical macrographs obtained for Run 3 and for the three levels of the laser focus shifts above the surface. Considering the measured re-melting depth reported in Table 8.14, the results are also in this case in agreement with the previous considerations about the surface roughness improvements. More specifically, the increase of the re-melting depth with the laser focus shift above the surface indicates that the increased OV% between the re-melting tracks caused by the bigger spot diameter gives a significant contribution to the further reduction of surface roughness observed. This result suggests also that the overall energy input increases over the value established for Run 3.

Furthermore, the effect of the focus shift on the re-melting depth becomes particularly remarkable for the highest value investigated (+3 mm), as also observed from the further reduction of surface roughness in this process condition. On the other hand, among the drawbacks observed in the previous section, the defocused beam condition leads also to a greater extent of the microstructure alteration induced by the surface treatment, opposed to the original aim of these tests. Moreover, as a consequence of the increased energy input, the re-melting pool temperature increases as well as the gas solubility limit of the re-molten metal, leading to a higher number of gas inclusions trapped in the solidified material.
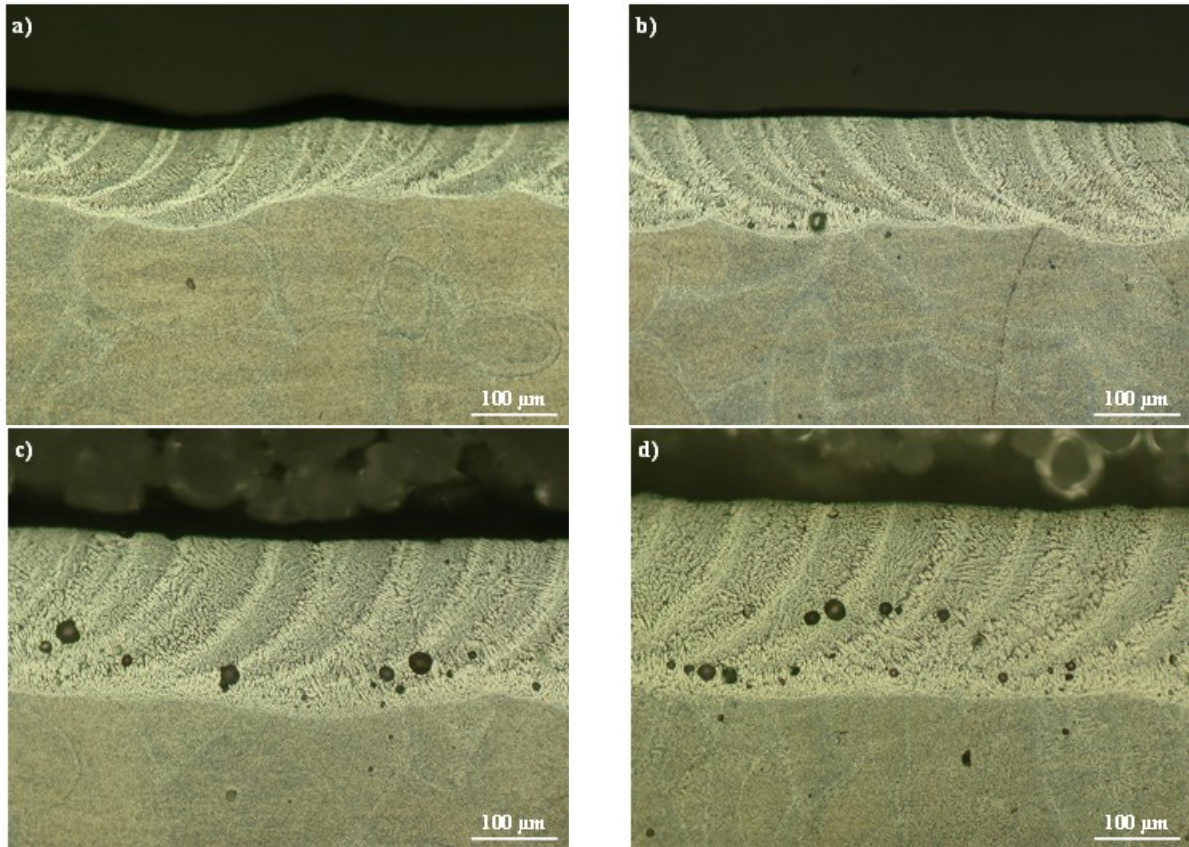
Figure 8.36. Comparison between the optical macrographs that illustrates the effects of the laser defocusing above the surface, starting from Run 3 as the reference: (a) Run 3, (b) Run 3 F+1 mm, (c) Run 3 F+2 mm and (d) Run 3 F+3 mm (magnification 200x).

Table 8.14. Re-melting depth measures for Run 3, as a function of the laser focus shift above the surface.

	Re-melting depth avg. (µm)	Re-melting depth st. dev. (±σ) (µm)
Run 3	113	9,8
Run 3 F+1	135	15,1
Run 3 F+2	144	5,2
Run 3 F+3	180	4,5

In order to show in detail the effects of the laser focus shifting on the microstructure of the processed material, in Fig. 8.37 are reported the SEM images of the different microstructure regions for Run 3 F+3, as it represents the most significant condition in the defocused beam tests. From the results it can be observed that, similarly to the Run 3 of the DoE tests, comparable microstructure features were formed after the treatment in terms of grains orientation and dimension of the dendrites. However, as for the previous tests, also in this case is not possible to distinguish clearly the effects of the energy input on the microstructure evolution, due to the mentioned multiple thermal cycles experienced by the material.

This result was confirmed for all the investigated focus shifts in the experimental campaign, as observable from the comparison of the microstructures in the RZ reported in Fig. 8.38. Therefore, the observed microstructures induced by the treatment in the defocused beam condition suggests that more proper combinations of the OV% and laser focus shift needs to be investigated. This

experimental outcome takes into consideration also the drawbacks discussed before such as the overmelting of the edges, the higher sensitivity of the material to oxidation, the increased sensitivity to gas inclusions and the higher re-melting depth.

Finally, on the basis of the observed results, more proper values of the shielding Argon pressure are needed in order to enhance the environment control during LSR against surface oxidation and absorption of gas bubbles in the melting pool.
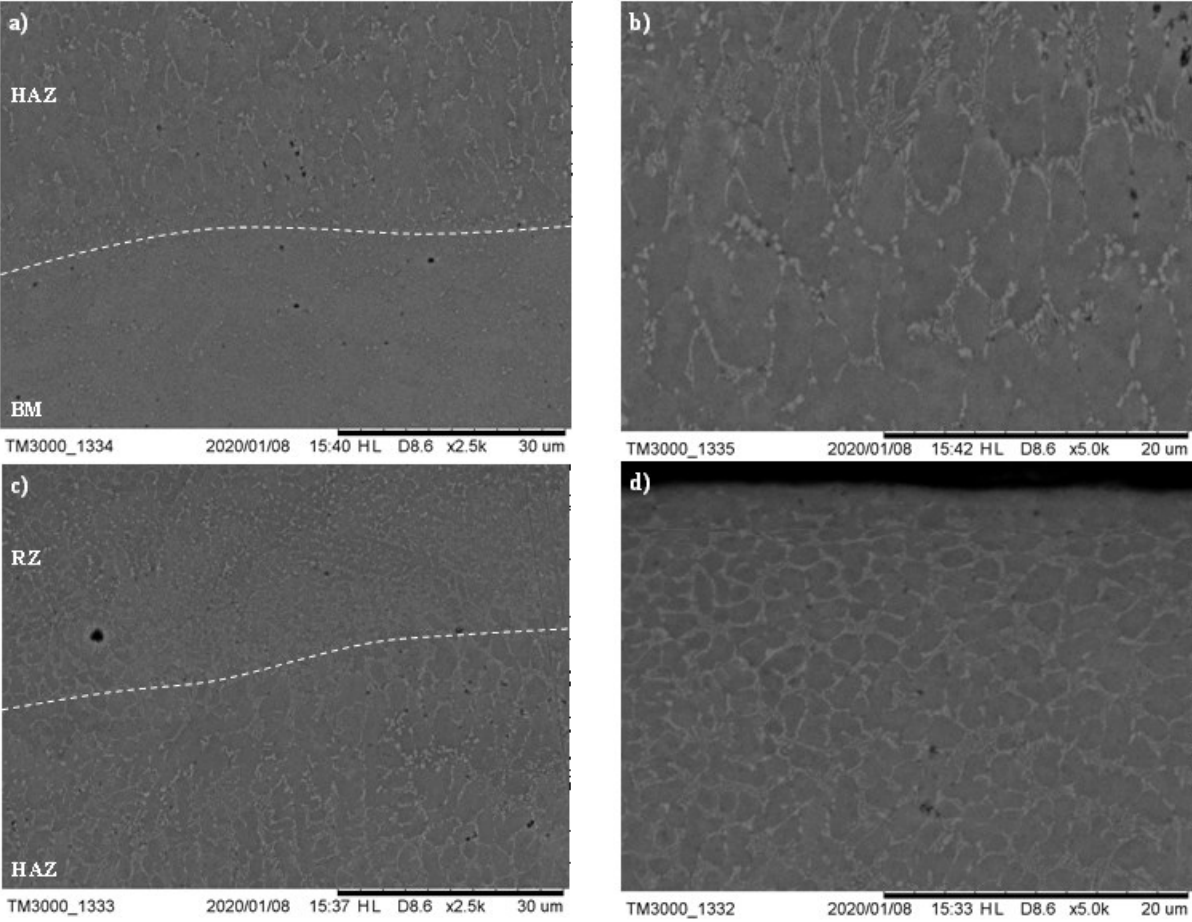

Figure 8.37. SEM images of the different microstructure regions observed after re-melting (Run 3 F+3): (a) BM-HAZ interface (2500x), (b) higher magnification of the HAZ reported in (a) (5000x), (c) HAZ-RZ interface (2500x) and (d) higher magnification of RZ reported in (c) (5000x).
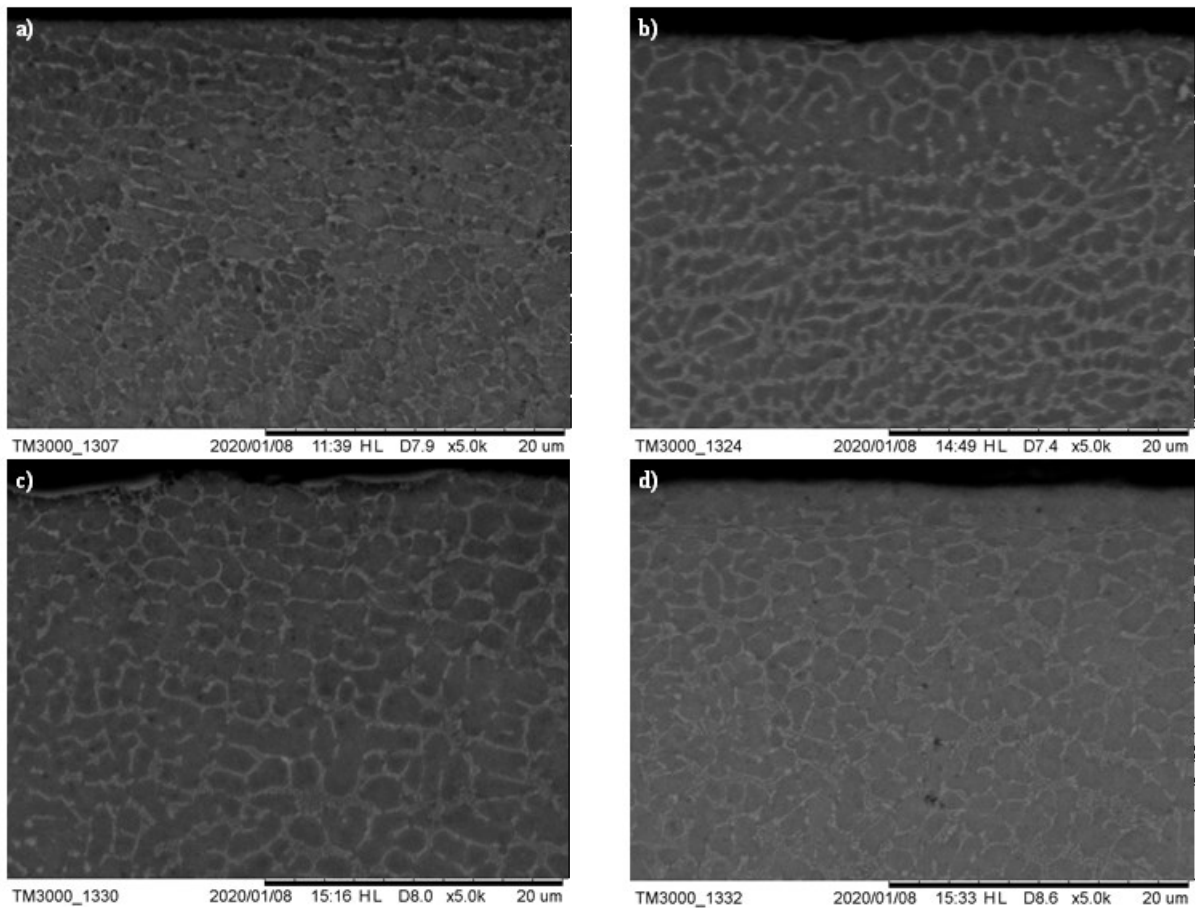
Figure 8.38. Comparison between the microstructures in the re-molten zone for the considered defocused beam tests and Run 3: (a) Run 3, (b) Run 3 F+1, (c) Run 3 F+2 and (d) Run 3 F+3.

8.5. Conclusions

In this Chapter, the results of the CO_2 LSR process for AlSi10Mg alloy samples made by means of SLM were reported and discussed. The aim of the presented experimental campaign was to evaluate the feasibility of a CO_2 laser beam to perform a surface re-melting, taking advantage of the high surface roughness of the as-built samples that enhances the very low CO_2 laser radiation absorption from the considered AlSi10Mg alloy. At the best knowledge of the author, the experimental study of this specific LSR process configuration represents a completely novel work. This essay takes into consideration that the most contributions reported in literature are related to the use of shorter wavelength lasers, whose absorption from Aluminum alloys is quite higher both for the LSR of traditional and AM parts. Based on the description of the methodology approach and the observed results, the following conclusions can be drawn:

- Within the process parameters window investigated during the DoE tests, determined on the basis of preliminary tests, the finishing treatment provides a consistent surface improvement compared to the as-built samples.
  Considering S_a as the primary roughness parameter to take into consideration for the evaluation of the treatment effects, a reduction of approximately 60% was observed regardless of the specific starting value of the untreated surface. The feasibility of the process was proved also by means of the different surface texture indicators chosen in this work, suggesting a remarkable improvement of the surface symmetry (S_{sk}) and brilliance (P_{dq}). In this context, the best results were achieved with respect to the process parameters

sets that provided the highest energy density values within the DoE process window;

- The process repeatability related to the cases investigated within the DoE experiments provided a remarkable dispersion of the surface texture parameters, especially for high energy density-related process conditions. This result might be due to the high sensitivity of the laser-surface interactions as a function of the different heights of the peaks and valleys on the surface, as observed by the high dispersion of the initial values of S_a and S_z. This point represented the premise of the further experimental investigations carried out in the best case, for which the laser focus position with respect to the peaks of the surface was considered as a further process parameter;

- The defocused beam experiments proved that, starting from a focal position set on the peaks of the surface, a focus shift above the surface provides further surface quality improvements. The highest S_a and S_z reductions (85% and 81% respectively) were measured for the focus shift of 3 mm, whereas S_{sk}, S_{ku} and P_{dq} were not significantly improved in comparison with the results obtained from the starting best case of the DoE tests;

- The observed surface improvements for the laser focus shift above the surface were also due to an increased OV% between the single re-melting tracks, counteracting the energy density reduction caused by the increased spot size in the investigated defocused beam conditions. The combination of these two changes, with respect to the DoE tests, provided the discussed surface quality improvements at the previous point, but also some drawbacks such as the overmelting of the samples edges and an increased molten surface sensitivity to gas inclusions, due to a reduced effect of the shielding gas.
To overcome these issues, the OV% between the tracks and the shielding gas pressure should be considered as factors for a new DoE, aimed to optimise the results achievable from the defocused beam process configuration under the best laser power and scanning speed values determined by means of the DoE tests;

- All the experimental outcomes observed in terms of surface roughness analysis were also in agreement with the measured re-melting depths. For the DoE tests, the latter were higher for the process conditions that led to the highest surface improvements, whereas shallower depths were observed for the low areal energy density-related experiments, whose related surface quality improvement were less significant.
Moreover, the re-melting depth increased for the defocused beam experiments, according to the greater overall heat input provided based on previous point. This result was in contrast to the original aim of the defocused beam tests, i.e. the reduction of the microstructure alteration observed from the DoE tests. Therefore, a further experimental investigation of the defocused beam configuration is needed, in order to find the best combination of focus position and OV%. It is worth to note that the need for the latter is also related to the aim of minimizing the gas inclusions observed in the defocused beam condition, as a consequence of the increased areal energy density that promoted a higher gas solubility from the re-molten material and the less effective protection from the shielding gas;

- In terms of microstructure evolution, the LSR process led to coarser grains compared to the ones related to the as-built samples, considering both the DoE and the defocused beam experiments. However, a proper investigation of the LSR process parameters effect on the grain size was not possible, due to the multiple re-melting and re-heating cycles experienced by the material, according to the significant OV% related to the investigated process conditions. As expectable, the grain coarsening could lead to a decrease of the mechanical properties of the re-melted surface, an aspect that deserves further investigations.

9. General conclusions

This work was focused on the post-process surface treatments for AlSi10Mg parts made by means of SLM. A consistent experimental activity was carried out on simple geometry samples in order to provide a detailed explanation of the phenomena occurring under the effect of three different surface treatments. The latter were chosen according to their different nature, i.e. Fluidised Bed Machining (FBM) as a mechanical interaction-based treatment, Chemical Polishing (CP) as the chemical interaction-based treatment and CO_2 laser re-melting (LSR) as the thermal interaction-based treatment. Besides the main focus of surface roughness improvement, a specific attention was also paid on the effects on the material chemistry alteration as well as on the microstructure changes involved for the different treatments investigated.
In order to evaluate the surface modifications determined by the treatments, Confocal Microscopy was used as a quantitative surface characterisation technique, given its capabilities to analyse areas and to provide the related surface texture parameters. Moreover, the results were supported by qualitative analyses carried out by means of SEM, as well as by further quantitative analyses carried out by means of EDS, Optical Microscopy and weight loss measurements.

Based on the preliminary conclusions reported for each surface treatment and given the investigated parameters for the different processes, the aim of this Chapter is to provide more general conclusions, divided in three sections. The first section provides a surface quality benchmark for the considered finishing processes, considering the best case obtained for each treatment and describing the related surface characteristics. Subsequently, the second section points out which are the main limitations of the experimental approach followed in this work. Finally, the last section provides a critical comparative analysis of the three investigated processes, according to different criteria such as process feasibility for a given geometry, costs, process time and environmental sustainability.

9.1. Surface quality benchmark between the investigated treatments

In Table 9.1 are reported, in comparison, the surface texture parameters values before and after the treatments, according to the respective best cases, i.e.:

- FBM: according to the results reported in Chapter 6, the best case was obtained in the rotating sample configuration, using irregular stainless steel abrasives. The best impact angle investigated was 25° and a relative tangential speed between the surface and the fluidized abrasives of 2 m/s. Moreover, it was observed that a proper process strategy promoted a great homogeneity of the surface, by means of dividing the total process time (30 min) into the sum of 5 min steps and alternating the rotation verse of the sample between each step;

- CP: according to the results reported in Chapter 7, the best case was obtained for the combination of the highest bath temperature, both for the Chemical Machining (85 °C) and Chemical Brightening stages (95 °C);

- CO_2 LSR: according to the results reported in Chapter 8, the best case was obtained for the defocused beam configuration, considering the process parameters related to Run 3 and the highest focus shift considered (i.e. 3 mm above the peaks of the surface).

The results are reported both in terms of actual values and in terms of percentage variation. Generally speaking, it can be observed that all the investigated treatments led to significant surface quality improvements, besides some drawbacks observed and discussed for each of the investigated processes.

In first instance, the surface smoothing can be appreciated from the consistent reductions of S_a and S_z. However, as stated several times in this work and as observable from Table 9.1, the different initial surface status of the samples makes difficult a precise quantification of the surface quality improvements induced by the investigated treatments, given the high dispersion of the starting values. As stated for the first time in Chapter 6, this result is due to the presence of sintered powders on the surface, whose size is different as a function of the powder feedstock size distribution, the build-up of different sintered powders on the surface and the presence of defects due to the SLM process, such as lack of fusion. In relation to the results obtained, it can be observed that comparable percentage reductions of S_a and S_z were achieved for the FBM and CO_2 LSR treatments, whereas slightly lower reductions were observed for the CP treatment.

In terms of surface symmetry evolution, investigated through the analysis of S_{sk}, a different behavior can be easily observed for the FBM treatment if compared to CP and CO_2 LSR. More specifically, the surface treated with FBM presents a significant asymmetry from the valley side, whereas S_{sk} is closer to 0 for the other two treatments. As stated in Chapter 6, the asymmetry of the FBM treated surface was due to the more effective erosion of the surface peaks from the fluidized abrasives. For an optimization of this parameters, longer process times could be considered for instance. The latter could increase the erosion of the surface morphology underlying the sinter powders layer, promoting therefore the removal of the residual valleys and defects caused by the SLM process.

Concerning the analysis of the sharpness of the peaks, represented by the evolution of S_{ku}, a different behavior between FBM with respect to CP and CO_2 LSR can be observed again. In this case, the latter led to an appreciable smoothing of the surface, whereas a sharpening effect was observed in the case of FBM. This result could be ascribed to the random impacts of the fluidized abrasives on the surface, whose features dictated by the presence of sintered powders are also random. Moreover, considering the less sensitivity of S_{ku} to the roughness scale, this surface texture parameter could not represent a good descriptor of SLM processed surfaces. It is worth to note that this consideration was also statistically proved in the ANOVA analysis carried out for the CO_2 LSR treatment, despite the appreciable reduction observed for all the tests.

Finally, in agreement with the evolution of S_a and S_z, the average slope analysis carried out through the investigation of P_{dq} confirmed the remarkable surface quality improvements induced from all the three surface treatments. In fact, the same benchmark results could be observed for this parameter in Table 9.1., with very similar conclusions with respect to S_a and S_z. On the other hand, it was also stated in Chapters 6,7,8 that this parameter was the most sensitive with respect to the investigated processes conditions. This is due to the removal of the sintered powders on the surface that, as easily observable, contributes to the high slope measured for the starting surfaces. Moreover, given the wide size distribution of the sintered powders, the slope could change accordingly and justifying the very different starting values observed for P_{dq}. However, the presented results suggests that the surface brilliance can be effectively improved within the process parameters window investigated for each surface finishing process reported in this work.

Table 9.1. Surface texture parameters benchmark between the best cases for the three surface treatments investigated.

	FBM	CP	CO$_2$ LSR
S$_a$ (NT) (µm)	24,8	21,3	21,5
S$_a$ (µm)	4,9	6,7	3,1
S$_z$ (NT) (µm)	448	228	359
S$_z$ (µm)	77	73	43
S$_{sk}$ (NT)	0	0,1	-0,3
S$_{sk}$	-0,8	0	-0,1
S$_{ku}$ (NT)	3,5	3,6	5,5
S$_{ku}$	5,4	2,9	2,8
P$_{dq}$ (NT) (°)	71	41	47
P$_{dq}$ (°)	5	4	6
ΔS$_a$ (%)	-80%	-69%	-86%
ΔS$_z$ (%)	-83%	-68%	-88%
ΔS$_{sk}$ (%)	-80%	+10%	+33%
ΔS$_{ku}$ (%)	+36%	-20%	-50%
ΔP$_{dq}$ (%)	-99%	-90%	-88%

9.2. Main limitations of the experimental methodology

Regardless of the specific surface treatment investigated, it is worth to mention some of the main issues and limitations related to the experimental work reported in this thesis. One of the most important issues observed is the high dispersion of the surface texture parameters measured for the samples before the treatment. As stated several times in this work, this issue makes more difficult a proper quantification of the real surface roughness status, as well as the improvements provided by the investigated treatments. This result is due to different factors involved in the whole experimental chain, such as the high dispersion of the powder size distribution related to the feedstock used in the SLM process. This leads to a surface characterised by peaks and valleys whose height is directly dependent on the powder size. Moreover, the presence of parts defects such as lack of fusion and undercuts caused by the sintered powders on the surface alter significantly the quality of the surface acquisition and reconstruction by means of the confocal microscopy.

With this premise, an SLM process parameters optimization would represent the first point of further investigation, in order to generate surfaces with less dispersed surface features and defects. Consequently, in order to obtain more accurate estimates of the surface status, the use of more sophisticated surface characterisation techniques such as X-Ray Computed Tomography (X-CT) would represent an intriguing solution for an in-depth analysis, overcoming the typical limitations of contact probe-based and non- contact light-based surface characterisation methods.

Finally, in relation to the main limitations of the experimental campaign reported in this work, it is worth to mention that an extremely important SLM process variable was not considered at this stage: the build angle of the samples with respect to the building platform. According to the influence of this process parameter on the surface roughness described in Chapter 3, the introduction of the stair-step effect and a surface roughness difference between the downskin and upskin surfaces represents a fundamental factor to take into account in the surface finishing analysis. More specifically, the capability of the investigated surface treatments to give the desired stable surface improvements on surfaces produced with different building angles represent the primary goal to pursue in order to consider their feasibility for complex geometry parts.

9.3. Critical comparison of the investigated surface treatments

Given the results discussed in the previous Chapters and the benchmark results reported previously for the best cases, this work is concluded by providing a brief critical comparison between the three investigated surface finishing processes. The comparison is reported considering different aspects, including the feasibility for complex parts, costs and times, ease to processes scale-up and environmental sustainability.

However, it is worth to note that most of the equipment used in this work is related to laboratory scale experiments. Therefore, a proper cost analysis is not possible at this stage.

FBM

As discussed in Chapters 3 and 6, the FBM treatment consists in the immersion of a part into a fluidised bed. Given the high mobility of the fluidised particles, this surface treatment surely represents a promising solution for the finishing of complex geometry parts such as the Additive Manufactured ones. However, according with the experimental setup used in this work, some complex part features would be difficult to be polished, such as lattice structures. Therefore, complex parts features such as internal open channels, holes and inclined surfaces could represent the main target for FBM.

Concerning the whole process, the experimental apparatus and the process inputs needed, it can be easily concluded that FBM does not represent a high cost solution for the post-AM surface finishing. Given the simplicity of the reactors, the use of air to fluidise the abrasive particles and the simple motion systems for the parts to be treated, the process is also easy to scale-up. Considering the costs, the major contribution to this aspect is given from the abrasives, whose cost could change in a considerable way depending on the chosen material (for instance, stainless steel particles are more expensive compared to alumina particles).

The low cost of FBM is also related to the relatively short times needed for the surface finishing process. As observed in this work as well as in similar works reported in literature, the surface polishing of metal AM parts by means of FBM is generally carried out within 1 hour. This aspect, combined with the low operating cost of the reactor, surely represents an advantage of FBM compared to other surface treatments, such as CP and LSR.

Finally, considering that solid abrasive particles are used in combination with air in a closed reactor, FBM represents also a viable and environment-friendly solution.

CP

CP consists in the immersion of a part into a chemical bath, whose composition is tailored for the specific material of the part to be polished and kept under controlled temperature and stirring conditions. From the feasibility point of view for the treatment of complex parts, CP probably represents the most intriguing solution due to the high physical accessibility of the chemical solution into the parts features. This leads to a higher process feasibility for complex AM parts with respect to FBM and LSR, even considering small size and highly ordered features such as lattice structures. However, careful considerations are needed in this case with respect to the process control, since the smoothing effect can be stopped only with a complete removal of the solution from the whole surface of a part. The latter operation, depending on the specific feature, could not be always an easy task.

On the other hand, according to the experimental results obtained and reported in Chapter 7, another process benefit in relation to the feasibility for complex parts is the constant etch rate as a function of the evolving surface morphology under treatment once the process parameters set is fixed. More specifically, the constant etch rate combined with the high accessibility of the solution in different parts features ensure that even if the latter possesses a different initial surface quality, an homogeneous result can be still achieved.

Still according to the experimental results reported in Chapter 7, the CP process times with respect to FBM are comparable: even considering the need for two finishing stages and the intermediate rinsing in CP, the total process time is, in general, no longer than 1 hour, representing a positive aspect in relation to the lead time of the AM produced part. On the other hand, the process costs are quite higher in relation to the whole CP process chain. More specifically, given the use of acid baths under high temperature, the process equipment is surely less cost-effective and more complex compared to FBM and LSR. This essay is particularly true when the process needs to be scaled. Another significant cost voice is related to the higher process safety risks: as a consequence of the use of acids, the need for more specialised labor as well as for more sophisticated safety and toxic waste disposal procedures leads to remarkable costs. Nevertheless, compared to FBM and LSR, the use of chemical baths surely makes the CP process less environmental-friendly.

CO$_2$ LSR

Regardless of the specific case investigated in this work by means of a CO$_2$ laser source, LSR represents an intriguing surface polishing technique for metal AM parts, as also observed in Chapter 8. However, one of the main drawbacks in this case is the poor accessibility of the laser beam into specific features of AM parts. Therefore, this treatment has surely a more narrow application span in comparison with FBM and CP, unless in-situ solutions are adopted. Furthermore, if LSR is performed in proper conditions without material ablation, no material loss occurs during the process. This result, as expectable, represents a great advantage in terms of dimensional accuracy of the final products and their related design. More specifically, the latter case refers to the absence of extra material needed build a part, in order to compensate the amount removed during surface finishing operations. This represents an undoubted benefit of LSR compared to FBM and CP.

In terms of process time, LSR is quite more convenient compared to FBM and CP: in general, the polishing process time is limited to a few minutes. Moreover, the high degree of the process automation guarantees a high process stability and repeatability. However, according to the results obtained in Chapter 8, the random nature of the surface texture of SLM parts hamper this well known advantage of LSR. Therefore, as also observed at the end of Chapter 8, this effect needs to be compensated through the beam defocusing operation. The latter, if combined with proper values of OV% between the single re-melting tracks, surely mitigates this issue as well as the mechanical properties alteration.

The costs related to LSR could be mainly ascribed to the laser purchase, operation and labor. The cost voices are expected to be higher for LSR if compared to FBM and CP. On the other hand, a high flexibility is achieved, since in LSR there are no physical tools subjected to wear. This represents a great advantage over FBM and CP, considering the abrasive particles wear in the former process and the saturation and end of life of the chemical bath in the latter. On the other hand, the process setup times, as well as the surface extension, could largely change depending on the specific geometry to be polished, making very difficult a general process cost analysis in the case of LSR.

Finally, in terms of environment sustainability, LSR is surely an effective solution considering the absence of toxic substances needed and the very low risks for operators, the latter achievable through a closed environment operation under controlled atmospheres.

References

[1] I. Gibson, D. Rosen, B. Stucker, *Additive Manufacturing Technologies* (Springer, New York, 2015), 30–41;

[2] ISO/ASTM 52900:2015(E), *Standard Terminology for Additive Manufacturing Technologies-General Principles-Terminology*, ASTM International, West Conshohocken, PA, 2015;

[3] T. Wohlers, T. Gornet, *Hystory of Additive Manufacturing*, Wohlers report 2016;

[4] A.Gebhardt, *Understanding Additive Manufacturing* (Hanser, Munich, 2012), 2-5;

[5] M.K. Thompson, G. Moroni, T. Vaneker, G. Fadel, R.I. Campbell I. Gibson, A. Bernard, J. Schulz, P. Graf, B. Ahuja, F. Martina, *Design for Additive Manufacturing: Trends, opportunities, considerations, and constraints*, CIRP Annals Vol. 65 (2), 2016, 737-760;

[6] J. Faludi, C. Bayley, S. Bhogal, M. Iribarne, *Comparing environmental impacts of additive manufacturing vs traditional machining via life-cycle assessment*, Rapid Prototyping Journal Vol. 21 (1), 2015, 14-33;

[7] S. Ford, M. Despeisse, *Additive manufacturing and sustainability: an exploratory study of the advantages and challenges*, Journal of Cleaner Production Vol. 137, 2016, 1573-1587;

[8] U.M. Dilberoglu, B. Gharehpapagh, U. Yaman, M. Dolen, *The Role of Additive Manufacturing in the Era of Industry 4.0*, Procedia Manufacturing Vol. 11, 2017, 545-554;

[9] S.H. Masood, *Advances in Fused Deposition Modeling*, Comprehensive Materials Processing Vol. 10, 2014, 69-91;

[10] J. Kruth, X. Wang, T. Laoui, L. Froyen, *Lasers and materials in selective laser sintering*, Assembly Automation Vol. 23 (4), 2003, 357-371;

[11] W. E. Frazier, Metal *Additive Manufacturing: A Review*, Journal of Materials Engineering and Performance Vol. 23, 2014, 1917-1928;

[12] J. Li, B. Wu, C. Myant, *The current landscape for additive manufacturing research* (ICL AMN report, London, 2016);

[13] J. Deckers, J. Vleugels, J.P. Kruth, *Additive Manufacturing of Ceramics: A Review*, Journal of Ceramics Science and Technology Vol. 5 (2014), 245-260;

[14] J.W. Halloran, *Ceramic Stereolithography: Additive Manufacturing for Ceramics by Photopolymerization,* Annual Review of Materials Research Vol. 46, 2016, 19-40;

[15] A. Zocca, P. Colombo, C.M. Gomes, J. Günster, *Additive Manufacturing of Ceramics: Issues, Potentialities, and Opportunities*, Journal of the American Ceramic Society Vol. 98 (7), 2015, 1983-2001;

[16] P. Parandoush, D. Lin, *A review on additive manufacturing of polymer-fiber composites*, Composite Structure Vol. 182, 2017, 36-53;

[17] B. AlMangour, *Additive Manufacturing of Emerging Materials* (Springer, Cambridge, MA, USA, 2019);

[18] A. Bandyopadhyay, B. Heer, *Additive manufacturing of multi-material structures*, Material Science and Engineering: R: Reports Vol. 129, 2018, 1-16;

[19] G.H. Loh, E. Pei, D. Harrison, M.D. Monzónb, *An overview of functionally graded additive manufacturing*, Additive Manufacturing 23 (2018), 34-44;

[20] D. Bourell, J.P. Kruth, M. Leu, G. Levy, D. Rosen, A.M. Beese, A. Clare, *Materials for Additive Manufacturing*, CIRP Annals Vol. 66 (2), 2017, 659-681;

[21] M. Baumers, C. Tuck, R. Hague, *Selective Heat Sintering versus Laser Sintering: Comparison of Deposition Rate, Process Energy Consumption and Cost Performance*, Proceedings of SFF Symposium, 2015, 109–121;

[22] V.K. Balla, S. Bose, A. Bandyopadhyay, *Processing of Bulk Alumina Using Laser Engineered Net Shaping*, International Journal of Applied Ceramic Technology Vol. 5(3), 2008, 234–242;

[23] F.Y. Niu, D.J. Wu, S. Yan, G.Y. Ma, B. Zhang, *Process optimization for suppressing cracks in laser engineered net shaping of Al2O3 ceramics,* The Journal of the Minerals Vol. 69 (3), 2017, 557–562;

[24] Y.C. Hagedorn, N. Balachandran, W. Meiners, K. Wissembach, R. Poprawe, *SLM of Net-Shaped High Strength Ceramics: New Opportunities for Producing Dental Restorations,* Proceedings of the SFF Symposium, Austin TX USA 2011, 536–546;

[25] J. Wilkes, Y.C. Hagedorn, W. Meiners, K. Wissenbach, *Additive Manufacturing of ZrO2-Al2O3 Ceramic Components by Selective Laser Melting*, Rapid Prototyping Journal Vol. 19 (1), 2013, 51–57;

[26] D. Klosterman, R. Chartoff, N. Osborne, G. Graves, *Automated Fabrication of Monolithic and Ceramic Matrix Composites via Laminated Object Manufacturing (LOM)*, Proceedings of SFF Symposium, Austin TX USA, 1997, 537–550;

[27] D. Klosterman, R. Chartoff, N. Osborne, G. Graves, *Laminated Object Manufacturing, a New Process for the Direct Manufacture of Monolithic Ceramics and Continuous Fiber CMCs*, Proceedings of the 21st Annual Conference on Composites Ceramics Materials and Structures Vol. 8, 1997, 112–120;

[28] E. Griffin, D.R. Mumm, D.B. Marshall, *Rapid Prototyping of Functional Ceramic Composites*, American Ceramic Society Bulletin Vol. 75 (7), 1996, 65–68;

[29] M.L. Griffith, J. W. Halloran, *Freeform Fabrication of Ceramics via Stereolithography*, Journal of the American Ceramic Society Vol. 79 (10), 1996, 2601–2608;

[30] J. W. Halloran, M.L. Griffith, T.M. Chu, *Stereolithography resin for rapid prototyping of ceramics and metals*, US Patent #6,117,612;

[31] J. Deckers, K. Shahzad, J. Vleugels, J.P. Kruth, Isostatic Pressing Assisted Indirect Selective Laser Sintering of Alumina Components. Rapid Prototyping Journal Vol. 18 (5), 2012, 409–419;

[32] D. Espalin, A. J. Ramirez, F. Medina , R. Wicker, *Multi-Material, Multi- Technology FDM: Exploring Build Process Variations,* Rapid Prototyping Journal Vol. 20 (3), 2014, 236–244;

[33] T. Isobe, T. Tanaka, T. Nomura, R. Yuasa, *Comparison of strength of 3D printing objects using short fiber and continuous long fiber*, 13th International Conference on Textile Composites (TEXCOMP-13), 2018;

[34] D. Espalin, D. W. Muse, E. MacDonald, R. B. Wicker, *3D Printing multifunctionality: structures with electronics*, The International Journal of Advanced Manufacturing Technology Vol. 72 (5–8), 2014, 963–978;

[35] J. Duro-Royo, L. Mogas-Soldevila , N. Oxman, *Flow-Based Fabrication: an Integrated Computational Workflow for Digital Design and Additive Manufacturing of Multifunctional Heterogeneously Structured Objects*, Computer Aided Design Vol. 69, 2014, 143–154;

[36] J.P. Kruth, G. Levy, F. Klocke, *Consolidation Phenomena in Laser and Powder-bed Based Layered Manufacturing. CIRP Annals Manufacturing Technology* Vol. 56 (2), 2007, 730–759;

[37] A. Gasper, S. Catchpole-Smith, A.T. Clare, *In-Situ Synthesis of Titanium Aluminides by Direct Metal Deposition,* Journal of Materials Processing Technology Vol. 239, 2017, 230–239;

[38] P.K. Farayibi, J.A. Folkes, A.T. Clare, *Laser Deposition of Ti–6Al–4V Wire with WC Powder for Functionally Graded Components*, Materials and Manufacturing Processes 28(5), 2013, 514–518;

[39] P.K. Farayibi, J.A. Folkes, A.T. Clare, O. Oyelola, *Cladding of Pre-Blended Ti–6Al–4V and WC Powder for Wear Resistant Applications. Surface and Coatings Technology* Vol. 206 (2–3), 2011, 372–377;

[40] T.E. Abioye, P.K. Farayibi, D.G. McCartney, A.T. Clare, *Effect of Carbide Dissolution on the Corrosion Performance of Tungsten Carbide Reinforced Inconel 625 Wire Laser Coating*, Journal of Materials Processing Technology Vol. 231, 2016, 89–99;

[41] T.E. Abioye, J. Folkes, A.T. Clare, D.G. McCartney*, Concurrent Inconel 625 Wire and WC Powder Laser Cladding: Process Stability and Microstructural Characterisation*, Journal of Surface Engineering Vol. 29 (9), 2013, 647–653;

[42] E.E. de Obaldia, C. Jeong, L.K. Grunenfelder, D. Kisailus, P. Zavattieri, *Analysis of the Mechanical Response of Biomimetic Materials with Highly Oriented Microstructures Through 3D Printing*, Mechanical Testing and Modeling Journal of the Mechanical Behavior of Biomedical Materials Vol. 48, 2015, 70–85;

[43] J. Suwanprateeb, R. Sanngam, W. Suvannapruk, T. Panyathanmaporn, Mechanical and In Vitro *Performance of Apatite–Wollastonite Glass Ceramic Reinforced Hydroxyapatite Composite Fabricated by 3D-printing*, Journal of Materials Science: Materials in Medicine Vol. 20 (6), 2009, 1281–1289;

[44] M.C. Leu, B.K. Deuser, L. Tang, R.G. Landers, G.E. Hilmas, J.L. Watts, *Freeze-form Extrusion Fabrication of Functionally Graded Materials,* CIRP Annals Manufacturing Technology Vol. 61, 2012, 223–226;

[45] A. Li, A.S. Thornton, B. Deuser, J.L. Watts, M.C. Leu, G.E. Hilmas, R.G. Landers, *Freeze-form Extrusion Fabrication of Functionally Graded Material Composites Using Zirconium Carbide and Tungsten*, Proceedings of SFF Symposium, Austin TX USA, 2012, 467–479;

[46] A. El Hassanin, C. Velotti, F. Scherillo, A. Astarita, A. Squillace, L. Carrino, *Study of the solid state joining of additive manufactured components,* 2017 IEEE 3rd International Forum on Research and Technologies for Society and Industry (RTSI), Modena Italy, 2017, 4 pages;

[47] P.H. Lee, H. Chung, S.W. Lee, J. Yoo, J, Ko, *Review: Dimensional Accuracy in Additive Manufacturing Processes*, ASME 2014 International Manufacturing Science and Engineering Conference, Detroit USA, 2014, 8 pages;

[48] O. Pandey, N.V. Reddy, S. Dhande, *Part deposition orientation studies in layered manufacturing*, Journal of Materials Processing Technology Vol. 185, 2007, 125–131;

[49] W. Gao, Y. Zhang, D. Ramanujan, K. Ramani, Y. Chen, C.B. Williams, C.C.L. Wang, Y. C. Shin, S. Zhang, P.D. Zavattieri, *The status, challenges and future of additive manufacturing in engineering*, Computer Aided Design Vol. 69, 2015, 65–89;

[50] J.A. Slotwinski, E.J. Garboczi, P.E. Stutzman, C.F. Ferraris, S.S. Watson, M.A. Peltz, *Characterisation of Metal Powders Used for Additive Manufacturing*, Journal of Research of the National Institute of Standards and Technology Vol. 119, 2014, 460–493;

[51] O. Abdulhameed, A. Al-Ahmari, W. Ameen, S.H. Mian, *Additive Manufacturing: Challenges, Trends and Applications,* Advances in Mechanical Engineering Vol.11, 2019, 1-27;

[52] D. Herzog, V. Seyda, E. Wycisk, C. Emmelmann, *Additive Manufacturing of Metals*, Acta Materialia Vol. 117, 2016, 371-392;

[53] SLM Solutions GmbH, www.slm-solutions.com;

[54] EOS Electro Optical Systems GmbH, www.eos.info;

[55] Concept Laser GmbH, www.concept-laser.com;

[56] Trumpf GmbH & Co. KG, www.trumpf.com;

[57] H. Rafi, N. Karthik, H. Gong, T.L. Starr, B.E. Stucker, *Microstructures and mechanical properties of Ti6Al4V parts fabricated by selective laser melting and electron beam melting*, Journal of Materials Engineering and Performance Vol. 22 (12), 2013, 3872–83;

[58] C.J. Smith, F. Derguti, E. Hernandez, M. Thomas, S. Tammas-Williams, S. Gulizia, D. Fraser, I. Todd, *Dimensional accuracy of Electron Beam Melting (EBM) additive manufacture with regard to weight optimized truss structures*, Journal of Materials Processing Technology Vol. 229, 2016, 128–138;

[59] A. Gisario, M. Kazarian, F. Martina, M. Mehrpouya, *Metal additive manufacturing in the commercial aviation industry: A review*, Journal of Manufacturing Systems Vol. 53, 2019, 124–149;

[60] U. Prisco, A. Astarita, A. El Hassanin, S. Franchitti, *Influence of processing parameters on microstructure and roughness of electron beam melted Ti-6Al-4V Titanium alloy*, Materials and Manufacturing Processes, 2019, 9 pages;

[61] B. Vayssette, N. Saintiera, C. Brugger, M. Elmay, *Surface roughness of Ti-6Al-4V parts obtained by SLM and EBM: Effect on the High Cycle Fatigue Life,* Procedia Engineering Vol. 213, 2018, 89–97;

[62] A. Busachi, J. Erkoyuncu, P. Colegrove, F. Martina, C. Watts, R. Drake, *A review of additive manufacturing technology and cost estimation techniques for the defence sector*, CIRP Journal of Manufacturing Science and Technology Vol. 19, 2017, 117–28;

[63] A. Dass, A. Moridi, *State of the Art in Directed Energy Deposition: From Additive Manufacturing to Materials Design*, Coatings Vol. 9 (7), 2019, 26 pages;

[64] I. Gibson, D. Rosen, B. Stucker, Directed energy deposition processes (book chapter), *Additive Manufacturing Technologies* (Springer, New York, 2015), 245–268;

[65] ISO/ASTM 52911:2019(E), *Additive Manufacturing – Design – Part 1:Laser-based powder bed fusion of metals*, ASTM International, West Conshohocken, PA, 2019;

[66] A. Popovich, V. Sufiiarov, I. Polozov, E. Borisov, D. Masaylo, A. Orlov, *Microstructure and mechanical properties of additive manufactured copper alloy*, Materials Letters Vol. 179, 2016, 38-41;

[67] S. Scudino, C. Unterdörfer, K.G. Prashanth, H. Attar, N. Ellendt, V. Uhlenwinkel, J. Eckert, *Additive manufacturing of Cu-10Sn bronze*, Materials Letters Vol. 156, 2015, 202-204;

[68] I. Yadroitsev, P. Bertrand, B. Laget, I. Smurov, Annals of DAAAM for 2008 and Proceedings of the 19th International DAAAM Symposium, Vienna, 2008, 1535–1536;

[69] J.P. Kruth, B. Vandenbroucke, J. Van Vaerenbergh, and I. Naert, *Digital Manufacturing of Biocompatible Metal Frameworks for Complex Dental Prostheses by Means of SLS/SLM*, Taylor & Francis, 2005, 139–145;

[70] G.X. Chen, X.Y. Zeng, Z.M. Wang, K. Guan, C.W. Peng, *Fabrication of Removable Partial Denture Framework by Selective Laser Melting*, Advanced Materials Research Vol. 317-319, 2011, 174–178;

[71] V.E. Beal, P. Erasenthiran, C.H. Ahrens, P. Dickens, *Evaluating the use of functionally graded materials inserts produced by selective laser melting on the injection moulding of plastics parts*, Proceedings of the Institution of Mechanical Engineers, Part B: Journal of Engineering Manufacture Vol. 221, 2007, 945-954;

[72] M. Santorinaios, W. Brooks, C.J. Sutcliffe, R.A.W. Mines, *Crush behaviour of open cellular lattice structures manufactured using selective laser melting*, WIT Transactions on the Built Environment Vol. 85, 2006, 481-490;

[73] F. Feuerhahn, A. Schulz, T. Seefeld, F. Vollertsen, *Microstructure and properties of selective laser melted high hardness tool steel*, Physics Procedia Vol. 41, 2013, 836 – 841;

[74] T Laoui, E Santos, K Osakada, M Shiomi, M Morita, S K Shaik, N K Tolochko, F Abe, M Takahashi, *Properties of Titanium Dental Implant Models Made by Laser Processing*, Proceedings of the Institution of Mechanical Engineers, Part C: Journal of Mechanical Engineering Science Vol. 220 (6), 2006, 857-863;

[75] D. E. Cooper, M. Stanford, K. A. Kibble, G. J. Gibbons, *Additive Manufacturing for Product Improvement at Red Bull Technology*, Materials and Design Vol. 41, 2012, 226-230;

[76] S.P. Ringer, K. Raviprasad, *Development in age-hardenable Aluminum alloys and rational design of microstructure*, Materials Forum Vol. 24, 2000, 59-94;

[77] Y. Ding, J.A. Muñiz-Lerma, M. Trask, S. Chou, A. Walker, M. Brochu, *Microstructure and mechanical property considerations in additive manufacturing of Aluminum alloys*, Materials Research Society Vol. 41 (10), 2016, 745-751;

[78] K. Kempen, L.Thijs, J.Van Humbeeck, J.P. Kruth, *Mechanical Properties of AlSi10Mg Produced by Selective Laser Melting*, Physics Procedia Vol. 39, 2012, 439-446;

[79] S. Romano, A. Brückner-Foit, A. Brandão, J.Gumpinger, T.Ghidini, S.Beretta, *Fatigue properties of AlSi10Mg obtained by additive manufacturing: Defect-based modelling and prediction of fatigue strength*, Engineering Fracture Mechanics Vol. 187, 2018, 165-189;

[80] N.T. Aboulkhair, N.M. Everitt, I. Ashcroft, C. Tuck, *Reducing porosity in AlSi10Mg parts processed by selective laser melting*, Additive Manufacturing Vol. 1–4, 2014, 77-86;

[81] F. Caiazzo, V. Alfieri, P. Argenio, V. Sergi, *Additive manufacturing by means of laser-aided directed metal deposition of 2024 Aluminum powder: Investigation and optimization*, Advances in Mechanical Engineering 9 (2017), 1-12;

[82] M.J. Donachie, S.J. Donachie, *Superalloys a Technical Guide*, 2nd edn. (ASM International, Ohio, 2002);

[83] K.N. Amato, S.M. Gaytan, L.E. Murra, E. Martinez, P.W. Shindo, J. Hernandez, S.Collins, F.Medina, *Microstructures and mechanical behavior of Inconel 718 fabricated by selective laser melting*, Acta Materialia Vol. 60 (5), 2012, 2229-2239;

[84] L. Rickenbacher, T. Etter, S.Hövel, K. Wegener, *High temperature material properties of IN738LC processed by selective laser melting (SLM) technology*, Rapid Prototyping Journal Vol. 19 (4), 2013, 282-290;

[85] A. El Hassanin, F. Scherillo, A. Astarita, A. Squillace, *Cold Spinning of Nimonic 75 Parts: Microstructure Evolution and Heat Treatment*, Metallography, Microstructure and Analysis Vol. 8 (4), 2019, 488–494;

[86] L. E. Criales, Y.M. Arısoy, B. Lane, S. Moylan, A. Donmez, T. Özel, *Laser powder bed fusion of Nickel alloy 625: Experimental investigations of effects of process parameters on melt pool size and shape with spatter analysis*, International Journal of Machine Tools and Manufacture Vol. 121, 2017, 22-36;

[87] Q. Jia, D. Gu, *Selective laser melting additive manufacturing of Inconel 718 superalloy parts: Densification, microstructure and properties*, Journal of Alloys and Compounds Vol. 585, 2014, 713-721;

[88] A.A. Popovich, V. Sh. Sufiiarov, I. A. Polozov, E.V. Borisov, *Microstructure and Mechanical Properties of Inconel 718 Produced by SLM and Subsequent Heat Treatment*, Key Engineering Materials Vol. 651-653, 2015, 665-670;

[89] A. El Hassanin, F. Scherillo, A.T. Silvestri, A. Caraviello, R. Sansone, A. Astarita, A. Squillace, *Heat Treatment of Inconel Selective Laser Melted Parts: Microstructure Evolution*, AIP Conference Proceedings 2113, 2019, 6 pages;

[88]J. Dawes, R. Bowerman, R. Trepleton, *Introduction to the Additive Manufacturing Powder Metallurgy Supply Chain*, Johnson Matthey Technology Review Vol. 59 (3), 2015, 243-256;

[89] M.G. Pavlović, L.J. Pavlović, E.R. Ivanović, V. Radmilović, K.I. Popov, *The effect of particle structure on apparent density of electrolytic copper powder*, Journal of the Serbian Chemical Society Vol. 66 (11-12), 923-933;

[90] E.M. Trent, *mechanical methods of powder production as used in the carbide industry*, Powder Metallurgy Vol 1 (1-2), 1958, 65-72;

[91] A.J. Pinkerton, L. Lin, Direct additive laser manufacturing using gas- and water-atomised H13 tool steel powders, International Journal of Manufacturing Technology Vol. 25, 2005, 471-479;

[92] T.L. Starr, K. Rafi, B. Stucker, C.M. Scherzer, *Controlling phase composition in selective laser melted stainless steels*, Proceedings of SFF Symposium, 2012, 439-446;

[93] L.E. Murr, E. Martinez, J. Hernandez, S. Collins, K.N. Amato, S.M. Gaytan, P.W. Shindo, *Microstructures and properties of 17-4 PH Stainless steel fabricated by selective laser melting*, Journal of Materials and Research Technology Vol. 1 (3), 2012, 167-177;

[94] U. Ali, Y. Mahmoodkhani, S. I. Shahabad, R. Esmaeilizadeh, F. Liravi, E. Sheydaeian, K.Y. Huang, E. Marzbanrad, M. Vlasea, E. Toyserkani, *On the measurement of relative powder-bed compaction density in powder-bed additive manufacturing processes*, Materials and Design Vol. 155, 2018, 495–501;

[95] J. Hao,T. W. L. E. Wong, K.W. Dalgarno, *An overview of powder granulometry on feedstock and part performance in the selective laser melting process*, Additive Manufacturing Vol. 18, 2017, 228-255;

[96] H. Gong, *Generation and detection of defects in metallic parts fabricated by selective laser melting and electron beam melting and their effect on mechanical properties*, (2013), PhD thesis, Available from University of Louisville, completed in December 2013;

[97] T. Debroy, H.L. Wei, J.S. Zubach, T. Mukherjee, JW. Elmer, J.O. Milewski, A.M. Beese, A. Wilson-Heid, A. De, W. Zhang, *Additive manufacturing of metallic components - Process, structure and properties*, Progress in Materials Science Vol. 92, 2018, 112-224;

[98] R. Rashid, S.H. Masood, D. Ruana, S. Palanisamy, R.A. Rahman Rashid, M.Brandt, *Effect of scan strategy on density and metallurgical properties of 17-4PH parts printed by Selective Laser Melting (SLM)*, Journal of Materials Processing Technology Vol. 249, 2017, 502-511;

[99] H. Ali, H. Ghadbeigi, K. Mumtaz, *Effect of scanning strategies on residual stress and mechanical properties of Selective Laser Melted Ti6Al4V*, Materials Science and Engineering: A Vol. 712, 2018, 175-187;

[100] Y. Tian, D. Tomus, P. Rometsch, X. Wu, *Influences of processing parameters on surface roughness of Hastelloy X produced by selective laser melting,* Additive Manufacturing Vol. 13, 2017, 103–112;

[101] P. Hanzl, M. Zetek, T. Bakša e T. Kroupa, *The Influence of Processing Parameters on the Mechanical Properties of SLM parts*, Procedia Engineering Vol. 100, 2015, 1405-1413;

[102] M. Iebba, A. Astarita, D. Mistretta, I. Colonna, M. Liberini, F. Scherillo, C. Pirozzi, R. Borrelli, S. Franchitti, A. Squillace, *Influence of Powder Characteristics on Formation of Porosity in Additive*

Manufacturing of Ti-6Al-4V Components, Journal of Materials Engineering and Performance Vol. 26 (8), 4138-4147;

[103] B. Zhang, Y. Li, Q. Bai, *Defect Formation Mechanisms in Selective Laser Melting: A Review*, Chinese Journal of Mechanical Engineering Vol. 30, (2017), 515–527;

[104] F.H. Kim, S.P. Moylan, *Literature Review of Metal Additive Manufacturing Defects*, NIST Advanced Manufacturing Series Vol. 100, 2018, 17 pages;

[105] S.K. Everton, M. Hirsch, P. Stravroulakis, R.K. Leach, A.T. Clare, *Review of in-situ process monitoring and in-situ metrology for metal additive manufacturing*, Materials and Design Vol. 95, 2016, 431–445;

[106] C.A. Brown, H.N. Hansen, X.J. Jiang, F. Blateyron, J. Berglund, N. Senin, T. Bartkowiak, B. Dixon, G. Le Goïc, Y. Quinsat, W. J. Stemp, M.K. Thompson, P.S. Ungar, E.H. Zahouani, *Multiscale analyses and characterisations of surface topographies*, CIRP Annals - Manufacturing Technology Vol. 67, 2018, 839–862;

[107] S. Rahmati, E. Vahabli, *Evaluation of analytical modeling for improvement of surface roughness of FDM test part using measurement results*, International Journal of Advanced Manufacturing Technology Vol. 79 (5-8), 2015, 823-829;

[108] G. Strano, L. Hao, R. M. Everson, K. E. Evans, *Surface roughness analysis, modelling and prediction in selective laser melting*, Journal of Materials Processing Technology Vol. 213, 2013, 589-597;

[109] A. Gusarov, I. Smurov, *Modeling the interaction of laser radiation with powder bed at selective laser melting*, Physics Procedia Vol. 5, 2010; 381-394;

[110] S.A. Khairallah, A.T. Anderson, A. Rubenchik, W.E. King, *Laser powder-bed fusion additive manufacturing: Physics of complex melt flow and formation mechanisms of pores, spatter, and denudation zones*, Acta Materialia Vol. 108, 2016, 36-45;

[111] B. Xiao, Y. Zhang, Marangoni and Buoyancy Effects on Direct Metal Laser Sintering with a Moving Laser Beam, Numerical Heat Transfer, Part A: Applications Vol. 51(8), 2007, 715-733;

[112] P. Shoo, M.M. Collur, T. Debroy, Effect of oxygen and sulphur on alloying element vaporization rates during laser welding, Journal of Material Transaction B Vol. 19(6), 1988, 967-972;

[113] R.I. Campbell, M. Martorelli, H.S. Lee, Surface roughness visualization for rapid prototyping models. Computer Aided Design Vol. 34, 2002, 717–725;

[114] DMG Mori Seiki AG, https://it.dmgmori.com/prodotti/macchine/additive manufacturing/procedura-con-iniettore-di-polvere/lasertec-65-3d-hybrid;

[115] J.M. Flynn, A. Shokrani, S.T. Newman, V. Dhokian, *Hybrid additive and subtractive machine tools – Research and industrial developments*, International Journal of Machine Tools & Manufacture Vol. 101, 2016, 79–101;

[116] W. Du, Q. Bai, B. Zhang, *A Novel Method for Additive/Subtractive Hybrid Manufacturing of Metallic Parts*, Procedia Manufacturing Vol. 5, 2016, 1018–1030;

[117] A.H. Maamoun, M. A. Elbestawi, S.C. Veldhuis, *Influence of Shot Peening on AlSi10Mg Parts Fabricated by Additive Manufacturing*, Journal of Manufacturing and Materials Processing Vol. 40 (2), 2018, 16 pages;

[118] B. AlMangour, J.M. Yang, *Improving the surface quality and mechanical properties by shot-peening of 17-4 stainless steel fabricated by additive manufacturing*, Materials and Design Vol. 110, 2016, 914-924;

[119] A. D. Brandão, E. Beevers, S. Beretta, S. Romano, *Expression of Additive Manufacturing Surface Irregularities Through a flaw-Based Assessment*, STP ASTM symposium AM structural integrity, Washington D.C., 2018, 17 pages;

[120] M.A. Bernevig-Sava, C. Stamate, N.M. Lohan, A.M. Baciu, I. Postolache, C. Baciu, E.R. Baciu, *Considerations on the surface roughness of SLM processed metal parts and the effects of subsequent sandblasting*, IOP Conference Series: Materials Science and Engineering Vol. 572, 2019, 8 pages;

[121] A.C. Petare, N.K. Jain, *A critical review of past research and advances in abrasive flow finishing process,* The International Journal of Advanced Manufacturing Technology Vol. 97, 2018, 741–782;

[122] P. Tyagi, T. Goulet, C. Riso, F.G. Moreno, *Reducing surface roughness by chemical polishing of additively manufactured 3D printed 316 stainless steel components*, The International Journal of Advanced Manufacturing Technology Vol. 100, 2019, 2895–2900;

[123] J. Arredondo, B. Colleary, S. Miskell, B. Sweet, *Chemical milling and removal of the alpha* case, (Bachelor thesis), Worcester Polytechnic Institute, available online since Apr 26th 2010;

[124] L. Yang, H. Gu, A. Lassell, Surface treatment of Ti6Al4V parts made by powder bed fusion additive manufacturing processes using electropolishing, Department of Industrial Engineering, University of Louisville (2014);

[125] V. Urlea, V. Brailovski, *Electropolishing and electropolishing-related allowances for powder bed selectively laser-melted Ti-6Al-4V alloy components,* Journal of Materials Processing Technology Vol. 242 , 2017, 1–11;

[126] A. Kumar, N. S. Bandeshah, Dr. Nripjit, A. Nanda, R.K. Bandeshah, C. Gupta, *State of the art of CO2 Laser Beam Machining*, International Journal of Emerging Technology and Advanced Engineering Vol. 4 (4), 2014, 4 pages;

[127] R. Poprawe, *Tailored Light 2 – Laser Application Technology* (Springer, Aachen, 2011), 173–241;

[128] E. Yasa, J. Kruth, *Application of laser re-melting on selective laser melting parts*, Advances in Production Engineering & Management Vol. 6(4), 2011, 259-270;

[129] B. Rosa, P. Mognol, J.Y. Hascoët, *Laser polishing of Additive Manufacturing surfaces*, Journal of Laser Applications Vol. 27, 2015, 9 pages;

[130] B. Burzic, M. Hofele, S. Mürdter, H. Riegel, *Laser polishing of ground Aluminum surfaces with high continuous wave laser*, Journal of Laser Applications Vol. 29, 2017, 8 pages;

[131] J. Vaithilingam, R.D. Goodridge, R.J.M. Hague, S.D.R. Christie, S. Edmondson, *The effect of laser remelting on the surface chemistry of Ti6al4Vcomponents fabricated by selective laser melting*, Journal of Materials Engineering and Performance Vol. 212, 2016, 1-8;

[132] J.F. Davidson, R. Clift, D. Harrison, *Fluidisation*, (Academic Press, Stanford, 1985), 733 pages;

[133] D. Kunii, O. Levenspiel, *Fluidisation Engineering-2nd Edition*, (Butterworth-Heinemann, Boston, 1991), 491 pages;

[134] D. Geldart, *Types of gas fluidisation*, Powder Technology Vol. 7 (5), 1973, 285-292;

[135] E. Atzeni, M. Barletta, F. Calignano, L. Iuliano, G. Rubino, V. Tagliaferri, *Abrasive Fluidised Bed (AFB) finishing of AlSi10Mg substrates manufactured by Direct Metal Laser Sintering (DMLS)*, Additive Manufacturing Vol. 10, 2016, 15-23;

[136] M. Barletta, *Progress in Fluidised Bed Machining*, Journal of Material Processing Technology Vol. 209, 2009, 6087-6102;

[137] A. Yabuki, K. Matsuwaki, M. Matsumura, *Critical impact velocity in the solid particles impact erosion of metallic materials*, Wear Vol. 233-235, 1999, 468–475;

[138] A. Yabuki, M. Matsumura, *Theoretical equation of the critical impact velocity in solid particles impact erosion*, Wear Vol. 233-235, 1999, 476–483;

[139] M. Barletta, *A new technology in surface finishing: Fluidised bed machining (FBM) of Aluminum alloys*, Journal of Materials Processing Technology Vol. 173, 2006, 157–165;

[140] M. Barletta, S. Guarino, G. Rubino, V. Tagliaferri, *Progress in fluidised bed assisted abrasive jet machining (FB-AJM): Internal polishing of Aluminum tubes*, International Journal of Machine Tools and Manufacture Vol. 47 (3–4), 2009, 483-495;

[141] R. Polini, M. Barletta, M. Delogu, *Fluidised bed micro-machining and HFCVD of diamond films onto Co-cemented tungsten carbide (WC-Co) hardmetal slabs*, Thin Solid Films Vol. 515 (1), 2006, 87-94;

[142] I. Finnie, *Erosion of surface by solid particles*, Wear Vol. 3, 1960, 87‑103;

[143] Z. Gahr, *Wear by hard particles*, Tribology International Vol. 31(10), 1998, 587‑596;

[144] N.K. Jain, V.K. Jain, *Modelling of material removal in mechanical type advanced machining processes: a state of art review*, Journal of Machine Tools and Manufacture Vol. 41, 2001, 1573‑1635;

[145] P. Jacquet, *Electrolytic and Chemical Polishing*, Metallurgical Reviews Vol. 1(1), 1956, 157-238;

[146] G. Yang, K. Tawfiq, H. Wei, G. Chen, *Electropolishing of surfaces: theory and applications*, Surface Engineering Vol. 33, 2016, 1-18;

[147] Gleekman, L. W., et al., *An Improved Cell for Electrolytic Polishing*, Metal Progress Vol. 61, 1952, 92–93;

[148] M. Halfaway: Experientia, 1951, 7, 175;

[149] J. Edwards, *The mechanism of electropolishing of copper in phosphoricacid solutions ii. The mechanism of smoothing*, Journal of the Electrochemical Society Vol. 100, 1953, 223–230;

[150] C. Wagner, *Contribution to the theory of electropolishing*, Journal of the Electrochemical Society Vol. 101, 1954, 225–228;

[151] E.J. Casey, R.E. Bergeron, *On the mechanism of the dissolution of magnesium acidic salt solutions: I. Physical control by surface films*, Canadian Journal of Chemistry Vol. 31(9), 1953, 849-867;

[152] H. Kepling, F. Jingli, *Study on Chemical Polishing for Stainless Steel*, The International Journal of Surface Engineering and Coatings Vol. 76(1), 1998, 24-25;

[153] A.V. Balyakin, A.N. Shvetcov, E.I. Zhuchenko, *Chemical polishing of samples obtained by selective laser melting from Titanium alloy Ti6Al4V*, International Conference on Modern Trends in Manufacturing Technologies and Equipment (ICMTMTE) Vol. 224, 2018, 7 pages;

[154] Hérenguel et al, *Chemical polishing of Aluminum and its alloys*, 1959;

[155] C.M. Cotell, J.A. Sprague, F.A. Smidt, Jr, *Surface Engineering of Aluminum and Aluminum Alloys*, ASM Handbook Vol. 5, 1994, 784-804;

[156] A. Smithells, *Aggregation and Flow of Solids: Being the Records of an Experimental Study of the Micro-structure and Physical Properties of Solids in Various States of Aggregation, 1900–1921*, Nature Vol. 109, 1922, 262-265;

[157] E. Willenborg, K. Wissenbach, R. Poprawe, *Polishing by laser radiation*, International Conference on Lasers in Manufacturing, München, 2003;

[158] S.M. Pimenov, V.V. Kononenko, V.G. Ralchenko, V.I. Konov, S. Gloor,W. L¨uthy, H.P. Weber, A.V. Khomich, Laser polishing of diamond plates, Applied Physics A Vol. 69 (1), 1999, 81–88;

[159] A.P. Malshe, B.S. Park, W.D. Brown, N.A. Naseem, *A review of techniques for polishing and planarizing chemically vapor-deposited (CVD) diamond films and substrates*, Diamond and related materials Vol. 8 (7), 1999, 1198–1213;

[160] A. Bestenlehrer, Verfahren und Vorrichtung zum Bearbeiten von beliebigen 3D-Formfl¨achen mittels Laser, Europ¨aische Patentschrift EP 0 819 036 B1, 1996;

[161] D. Bergström, *The Absorption of Laser Light by Rough Metal Surfaces (Doctoral-Thesis)*, Luleå University of Technology, Sweden, 2008;

[162] K. Kanayama, H. Baba, *Directional Monochromatic Emittances of the Random Rough Surfaces of Metal and Nonmetals*, Transactions of the Japan Society of Mechanical Engineers Vol. 41, 1975, 30 pages;

[163] M.A. Obeidi, E. McCarthy, S.I. Ubani, I. Ul Ahad, D. Brabazon, *Effect of Surface Roughness on CO2 Laser Absorption by 316L Stainless Steel and Aluminum*, Materials Performance and Characterisation Vol. 8(6), 2019, 1167–1177;

[164] https://www.eos.info/material-m;

[165] F. Del Re, V. Contaldi, A. Astarita, B. Palumbo, A. Squillace, P. Corrado, P. Di Petta, *Statistical approach for assessing the effect of powder reuse on the final quality of AlSi10Mg parts produced by laser powder bed fusion additive manufacturing*, The International Journal of Advanced Manufacturing Technology Vol. 97(5-8), 2018, 2231–2240;

[166] ASTM B822-17, *Standard Test Method for Particle Size Distribution of Metal Powders and Related Compounds by Light Scattering*, ASTM International, West Conshohocken, PA, 2017;

[167] ASTM F1877-16, *Standard Practice for Characterisation of Particles*, ASTM International, West Conshohocken, PA, 2016;

[168] A. Townsend, N. Senin, L. Blunt, R.K. Leach, J.S. Taylor, *Surface texture metrology for metal additive manufacturing: a review*, Precision Engineering Vol. 46, 2016, 34–47;

[169] T. Grimm, G. Wiora, G. Witt, *Characterisation of typical surface effects in additive manufacturing with confocal microscopy*, Surface Topography: Metrology and Properties Vol. 3, 2015, 13 pages;

[170] BS EN ISO 25178-2, *Geometrical product specifications (GPS) — Surface texture: Areal Part 2: Terms, definitions and surface texture parameters*, British Standards Institution, 2012;

[171] BS EN ISO 4287, Geometrical product specifications (GPS) — *Surface texture: Profile method: Terms, Definitions and surface texture parameters*, British Standards Institution, 1998;

[172] https://www.olympus-ims.com/it/metrology/surface-roughness-measurement-portal/parameters/#!cms[focus]=areal-method (accessed in May 15th 2018)

[173] M. Yonehara, T. Matsui, K. Kihara, H. Isono, A. Kijima, T. Sugibayashi, *Evaluation Method of Surface Texture by Surface Roughness based on Geometrical Product Specifications (GPS)**, Materials Transactions Vol. 45, 2004, 1019 to 1026;

[174] K. Geels, D.B. Fowler, W.U. Kopp, M. Rückert, *Metallographic and Materialographic Specimen Preparation, Light Microscopy, Image Analysis and Hardness Testing* (ASTM International, Lancaster, 2007);

[175] https://www.pfonline.com/articles/abrasive-blasting-understanding-the-basics-of-media-selection;

[176] B. Chatterjee, Chemical Brightening of Aluminum, Materials Chemistry and Physics Vol. 10, 1984, 357-364;

[177] E. Brandl, U. Heckenberger, V. Holzinger, D. Buckbinder, Additive Manufactured AlSi10Mg samples using Selective Laser Melting (SLM), Materials & Design Vol. 34, 2012, 159-169;

[178] C.M. Cotell, J.A. Sprague, F.A. Smidt, Jr., *Surface Engineering of Aluminum and Aluminum Alloys*, ASM International Vol. 5, 1994, 704-804;

[179] L.C. Branch, *Bright Dipping Aluminum*, Metal Finishing Vol. 96, 1998, 24-29;

[180] https://www.rofin.com/fileadmin/user_upload/biografien/COHR_DC_Series_DS_0619web.pdf;

[181] D.C. Montgomery, *Design and Analysis of Experiments - 8th Edition* (Wiley, Arizona State University, 2012);

[182] S.M. Thompson, L. Bian, N. Shamsaei, A.Yadollahi, An overview of Direct Laser Deposition for additive manufacturing; Part I: Transport phenomena, modeling and diagnostics, Additive Manufacturing Vol. 8, 2015, 36–62.

Acknowledgements

Appendix: Methodology for data reported in Chapter 3

The collected data on global research trend reported in Fig. 3.1 is based on online research via Scopus (https://www.scopus.com/), accessed on 7th February 2020 unless specifically cited. The research was based on different key words according to each surface treatment considered, as shown in Table I. The number of publication on post-process surface finishing of metal AM parts collected here is referred to global scale, including article, conference paper, review, book chapter and article in Press. The analysis does not take into account of the impact factor due to complexity to weigh in and lack of unified and consistent terminology for different AM finishing techniques.

Table I. Scopus keywords used to collect the data illustrated in Fig. 3.1.

Surface treatment	Keywords
Shot peening	"shot peening additive manufacturing"
Sand blasting	"sand blasting additive manufacturing"
CNC machining	"cnc machining additive manufacturing" "hybrid manufacturing" "machining of additive manufactured parts"
Abrasive Flow Machining	"abrasive flow machining additive manufacturing"
Fluidised Bed Machining	"fluidized bed machining additive manufacturing" "abrasive fluidized bed additive manufacturing" "abrasive fluidized bed"
Vibratory polishing	"vibratory polishing additive manufacturing"
Chemical Polishing	"chemical finishing additive manufacturing" "chemical polishing additive manufacturing"
Electrochemical polishing	"electropolishing additive manufacturing" "electrochemical polishing additive manufacturing"
Laser polishing	"laser polishing additive manufacturing" "laser re melting additive manufacturing"